



저작자표시-비영리-변경금지 2.0 대한민국

이용자는 아래의 조건을 따르는 경우에 한하여 자유롭게

- 이 저작물을 복제, 배포, 전송, 전시, 공연 및 방송할 수 있습니다.

다음과 같은 조건을 따라야 합니다:



저작자표시. 귀하는 원저작자를 표시하여야 합니다.



비영리. 귀하는 이 저작물을 영리 목적으로 이용할 수 없습니다.



변경금지. 귀하는 이 저작물을 개작, 변형 또는 가공할 수 없습니다.

- 귀하는, 이 저작물의 재이용이나 배포의 경우, 이 저작물에 적용된 이용허락조건을 명확하게 나타내어야 합니다.
- 저작권자로부터 별도의 허가를 받으면 이러한 조건들은 적용되지 않습니다.

저작권법에 따른 이용자의 권리는 위의 내용에 의하여 영향을 받지 않습니다.

이것은 [이용허락규약\(Legal Code\)](#)을 이해하기 쉽게 요약한 것입니다.

[Disclaimer](#)

공학박사 학위논문

**Impact Resistance of High
Performance Concrete Panels under
High Velocity Projectile Collision**

고속충돌 하중을 받는 고성능 콘크리트 패널의
내충격성 평가 및 설계식 개발

2018 년 8 월

서울대학교 대학원

건축학과

김 상 희

공학박사 학위논문

**Impact Resistance of High
Performance Concrete Panels under
High Velocity Projectile Collision**

고속충돌 하중을 받는 고성능 콘크리트 패널의
내충격성 평가 및 설계식 개발

2018 년 8 월

서울대학교 대학원

건축학과

김 상 희

Impact Resistance of High Performance Concrete Panels under High Velocity Projectile Collision

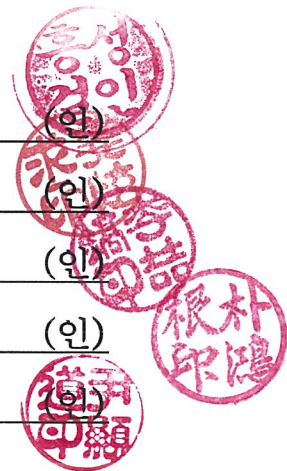
지도 교수 강 현 구

이 논문을 공학박사 학위논문으로 제출함
2018 년 8 월

서울대학교 대학원
건축학과
김 상 희

김상희의 공학박사 학위논문을 인준함
2018 년 8 월

위 원 장	홍 성 결	(인)
부위원장	강 현 구	(인)
위 원	이 철 호	(인)
위 원	박 홍 근	(인)
위 원	윤 현 도	(인)



Abstract

Impact Resistance of High Performance Concrete Panels under High Velocity Projectile Collision

Sanghee Kim

Department of Architecture and Architectural Engineering
College of Engineering
Seoul National University

Although many studies on impact and explosions have been made due to the frequent occurrence of collisions and explosions that threaten the safety of concrete structures, it is not easy to predict damage to a concrete panel under high velocity impact loads due to the complexity of the impact mechanism of concrete. In this paper, various experimental and analytical studies are carried out to evaluate the impact resistance of concrete, and a new local impact formula is proposed to predict local damage levels.

In order to evaluate the impact resistance of a concrete panel with various parameters that were not investigated much, three experiments are carried out different. In the first experiment, the effect of steel fibers and wire mesh on impact resistance is investigated. In addition, aggregate size, panel thickness and projectile speed are used as parameters. The second experiment uses concrete strengths of 30

~ 150 MPa and five kinds of bullets in order to evaluate the impact strength according to both concrete strength and the nose shape of the projectile. The third experiment evaluates the impact resistance of a thin panel using 180 MPa concrete. For the second and third experiments, a small impact test device developed by the author is used.

Based on the experimental results, the impact mechanism is classified into six categories: deformed energy of the projectile, elastic penetration resistance energy of the panel, overall deformed energy of the panel, spalling-resistant energy, tunneling-resistant energy, and scabbing-resistant energy. Using these impact mechanism and energy conservation laws, new penetration depth, scabbing depth, scabbing limit thickness, and perforation limit thickness are proposed. The validity of the proposed impact formula is verified using the results of the current experiment and other research.

Supplementary nonlinear analysis is performed to investigate how reinforcing bars affect the impact resistance of reinforced concrete panels, as the presence of reinforcing steel was identified as one of the unclarified parameters during the test. In addition, the effects of projectile size, panel area, and thickness on impact resistance, which are insufficiently studied in the experiments, are examined through nonlinear analysis.

Keywords: Collision, impact formula, high velocity impact load, impact resistance, concrete slab, dynamic cavity expansion model, energy conservation, energy density, Hertzian contact theory, small impact test device.
Student Number: 2014-30188

Contents

Abstract.....	i
Contents.....	iii
List of Tables	viii
List of Figures.....	x
List of Symbols	xviii
Chapter 1. Introduction	1
1.1 Motivation for Research	1
1.2 Scope and Objectives.....	9
1.3 Organization	12
Chapter 2. Literature Review	15
2.1 History of Research on Impact Formulae	15
2.2 Existing Impact Formulae.....	20
2.3 Existing Impact Experiment.....	36
2.4 Nonlinear Analysis	43
2.4.1 Nonlinear analysis programs.....	43
2.4.2 Concrete model for nonlinear analysis	47
2.5 Discussion	55

Chapter 3. Design of Small Impact Test Device.....57

3.1 Purpose of Contravening Impact Test Device..... 57

3.2 Impact Test Device Type..... 60

3.3 Design Process of Impact Test Device..... 61

 3.3.1 Design objectives 61

 3.3.2 Overall plan 64

 3.3.3 Design of air-compressor and air tank capacity 65

 3.3.4 Design of barrel size and details 67

 3.3.5 Solenoid valve..... 74

 3.3.6 Experimental chamber 76

 3.3.7 Modification of impact test device 78

3.4 Manufacturing Process..... 81

 3.4.1 Air compressor system 81

 3.4.2 Barrel and experimental chamber 83

 3.4.3 Installation of impact test device..... 87

3.5 Discussion 90

**Chapter 4. Impact Experiment and Performance Evaluation
..... 93**

4.1 Specimen Construction 94

 4.1.1 First experiment plan 94

 4.1.2 Second experiment plan..... 101

 4.1.3 Third experiment plan 105

4.2 Impact Experiment..... 109

 4.2.1 First experiment 109

 4.2.2 Second experiment 111

 4.2.3 Third experiment 113

4.3 Material Test and Results 115

4.3.1 Material test	115
4.3.2 Discussion of concrete properties for experiment	116
4.4 Analysis of Experimental Results	121
4.4.1 First Experiment	121
4.4.2 Second experiment	139
4.4.3 Third experiment	147
4.5 Empirical Parameters	156
4.6 Discussion	158

Chapter 5. Development of New Energy-Based Impact Formula.....163

5.1 Concept of New Formula	164
5.1.1 Materials for impact mechanism	164
5.1.2 Impact mechanism and energy conservation	164
5.1.3 Forces acting in impact mechanism	167
5.1.4 Force on nose of projectile.....	174
5.2 Properties of Materials Affected by Strain Rate.....	180
5.2.1 Definition of strain rate.....	180
5.2.2 Properties of concrete affected by strain rate.....	186
5.2.3 Properties of steel affected by strain rate.....	188
5.3 Involved Energies in Impact Mechanism.....	189
5.3.1 Kinetic energy (E_K)	189
5.3.2 Deformed energy of projectile (E_{DP})	189
5.3.3 Resistance energy to penetration.....	190
5.4 Derivation of New Energy-Based Impact Formula	204
5.4.1 Penetration depth formula.....	204
5.4.2 Scabbing depth formula.....	206
5.4.3 Scabbing limit thickness formula.....	207
5.4.4 Perforation limit thickness formula	209

5.5 Verification of Developed Impact Formula.....	210
5.5.1 Comparison between test results and predictions.....	210
5.5.2 Penetration depth assessment.....	213
5.5.3 Scabbing depth assessment.....	226
5.5.4 Scabbing limit thickness assessment.....	228
5.5.5 Perforation limit thickness assessment.....	230
5.6 Critical Impact Mechanism.....	233
5.7 Potential Application Example.....	238
5.8 Discussion.....	241
Chapter 6. Supplementary Nonlinear Analysis	245
6.1 Modeling of Impact Test Model.....	246
6.1.1 Validation of concrete model.....	246
6.1.2 Plan of nonlinear analysis on effect of rebar.....	251
6.1.3 Projectile aspect ratio.....	257
6.1.4 Panel area.....	261
6.1.5 Panel thickness.....	263
6.2 Results of Nonlinear Analysis.....	265
6.2.1 Reinforcing bars.....	265
6.2.2 Projectile aspect ratio.....	272
6.2.3 Panel area.....	277
6.2.4 Panel thickness.....	280
6.3 Discussion.....	285
Chapter 7. Summary and Conclusions	287
7.1 Summary.....	287
7.2 Conclusions.....	288
References.....	295

국 문 초 록315

Acknowledgement317

List of Tables

Table 1-1 Recommended impact formulae in manuals or guidelines (Li <i>et al.</i> , 2005)	4
Table 2-1 Parameters of concrete and projectile	19
Table 2-2 Summary of impact formulae (Kojima, 1990; Bangash, 2001; Li <i>et al.</i> , 2005; Teland, 2007; Ben-Dor <i>et al.</i> , 2013; Kim <i>et al.</i> , 2017).....	20
Table 2-3 Applications of explicit dynamics of ANSYS benchwork 12 (Kim, 2009)	44
Table 3-1 Carbon steel pipe for pressure service (KS D 3562 (Korea Agency for Technology and Standards, 2018))	71
Table 4-1 First experiment plan and specimen details.....	95
Table 4-2 Mix proportion of concrete.....	97
Table 4-3 Properties of end-hooked steel fibers.....	100
Table 4-4 Mixed proportions of concrete for second experiment	102
Table 4-5 Mix proportion of K-UHPC for third test	106
Table 4-6 Measured properties of concrete (unit: MPa).....	119
Table 4-7 Normalized average of penetration depth to G -/ I -functions according to steel fiber volume fraction (unit: mm)	124
Table 4-8 Number of specimens with scabbing failure (including perforation)...	127
Table 4-9 Comparison of specimens with and without wire mesh.....	128
Table 4-10 Average ratios of tested penetration depth to I -Haldar	134
Table 4-11 Average ratios of tested scabbing depth to I -Haldar	135
Table 4-12 Nose shape factor in formulae	140

Table 4-13 Results of second test.....	143
Table 4-14 Selected specimen of UHPC.....	150
Table 4-15 Empirical parameters involved in impact.....	157
Table 5-1 Summary of previous test and current test programs.....	212
Table 5-2 Average ratio of tested to predicted penetration	214
Table 5-3 Number of specimens with scabbing failure	227
Table 5-4 Accuracy of scabbing limit thickness formula.....	230
Table 5-5 Accuracy of scabbing limit thickness formula.....	232
Table 5-6 Energy Portion.....	234
Table 5-7 Average ratio of tested to predicted penetration according to proposed and simplified formulae	237
Table 5-8 Characteristics of small arms and aircraft cannon	240
Table 6-1 Key parameters of concrete for explicit analysis.....	247
Table 6-2 Results of nonlinear analysis for 30, 70 mm thickness	249
Table 6-3 Key parameters of steel for explicit analysis.....	251
Table 6-4 Plan of nonlinear analysis	252
Table 6-5 Projectiles in nonlinear analysis	259
Table 6-6 Penetration depth according to proposed formula and nonlinear analysis	266
Table 6-7 Results of nonlinear analysis with various projectiles	272
Table 6-8 Results of nonlinear analysis with various panel areas	278
Table 6-9 Results of nonlinear analysis according to various thicknesses.....	284

List of Figures

Figure 1-1 Special-level buildings categorized by KBC-16.....	2
Figure 1-2 Local damage by mechanical impact accident.....	3
Figure 1-3 Development history of ultra-high strength concrete (UHPC) (redrawn from Lee <i>et al.</i> , 2011).....	5
Figure 2-1 History of impact formulæ (Kojima, 1990; Bangash, 2001; Li <i>et al.</i> , 2005; Teland, 2007; Ben-Dor <i>et al.</i> , 2013; Kim <i>et al.</i> , 2017).....	17
Figure 2-2 Missile impact phenomena (Kennedy, 1976).....	18
Figure 2-3 Used penetration model on Hughes (1984)	28
Figure 2-4 Used experimental data for scabbing and perforation limit thickness formula (Hughes, 1984)	30
Figure 2-5 Response regions (Forrestal and Luk, 1988)	33
Figure 2-6 Nose shape and definition by Chen and Li (2002).....	35
Figure 2-7 Specimen plan by Almusallam <i>et al.</i> (2013).....	36
Figure 2-8 Test results by Almusallam <i>et al.</i> (2013)	37
Figure 2-9 Three types of projectiles with various ogive noses (CRH (caliber radius head) is top of 3.0, middle of 4.25, bottom of 2.0) (Forrestal <i>et al.</i> , 1994)	38
Figure 2-10 Relationship between penetration depth and concrete compressive strength (Zhang <i>et al.</i> , 2005)	39
Figure 2-11 Detail of reinforced concrete slab (Abdel-Kader and Fouda, 2014)...	40
Figure 2-12 Photos of impacted specimens (Frew <i>et al.</i> , 2006).....	42
Figure 2-13 Process of ANSYS explicit dynamic analysis (ANSYS, 2011).....	43
Figure 2-14 Representative application shown on ANSYS website	45

Figure 2-15 Material data library in ANSYS AUTODYN	47
Figure 2-16 Elastic and failure surfaces in RHT model based on Chen’s concept (1982) with stress points and areas measurable by different static and dynamic loadings (Thoma, 2009)	48
Figure 2-17 RHT strength surfaces of elasticity, ultimate strength and post failure shear resistance strength (Thoma, 2009).....	50
Figure 2-18 RHT representation of compressive meridian (ANSYS, 2015).....	50
Figure 2-19 Third invariant dependence (ANSYS, 2015).....	51
Figure 2-20 Bilinear strain hardening (Hu <i>et al.</i> , 2016).....	52
Figure 2-21 RHT elastic, fracture and residual failure surfaces (ANSYS, 2017)..	54
Figure 3-1 Impact test devices	58
Figure 3-2 Strain rate domains, strain rates due to real loading sources (Hong and Kang, 2016).....	60
Figure 3-3 Key items for developing small impact test device.....	62
Figure 3-4 Overall plan	64
Figure 3-5 Pressure ratio and tank capacity relationship.....	67
Figure 3-6 Free body diagram of projectile.....	69
Figure 3-7 Conception of carrier-blocking	72
Figure 3-8 Details of end of barrel (unit: mm)	72
Figure 3-9 Drawing of loading chamber and retrieving chamber (unit: mm).....	73
Figure 3-10 Cutting of barrel.....	73
Figure 3-11 Cover with wings of loading chamber	74
Figure 3-12 Details of solenoid valve	75
Figure 3-13 Foot button and solenoid valve	75
Figure 3-14 Drawing of chambers (unit: mm).....	76
Figure 3-15 Velocity measurement with lighting system and jig to fix position and provide protection.....	77

Figure 3-16 Modification of chamber (unit: mm).....	78
Figure 3-17 Breathing holes	79
Figure 3-18 PVC pipe (www.abwplastics.co.uk).....	80
Figure 3-19 Manufacturing air compressor and air tank system.....	82
Figure 3-20 Details of air compressor system	83
Figure 3-21 V-band clamp and C-channel for installing barrel.....	84
Figure 3-22 Honing process (dev.carlsontool.com)	85
Figure 3-23 Manufacturing barrel and experimental chamber	86
Figure 3-24 Installation of impact test device.....	88
Figure 3-25 Impact test device.....	89
Figure 4-1 Dimension of specimen (unit: mm).....	97
Figure 4-2 Specimen ID of first experiment.....	97
Figure 4-3 Dimensions of specimen and layout of wire mesh (unit: mm)	98
Figure 4-4 Steel wire mesh.....	98
Figure 4-5 Dimension of single hooked steel fiber (unit: mm).....	99
Figure 4-6 Process of production of specimens	100
Figure 4-7 Specimen ID of second experiment	103
Figure 4-8 Production of test panels and mold	104
Figure 4-9 Application of ultra-high performance concrete (Musée des Civilisations de l'Europe et de la Méditerranée, France (http://www.mucem.org)).....	105
Figure 4-10 Specimen ID of third experiment.....	107
Figure 4-11 Production of UHPC panel	108
Figure 4-12 Impact test device at Chungnam National University	110
Figure 4-13 Specimen set-up (top) and size of frame (bottom) (unit: mm).....	110

Figure 4-14 Types of projectiles (unit: mm)	112
Figure 4-15 Muzzle energy of various cartridges (kgf.m) (http://www.shooterscalculator.com)	113
Figure 4-16 Test set-up	114
Figure 4-17 Material properties tests	116
Figure 4-18 Compressive and flexural strengths in first experiment	117
Figure 4-19 Vertical section of cylinders after splitting test	119
Figure 4-20 Tensile stress-strain curve of steel fibers	120
Figure 4-21 Relationship between penetration depth and steel fiber volume fraction	121
Figure 4-22 Ratio of tested penetrations depth to G-function or impact factors..	123
Figure 4-23 Relationship between weight loss and steel fiber volume fraction ..	126
Figure 4-24 Relationship between area loss on front face and steel fiber volume fraction	126
Figure 4-25 Definition of $D_{eq,front}$, $D_{eq,hole}$ and $D_{eq,rear}$	129
Figure 4-26 $D_{eq,front}$ to d_p ratio and $D_{eq,front}/D_{eq,hole}$ or $D_{eq,rear}/D_{eq,hole}$ according to steel fiber volume fraction.....	130
Figure 4-27 Penetration depth for specimens with spalling and spalling (R).....	133
Figure 4-28 Average ratio of tested penetration depth normalized to Haldar impact factor for penetrated specimens	134
Figure 4-29 Average ratio of tested scabbing depth normalized to Haldar impact factor for scabbed or perforated specimens	135
Figure 4-30 Front area loss to rear area loss ratio for specimens with perforation	136
Figure 4-31 Loss-weight for specimens with perforation due to 350 m/s velocity impact.....	137
Figure 4-32 Scabbing theory and tension force ($f_{yt, mesh}$ = tensile strength of steel wire mesh, f_t = tensile strength of concrete)	139

Figure 4-33 Long-conical and long-hemisphere (unit: mm).....	140
Figure 4-34 Relationship of measured compressive strength of concrete and penetration depth	141
Figure 4-35 Relationship of measured compressive strength of concrete and penetration depth normalized by kinetic energy	141
Figure 4-36 Relationship of measured concrete strength and ratio of tested penetration depth to predicted penetration depth of modified NDRC formula	145
Figure 4-37 Relationship of measured concrete strength and ratio of tested penetration depth to predicted penetration depth of Hughes formula.....	145
Figure 4-38 Predicted penetration depth of the modified NDRC and Hughes formula according to concrete compressive strength.....	146
Figure 4-39 Comparison of appearance of each material	148
Figure 4-40 Weight loss for specimens	151
Figure 4-41 Area loss of specimens	152
Figure 4-42 Shear plug model (Li and Tong, 2003).....	152
Figure 4-43 Strain history of rear face of tested specimens.....	154
Figure 4-44 Normalized strain history of rear face	155
Figure 5-1 Energies involved in impact mechanism	166
Figure 5-2 Stress flow on interface between spalled concrete and slab	168
Figure 5-3 Stress flow on interface between scabbled concrete and slab.....	168
Figure 5-4 Principal stress failure criteria of concrete subjected to shear-compression (Park <i>et al.</i> , 2011; Choi <i>et al.</i> , 2014).....	169
Figure 5-5 Distributions of normal stress and shear stress capacity according to the curvature at cross section (Park <i>et al.</i> , 2011).....	172
Figure 5-6 Compressive force acting upon all surfaces (hydrostatic condition)..	176
Figure 5-7 Strength of brittle materials affected by strain-rate (redrawn from Qi <i>et al.</i> , 2009)	180
Figure 5-8 Schematic of compression Kolsky bar (Ramesh, 2008).....	181

Figure 5-9 Wave propagation diagram using Kolsky Bar (Ramesh, 2008).....	182
Figure 5-10 Hertz contact theory (www.wikipedia.org).....	191
Figure 5-11 Spalled cone and truncated shape.....	194
Figure 5-12 Scabbing theory (Kolsky, 1963; Society of Material Science of Japan, 1988).....	199
Figure 5-13 Stress distribution when sphere (a) or cylinder (b) contact half-space with Poisson's ratio of 0.3 (Williams and Dwyer-Joyce, 2000)	201
Figure 5-14 Definition of a_{ct}	202
Figure 5-15 Relationship of the distance (z) and the penetration depth (x_{pe}).....	203
Figure 5-16 Idealized spalled cone	206
Figure 5-17 Perforation definition in this study.....	209
Figure 5-18 Ratio of tested to predicted penetration depth (Avg. is the average and SD is the standard deviation).....	215
Figure 5-19 Ratio of tested to predicted penetration depth according to h to d_p (Avg. is the average and SD is the standard deviation)	218
Figure 5-20 Ratio of tested to predicted penetration depth according to velocity (Avg. is the average and SD is the standard deviation).....	221
Figure 5-21 Ratio of tested to predicted penetration depth according to concrete compressive strength (Avg. is the average and SD is the standard deviation)	223
Figure 5-22 Ratio of tested to predicted penetration depth according to kinetic energy per contact area (Avg. is the average and SD is the standard deviation)	225
Figure 5-23 Ratio of tested to predicted scabbing depth	226
Figure 5-24 Ratio of tested penetration depth to scabbing depth.....	228
Figure 5-25 Panel thickness (h) divided by predicted scabbing limit thickness (h_{sc})	229
Figure 5-26 Panel thickness (h) divided by predicted perforation limit thickness (h_{pf}).....	231

Figure 5-27 Average energy portion.....	235
Figure 5-28 Tested to penetration depth by detailed formula and simplified formula	237
Figure 5-29 Classification of flying objects and concrete structures	238
Figure 6-1 Penetrated specimen with provided concrete materials.....	248
Figure 6-2 Equivalent stress on sectional, top, and bottom of 30 mm thickness ..	249
Figure 6-3 Equivalent stress on sectional, top, and bottom of 70 mm thickness ..	250
Figure 6-4 Dimensions of concrete panel for nonlinear analysis.....	252
Figure 6-5 Plan of reinforcing bar lay-out.....	253
Figure 6-6 Plan of projectile	255
Figure 6-7 Modeling in Modeler.....	255
Figure 6-8 Mesh of reinforced concrete panel with spacing of 40 mm.....	256
Figure 6-9 Boundary conditions and initial velocity.....	256
Figure 6-10 Models with various shapes of projectile	260
Figure 6-11 Models with various areas	262
Figure 6-12 Analysis results of specimen of 600 × 600 × 200 mm with 10 mm mesh size	262
Figure 6-13 Nonlinear analysis model with various thicknesses	264
Figure 6-14 Equivalent stress of concrete body at peak stage (MPa)	267
Figure 6-15 Shear stress of reinforced concrete panel (MPa).....	268
Figure 6-16 Penetration depth of results of reinforced concrete panel with spacing of 50 mm	269
Figure 6-17 Plastic energy in concrete body.....	270
Figure 6-18 Stress reflection and merge on projection line.....	271
Figure 6-19 Equivalent stress of concrete body at peak stage (MPa)	276
Figure 6-20 Equivalent stress of various panel models (MPa)	279

Figure 6-21 Contour maps of vertical displacement on bottom face (unit: mm).	280
Figure 6-22 Equivalent stress of analyzed specimens (MPa).....	283
Figure 6-23 Plastic energy of specimens	284

List of Symbols

a	=	acceleration
a_{ct}	=	radius of contact area
a_{gg}	=	maximum size of coarse aggregate
$A_{carrier}$	=	cross-sectional area of carrier
A_{cube}	=	area of one cube's face
A_{Fail}	=	user defined parameters
$A_{in,barrel}$	=	inner cross sectional area of barrel
A_s	=	cross-sectional area of specimen of Kolsky Bar
A_{sc}	=	base area of scabbed cone
$A_{sp,big}$	=	base area of spalled cone
$A_{sp,lateral}$	=	lateral area of spalled cone
$A_{sp,little}$	=	top area of spalled cone
A_t	=	sectional area of tunnel
b_{panel}	=	width of specimens
BQ	=	coefficient that defines rate at which fracture surface transitions from being approximately triangular in form to a circular form with increasing pressure
c_b	=	bar wave speed in Kolsky Bar test
c_u	=	depth of concrete compression zone
$d_{elastic}$	=	elastic penetration depth by Hertzian contact theory
d_f	=	steel fiber diameter

$d_{in,barrel}$	=	inner diameter of barrel
d_p	=	diameter of projectile
d_{panel}	=	average effective depth
$D_{eq,front}$	=	equivalent circle diameter of spalling area
$D_{eq,hole}$	=	equivalent circle diameter of internal perforation area
$D_{eq,rear}$	=	equivalent circle diameter of scabbing area
D_{pipe}	=	outer diameter of steel pipe
E_b	=	elastic modulus of input or output bar Kolsky Bar test
$E_{b,in}$	=	elastic modulus of input bar Kolsky Bar test
$E_{b,out}$	=	elastic modulus of output bar Kolsky Bar test
$E_{c,st}$	=	elastic modulus of concrete under static loading
$E_{c,st}$	=	elastic modulus of concrete under static loading
$E_{carrier}$	=	Young's modulus of carrier
$E_{cc,dyn}$	=	compressive elastic modulus of concrete under dynamic loading
$E_{cc,st}$	=	compressive modulus of concrete under static loading
$E_{cc,st}$	=	elastic modulus of concrete under static loading
$E_{ct,dyn}$	=	tensile elastic modulus of concrete under dynamic loading
E_{DP}	=	deformed energy of projectile
E_{DS}	=	overall deformed energy of concrete panel
E_{EP}	=	elastic deformed energy of concrete panel
$E_{internal}$	=	internal energy.
E_K	=	kinetic energy
$E_{p,dyn}$	=	elastic modulus of projectile affected by strain rate

$E_{p,st}$	=	elastic modulus of projectile under static loading
E_{SC}	=	scabbing-resistant energy
$E_{sc,max}$	=	maximum energy on contact point
$E_{SC,remain}$	=	remaininig energy
$E_{sc,z}$	=	scabbing energy at z point
E_{SP}	=	spalling-resistant energy
E_T	=	tunneling-resistant energy
f'_c	=	compressive strength of concrete
$f'_{c,design}$	=	design compressive strength of concrete
$f'_{c,dyn}$	=	dynamic compress stress of concrete
$f'_{c,dyn}$	=	compressive stress of concrete under dynamic loading
$f'_{c,meas}$	=	measured compressive strength of concrete
$f'_{c,st}$	=	static compressive stress of concrete
$f'_{c,st}$	=	compressive stress of concrete under static loading
$f_{failure}$	=	failure surface
f_r	=	modulus rupture of concrete
$f_{r,dyn}$	=	modulus of rupture of concrete (MPa) affected by strain rate
$f_{r,meas}$	=	measured flexural strength of concrete
f_{sp_meas}	=	measured concrete splitting strength
$f_{t,dyn}$	=	dynamic tensile stress of concrete
$f_{t,dyn}$	=	tensile stress of concrete under dynamic loading
$f_{t,st}$	=	static tensile stress of concrete
$f_{t,st}$	=	tensile stress of concrete under static loading

$f_{ts,dyn}$	=	dynamic tensile stress of steel fiber-reinforced concrete affected by strain rate
$f_{ts,st}$	=	static tensile stress of steel fiber-reinforced concrete
$f_{y,dyn}$	=	tensile stress of steel under the dynamic loading
$f_{y,st}$	=	tensile stress of under the static loading
$f_{yt,mesh}$	=	tensile strength of steel wire mesh
F	=	acting force
F_a	=	air tank force
F_b	=	atmospheric force
F_{cap}	=	elliptical cap
F_{cube}	=	acting force on surface of cube
F_{drag}	=	drag force
F_k	=	frictional force
F_p	=	applied force on projectile
F_{Rate}	=	rate dependent enhancement factor
F_{sc}	=	force upon between the scabbed concrete cone and the concrete panel
F_{sp}	=	force between the spalled cone and the concrete slab
G	=	impact function
$G_{elastic}$	=	elastic shear modulus
$G_{fractured}$	=	fractured shear modulus
$G_{plastic}$	=	plastic shear modulus
$G_{residual}$	=	residual shear modulus
h	=	panel thickness
h_{pf}	=	perforation limit thickness

h_{sc}	=	scabbing limit thickness
I	=	impact factor
I_g	=	moment of inertia of gross concrete section about centroidal axis
J_2	=	invariants of stress tensor
J_3	=	invariants of stress tensor
k	=	reference value related to the panel thickness and diameter of projectile
K	=	concrete penetrability factor
K	=	bulk modulus
$l_{carrier}$	=	length of carrier
l_f	=	steel fiber length
l_o	=	length of specimen of Kolsky Bar
l_p	=	length of projectile
L_s	=	long direction length of slab
M_{cr}	=	cracking moment
M_p	=	mass of projectile
M_{sp}	=	mass of spalled concrete cone
N_{Fail}	=	user defined parameters
N_p	=	nose shape factor
P^*	=	pressure normalized with respect to f'_c
P^*_{spall}	=	normalized hydrodynamic tensile limit
P_1	=	normal force at interface 1 of Kolsky Bar
P_2	=	normal force at interface 2 of Kolsky Bar
$P_{changed}$	=	changed pressure of gas

$P_{ct,max}$	=	maximum force on contact point
$P_{initial}$	=	initial press of the gas
P_{max}	=	maximum tensile pressure
P_{pipe}	=	pressure in the steel pipe
$Q_{2,0}$	=	ratio of strength at zero pressure
R_3	=	third invariant dependence
$r_{in,barrel}$	=	inner radius of barrel
r_p	=	radius of projectile
s	=	displacement
S/a	=	fine aggregate ratio
S_{Hughes}	=	dynamic increase factor in Hughes formula
$SFMAX$	=	current fracture strength
t	=	time
t_{pipe}	=	required thickness of steel pipe
v_1	=	particle velocity at the interaction of 1 of Kolsky Bar
v_2	=	particle velocity at the interaction of 2 of Kolsky Bar
ν_c	=	Poisson's ratios of concrete
$\nu_{c,st}$	=	Poisson's ratio of the concrete under static loading
V_f	=	steel fiber volume fraction
V_{imp}	=	impact velocity of projectile
$Vol_{airtank}$	=	volume of air tank
Vol_{barrel}	=	total volume of barrel
Vol_{change}	=	changed volume of gas
Vol_{def}	=	deformed volume

$Vol_{initial}$	=	initial volume of gas
Vol_{ori}	=	original volume
Vol_{sc}	=	volume of scabbed cone
Vol_{sp}	=	volume of idealized concrete cone
V_{out}	=	projectile velocity at end of barrel
V_{sp}	=	velocity of spalled concrete cone
V_{start}	=	initial velocity of projectile in loading chamber
x_{pe}	=	penetration depth
x_{sc}	=	scabbing depth
$Y_{elastic}$	=	elastic surface
$Y_{failure}$	=	failure surface
$Y_{fractured}$	=	fractured surface
$Y_{pre-peak}$	=	prepeak loading surface
$Y_{residual}$	=	residual surface
Y_{TXC}	=	fracture surface
z	=	distance from the neutral axis
z_{ct}	=	distance from a contact point along z -direction
α	=	ratio of current compressive strain $\alpha\varepsilon_o$ to strain ε_o related to uniaxial concrete compressive strength
α_1	=	velocity effect factor
α_2	=	projectile length factor
α_3	=	factor related panel thickness and diameter of projectile
ΔVol	=	reduced volume
ε_p	=	strain of the projectile

ε_{cr}	=	concrete strain at cracking
ε_I	=	incident pulse
ε_o	=	compressive strain corresponding to compressive concrete strength
ε_{peak}	=	strain at ultimate compressive strength of concrete
ε_{pl}	=	plastic strain before failure
ε_{pl-pre}	=	total plastic strain
ε_R	=	reflected pulse
e_s	=	nominal strain of Kolsky Bar
ε_T	=	transmitted pulse
$\dot{\varepsilon}_s$	=	true strain rate
$\dot{\varepsilon}_s$	=	mean axial strain rate Kolsky Bar test
θ_{sc}	=	angle of the scabbed cone
θ_{sp}	=	slant angle of spalled cone
ρ	=	density
ρ_b	=	density of the input or output bar of Kolsky Bar
ρ_c	=	density of concrete
ρ_P	=	density of projectile
ρ_{steel}	=	bottom reinforcing ratio
$\sigma_{c,st}$	=	compressive strength of concrete under static loading
σ_{eq}	=	equivalent stress
σ_{max}	=	maximum compressive stress
σ_{nose}	=	stress on the nose of projectile
S_{pipe}	=	allowable stress of steel pipe

σ_i	=	rate-dependent strength of the concrete
$\sigma_{u,dyn}$	=	dynamic compressive stress affected by strain rate
$\sigma_{u,st}$	=	static compressive stress
σ_z	=	stress at z point
$\tau_{0,st}$	=	shear stress without uniaxial load
τ_{dyn}	=	bond stress under the dynamic loading
$\tau_{m,st}$	=	static shear stress under triaxial loads
$v_{nc,dyn}$	=	dynamic shear stress capacity (MPa) controlled by dynamic compression
$v_{nc,st}$	=	static shear stress capacity controlled by static compression
$v_{nt,dyn}$	=	dynamic shear stress capacity controlled by dynamic tension
$v_{nt,st}$	=	static shear stress capacity controlled by static tension
ν_p	=	Poisson's ratios of projectile
ξ	=	shear damage
ψ_1	=	material constants
ψ_2	=	material constants
ψ_3	=	material constants
ψ_4	=	material constants

Chapter 1. Introduction

1.1 Motivation for Research

Concrete is a primary material used in concrete structures. It has also contributed to the development of the construction industry. It became the main axis of the construction industry over a hundred years ago before the First World War broke out. This led to an increased interest in preserving human life and the safety of concrete structures. There has been also a great deal of interest in the impact resistance of concrete against conventional weapons. Petry began research on the impact resistance of concrete and developed the formula for evaluating it in 1910 (Kennedy, 1964). Research on the impact resistance of concrete has been carried out since the First World War began, and the research continues in the present day. The importance of concrete structures has increased for over a hundred years, and safety-threatening factors have become more diverse. Concrete materials and structural design techniques have advanced a great deal in the academic field.

The buildings are classified according to their importance in accordance with KBC-16 (Korean Building Code; Architectural Institute of Korea, 2016). There are many important concrete structures with Special-Level that must be protected for safety reasons. That includes such as hospitals with emergency rooms, power plants spread out over areas of over a thousand square meter, broadcast stations,

hazardous waste storage or disposal facilities, and shelters (**Figure 1-1**). Certain design features are intended to make these buildings safer. Even if they are not Special-level or Important Level-1 buildings, their safety performance should be secured in order to protect and preserve life and property.



(a) Hazardous waste storage
(www.pelco.gr)



(b) Nuclear electric power plants
(www.japantimes.co.jp)



(c) Hospital with emergency room
(www.slate.com)



(d) Shelter
(www.londonist.com)

Figure 1-1 Special-level buildings categorized by KBC-16

Buildings such as military facilities and petroleum-based facilities are designed to protect against explosions. Many protective design manuals such as TM 5-1330 (Department of the Army, 1990), ASCE Manual 42 (ASCE, 1985), ASCE Guidelines for Blast-Resistant Building in Petrochemical Facilities (ASCE, 1997) and ASCE Structural Design for Physical Security (1999) use uniform

distributed loads on members and employ a structural member load-resistance model (Krauthammer, 2008). Blast and explosion design is important for preventing building collapse, as well as minimizing local impact damage. Small fragments from explosions or conventional weapons (e.g., bullets and missiles) or car/airplane crashes can cause local damage (**Figure 1-2**). This also poses a safety threat. The local damage may cause the entire building to collapse due to the lack of structural integrity, ductility and irregularities that prevent the propagation of local damage (Lee, 2007). Therefore, the explosion/collapse-proof design of the entire structure is important, but a design for containing local damage is also necessary. A study of local damage to concrete can be extended to structural members and the entire building.



(a) Gun-fight in Macedonia
(www.afpbnews.co.kr)



(b) Bombardment in Yeonpyeong-do
(www.dailian.co.kr)



(c) Car hurled into building
(www.bbc.com)



(d) Wall demolished by hammer
(www.maannnews.com)

Figure 1-2 Local damage by mechanical impact accident

There are several manuals or guidelines that recommend impact formulae for assessing local damage to reinforced concrete panels (**Table 1-1**). The US Army recommends the ACE formula for evaluating local damage to concrete panels, while the US Air Force recommends the modified NDRC formula for evaluating penetration depth and the ACE formula for assessing perforation and scabbing failure. The British Army recommends the UKAEA and CEA-DEF formulae. Because these recommended formulae are old, they do not reflect the characteristics of today’s concrete matrices. In addition, the existing impact formulae are inaccurate when the ratio of a projectile’s diameter to the panel’s thickness is low. For these reasons, it is necessary to develop a new impact formula that is highly accurate even in cases involving a low ratio of projectile diameter to panel thickness.

Table 1-1 Recommended impact formulae in manuals or guidelines (Li *et al.*, 2005)

Department	Manual or guideline	Recommended impact formula
US Army	TM-5-855-1 (1986)	ACE formula for penetration
US Air Force	ESL-TR-87-57 (1987)	Modified NDRC formula for penetration ACE formula for perforation and scabbing
US Department of Defense Explosive Safety Board	ARLCD-SP-84001(1987)	Modified NDRC formula
British Army	British Army manual (Mays and Williams, 1992)	UKAEA formula for penetration and scabbing CEA-EDF formula for perforation
British Nuclear Fuels Ltd.	R3 Impact Assessment Procedure (2003)	UMIST formula

From the material point of view, the mechanical properties of concrete have been upgraded, and the types were diversified over 100 years ago (**Figure 1-3**). Concrete with a strength of 250 MPa was developed, and a variety of materials were developed to complement the weakness of concrete. Concrete exceeding 100 MPa is now being used in the field beyond research applications. Various fibers were added to increase the ductility and energy dissipation capacity. Blast furnace slag was added to improve the fluidity and strength. Concrete with various properties were produced by changing the concrete mixture and methods (Kim and Hahm, 2015). Studies of local impact were continued to understand the impact of the resistance performance of various concrete properties that have been recently developed. For these reasons, numerous studies were carried out to reflect the importance of these concrete structures and academic development in the field of protection.

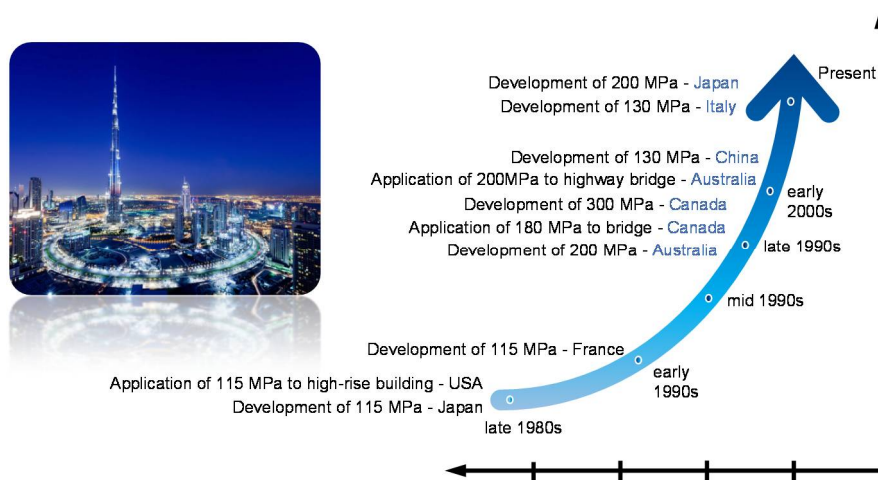


Figure 1-3 Development history of ultra-high strength concrete (UHPC) (redrawn from Lee *et al.*, 2011)

In particular, new concrete matrices have improved tensile strength due to incorporation of steel fibers. Most high-strength concrete is mixed with steel fibers, which greatly improves its tensile characteristics. However, there are few impact formulae that can be applied to high-strength concrete. And there is no impact formula that reflects this increased tensile strength due to steel fibers, except for the Hughes formula. Therefore, it is necessary to develop a new impact formula that can be applied to high-strength concrete and reflects its increased tensile strength due to the steel fiber that it frequently uses.

As described above, the ultimate goal of studying the impact resistance of concrete is the protection of human life by means of concrete structures. If a concrete structure is damaged by unexpected extreme short-term loads, any member on loads could have local failures and this can lead to the collapse of the structure in the worst case. Secondary critical threats such as chemical and biological weapons, conventional weapon, soldiers, etc. can also enter into concrete structures through perforated holes, even if a building does not collapse. When a spalling/scabbing failure occurs due to impact loadings, the fragments/debris can fly into people/things in concrete structures, resulting in secondary physical and personal damage. As the thickness of the concrete panels increases, the safety of the concrete structures will be enhanced against external threats. However, the thickness of concrete cannot be increased unlimitedly and requires a great deal of money. Therefore, the degree of impact resistance should be determined in accordance with the purpose of the concrete structure, and it is important to understand the precise degree of impact resistance of the concrete.

In order to estimate the impact resistance of concrete, many experimental studies have been conducted during the last 100 years and impact formulae were developed to predict impact resistance. However, most of the models were derived from experiments using a limited number of variables. There are some errors in the predicted values assigned to different experimental results. Recently, the dynamic cavity expansion model (Forrestal and Luk, 1988, discussed in **Chapter 2**) was introduced, and it has become popular to develop impact formula using that (Forrestal *et al.*, 1994; Li and Chen, 2003; Feng *et al.*, 2015; Kong *et al.*, 2017; Zhang *et al.*, 2017). The relationship of compression and shear stress in the triaxial condition of concrete cannot be defined. It was necessary to calibrate the impact formula based on results from high velocity impact experimental results. Moreover, most impact formulae based on the dynamic cavity model have considered only the penetration depth equation and did not provide equations for scabbing limit thickness and perforation limit thickness. Models using only the dynamic-cavity expansion model are also derived from the relationship between force and penetration.

Therefore, a new theoretical model is needed, not a model based on experimental results, and theoretical framework is required to develop it. A new theoretical model should provide the penetration depth, scabbing limit thickness and perforation limit thickness, and consider comprehensive variables.

In order to develop a new impact formula, experimental data using various parameters must be obtained. It is difficult to use existing experimental data conducted by other researchers because they were not consistent in experimental design. There are no regulations or guidelines for local impact testing, and furthermore, each experimental method differed depending on the research purpose

and researchers' backgrounds. To develop an accurate formula, it is necessary to collect data under the same experimental conditions or with calibration. And in order to understand the impact resistance of steel fiber-reinforced concrete, it is necessary to examine various steel fiber volume fractions under the same conditions. However, there is a lack of existing experimental data on the impact resistance of steel fiber-reinforced concrete. In some cases, only one or two steel fiber volume fractions were used. Therefore, it is necessary to evaluate the impact resistance performance of steel fiber-reinforced concrete that contains various steel fiber mixture fractions but with under the same other experimental conditions.

To summarize, the impact formulae recommended by existing manuals and guidelines are dated and do not accurately reflect modern concrete characteristics. Therefore, a new formula is needed to reflect current trends in concrete composition, such as high-strength and very-high-strength concrete, along with the impact resistance characteristics of steel fiber-reinforced concrete, which is widely used in the construction industry. Some of the existing impact formulae have sub-equations according to thickness, so it may be necessary to make equations that are applicable regardless of thickness. In order to develop a new impact formula, impact test data under various parameters are needed. However, since previous experimental data are either lacking or inconsistent, new experiments using the same test design should be performed.

1.2 Scope and Objectives

The previous section mentioned the necessity of studying the impact resistance of concrete members/materials. However, the existing impact resistance evaluation formula does not include recent concrete trends and research results. Formulae were developed based on experiments conducted for its limited condition rather than comprehensive studies. The conventional impact resistance evaluation formula is a semi-analytical model based on experimental results. Moreover, most equations are force-penetration models based on equations of motion. Therefore, this study aims to present a new impact formula based on other approaches. The proposed impact model will be verified based on the experimental data of the other researchers and the experimental data and analysis data conducted in this study.

Although many different kinds of objects can cause local damage to concrete, this study assumes a scenario in which explosive fragments threaten the safety of a reinforced concrete structure. Generally, when a bomb explodes, it splits into many metal fragments. TM 5-855-1 (Department of Army, 1986) addresses the need for concrete structures to be prepared for the shattering of the bomb casing. The shattered fragments are usually small in size and travel at velocities in the hundreds of meters per second. Unlike explosive pressure, these fragments can penetrate and/or scab a structure. Many small fragments may be created in a real explosion, and TM 5-855-1 notes that such debris can damage concrete structures through multiple, simultaneous collisions. TM 5-855-1 calculates the number of possible fragments depending on the shape of the warhead, and also warns of scabbing damage caused by secondary debris. In order to avoid such scabbing damage, a concrete wall is designed to be thicker than the calculated thickness (Krauthammer,

2008). In addition to bombs, hard fragments in everyday life threaten the safety of structures. Fragments resulting from the explosion of a silo or a car may threaten the safety of a concrete structure. Hard fragments can also damage structures during strong winds or typhoons. Considering these scenarios, this study examines high-speed, hard projectiles colliding with concrete structures.

In this hypothetical scenario, the most important factors are the weight and velocity of the projectile, which define its kinetic energy. The experiments in this study will be designed using velocities of more than 100 m/s, and will collect experimental data at velocities of more than 100 m/s. This is because “high velocity” is normally defined as between 100 m/s and 3000 m/s. Speeds of over 3000 m/s are known as hyper-velocity. In this study, a high-velocity range of 91 ~ 1358 m/s will be covered.

It is necessary to summarize and review existing impact formulae and experiments studied by other researchers. It will examine what kind of experimental data to use for the model development and how the model is developed. The purpose of model development and experimentation will be examined.

In order to obtain needed experimental data, the impact test will be conducted using variables such as the thickness of concrete panel, the impact velocity, the size of the aggregate, the presence/absence of steel fibers and the properties of concrete. It is possible to use other researchers' experimental results, but some data are lacking. The author decided to conduct the experiment in order to obtain detailed and wide-ranging data. The impact test device will be designed and manufactured to carry out the impact experiments in a cost-effective way and to obtain new data.

The developed impact test device meets the basic performance requirement of launching the projectile at high speeds to evaluate the impact performance of the concrete panel, and it can be installed in a limited space. The new equipment will also be economical and convenient.

The proposed impact formula in this study uses the energy equilibrium as the new approach. Most existing formulae use force-penetration methods and are calibrated using experimental data. The force-penetration methods have 2 sub-formulae at force peak; force and penetration depth has linear relationship from contact time to peak time. Their other relationship has a decreasing branch at a decreasing rate after the peak of force. In this dissertation, the new impact formulae will be derived using energy equilibrium from deformed energy of the projectile, deformed energy of slab and elastic deformed energy, etc. Energies that involved impact mechanisms will be defined and new impact formulae will be derived from its relationship.

Since all of the data needed to verify a new formula could not be obtained from impact experiments, nonlinear analysis will be performed to obtain new data such as stress flow, scale effects, etc.

1.3 Organization

This dissertation involved obtaining new experimental data that were insufficiently collected in previous studies, designing a small impact test device to carry out impact experiments, developing a new impact formula reflecting recent trends in the concrete industry, and using complementary nonlinear analysis to examine aspects of this subject that are difficult to investigate experimentally. Based on the aforementioned scenarios, **Chapter 2** will introduce and summarize the existing impact formulae, impact experiments conducted by other researchers, and ANSYS AUTODYN as the nonlinear analysis to be used in this study.

In order to perform a high-velocity impact experiment, an impact test device capable of launching a projectile at high velocity to collide with a concrete panel was required. It was decided to design and install an impact test device to evaluate the impact resistance of a concrete panel. In **Chapter 3**, the engineering design process of the test device is addressed, and the selection and design of each component of the equipment are described in detail.

Chapter 4 describes impact experiments that were planned to evaluate the impact resistance of concrete panels, using various important parameters that have been overlooked or insufficiently tested by other researchers. As mentioned above, the evaluation of impact resistance tests of high-strength concrete, ultra high-performance concrete (UHPC), and steel fiber-reinforced concrete using various steel fiber volume fractions was the main objective, although various additional sub-parameters were also examined. Using the experimental results, the impact resistance of concrete panels was investigated according to each parameter, distinguishing critical and non-critical variables involved in the impact resistance

mechanism. Defining empirical parameters is an important aspect of developing a new impact formula.

Experimental results were then used to define a new impact mechanism, and a new impact formula was proposed using empirical parameters in **Chapter 5**. A concrete panel has various resistance energies against external energy, also known as kinetic energy. Various resistance energies are defined using a dynamic cavity model, shear stress controlled by compression stress/tensile stress, Hertzian contact theory, drag force, and stress propagation in a solid based on Hertzian contact theory. A new impact formula is derived using the energy equilibrium to be applied in all cases, including steel fiber-reinforced concrete and UHPC.

To define the effects of various factors that were unclarified by the experiment, a nonlinear analysis was conducted in **Chapter 6**. The properties of the materials used in the experiment were input into a nonlinear analysis to model experimental conditions, but varied in subsequent analytical studies. Finally, a summary of and conclusions from this research are presented.

Chapter 2. Literature Review

2.1 History of Research on Impact Formulae

A study of the impact resistance of concrete slabs rapidly progressed in the era of World War One and Two, as well as in the progress of the design and construction of nuclear power plants (Kennedy, 1976; Li *et al.*, 2005). The impact formulae were based on various experimental results and theories. **Figure 2-1** shows the summarized history of a well-known formula, the Petry formula of 1910 up to recent proposed formula, and presents the features and correlations between the formulae. The formulae were studied and developed in the 1940s and 1980s, which are consistent with the World War Two period and the time when many nuclear power plants were designed and constructed. The research on concrete impact resistance was carried out by the military in the 1940s, and it was carried out by nuclear-related organizations in the 1980s. The most representative formula of the 1940s is the NDRC formula, in the 1980s is the Hughes formula. In recent years, the importance of protected structures in war zones and nuclear power plants has continued, and studies are continuing to better understand the protection performance of various buildings such as high-rise buildings and special-purpose buildings. Those external objects which can produce impacts have been diversified and developed, and the concrete materials which can improve impact resistance

have also been developed. For this reason, studies of the impact resistance of concrete have continued in recent years. There are about 25 formulae in **Figure 2-1**. Researchers have developed a formula that can calculate three values of as penetration depth (x_{pe}), scabbing limit thickness (h_{sc}) and perforation limit thickness (h_{pf}). This is related to the impact phenomena under an impact load. When a concrete panel is destroyed by collision with a projectile, the failure mode can be classified into four categories shown in **Figure 2-2**. Although some researchers (Li *et al.*, 2005) may further subdivide the classes, the general failure modes are classified in terms of penetration, scabbing, perforation, and overall response.

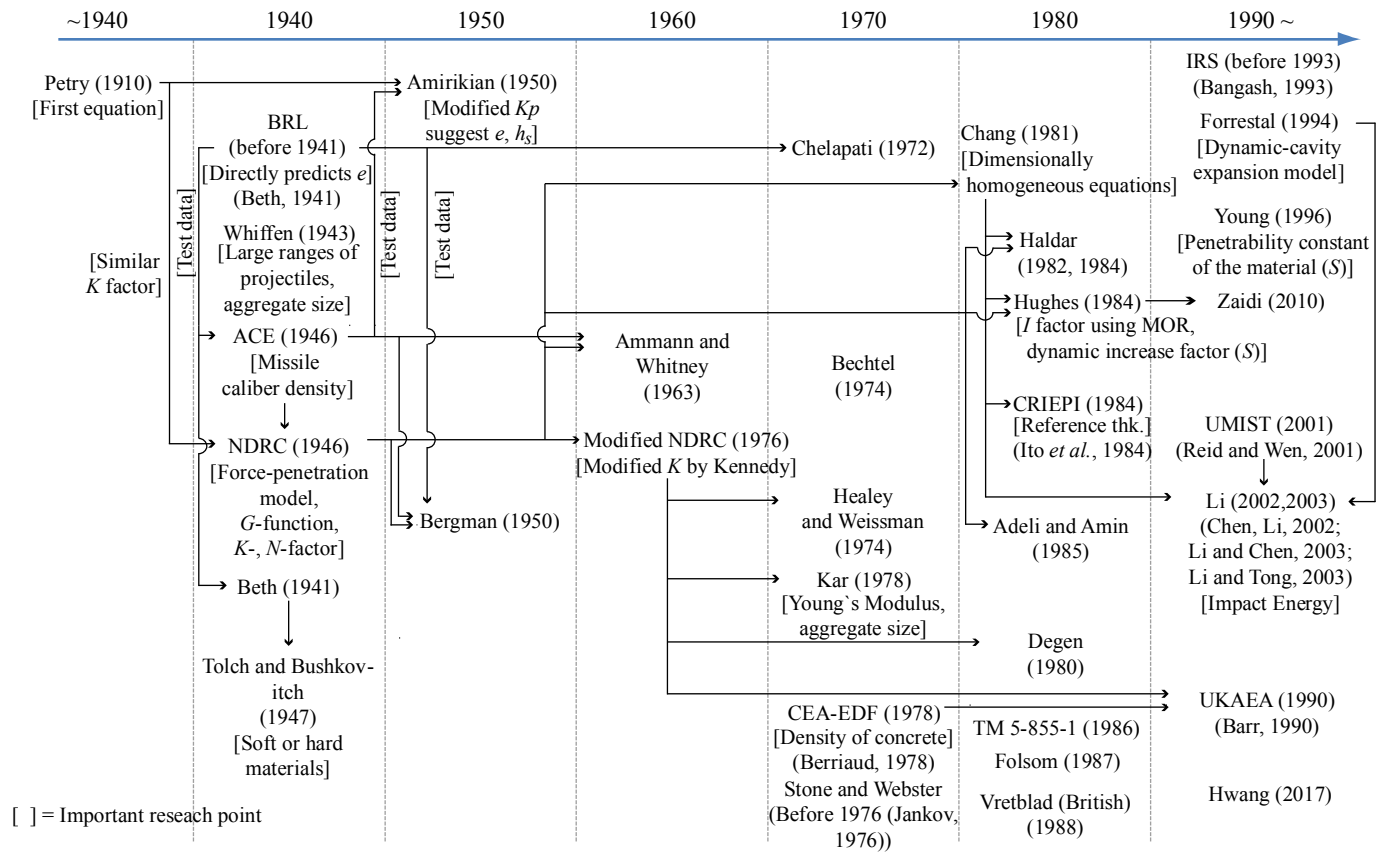


Figure 2-1 History of impact formule (Kojima, 1990; Bangash, 2001; Li *et al.*, 2005; Teland, 2007; Ben-Dor *et al.*, 2013; Kim *et al.*, 2017)

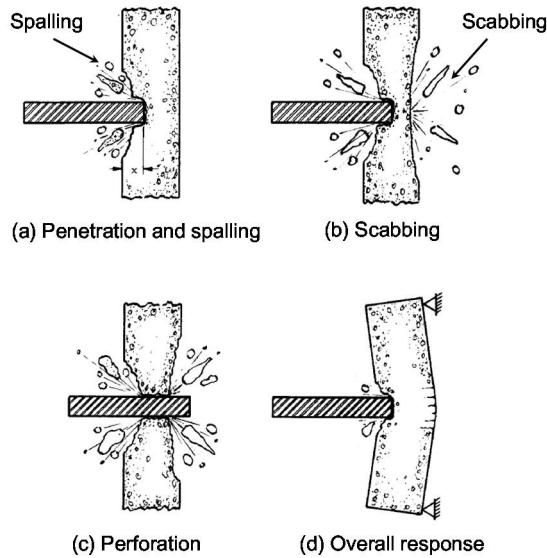


Figure 2-2 Missile impact phenomena (Kennedy, 1976)

- 1) Penetration: When the projectile collides with the concrete panel, the projectile enters into the concrete panel from the contact point without making a tunnel. The projectile could be embedded or rebounded at this point in time. In most cases, the spalling as a cone shape is accompanied by the failure of the concrete around the contact.
- 2) Scabbing: Scabbing is the failure on the rear face of concrete panel and occurs with spalling phenomenon. Normally the shape of scabbing is cone-shaped.
- 3) Perforation: The projectile makes a tunnel in the concrete panel. In general, penetration and scabbing occur at the same time. When a projectile with a huge kinetic energy collides, penetration may occur without the scabbing phenomenon.

- 4) Overall response: When a concrete panel receives impact energy, the panel instantaneously causes an overall deformation. The overall response occurs in the flexural failure or shear failure.

In order to predict this failure mode, various formulae were developed, and the parameters involved in the collision mechanism were used in these formulae. The impact resistance evaluation of concrete is basically related to the correlation between concrete and the projectile as shown in **Table 2-1**. The projectile has the kinetic energy known as impact energy that can occur upon the failure of concrete, because a concrete panel has resistance against external energy. The difference between impact energy and resistance energy determines whether the concrete panel has experienced damage and how much damage it has taken. The velocity and mass are key parameters for determining impact energy, while the thickness and properties of a concrete panel constitute resistance energy. There is a difference in the parameters used for each impact formula, and some of the parameters used under certain conditions.

Table 2-1 Parameters of concrete and projectile

	Concrete panel	Projectile
Parameter	Thickness of panel Compressive strength Tensile strength Elastic modulus Aggregate size Steel fiber volume fraction Amount of rebar Strain rate effect	Velocity Mass Sectional area Material Density Elastic modulus Strain rate effect Shape

2.2 Existing Impact Formulae

In this section, the extant impact formula for penetration, scabbing and perforation limit thickness is reviewed. Previous reviewers (Kennedy, 1976; Li *et al.*, 2005) summarized the existing impact formulae in order to evaluate concrete impact resistance. The summary work is important for understanding the concept of existing impact formulae and to develop a new formula with additional experimental data. Most formulae predict the penetration depth, scabbing limit thickness and perforation limit thickness (**Table 2-2**).

Table 2-2 Summary of impact formulae (Kojima, 1990; Bangash, 2001; Li *et al.*, 2005; Teland, 2007; Ben-Dor *et al.*, 2013; Kim *et al.*, 2017)

Name of formula	Author(s)	Year	Prediction value
Modified Petry formula	Petry	1910	x_{pe}
Amirikian formula	Amirikian	1950	h_{sc}, h_{pf}
BRL formula	Ballistic Research Laboratory	1941	h_{sc}, h_{pf}
ACE formula	Army Corps of Engineers	1943	x_{pe}, h_{sc}, h_{pf}
Modified NDRC formula	National Defense Research Committee	1966 (Original in 1946)	x_{pe}, h_{sc}, h_{pf}
Ammann and Whitney formula	Ammann and Whitney	1963	x_{pe}
Chelapati perforation limit formula	Chelapati	1972	h_{pf}
Whiffen formula	Whiffen	1943	x_{pe}
Kar formula	Kar	1978	x_{pe}, h_{sc}, h_{pf}
CEA-EDF perforation limit formula	French Atomic Energy and Electricite de France	1978	h_{pf}

Bechtel formula	Bechtel Power Corporation	1974	h_{sc}
Stone and Webster formula	Stone and Webster	Before 1976	h_{sc}
Degen perforation formula	Degen	1980	h_{pf}
Chang formula	Chang	1981	h_{sc}, h_{pf}
Haldar and Hamieh formula	Haldar and Hamieh	1984	x_{pe}, h_{sc}
Hughes formula	Hughes	1984	x_{pe}, h_{sc}, h_{pf}
Adeli and Amin formula	Adeli and Amin	1985	x_{pe}, h_{sc}, h_{pf}
Healey and Weissman formula	Healey and Weissman	1974	x_{pe}
IRS formula	IRS	Before 1993	x_{pe}
CRIEPI formula	Central Research Institute of the Electric Power Industry	1984	x_{pe}, h_{sc}, h_{pf}
UKAEA formula	Barr	1990	x_{pe}, h_{sc}
Young formula	Young	1997	x_{pe}
UMIST formula	The UK Nuclear Electric	2001	x_{pe}
Forrestal formula	Forrestal	1994	x_{pe}
Li and Chen formula	Li and Chen	2003	x_{pe}

x_{pe} is the penetration depth; h_{sc} is the scabbing limit thickness; and h_{pf} is the perforation limit thickness.

- 1) Penetration depth (x_{pe}): This is the depth which determines the extent to which the projectile penetrates into concrete from the contact point (or face). It may not penetrate in a single impact, but perforation and scabbing may occur when there are continuous collisions at the same hit point. Therefore, predicting penetration depth is fundamental to assessing impact resistance.

- 2) Scabbing limit thickness (h_{sc}): This is the minimum thickness that will prevent scabbing. In case of scabbing, the fragments of the concrete panel will become secondary projectiles, which may present a safety risk to the inside. Therefore, it is important to determine how much thickness is needed to prevent scabbing.
- 3) Scabbing depth (x_{sc}): This is the depth from the rear face when the back of concrete is peeled.
- 4) Perforation limit thickness (h_{pf}): This is the minimum thickness required to prevent perforation. It is easy for the secondary attack/collision to enter the inside only when perforation occurs. Therefore, it is very important to prevent perforation for the sake of safety.

Prior to 1943, the Ordnance Department of the US Army and the Ballistic Research Laboratory (BRL) conducted multiple impact tests on concrete structures (Li *et al.*, 2005). Based on their experimental data, the Army Corps of Engineers (ACE, 1943) developed the penetration formula (**Eqs. (2-1) and (2-2)**). In this formula, the term of M_p/d_p^3 is called the missile caliber density (Li *et al.*, 2005). Based on regression analyses of experimental data for 37, 75, 76.2 and 155 mm steel cylindrical missiles, scabbing and perforation limit thickness formulae were proposed as shown in **Eqs. (2-3) and (2-4)**.

$$\frac{x_{pe}}{d_p} = \frac{282.6}{\sqrt{f'_c}} \left(\frac{M_p}{d_p^3} \right) d_p^{0.215} \left(\frac{V_{imp}^{1.5}}{1000} \right) + 0.5 \text{ (US)} \quad (2-1)$$

$$\frac{x_{pe}}{d_p} = \frac{3.5 \times 10^{-4}}{\sqrt{f'_c}} \left(\frac{M_p}{d_p^3} \right) d_p^{0.215} V_{imp}^{1.5} + 0.5 \text{ (SI)} \quad (2-2)$$

$$\frac{h_{pf}}{d_p} = 1.32 + 1.24 \frac{x_{pe}}{d_p} \text{ for } 1.35 < \frac{x_{pe}}{d_p} < 13.5 \text{ or } 3 < \frac{h_{pf}}{d_p} < 18 \quad (2-3)$$

$$\frac{h_{sc}}{d_p} = 2.12 + 1.36 \frac{x_{pe}}{d_p} \text{ for } 0.65 < \frac{x_{pe}}{d_p} \leq 11.75 \text{ or } 3 < \frac{h_{sc}}{d_p} \leq 18 \quad (2-4)$$

where, x_{pe} is the penetration depth (m, in); M_p is the mass of the projectile (kg, lb); d_p is the diameter of the projectile (m, in); V_{imp} is the impact velocity of the projectile (m/s, ft/s); f'_c is the compressive strength of concrete (Pa, psi); h_{pf} is the perforation limit thickness (m, in); and h_{sc} is the scabbing limit thickness (m, in).

After obtaining additional experimental data for 0.5 caliber bullets in 1994, scabbing and perforation limit thickness formulae were modified (**Eqs. (2-5)** and **(2-6)**). Additional tests were carried out with a panel thickness of 3 to 18 times the diameter of projectiles and a concrete strength of 10 to 50 MPa. The difference between **Eqs. (2-3) ~ (2-4)** and **Eqs. (2-5) ~ (2-6)** is within 10%. The data for larger missiles were analyzed in the original formula. Therefore, **Eqs. (2-3)** and **(2-4)** are more appropriate for the design of the impact resistance of nuclear power plants (Kennedy, 1976)

$$\frac{h_{pf}}{d_p} = 1.23 + 1.07 \frac{x_{pe}}{d_p} \text{ for } 1.35 < \frac{x_{pe}}{d_p} < 13.5 \text{ or } 3 < \frac{h_{pf}}{d_p} < 18 \quad (2-5)$$

$$\frac{h_{sc}}{d_p} = 2.28 + 1.13 \left(\frac{x_{pe}}{d_p} \right) \text{ for } 0.65 < \frac{x_{pe}}{d_p} \leq 11.75 \text{ or } 3 < \frac{h_{sc}}{d_p} \leq 18 \quad (2-6)$$

where, x_{pe} is the penetration depth (m, in); d_p is the diameter of projectile (m, in); h_{pf} is perforation limit thickness (m, in); and h_{sc} is the scabbing limit thickness (m, in).

In 1946, the National Defense Research Committee (NDRC) carried out further experiments based on the ACE proposal formula and developed the NDRC formula (**Eqs. (2-7) and (2-8)**). This formula assumed that a rigid missile impacts massive concrete targets. The characteristics of the NDRC formula are the introduction of the concrete penetrability factor (K), the impact function G -function and the nose shape factor (N_p) according to the shape of the projectile. The NDRC formula defines a concrete penetrability factor, K , which is similar to the K_p of the Petry formula. However, after 1946, there was less interest in the impact resistance of concrete, and further studies on K were not conducted. G -function was proposed, and it takes into consideration the scale-effect, caliber density, shape and velocity of the bullet (NDRC, 1946). The nose shape factor (N_p) for the NDRC formula is 0.72, 0.84, 1.0 and 1.14 for flat, hemispherical, blunt and very sharp noses, respectively (Li *et al.*, 2005). In order to calculate the perforation and scabbing limit thickness (**Eqs. (2-9) to (2-12)**), the NDRC formula extended the range of the ACE formula (Li *et al.*, 2005). Kennedy (1966) conducted additional research on K , which was lacking in the NDRC formula. Additional study defined K as $180/(f'_c)^{0.5}$ for the relationship between concrete compressive strength and concrete

penetrability. The modified NDRC formula (Eq. (2-13)) was proposed with new K value. For now, it can be that NDRC formula is recognized as the modified NDRC formula.

$$G = \frac{KN_p M_p}{d_p} \left(\frac{V_{imp}}{1000d_p} \right)^{1.8} \text{ (US), original formula} \quad (2-7)$$

$$G = \left(\frac{x_{pe}}{2d_p} \right)^2 \text{ for } \frac{x_{pe}}{d_p} \leq 2 \quad (2-8)$$

$$G = \frac{x_{pe}}{d_p} - 1 \text{ for } \frac{x_{pe}}{d_p} > 2$$

$$\frac{h_{pf}}{d_p} = 3.19 \left(\frac{x_{pe}}{d_p} \right) - 0.718 \left(\frac{x_{pe}}{d_p} \right)^2 \text{ for } \frac{x}{d} \leq 1.35 \quad (2-9)$$

$$\frac{h_{pf}}{d_p} = 1.32 + 1.24 \left(\frac{x_{pe}}{d_p} \right) \text{ for } 1.35 < \frac{x_{pe}}{d_p} < 13.5 \quad (2-10)$$

$$\frac{h_{sc}}{d_p} = 7.91 \left(\frac{x_{pe}}{d_p} \right) - 5.06 \left(\frac{x_{pe}}{d_p} \right)^2 \text{ for } \frac{x_{pe}}{d_p} \leq 0.65 \quad (2-11)$$

$$\frac{h_{sc}}{d_p} = 2.12 + 1.36 \left(\frac{x_{pe}}{d_p} \right) \text{ for } 0.65 < \frac{x_{pe}}{d_p} \leq 11.75 \quad (2-12)$$

$$G = 3.8 \times 10^{-5} \frac{NM_p}{d_p \sqrt{f_c}} \left(\frac{V_{imp}}{d_p} \right)^{1.8} \text{ (SI), modified formula} \quad (2-13)$$

where, G is the impact function; x_{pe} is the penetration depth (m, in); N_p is the nose shape factor (0.72, 0.84, 1.0 and 1.14 for flat, hemispherical, blunt and very sharp noses, respectively); M_p is the mass of the projectile (kg, lb); d_p is the diameter of the projectile (m, in); V_{imp} is the impact velocity of the projectile (m/s, ft/s); h_{pf} is the perforation limit thickness (m, in); h_{sc} is the scabbing limit thickness (m, in); and f'_c is the compressive strength of concrete (Pa, psi).

Haldar's group studied the safety of nuclear power plants with respect to missiles (Haldar and Miller, 1982; Haldar and Hamieh, 1984). They focused on the local impact damages to concrete with respect to turbine missiles. Haldar and Miller (1982) proposed penetration and scabbing design equations using an impact factor (I) that is composed of M_p , N_p , V_{imp} , d_p and f'_c (**Eq. (2-14)**). Haldar and Hamieh (1984) modified the suggested penetration depth and scabbing limit thickness formulae (**Eqs. (2-15) to (2-18)**), after further analyzing additional experimental data conducted using small projectiles such as bullets. They argued that the penetration depth (x_{pe}) could be predicted for all types of missiles, from bullets to turbine missiles. However, the scabbing limit thickness (h_{sc}) could be predicted only for bullets (small scale) and the h_{sc} for turbine missiles should be extrapolated from scabbing limit thicknesses for bullets. In the formula, the value of nose shape factor (N_p) is defined in the modified NDRC formula.

$$I = \frac{M_p N_p V_{imp}^2}{d_p^3 f'_c} \quad (2-14)$$

$$\frac{x_{pe}}{d_p} = -0.0308 + 0.2251I \quad \text{for } 0.3 \leq I \leq 4.0 \quad (2-15)$$

$$\frac{x_{pe}}{d_p} = +0.6740 + 0.0567I \quad \text{for } 4.0 < I \leq 21.0 \quad (2-16)$$

$$\frac{x_{pe}}{d_p} = 1.1875 + 0.0299I \quad \text{for } 21.0 < I \leq 455 \quad (2-17)$$

$$\frac{h_{sc}}{d_p} = 3.3437 + 0.0342I \quad \text{for } 21.0 < I \leq 385 \quad (2-18)$$

where, x_{pe} is the penetration depth (m, in); N_p is the nose shape factor (0.72, 0.84, 1.0 and 1.14 for flat, hemispherical, blunt and very sharp noses, respectively); M_p is the mass of the projectile (kg, lb); d_p is the diameter of the projectile (m, in); V_{imp} is the impact velocity of the projectile (m/s, ft/s); f'_c is the compressive strength of the concrete (Pa, psi); and h_{sc} is the scabbing limit thickness (m, in).

Hughes (1984) proposed the impact formula using the force-penetration model (**Figure 2-3**). The formula considers the strain rate effect on concrete tensile strength using the dynamic increase factor (S_{Hughes} , **Eq. (2-19)**), which is defined by introducing an impact factor (I , **Eqs. (2-20) and (2-21)**) that is similar to the impact factor in Haldar and Hamieh (1984). The dimensionless impact factor (I) represents the concrete penetrability and consisted of M_p , V_{imp} , d_p and f_r (modulus rupture of concrete). Other formulae used the concrete compressive strength (f'_c), but this formula is characterized by a use of modulus rupture of concrete (f_r). The nose shape factor (N_p) was suggested as 1, 1.12, 1.26, and 1.39 for flat, blunt, spherical and very sharp noses, respectively. The penetration depth formula was derived from I , S_{Hughes} , and N_p as shown in **Eq. (2-22)** and is applicable only when the impact factor (I) is smaller than 3500. The perforation limit thickness and the

scabbing limit thickness were derived from the penetration depth and the diameter of the projectile (Eqs. (2-23) to (2-26)). This formula is conservative when impact factor (I) is lower than 40 and ratio h to d_p is lower than 3.5. The perforation limit thickness and scabbing limit thickness were proposed, they were the upper bounds of the data in **Figure 2-4**.

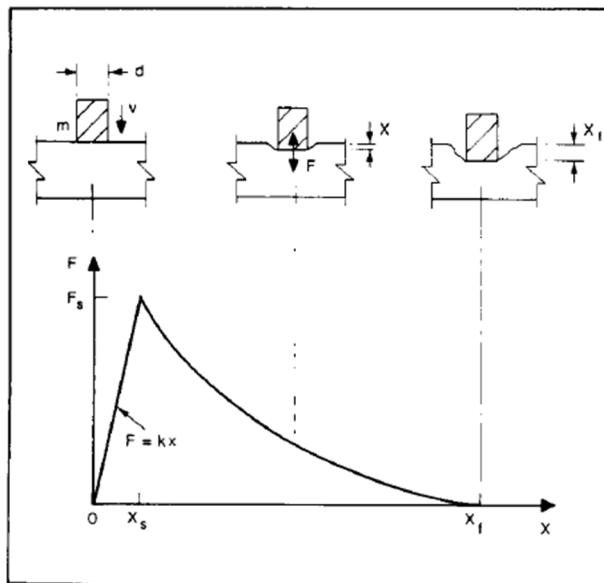


Figure 2-3 Used penetration model on Hughes (1984)

$$S_{Hughes} = 1 + 12.3 \ln(1 + 0.03I) \quad (2-19)$$

$$I = \frac{M_p V_{imp}^2}{f_r d_p^3} \quad (2-20)$$

$$f_r = 0.63 \sqrt{f'_c} \quad (2-21)$$

$$\frac{x_{pe}}{d_p} = 0.19N_p \frac{I}{S_{Hughes}}; I < 3500 \quad (2-22)$$

$$\frac{h_{pf}}{d_p} = 3.6 \frac{x_{pe}}{d_p} \text{ for } \frac{x_{pe}}{d_p} < 3.5 \quad (2-23)$$

$$\frac{h_{pf}}{d_p} = 1.58 \frac{x_{pe}}{d_p} + 1.4 \text{ for } \frac{x_{pe}}{d_p} \geq 3.5 \quad (2-24)$$

$$\frac{h_{sc}}{d_p} = 5.0 \frac{x_{pe}}{d_p} \text{ for } \frac{x_{pe}}{d_p} < 3.5 \quad (2-25)$$

$$\frac{h_{sc}}{d_p} = 1.74 \frac{x_{pe}}{d_p} + 2.3 \text{ for } \frac{x_{pe}}{d_p} \geq 3.5 \quad (2-26)$$

where, x_{pe} is the penetration depth (m, in); f_r is the modulus of rupture (Pa, psi); M_p is the mass of the projectile (kg, lb); d_p is the diameter of the projectile (m, in); V_{imp} is the impact velocity of the projectile (m/s, ft/s); N_p is the nose shape factor (1, 1.12, 1.26, and 1.39 for flat, blunt, spherical and very sharp noses, respectively); f'_c is the compressive strength of the concrete (Pa, psi); h_{sc} is the scabbing limit thickness (m, in); and h_{pf} is the perforation limit thickness (m, in).

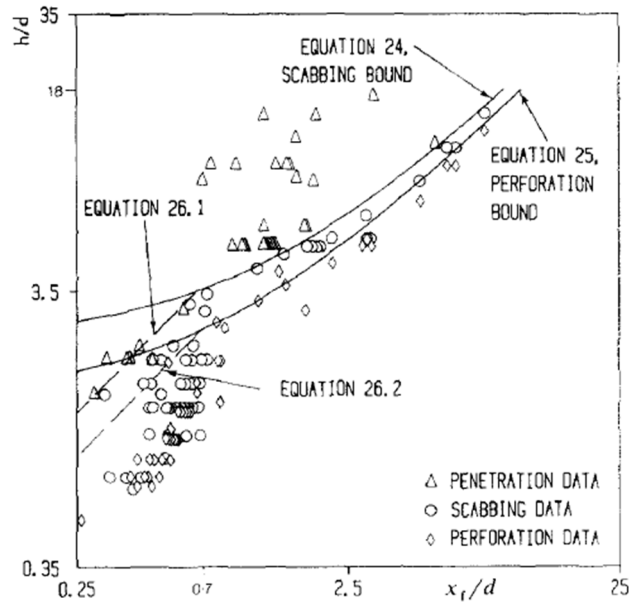


Figure 2-4 Used experimental data for scabbing and perforation limit thickness formula (Hughes, 1984)

Barr (1990) contributed to the compilation of the report made by the UK Atomic Energy Authority (UKAEA), Central Electrical Generating Board (CEGB) and National Nuclear Corporation. The report proposed the penetration depth formula in the report (**Eq. (2-27)**). G -function is the same as the modified NDRC formula (Li *et al.*, 2005). The ratio of x_{pe} to d_p is further subdivided as shown in **Eqs. (2-27) to (2-29)**, because the nuclear power plant has a relationship to low-velocities projectiles or fragments (Li *et al.*, 2005). The scabbing limit thickness formula was also proposed (**Eq. (2-30)**). The range of parameters for penetration depth is $25 < V_{imp} < 300$ m/s, $22 < f'_c < 44$ MPa, but the scabbing limit thickness is $29 < V_{imp} < 238$ m/s, $26 < f'_c < 44$ MPa.

$$\frac{x_{pe}}{d_p} = 0.275 - (0.0756 - G)^{0.5} \text{ for } G \leq 0.0726 \quad (2-27)$$

$$\frac{x_{pe}}{d_p} = (4G - 0.242)^{0.5} \text{ for } 0.0726 \leq G \leq 1.0605 \quad (2-28)$$

$$\frac{x_{pe}}{d_p} = G + 0.9395 \text{ for } 1.0605 \leq G \quad (2-29)$$

$$\frac{h_{sc}}{d_p} = 5.3G^{0.33} \quad (2-30)$$

where, x_{pe} is the penetration depth (m, in); G is the impact function in the modified NDRC formula; d_p is the diameter of the projectile (m, in); V_{imp} is the impact velocity of the projectile (m/s, ft/s); f'_c is the compressive strength of the concrete (Pa, psi); and h_{sc} is the scabbing limit thickness (m, in).

The UK Nuclear Electric (NE) launched a part of the General Nuclear Safety Research program (GNSR) to examine the impact behavior of reinforced concrete structures in 1985 (Reid and Wen, 2001; BNFL, 2003; Li *et al.*, 2005). The experiment was performed in the Structural Test Center (STC at Cheddar), Rogerstone Power Station, Horizontal Impact Facility (HIF), and Winfrith Technology Center (WTC). The UMIST (University of Manchester, Institute of Science and Technology) formula (2001) (Li *et al.*, 2005) was suggested regarding the critical kinetic energies of missiles, and the penetration depth formula is represented in **Eqs. (2-31) and (2-32)**. This formula was verified for $0.05 < d_p < 0.6$ m, $35 < M_p < 2500$ kg, $x_{pe}/d_p < 2.5$ and $3 < V_{imp} < 66.2$ m/s. The nose shape factor is 0.72 for a flat nose, 0.84 for a hemispherical nose, 1.0 for a blunt nose, and 1.13 for

a sharp nose.

$$\frac{x_{pe}}{d_p} = \left(\frac{2}{\pi} \right) \frac{N_p}{0.72} \frac{M_p V_{imp}^2}{\sigma_t d_p^3} \quad (2-31)$$

$$\sigma_t = 4.2 f'_c + 135 \times 10^6 + [0.014 f'_c + 0.45 \times 10^6] V_{imp} \quad (2-32)$$

where, x_{pe} is the penetration depth (m); N_p is the nose shape factor; M_p is the mass of the projectile (kg); d_p is the diameter of the projectile (m); d_r is the diameter of reinforcing bar (m); V_{imp} is the impact velocity of the projectile (m/s); σ_t is the rate-dependent strength of the concrete (Pa); f'_c is compressive strength of concrete (Pa); and h is the thickness of target (m).

Forrestal's research group has studied the dynamic cavity expansion model of materials (**Figure 2-5**). This has been applied to various materials such as soil, concrete, rock (Kong *et al.*, 2017). The dynamic cavity expansion model was originally proposed by Bishop *et al.* (1945) (Li and Tong, 2003), Hopkins (1960) studied dynamic-cavity expansion for incompressible materials, Forrestal and Luk (1988) developed and expanded the model to include compressible materials.

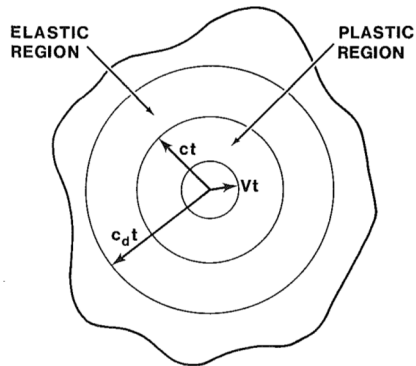


Figure 2-5 Response regions (Forrestal and Luk, 1988)

Luk and Forrestal (1987, paper for the dynamic-cavity expansion model was submitted ahead of paper for the penetration formula but published later than in 1988) proposed the penetration model for concrete using the dynamic cavity expansion model and also considered the spherical and ogive nose projectile. The force of the tip of the projectile was obtained through the subsequent study (Forrestal and Luk, 1992). The shear stress under triaxial conditions is a key to calculating using this formula, studies of the triaxial shear stress of concrete have been lacking. Later Forrestal *et al.* (1994) developed the semi-analytical penetration formula and calibrated the factors based on 6 impact experimental data for ogive nose projectile. Li and Chen (2003) developed penetration depth formula and suggested a new value of K_{Li} (Eqs. (2-33) to (2-40)). The impact factor used in the Chang, Hughes and Haldar formula was applied to this formula (Eqs. (2-33) to (2-40)). Li's research group also studied impact factor and applied their results to penetration depth prediction, as shown in **Figure 2-6** and Eqs. (2-33) to (2-40) (Chen and Li, 2002; Li and Chen, 2003). Term of $(M_p/\rho_p d_p^3)$ is the ratio between the missile section pressure and the target's areal density to consider a long

projectile. This formula can be applicable for x_{pe}/d_p over 0.5 (Li *et al.*, 2005). If the ratio of x_{pe}/d_p is less than 0.5, the penetration depth can be obtained from the **Eq. (2-41)**.

$$\frac{x_{pe}}{d_p} = \sqrt{\frac{(1+k\pi/4N)4k}{(1+I'/N)\pi}} I \text{ for } \frac{x_{pe}}{d_p} \leq k \quad (2-33)$$

$$\frac{x_{pe}}{d_p} = \frac{2}{\pi} N_{cb} \ln \left[\frac{1+I/N_{cb}}{1+k\pi/4N_{cb}} \right] + k \text{ for } \frac{x_{pe}}{d_p} > k \quad (2-34)$$

$$k = 2 \text{ for } \frac{x_{pe}}{d_p} \geq 5, k = \left(0.707 + \frac{l_{nose}}{d_p} \right) \text{ for } \frac{x_{pe}}{d_p} \leq 5 \quad (2-35)$$

$$I = \frac{1}{K_{Li}} \left(\frac{M_p V_{imp}^2}{d_p^3 f_c'} \right) \text{ and } K_{Li} = 72 (f_c')^{-0.5} \quad (2-36)$$

$$N_{cb} = \frac{1}{N_p} \left(\frac{M_p}{\rho_c d_p^3} \right) \quad (2-37)$$

$$N_p = \frac{1}{3(R_{nose}/d_p)} - \frac{1}{24(R_{nose}/d_p)^2} \text{ for an ogival nose} \quad (2-38)$$

$$N_p = \frac{1}{1+4(l_{nose}/d_p)^2} \text{ for a conical nose} \quad (2-39)$$

$$N_p = 1 - \frac{1}{8(R_{nose}/d_p)} \text{ for a blunt/spherical nose} \quad (2-40)$$

$$\frac{x_{pe}}{d_p} = 1.628 \left(\frac{1 + k\pi / 4N_{cb} \frac{4k}{\pi} I}{1 + I / N} \right)^{1.395} \quad \text{for } \frac{x_{pe}}{d_p} \leq 0.5 \quad (2-41)$$

where, x_{pe} is the penetration depth (m); N_p is the nose shape factor; M_p is the mass of the projectile (kg); d_p is the diameter of the projectile (m); V_{imp} is the impact velocity of the projectile (m/s); f'_c is compressive strength of concrete (Pa); h is the panel thickness (m); and ρ_c is the density of concrete (kg/m^3); K_{Li} is the concrete penetrability resistant function of Li-Chen formula; and k is the reference value related to the panel thickness and the diameter of the projectile.

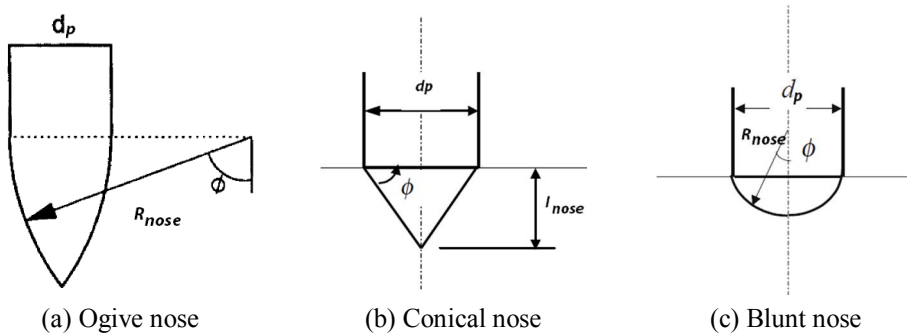


Figure 2-6 Nose shape and definition by Chen and Li (2002)

2.3 Existing Impact Experiment

Almusallam *et al.* (2013) conducted the impact test to study the effectiveness of hybrid-fibers when combined with steel fibers and plastic fibers. The concrete compressive strength was 27 to 71 MPa, the size of all of the specimens was $600 \times 600 \times 90$ mm, and the impact velocity was 91 to 135 m/s (**Figure 2-7**). The bottom reinforcing ratio ($A_s/b_{panel}d_{panel}$) was 7.488×10^3 for each face, where A_s is the total area of reinforcing bar, b_{panel} is the width of the specimens (600 mm), d_{panel} is the average effective depth (67 mm) and nominal stress of the steel bar was 420 MPa. The length of the projectile was 115 mm, sharp (bi-conical) and 800 g.

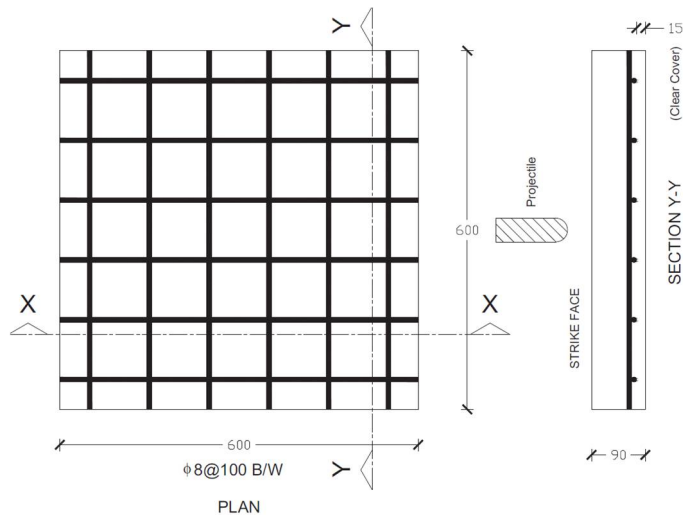


Figure 2-7 Specimen plan by Almusallam *et al.* (2013)

The test results showed that hybrid-fibers was effective for the purpose of reducing crater size and the volume of spalling and scabbing because the fibers arrested crack development (**Figure 2-8**). However, the penetration depth was not

affected by hybrid-fibers.



Figure 2-8 Test results by Almusallam *et al.* (2013)

Forrestal *et al.* (1994) conducted the impact test to study penetration depth by long projectiles with ogive noses, the projectile had a diameter of 13 to 27 mm, length of 89 to 242 mm, a mass of 0.064 to 0.912 kg, and the impact velocity was 277 to 800 m/s (**Figure 2-9**). The concrete strength was 13.5 to 108 MPa and was not reinforced. The sizes of the specimen were $1370 \times 1370 \times 760 \sim 1830$ or $1220 \times 1220 \times 1830$ mm. Based on the test results, Forrestal suggested the empirical penetration formula.

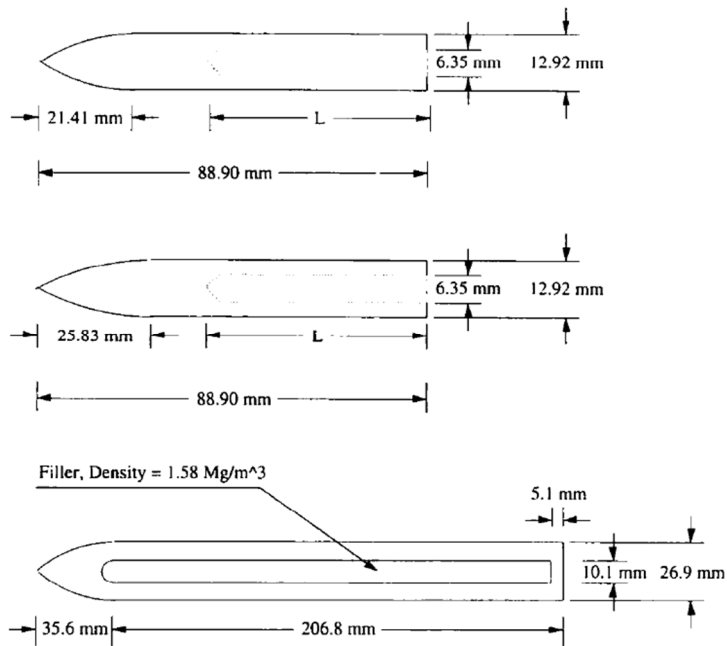


Figure 2-9 Three types of projectiles with various ogive noses (CRH (caliber radius head) is top of 3.0, middle of 4.25, bottom of 2.0) (Forrestal *et al.*, 1994)

Zhang *et al.* (2005) carried out the impact test in order to evaluate an impact resistance of normal to high strength concrete, 45 to 235 MPa, high strength concrete was added within steel fibers. The projectile has diameter of 12.6 mm, a length of 24 mm, mass of 15 g, an impact velocity of 620 to 704 m/s. the penetration depth decreased as the concrete compressive strength increased, but the trend was not linear (**Figure 2-10**). Steel fibers affected to reduce a crater diameter and crack propagation, but not to the penetration depth. The curing temperature was also a variable, but it did not greatly influence penetration depth.

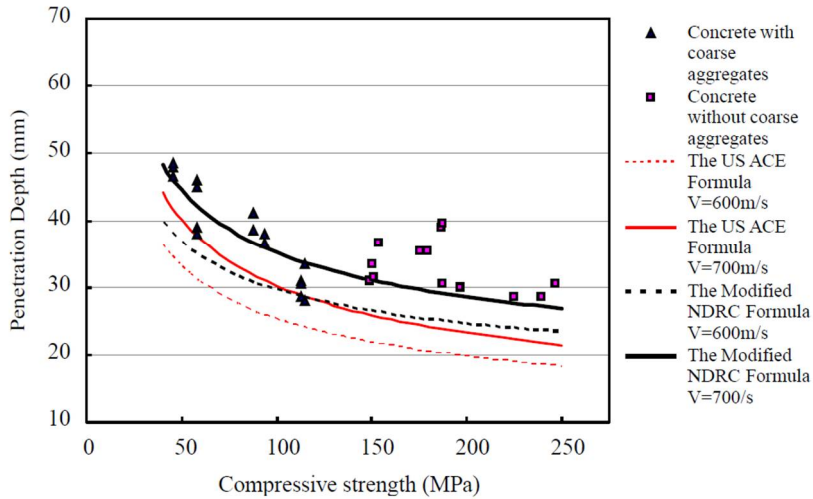


Figure 2-10 Relationship between penetration depth and concrete compressive strength (Zhang *et al.*, 2005)

Abdel-Kader and Fouda (2014) conducted the impact test in order to evaluate the effect of reinforcement in concrete slab (**Figure 2-11**) and steel plate added on to a concrete slab. The projectile has a diameter of 23 mm, a length of 64 mm, a mass of 0.175 kg, and a velocity of 200 ~ 430 m/s. The size of the panel was 500 × 500 × 100 mm, the nominal concrete compressive strength was 26 MPa with a maximum crushed aggregates of 10 mm. Rebars were placed on the top, middle and bottom, where the distance from the center of the top and bottom rebars to the panel face was 15 mm (**Figure 2-11**), the diameter of the rebar was 6 mm and its spacing was 80 mm. The nominal strength of the rebar was 240 MPa. Reinforcement did not exhibit any significant effect on penetration depth, but that reduced the scabbing area with all locations of reinforcement. The concrete panel with the steel plate had better perforation resistance. The damaged area on the rear face was larger than that on the front face.

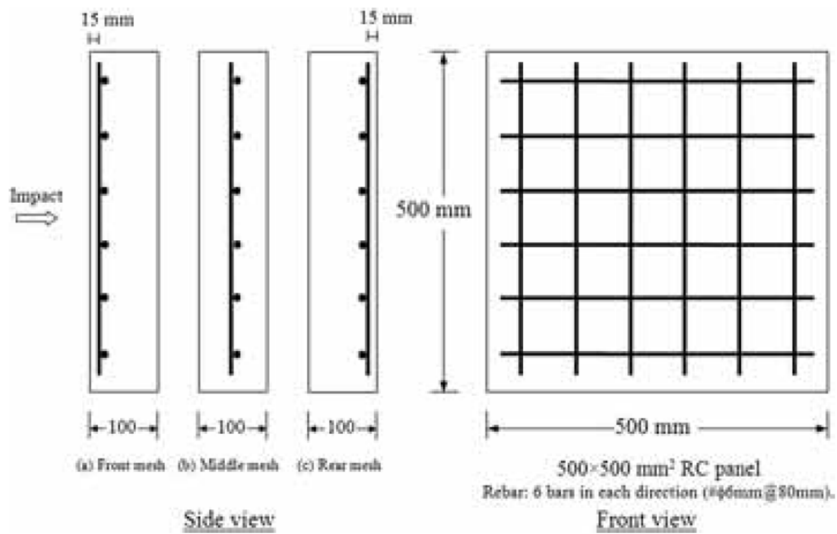


Figure 2-11 Detail of reinforced concrete slab (Abdel-Kader and Fouda, 2014)

Soe *et al.* (2013) conducted a comparison of impact resistance between normal to high strength concrete and a hybrid-fiber cementitious composite, in which the hybrid-fiber consisted of 1.75% polyvinyl alcohol fibers (PVA) and 0.58% steel fibers. The tensile strength of PVA and steel fiber were 2600 and 1600 MPa, respectively. The size of the panel was $300 \times 170 \times 55$ mm, the nominal compressive concrete strength was 45 ~ 90 MPa. The projectile had a length of 24 mm, a diameter of 12.6 mm, a mass of 15 g, caliber radius head (CRH) of 2.5. In this study, the concrete panel was impacted by once or twice. There has been once collision in the general impact test, but Soe *et al.* (2013) shot again another projectile to the point where had been already damaged by the first shoot. The penetration depth decreased as the concrete compressive strength increased. The combination of fibers contributed to the absorption of impact energy.

Forretal's research group suggested the impact formula in 1994 for an impact velocity 800 m/s. This test study was conducted to extend the range of the impact velocity from 400 to 1700 m/s (Forrestal *et al.*, 1996). The impact test was designed with 3 sets; 1) The projectile being of a 12.9 mm diameter and 64 g was shot to an unreinforced concrete target with 13.5 and 216 MPa; 2) The projectile being 20.3 mm diameter and 480 g was shot to an unreinforced concrete target with 62.8 MPa; 3) The projectile being 30.5 mm diameter and 1.6 kg was shot to an unreinforced concrete target with 51 MPa. The test results were good in the suggested impact formula.

Frew *et al.* (1998) in Forrestal's research team conducted additional impact testing in order to examine the accuracy of impact formula. The detailed impact test plan was similar to previous impact testing by Forrestal *et al.* (1996); The projectile was the same, the impact velocity was 442 to 1225 m/s, the thickness of the panel was 940 ~ 3050 mm, but the concrete compressive strength was only 58 MPa.

Forrestal *et al.* (2003) conducted the impact test to obtain penetration depth by long projectiles with ogive nose, the ratio length to diameter of projectile was about 7 and the caliber radius head (CRH) was 3 and 6, its mass was 13 kg. The impact velocity was 140 ~ 460 m/s. The concrete strength was 23, 39 MPa. Based on the test results, the Forrestal impact formula (Forrestal *et al.*, 1994; Forrestal *et al.*, 1996) was reviewed, but it was not accurate. The impact formula was developed based on a small projectile with high velocity, but these specific results were obtained from relative larger mass and lower velocity.

Frew *et al.* (2006) again performed the impact test to study the relationship between the diameter of the target and the projectile (**Figure 2-12**). The projectile was the same as was used in the test of Forrestal *et al.* (2003), but velocity was lower. The concrete compressive strength was only 23 MPa. This test showed that the relationship can be neglected.

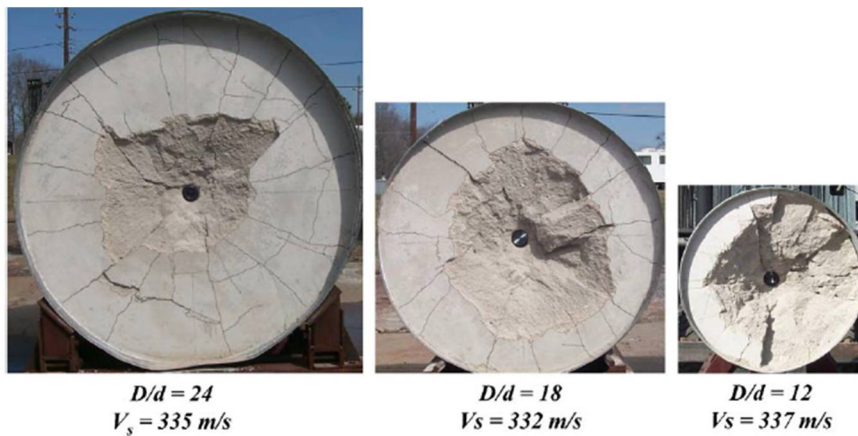


Figure 2-12 Photos of impacted specimens (Frew *et al.*, 2006)

2.4 Nonlinear Analysis

2.4.1 Nonlinear analysis programs

There are some programs for analyzing concrete failure under high-strain dynamic loads (**Figure 2-13**). They show similar results but there are difference depending on the purpose, usage and application (e.g., for ANSYS LS-DYNA, ABAQUS, ANSYS STR, ANSYS AUTODYN etc.). ANSYS Workbench integrated various nonlinear analysis programs, and serves 3 representative explicit dynamics solvers. **Table 2-3** shows a comparison of explicit dynamics solvers in ANSYS program. ANSYS AUTODYN can be applicable to more comprehensive analysis fields than others e.g., heat, acoustics, fluid-structure interference and Blast. The most famous program in collision analysis is ANSYS LS-DYNA, but ANSYS AUTODYN is also well known and is better suited for this study in cases where a projectile collides with a concrete panel.

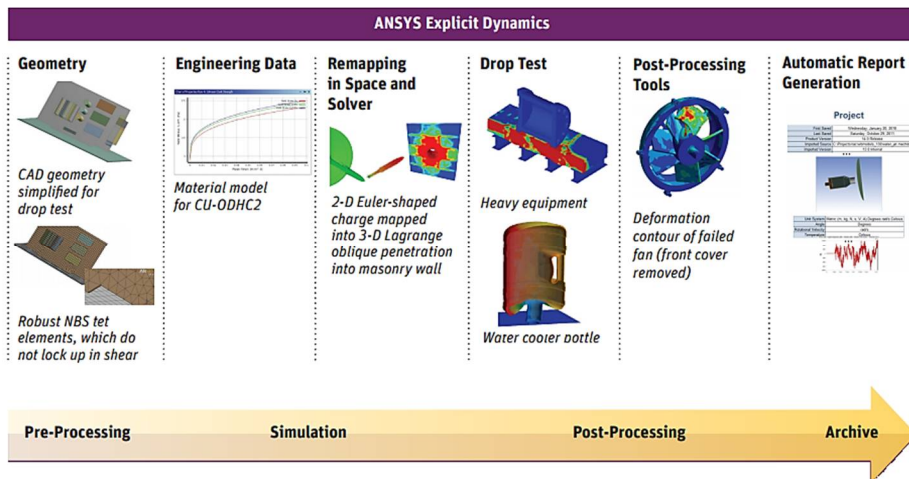


Figure 2-13 Process of ANSYS explicit dynamic analysis (ANSYS, 2011)

Table 2-3 Applications of explicit dynamics of ANSYS benchwork 12 (Kim, 2009)

Analysis range	Analysis field	ANSYS LS-DYNA	ANSYS STR	ANSYS AUTODYN
Nonlinear dynamic	Nonlinear dynamic behavior (Material nonlinear/ geometric nonlinear)	○	○	○
Impact contact	Impact or contact by car, airplane, ship, etc.	○	○	○
Forming	Various metal forming (sheet metal forming/hydro forming/ sheet hydro forming/hot forming)	○	○	○
Heat	Thermal and structural analysis - coupling problems with heat	○		○
Implicit	Eigenvalue, eigenmode analysis, static load analysis	○	○	○
Quasi-static	Static analysis of dynamic load (Car door intrusion/ Impact analysis of roof at car overturn)	○	○	○
Acoustic	Sound Pressure Analysis in Time Domain (Analysis of sound pressure distribution in vehicle by external vibration)	○		○
Fluid-structure interference	Analysis considering fluid-structure interference effect			○
Rigid body motion	Multi-body dynamics	○	○	○
Blast	Analysis of underwater explosions and other explosives			○
Crack propagation, fracture	Analysis of crack propagation and fracture phenomenon of structures	○	○	○

The ANSYS website describes that ANSYS LS-DYNA simulates complex models with many elements, contact, and materials models. It analyzes the response of materials to short periods of extreme loading using its explicit solver. This program can powerfully perform simulations of joints and articulation mechanisms exposed to drops or collisions. Moreover, it gives various contact formulations which can define interactions between all bodies as shown in **Figure 2-14**.

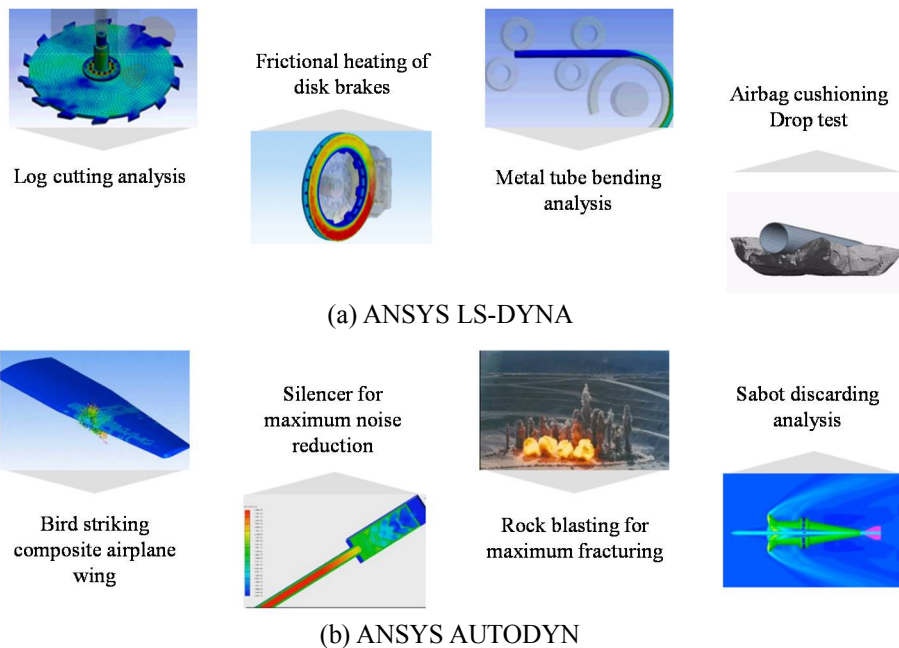


Figure 2-14 Representative application shown on ANSYS website

ANSYS website also introduces ANSYS AUTODYN that is the best program for simulating and analyzing large material deformation or failure due to extreme loadings generated by ballistic impact, high pressure and explosions. It can model the complex model with various fluid and its interaction and shock wave

propagation using solver coupling. It uses the Lagrangian for solid, Eulerian for liquids and extreme plastic flow of solid elements, smooth particle hydrodynamics (SPH) for hyper-velocity impacts and failures of brittle materials. The complicated model can use one or several solvers to obtain accurate results. ANSYS AUTODYN offers a solver coupling function that can automatically communicate between various solvers within one complicated model. This function combined remapping and rezoning is a powerful analytical program for blasts, weapon effects, ballistic impacts or hyper-velocity impact fields.

ANSYS AUTODYN also has a powerful “material data library” that offers over 150 types of material, from common engineering materials to energetic compounds (**Figure 2-15**). This helps simulate linear elastic analysis to highly complicate nonlinear analysis with failure behaviors and various material behaviors. Because it offers these powerful skills and advantages, ANSYS AUTODYN was most suitable for this study.

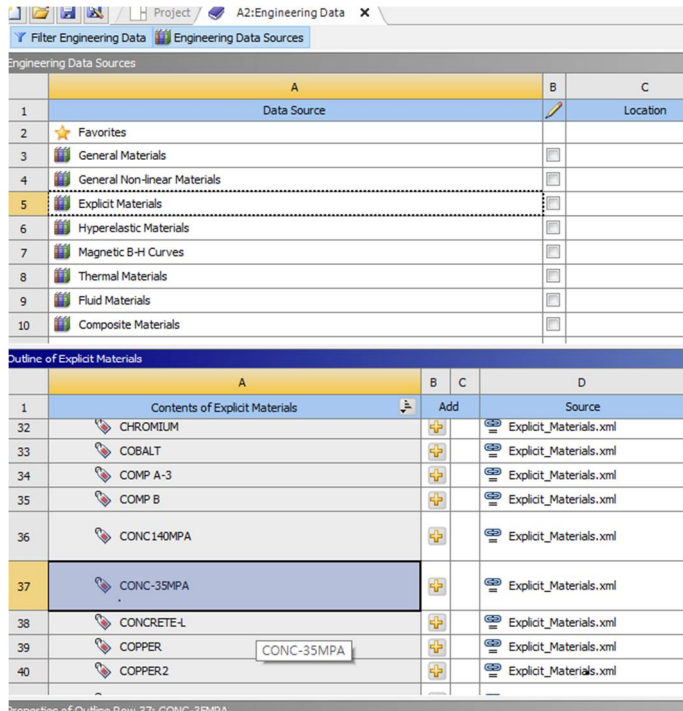


Figure 2-15 Material data library in ANSYS AUTODYN

2.4.2 Concrete model for nonlinear analysis

In order to analyze the behavior of concrete under dynamic loads, it is necessary to define the concrete material model. While there are many concrete failure models, the representative concrete model in ANSYS AUTODYN is the RHT concrete model. This will be used in the nonlinear analysis.

The concrete model for nonlinear analysis that is widely used is the RHT concrete model developed by (Riedel *et al.*, 1999; Riedel *et al.*, 2009; Thoma, 2009) that is an advanced plasticity model for brittle materials and is reasonable to use for concrete modeling under dynamic loadings such as projectile and shaped charge

penetration, contact detonation and blasting (Thoma, 2009). This model was inspired by Chen's study (1982) of triaxial stress-based failure surfaces. Chen summarized a closed failure surface under triaxial conditions and postulated that an elastic surface exists in failure envelope and will be closed towards high pressure stresses when pores start to get crushed (**Figure 2-16**).

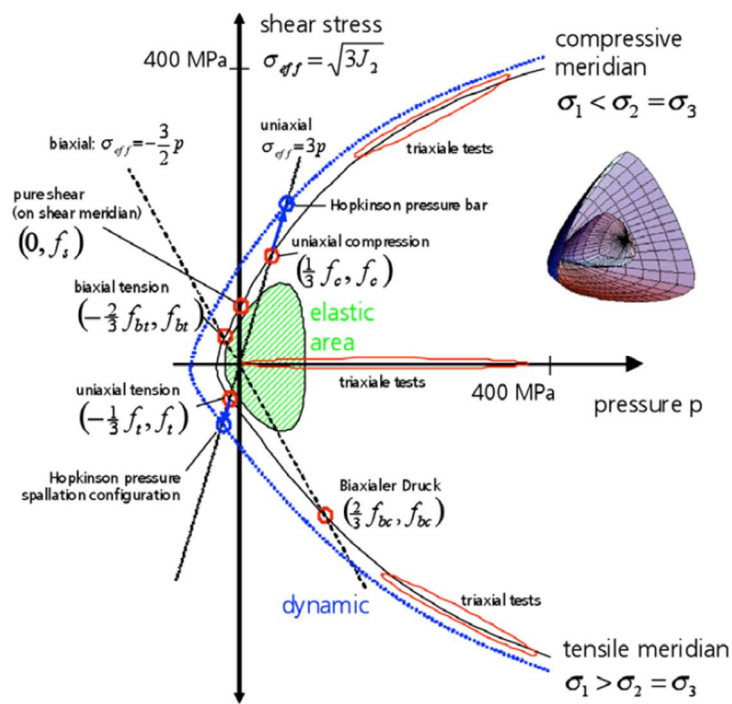


Figure 2-16 Elastic and failure surfaces in RHT model based on Chen's concept (1982) with stress points and areas measurable by different static and dynamic loadings (Thoma, 2009)

The RHT constitutive model can be expressed as a combined plasticity and shear damage model as shown in **Eq. (2-42)** (ANSYS, 2015). This model has six features such as pressure hardening, strain hardening, strain rate hardening in

tension and compression, third invariant dependence for compressive and tensile meridians, strain softening (shear induced damage) and coupling of damage due to porous collapse. The model is in module form and is designed to turn material behavior on and off. This helps the model be of practical usefulness.

$$f_{failure}(p, \sigma_{eq}, \theta, \dot{\epsilon}) = \sigma_{ea} - Y_{TXC(p)} F_{Cap(p)} R_3(\theta) F_{Rate(\dot{\epsilon})} \quad (2-42)$$

where, $f_{failure}$ is failure surface; σ_{eq} is equivalent stress; Y_{TXC} is the fracture surface; R_3 is the third invariant dependence; F_{cap} is the elliptical cap; and F_{Rate} is the rate dependent enhancement factor.

The fracture surface expressed as **Eqs. (2-43) and (2-44)**, and **Figure 2-17** that has the option of truncating the fracture surface to fit through the characteristic points at low pressures, while its surface in high pressure retains the flexibility to match data (**Figure 2-18**) (ANSYS, 2015).

$$Y_{TXC} = f'_c \left[A_{Fail} \left(P^* - P^*_{spall} F_{Rate} \right)^{N_{Fail}} \right] \quad (2-43)$$

$$F_{Rate} = \begin{cases} 1 + \left(\frac{\dot{\epsilon}}{30 \times 10^{-6}} \right)^{\psi_1} & \text{for } P > \frac{1}{3} f'_c \text{ (compression)} \\ 1 + \left(\frac{\dot{\epsilon}}{3 \times 10^{-6}} \right)^{\psi_2} & \text{for } P < \frac{1}{3} f'_c \text{ (tension)} \end{cases} \quad (2-44)$$

where, f'_c is the compressive strength; A_{Fail} and N_{Fail} are user defined parameters; P^* is pressure normalized with respect to f'_c ; P^*_{spall} is the normalized hydrodynamic tensile limit; F_{Rate} is a rate-dependent enhancement factor; ψ_1 and ψ_2 are material constants.

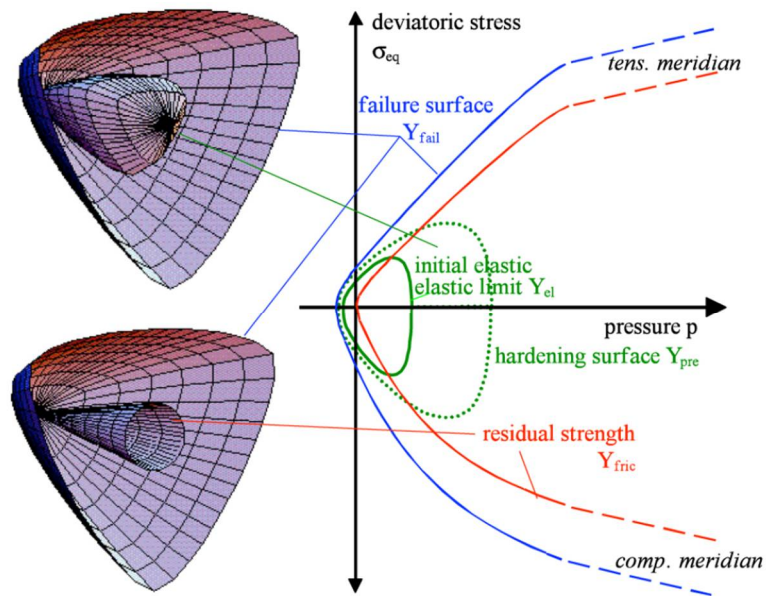


Figure 2-17 RHT strength surfaces of elasticity, ultimate strength and post failure shear resistance strength (Thoma, 2009)

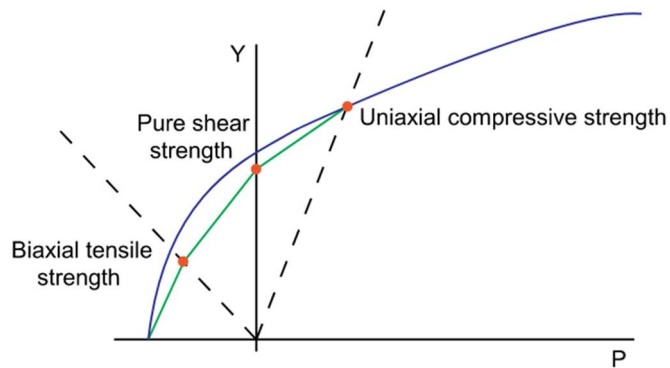


Figure 2-18 RHT representation of compressive meridian (ANSYS, 2015)

The third invariant dependence term (R_3) in the model is used to represent the difference between the compressive and tensile meridian in terms of material strength (Eqs. (2-45) to (2-47)).

$$R_3 = \frac{2(1-Q_2^2)\cos\theta + (2Q_2 - 1)\sqrt{4(1-Q_2^2)\cos^2\theta - 4Q_2}}{4(1-Q_2^2)\cos^2\theta + (1-2Q_2)^2} \quad (2-45)$$

$$\cos(3\theta) = \frac{3\sqrt{3}J_3}{2^{3/2}J_2} \quad (2-46)$$

$$Q_2 = Q_{2,0} + BQ.P^* \text{ and } 0.5 < Q_2 < 1, BQ = 0.0105 \quad (2-47)$$

where, $Q_{2,0}$ is the ratio of strength at zero pressure; J_2 and J_3 invariants of stress tensor; and BQ is the coefficient that defines the rate at which the fracture surface transitions from being approximately triangular in form to a circular form with increasing pressure (Figure 2-19).

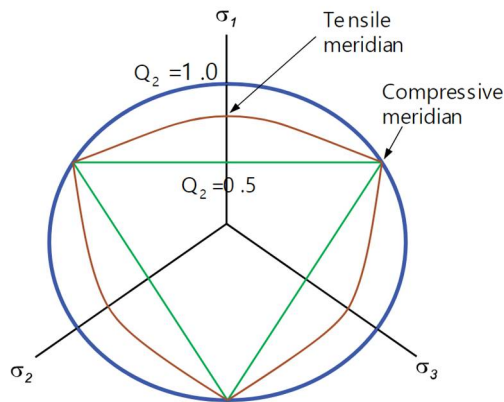


Figure 2-19 Third invariant dependence (ANSYS, 2015)

The model represents the strain hardening through an elastic limit surface and a hardening slope as shown in **Eqs. (2-48) and (2-49)**, and **Figure 2-20**. The elastic limit surface is scaled down from the fracture surface by ratios of the elastic strength to the compressive strength and the elastic strength to the tensile strength, these ratios are defined by users.

$$Y_{pre-peak} = Y_{elastic} + \frac{\varepsilon_{pl}}{\varepsilon_{pl-pre}} (Y_{fail} - Y_{elastic}) \quad (2-48)$$

$$\varepsilon_{pl-pre} = \frac{Y_{failure} - Y_{elastic}}{3G} \underbrace{\left(\frac{G_{elastic}}{G_{elastic} - G_{plastic}} \right)}_{\text{hardening slope}} \quad (2-49)$$

where, $Y_{pre-peak}$ is the prepeak loading surface; $Y_{elastic}$ is the elastic surface; $Y_{failure}$ is the failure surface; ε_{pl} is the plastic strain before failure; ε_{pl-pre} is the total plastic strain; $G_{elastic}$ is the elastic shear modulus; and $G_{plastic}$ is the plastic shear modulus.

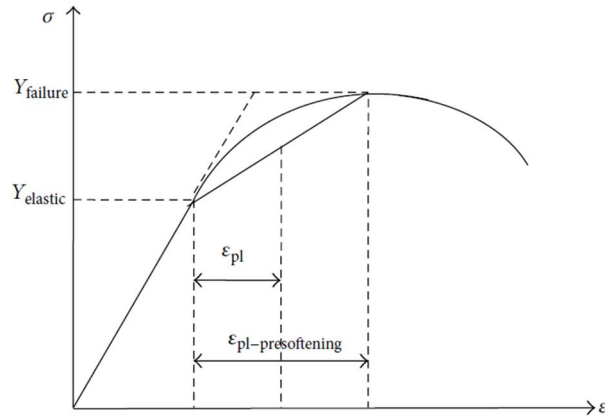


Figure 2-20 Bilinear strain hardening (Hu *et al.*, 2016)

The shear damage (ζ) is assumed to accumulate due to inelastic deviatoric strain (**Eq. (2-50)**) (ANSYS, 2015). The damage accumulation has two effects in the model in the forms of reduction in strength (strain softening) (**Eqs. (2-51)** and **(2-52)**) and reduction in shear stiffness (**Eq. (2-53)**). The product of Y_{XTC} and the fraction of the current fracture strength ($SFMAX$) is used to limit the maximum residual shear strength for completely damaged material to be $SFMAX$.

$$\zeta = \sum \frac{\Delta \varepsilon_{pl}}{\psi_3 (P^* - P_{spall}^*)^{\psi_4}} \quad (2-50)$$

$$Y_{fractured}^* = (1 - \zeta) Y_{failure}^* - \zeta Y_{residual}^* \quad (2-51)$$

$$Y_{residual}^* = \min [B(P^*)^M, Y_{XTC} \times SFMAX] \quad (2-52)$$

$$G_{fractured} = (1 - \zeta) G_{elastic} + \zeta G_{residual} \quad (2-53)$$

where, ζ is the shear damage; ε_{pl} is the plastic strain before failure; ψ_3 and ψ_4 are material constants; P^* is pressure normalized with respect to f'_c ; P_{spall}^* is the normalized hydrodynamic tensile limit; B and M are constant parameters from curve fitting of the experimental data; $Y_{fractured}$ is the fractured surface; $Y_{residual}$ is the residual surface; $SFMAX$ is the fraction of the current fracture strength; $G_{fractured}$ is the fractured shear modulus; $G_{elastic}$ is the elastic shear modulus; and $G_{residual}$ is the residual shear modulus.

The RHT model has the option of including a cap to limit the elastic deviatoric stress under large compressions (**Figure 2-21**), and this option reduces deviatoric strength.

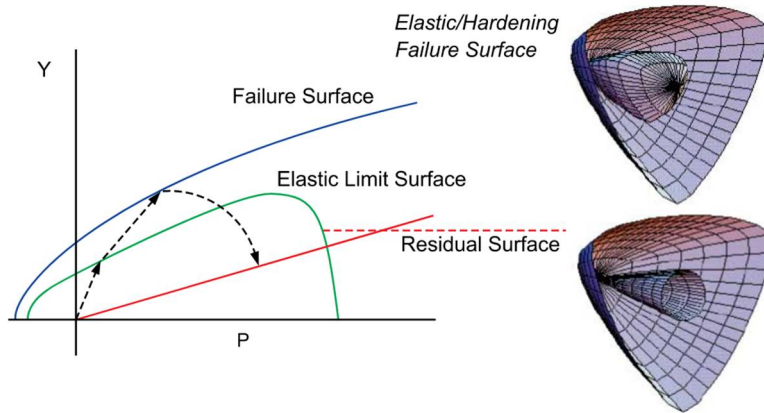


Figure 2-21 RHT elastic, fracture and residual failure surfaces (ANSYS, 2017)

If the material has the tensile failure, the maximum tensile pressure (P_{max}) is limited in **Eq. (2-54)**.

$$P_{max} = \max[(1 - \zeta) \times P_{min}, P(\rho, E_{internal})] \quad (2-54)$$

where, ζ can be obtained from **Eq. (2-50)**; P_{min} is derived from the tensile strength of concrete, which forms parts of the input for the strength model; ρ is the density; and $E_{internal}$ is the internal energy.

2.5 Discussion

In this chapter, the existing impact formulae were summarized and their characteristics were reviewed and impact tests using high-velocity projectile were summarized. The materials model and equations of state of ANSYS AUTODYN were reviewed. The main results of this chapter are summarized as below:

- 1) There were many impact formulae for predicting penetration depth, scabbing limit thickness, and perforation limit thickness. The representative impact formulae among them were the modified NDRC, Hughes, Forrestal and Li-Chen impact formulae. Existing impact formulae used a force-penetration depth relationship to develop a formula. The Forrestal impact formula, which is currently popular, also used the force-penetration depth relationship.
- 2) Impact experiments were performed by many researchers with variables. Here, the experimental data was used to verify the formula developed in this study was reviewed. The variables used in impact experiments were a concrete strength of 26 ~ 237 MPa, impact velocity 91 ~ 1358 m/s, steel fiber volume fraction of 0.5 ~ 2.33%, projectile length of 20 ~ 531 mm, and a projectile mass of 15 ~ 13000 g.
- 3) There are various nonlinear programs for modeling concrete impact phenomenon. AUTODYN is one of them. AUTODYN is specialized for the analysis of a conventional weapon impact and blast, the most important feature is coupling between solvers. The concrete model most commonly used for AUTODYN is the RHT model.

Chapter 3. Design of Small Impact Test Device

3.1 Purpose of Contravening Impact Test Device

Fragments or projectiles produced by various causes such as mechanical collisions, explosions and shooting have a large amount of kinetic energy, which poses a threat to the safety of important objects such as people, buildings, mechanical equipment and aerospace equipment. When a projectile with high velocity collides with a target, local damage such as penetration, scabbing on rear face, perforation, or cracks occur. Therefore, it is necessary to study the impact resistance and damage done to the target for the sake of safety. However there is no guideline or code for high velocity impact tests, so the test method and process used by each researcher has been inconsistent. Researchers who conducted the experiments used the different impact test device in different ways according to their diversity of purposes (**Figure 3-1**).



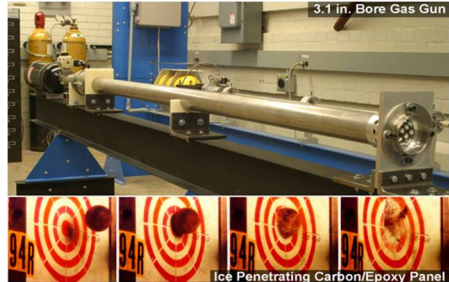
(a) Nitrogen gas gun test device at Chungnam national university (Lee *et al.*, 2018)



(b) Nitrogen gas gun test device at Seoul National university (EPTC, 2017)



(c) Canon (Lee *et al.*, 2013)



(d) high-velocity test device at UC San Diego (www.structures.ucsd.edu)



(e) Drop-weight test device (Hrynyk and Vecchino, 2014)



(f) Compressed Nitrogen and Helium gas gun test device (Soe *et al.*, 2013)

Figure 3-1 Impact test devices

In this study, experimental impact test is planned. There are not many research institutes that have impact resistance testing equipment, and institutes having device are far from being able to experiment frequently. It also takes significant cost to use the experiment device in other institutes in Korea or other countries. In order to conduct an impact experiment at low cost and with convenience, it is decided to design and manufacture a new and small impact test device as part of this study.

3.2 Impact Test Device Type

The test device for impact resistance of concrete and other materials for protection can be divided into two types. The first is a shooting method that uses the gas or gunpowder to increase the speed of a projectile. The second method is a drop-weight method that increases the mass or height of an object (**Figure 3-1**). In this study, a shooting method was selected to reflect the strain rate of materials. It is easily possible to create kinetic energy by increasing the weight or height in the drop weight method, but it is difficult to reflect the strain rate (**Figure 3-2**). Therefore, this design process intends to develop a small impact test device capable of launching a projectile at high speed.

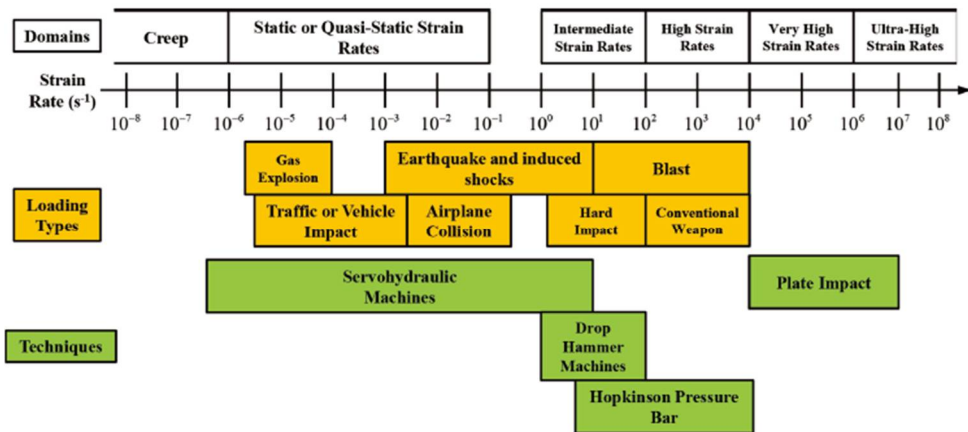


Figure 3-2 Strain rate domains, strain rates due to real loading sources (Hong and Kang, 2016)

3.3 Design Process of Impact Test Device

This chapter presents the design of an impact test device for evaluating the impact resistance of concrete by collision of a projectile traveling at a high velocity. More particularly, a new device can be applied to various sizes and shapes of projectiles and the device will be semi-permanently usable.

Reaching the goals involves design key-points and a detailed design process for the air-compressor system, barrel and experimental chamber.

3.3.1 Design objectives

The design of the impact test device is aimed at the development of a reduction in the size of the existing large impact test equipment. Considering the laboratory environment and research topic, there are three conditions in the development of the small impact test device.

- 1) Launch a 20 mm steel ball more than 300 m/s
- 2) Develop a small device to be installed in an 5×1.5 m area
- 3) Create a device that can be used semi-permanently and economically

In the first experiment conducted at Chungnam National University, the projectile was fired at 270 and 350 m/s. Therefore, it is reasonable to launch the new developed device to 300 m/s in order to improve the consistency of the research. The space for the new impact test device is given as 5×1.5 m. The small impact test device should not use nitrogen and gunpowder, and should minimize

the use of consumables in the experiment to be economical. In order to satisfy the three conditions above, various items were examined and five key items were finally selected as below (**Figure 3-3**).



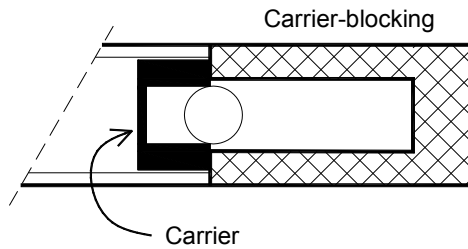
(a) Air-compressor
(www.dewalt.com)



(b) Carbon steel pipes for pressure service
(www.sinhwasteel.com)



(c) Solenoid valve
(www.electricsolenoidvalves.com)



(d) Carrier and carrier blocking



(e) Commercial velocity measurement
(www.competitionelectronics.com)

Figure 3-3 Key items for developing small impact test device

- 4) Air-compressor: Other existing impact test equipment used gunpowder or nitrogen gas as the supply of propellant, but these cost a great deal of money. In order to use economical and semi-permanent equipment, an air-compressor was adopted.
- 5) Carbon steel pipes for pressure service: By using the ready-made carbon steel pipes for pressure service as a barrel, the manufacturing cost of the barrel was dramatically reduced.
- 6) Solenoid valve: It is important to provide the air pressure in an air tank to a projectile in barrel instantly. The solenoid valve is an electronic valve that allows a valve to be opened for a moment as soon as the button is pressed.
- 7) Carrier and Carrier blocking: The carrier as cartridge is created to carry a projectile in a barrel. By using the carrier, it is possible to load various projectile shapes, and it is also helpful to increase the speed of a projectile by receiving pressure within a large area. Carrier blocking is a new device that stops the flying carrier. Since only the projectile must collide with the concrete panel, the carrier must be stopped by carrier blocking. The carrier stops due to carrier blocking, and only the projectile goes forward due to inertia.
- 8) Commercial velocity measurement: The velocity of the projectile is a very important factor in evaluating the impact resistance of concrete. A commercial velocity measurement instrument is used for the sake of economics and convenience.

3.3.2 Overall plan

An optimization design is important in considering that the length of the installation site is 5500 mm. The impact test device can be roughly divided into three main parts (**Figure 3-4**); 1) length of the air-compressor and the air tank that produces the force, 2) the length of the barrel, the projectile loading and the carrier retrieval length (added to each end of the barrel), 3) the length of the experimental chamber needed to install specimens and engage in commercial velocity measurement.

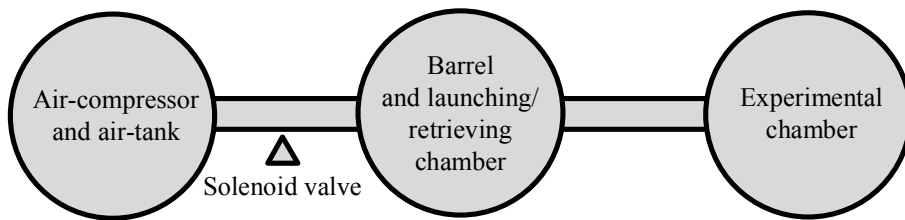


Figure 3-4 Overall plan

- 1) Air-compressor and air-tank: It was planned to have a space of 1000×800 mm where the air pump and the air tank can be installed. The connection between the air tank and the barrel was planned to be 500mm considering that a solenoid valve would also be installed.
- 2) Experimental chamber: A chamber requires space for installing a velocity measurement instrument and a specimen. The length of the velocity measurement instrument is 400 mm. The specimen types are 400×400 mm and 200×200 mm. Therefore, the total length of the experimental chamber is planned to be 1390 mm.

- 3) Barrel: The length of the space for loading and retrieving a carrier and/or projectile is 200 mm, respectively. The remaining length is 2000 mm except for the air-compressor and air-tank space, loading chamber and retrieving chamber. That is the length of the barrel to which a carrier and projectile will be subjected under pressure.

3.3.3 Design of air-compressor and air tank capacity

It was decided to use an air-compressor instead of using nitrogen pressure or gunpowder methods. The reason was that the nitrogen pressure equipment is bulky and requires a great deal of additional equipment. The gunpowder method presented several difficulties in handling. In addition, there was an additional cost involved in purchasing nitrogen or gunpowder. On the other hand, an air-compressor required a small area to install and it was possible to use it semi-permanently without incurring additional costs. The pressure of the air compressor was chosen to be 2 MPa. The pressure of 2 MPa or more requires a special order, so the price increases a great deal. Therefore, 2 MPa was a reasonable choice for the purpose of making compact low-cost equipment. The safety control box limits pressure only up to 1.75 MPa and must be installed, so the actual pressure in the air tank was 1.75 MPa.

The air-compressor compresses air into the air-tank. The compressed air in the air-tank is discharged through the barrel as soon as the valve is opened. It is important to determine how great a level of pressure the air-tank can hold up to the end of the barrel. If the pressure difference between the tank and the end of the barrel is large, the projectile will not be launched at high speed. When the pressure

in the tank is maintained to the end of the barrel, the projectile will be fired at full speed. Therefore, reducing the pressure difference between the tank and the barrel end is an important point of tank capacity design.

In order to maintain the level of pressure of the air-tank up to the end of barrel, the required capacity of an air-tank is calculated using Boyle's law (**Eq. (3-1)**).

$$P_a Vol_{initial} = P_b Vol_{changed} \quad (3-1)$$

where, $P_{initial}$ is the initial press of the gas (MPa); $Vol_{initial}$ is the initial volume of the gas (L); $P_{changed}$ is the changed pressure of the gas (MPa); and Vol_{change} is the changed volume of the gas (L).

For example, if the pressure at the end of the barrel is 95% of the air tank, the tank capacity should be 48 liters (**Eqs. (3-2) to (3-4)**). The length of the 50 L tank from the ready-made product is 820 mm, which is difficult to install in the space planned in this study.

$$1.7 \times Vol_{airtank} = 1.66 \times (Vol_{airtank} + 2.513 \times 10^{-3}) \quad (3-2)$$

$$Vol_{barrel} = 0.022 \times 2 \times \pi = 2.513 \times 10^{-3} \text{ m}^3 \text{ (Internal volume of barrel)} \quad (3-3)$$

$$Vol_{airtank} = 0.0477 \text{ m}^3 \approx 48\text{L} \quad (3-4)$$

where, $Vol_{airtank}$ is the volume of the air tank (L) and Vol_{barrel} is the total volume of the barrel (L).

The relationship between the pressure ratio of the end of barrel to air tank and a tank capacity is shown in **Figure 3-5**. A 20L air tank was selected for the receiver tank because it was thought that it would be better for retaining a pressure ratio of at least 90% of the limited space. The length of the 20 L air tank was 510 mm, and its diameter was 249 mm, which are optimal for the limited space, considering the air-compressor system and the small air tank.

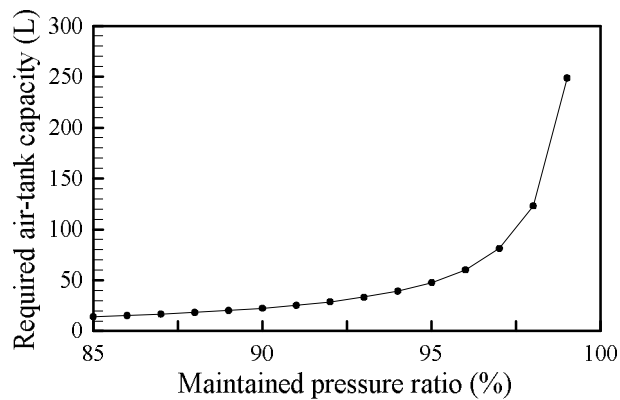


Figure 3-5 Pressure ratio and tank capacity relationship

3.3.4 Design of barrel size and details

The size of the barrel can be determined because the pressure and capacity of the air tank were determined in the previous chapter. An important design point is that a projectile with a diameter of 20 mm will be launched at a speed of 300 m/s or higher. The velocity of the projectile can be calculated using the acceleration formula (**Eq. (3-5)**) and the uniformly accelerated motion formula (**Eq. (3-6)**). **Equation (3-7)** can be derived from **Eqs. (3-5)** and **(3-6)**. Considering Newton's second law (**Eq. (3-8)**) of motion and the initial velocity zero ($V_{start} = 0$ m/s), **Eq.**

(3-9) can be obtained. Finally, the initial speed of the projectile at the end of barrel can be obtained as shown in Eq. (3-10). The distance between the end of the barrel and the concrete panel is close, so it can be considered that there is no decrease in velocity due to air resistance. Therefore, the initial velocity is equal to the impact velocity.

$$a = \frac{(V_{out} - V_{start})}{t} \quad (3-5)$$

$$s = V_{start}t + \frac{V_{out} - V_{start}}{2}t = V_{start}t + t \times \frac{at}{2} = V_{start}t + \frac{at^2}{2} \quad (3-6)$$

$$2as = V_{out}^2 - V_{start}^2 \quad (3-7)$$

$$F_p = M_p a \quad (3-8)$$

$$V_{out}^2 = 2 \times \left(\frac{F_p}{M_p} \right) \times s \quad (3-9)$$

$$V_{out} = V_{imp} = \sqrt{2 \times s \times \frac{F_p}{M_p}} \quad (3-10)$$

where, a is the acceleration (m/s^2); V_{start} is the initial velocity of the projectile in the loading chamber (m/s); V_{out} is the projectile velocity at the end of the barrel (m/s); t is the time taken (sec); s is the displacement (m); F_p is the applied force on the projectile (N); and M_p is the weight of the projectile (kg).

In **Eq. (3-10)**, the values of s and M_p are known, but the value of F_p is unknown. Therefore, the value of F_p must be defined in order to obtain the exact velocity of the projectile. In physics, a free body diagram of a projectile is graphically illustrated with the tank pressure, atmospheric pressure, and frictional force as shown in **Figure 3-6**. The equilibrium equation of three forces is given in **Eq. (3-11)**. Because the lubricant was used in the experiments, the coefficient of friction is 0.06, and it was judged that there was no friction. The atmospheric pressure is 0.1 MPa. The value of F_p can be obtained as in **Eq. (3-12)**. The barrel size can be calculated from **Eqs. (3-11)** and **(3-12)**. In order to have a speed of 300 m/s, F_p requires 738 N. Since the acting pressure on a projectile is 1.56 MPa, the internal cross-sectional area of the barrel capable of receiving the force of 738 N is 473 mm² (**Eqs. (3-13)** to **(3-16)**). In other words, if the inner diameter of the barrel is 24.54 mm or more, the projectile can be launched at a speed of 300 m/s or more (**Eq. (3-17)**). For this reason, a carrier of 24.54 mm in diameter or larger is required to mount a 20 mm diameter projectile.

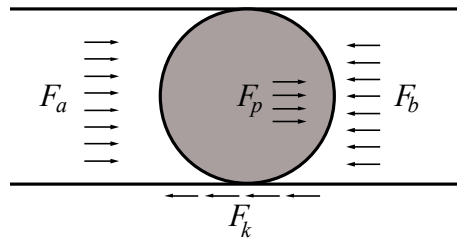


Figure 3-6 Free body diagram of projectile

$$F_p = F_a - F_b - F_k \quad (3-11)$$

$$F_p = (F_a - 0.1) \times A = 1.56 A_{barrel} \quad (3-12)$$

$$F_p = \frac{v^2}{2s} \times m = 1.56 A_{barrel} \quad (3-13)$$

$$F_p = \frac{(300 \text{ m/s})^2}{2 \times (2 \text{ m})} \times (0.0328 \text{ kg}) = 1.56 A_{barrel} \quad (3-14)$$

$$1.56 A_{barrel} = 738 \text{ N} \quad (3-15)$$

$$A_{barrel} = 473 \text{ mm}^2 \quad (3-16)$$

$$d_{in,barrel} = 24.54 \text{ mm} \quad (r_{in,barrel} = 12.27 \text{ mm}) \quad (3-17)$$

where, F_p is the acting force acting upon a projectile (N); F_a is the air tank force ($1.66 \times A_{in,barrel}$, N); F_b is the atmospheric force ($0.1 \times A_{in,barrel}$, N); F_k is the frictional force (N); $A_{in,barrel}$ is the inner cross sectional area of barrel (mm^2); $d_{in,barrel}$ is the inner diameter of the barrel (mm); and $r_{in,barrel}$ is the inner radius of the barrel (mm).

The barrel size can be chosen from among the manufactured carbon steel pipes for pressure service in accordance with KS D 3562 (Korea Agency for Technology and Standards, 2018). When the barrel pressure is 1.75 MPa, a Sch 20 or more is required (**Eqs. (3-18) and (3-19)**). Considering that an inner diameter of the barrel is 24.5 mm or more, and the expected speed is 300 m/s, the 25A-Sch40 pipe for pressure piping is a good option (**Table 3-1**).

$$\text{Sch.No} = 1000 \times \frac{P_{\text{pipe}}}{S_{\text{pipe}}} \quad (3-18)$$

$$t_{\text{pipe}} = \frac{P_{\text{pipe}}}{S_{\text{pipe}}} \times \frac{D_{\text{pipe}}}{1.75} + 2.54 \quad (3-19)$$

where, Sch.No is the schedule number; P_{pipe} is the pressure in the steel pipe (MPa); S_{pipe} is the allowable stress of the steel pipe (= max. stress/ safety factor (= 4), MPa); D_{pipe} is the outer diameter of the steel pipe (mm); and t_{pipe} is the required thickness of the steel pipe (mm).

Table 3-1 Carbon steel pipe for pressure service (KS D 3562 (Korea Agency for Technology and Standards, 2018))

Nominal Diameter (mm)	Outer diameter (mm)	Nominal wall thickness (mm)		
		Schedule 20	Schedule 40	Schedule 60
25	34	-	3.4	3.9
32	42.7	-	3.6	4.5
40	48.6	-	3.7	4.5
50	60.5	3.2	3.9	4.9
65	76.3	4.5	5.2	6.0

The carrier and projectile will move linearly within the barrel due to the acting pressure, the carrier will stop at the end of the barrel due to the carrier-blocking. The projectile will move forward to the concrete panel due to inertial force (**Figure 3-7**). In order to stop the carrier at the end of barrel, a carrier blocking that has the reduced inner cross-sectional area of the end of the barrel is also manufactured (**Figure 3-7**). The inner diameter of the carrier-blocking was set to 25 mm so that

the projectile could pass smoothly. The carbon steel pipe for pressure of 40A-Sch40 was finally selected in consideration of the area of contact between the carrier and the carrier blocking and the inner diameter of the carrier blocking (Figure 3-8).

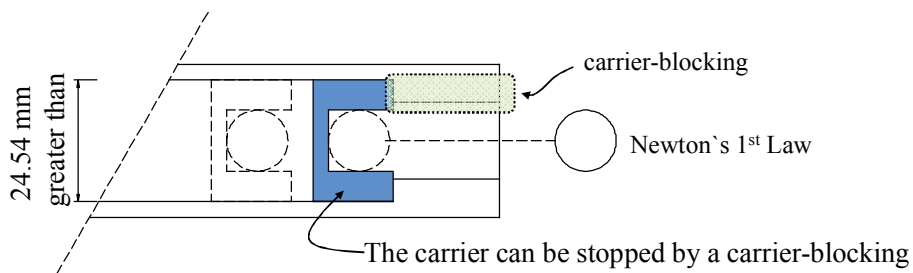


Figure 3-7 Conception of carrier-blocking

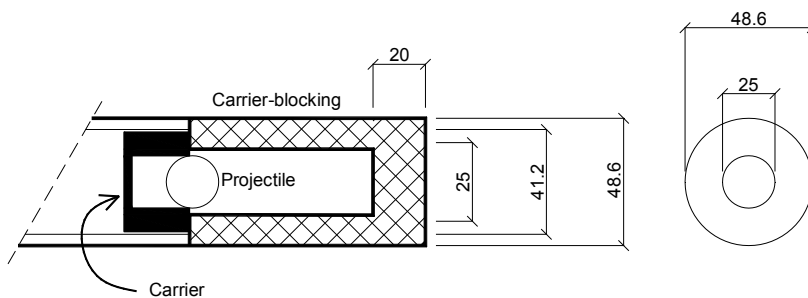


Figure 3-8 Details of end of barrel (unit: mm)

The loading chamber and the retrieving chamber were made the same shape (Figure 3-9). The part having an axial length of 100 mm was cut out at a distance 200 mm from both ends of the barrel (Figure 3-10). The cover with two wings was welded to the cut part (Figure 3-11). The loading/retrieving chamber cover was made by welding a part cut from the barrel and an additional semi-circular steel plate with additional wings that have 6 screw holes. The thickness of the semi-

circular steel plate and the wings is 5 mm. Each wing has three threaded holes of a diameter of 12 mm, so that the loading/retrieving chamber cover and barrel can be bolted together. The used bolts had the diameter of 10 mm and the length of 60 mm. The sealant was applied to the cover to prevent air from leaking from the gap between the barrel and the cover.

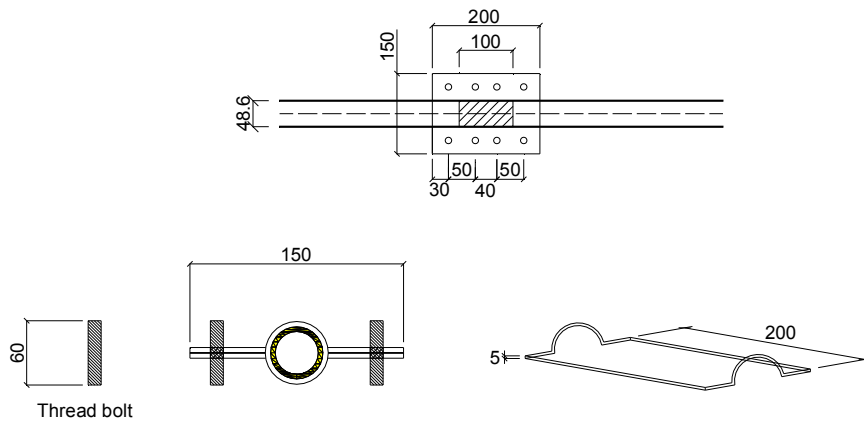


Figure 3-9 Drawing of loading chamber and retrieving chamber (unit: mm)

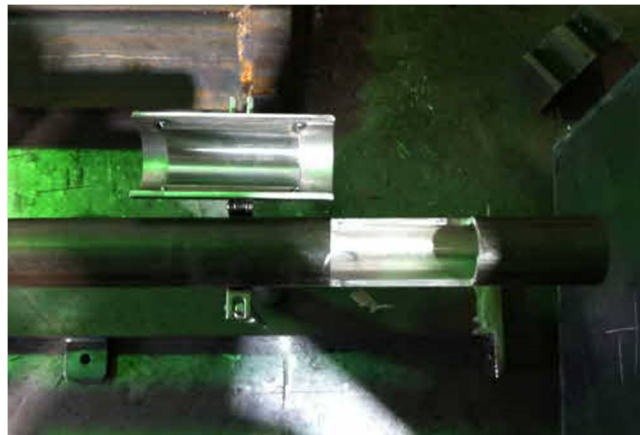


Figure 3-10 Cutting of barrel

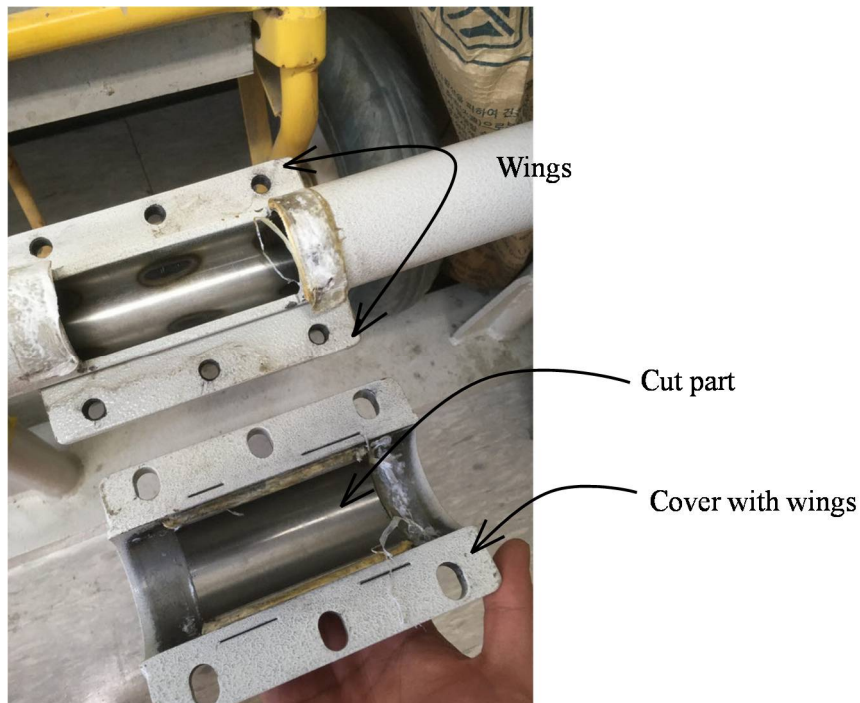


Figure 3-11 Cover with wings of loading chamber

3.3.5 Solenoid valve

A solenoid valve is a device that automatically opens and closes to transfer air from the air-tank into the barrel (**Figure 3-12**). One of existing impact test devices uses a pressure-sheet which screens off to prevent air-pressure transference. The air pressure can be transferred by piercing a pressure-sheet (**Figure 3-1(a)**). It means that every shooting requires the pressure-sheet. When using the solenoid valve, no additional cost is incurred. The solenoid valve is located between the air-tank and barrel to connect them. The size of the valve is determined by the barrel. In **Section 3.3.4**, it was determined that the inner diameter of barrel was 40 mm, so the solenoid valve should be also 40 mm. The selected type of switch is a foot-button

with a long lead wire to make easy turns on the solenoid valve and a dynamic data logger (**Figure 3-13**).



Figure 3-12 Details of solenoid valve



Figure 3-13 Foot button and solenoid valve

3.3.6 Experimental chamber

The chamber is the space where the concrete panel collides with the projectile at high velocity. Therefore, it is necessary to have a space for velocity measurement, a space for installing the concrete panel, and a backyard space when projectile passes throughout the concrete. Experiments were planned to test two types of 400×400 and 200×200 mm specimens, and the chamber was designed accordingly. The total size of the chamber was 1390×500 mm, and the space was separated into four rooms (Figure 3-14).

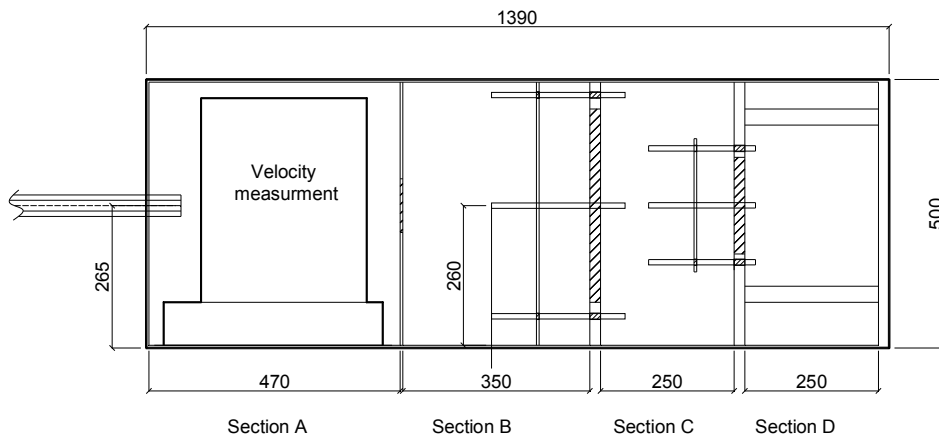


Figure 3-14 Drawing of chambers (unit: mm)

- 1) Section A: This section is for installing a velocity measurement. Since the length of the speed meter is 400 mm, 30 mm of marginal space is added to both sides. Therefore, the total length of Section A is 460 mm.
- 2) Section B: This section is for installing a 400×400 mm specimen.
- 3) Section C: This section is for installing a 200×200 mm specimen.

- 4) Section D: This section is for installing various types of specimens. This section is also a room for receiving a projectile which exits a concrete panel and fragments by scabbing failure.

Gun owners are widespread in the United States, and a variety of gun-related products are sold. Among them are various products that measure the speed of bullets and arrows. Because all sides of the chamber are covered, a velocity measurement was selected as being a product that can be used in a dark room (**Figure 3-15**). A jig was installed to keep the position of velocity measurement from air pressure and to prevent damage to the concrete debris.



Figure 3-15 Velocity measurement with lighting system and jig to fix position and provide protection

3.3.7 Modification of impact test device

Residual velocity measurement: Originally, there was no plan to measure the residual velocity of the projectile. However, the residual velocity is an important factor in evaluating the impact resistance of concrete in view of the law of conservation of energy. Therefore, Sections C and D are combined to provide space for installing a second velocity measurement. Four holes were made in the each of the corners of the 200 × 200 mm back steel frame. A 200 × 200 mm back steel frame with holes and a 400 × 400 mm back frame can be combined with bolts. It is possible to test both the 200 × 200 mm specimens and the 400 × 400 mm specimens. Therefore, the changed experimental chamber is divided into Section A, B and C as shown in **Figure 3-16**.

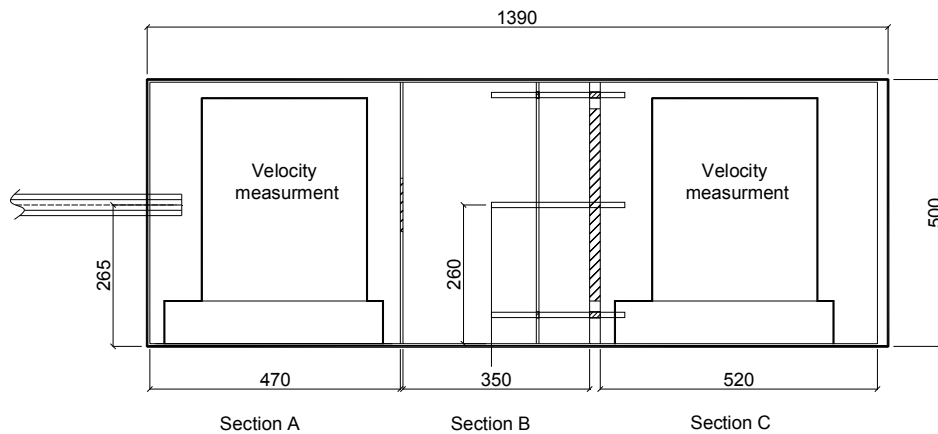


Figure 3-16 Modification of chamber (unit: mm)

Breathing holes: Numerous breathing holes were drilled in the panel of the chamber as shown in **Figure 3-17**. These holes allow air entering the chamber through the barrel to exit quickly without accumulating. Before punching breathing

holes, the door opened and closed with a bang because huge air pressure suddenly came into the chamber. In order to solve this problem, part of door was pierced with breathing holes.



Figure 3-17 Breathing holes

Design error and modification: The aluminum carrier was damaged due to the impact load in the pilot test. This was due to the impact load on a carrier that was not considered in the context of the design process. The impact stress on the carrier exceeded the allowable stress (55 MPa) of aluminum (AL 6061-0) (**Eqs. (3-20)** and **(3-21)**). An additional device was needed to protect the carrier. A 40 mm length of PCV pipe was used to protect the carrier instead of installing additional equipment (**Figure 3-18**). Placing a PCV pipe in the front of the carrier blocking helps the energy of the carrier dissipate.

$$\sigma_{\max} = \sqrt{\frac{M_p V_{\text{imp}}^2 E_{\text{carrier}}}{A_{\text{carrier}} l_{\text{carrier}}}} \quad (3-20)$$

$$\sigma_{\max} = 244 > 55 \text{ MPa} \quad (3-21)$$

where, σ_{\max} is the maximum compressive stress of the carrier (MPa); M_p is the weight of the projectile (kg); V_{imp} is the impact velocity of the projectile (m/s); E_{carrier} is Young's modulus of the carrier (MPa); A_{carrier} is the cross-sectional area of the carrier (mm^2); and l_{carrier} is the length of the carrier (mm).



Figure 3-18 PVC pipe (www.abwplastics.co.uk)

3.4 Manufacturing Process

3.4.1 Air compressor system

The purpose and goal of the air compressor and air tank were discussed with a specialist. The manufacturer provided additional information about the air compressor system and their cumulative experience and suggested good ideas regarding the solenoid valve, receiver tank, and a safety device which is a pressure control switch to stop air compressing if the air pressure in the tank exceeds the pre-set amount. The specialist also suggested that the electric power supplement could be three-phase electric power which could operate the air compressor more efficiently and reliably. Based on this information, the detailed impact test device was modified and advanced.

The compressor head and motor were installed on the steel base, and the small air tank was also installed, with the small air tank acting as the pressure control tank (**Figure 3-19**). After connecting a pressure control switch to the inlet of the air tank, a pressure gauge bar to measure pressure and a check valve on the left of the small air tank were connected where the check valve prevents the backflow of air and allows it to flow in one direction only. On the right side of the small tank, a receiver tank was installed, and then the compressor-head, the small tank, and the receiver tank were connected by a hose.



Figure 3-19 Manufacturing air compressor and air tank system

The receiver tank was drilled with a hole the diameter of 65 mm in the middle of that, and a pipe with an inner diameter of 65 mm was welded to the receiver tank. Since the diameter of the connecting pipe was 65 mm and the inside diameter of the barrel was 40 mm, they were connected using a reducer, an accessory to connect pipes of different diameters. Since it was difficult to disassemble the

reducer after installation, the union was installed in between the reducer and the solenoid valve, with the union there to help with assembly and disassembly. Finally, the solenoid valve was connected to the barrel by the union, with the receiver tank, reducer, union, and solenoid valve all installed in a straight line (**Figure 3-20**).

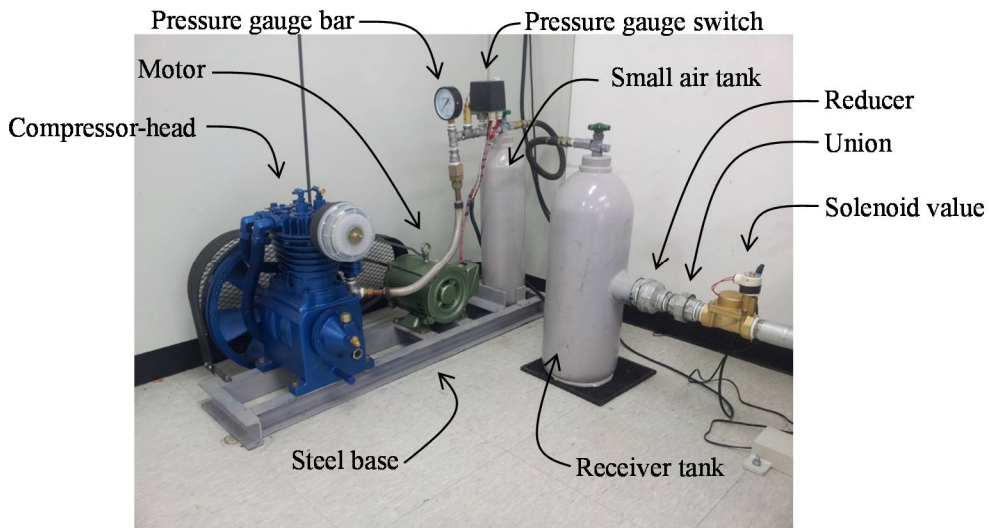


Figure 3-20 Details of air compressor system

3.4.2 Barrel and experimental chamber

The barrel and experimental chambers were designed to be made at the factory and assembled using air compressors in the laboratory. The V-band clamp and C-channel were added during the process of assembling the barrel and experimental chamber (**Figure 3-21**). The C-channel was used as part of the steel base which was anchored to the floor with anchor bolts and supported supporters. A V-band was welded at the end of the supporter, with the V-band gripping the barrel so that it did not move.



(a) V-band clamp
(www.normaamericasds.com)



(b) C-channel
(supertatarayasteel.com)

Figure 3-21 V-band clamp and C-channel for installing barrel

After a detailed plan was established, it was put into production. The inner surfaces of the ready-made carbon steel pipes for pressure service were not smooth, so the honing process was conducted first (**Figure 3-22**). The essence of the honing process was that an abrasive stone scrubs an inner surface along an inner path in order to produce a precision surface. This abrasive machining process helps the carrier and the projectile pass through the inner barrel and speed up. The ends of the barrel were cut out to make the loading/retrieving chamber. An additional steel plate was attached to the cut barrel to make wings on both sides, and six holes were drilled.

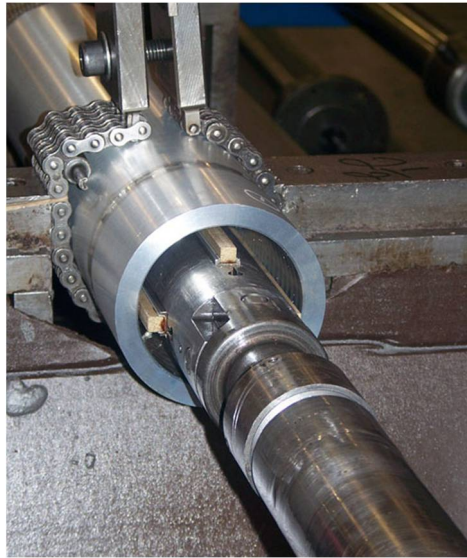


Figure 3-22 Honing process (dev.carlsontool.com)

In order to make the main experiment chamber, five outer walls and three inner partition walls were cut and welded according to the plan (**Figure 3-23**). The left outer wall was drilled to make a hole, and the barrel was inserted into this hole. One more outer wall was cut to make the door, and the door and main chamber were connected with three hinges. The door handle was welded at the lower middle of the door. The completed barrel and the main experimental chamber were painted white.

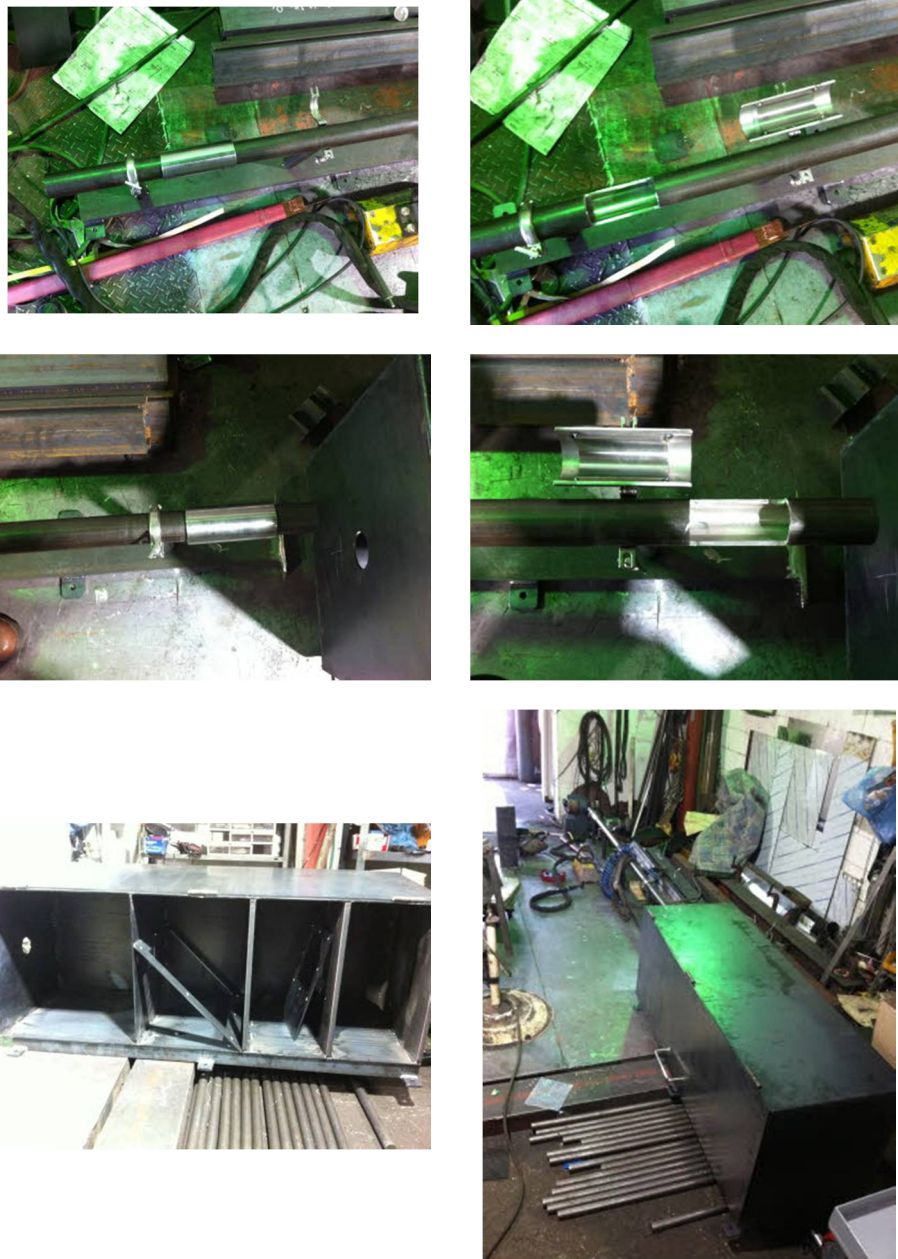


Figure 3-23 Manufacturing barrel and experimental chamber

3.4.3 Installation of impact test device

The manufactured air compressor system, barrel, and main experimental chamber were assembled in the laboratory. The C-channel and the main experimental chamber were anchored to the floor with anchor bolts. The air compressor system and barrel were connected, then a rubber plate was laid under the tank to match the height of the receiver tank and the barrel. A foot button was installed to operate the solenoid valve. Finally, the three-phase electric power was connected to the motor (**Figure 3-24** and **Figure 3-25**).



Figure 3-24 Installation of impact test device



Figure 3-25 Impact test device

3.5 Discussion

In this chapter, the design and manufacturing process of the impact test device are introduced. Some design and manufacturing points are summarized below:

- 1) The air tank capacity is important for maintaining the air-pressure from the solenoid valve to the end of barrel. The larger the size of the air tank, the higher the maintained air-pressure and the higher the speed of the projectile. However, in this study, a 20 L tank was selected it should be installed in a limited space. A sub air-tank was installed to allow continuous experiments to be conducted rapidly.
- 2) The velocity of the projectile can be calculated by the acceleration formula and the uniformly accelerated motion formula. Given that the other conditions are known at this time, the equation can be derived from the relationship between the velocity and the received force of the projectile. At this time, the force acting upon the body and the carrier is the same as the pressure of the tank after subtracting the atmospheric pressure according to the equilibrium condition of the force. Therefore, if the inner diameter of the barrel is determined, the launching speed of the projectile can thus be predicted.
- 3) The spaces in the experimental chamber consisted of a front section for velocity measurement capable of measuring the impact velocity of the projectile and a middle section for installing the specimen. The last section was used for measuring the residual velocity.

- 4) The manufactured impact test device fired a 20 mm ball at speeds of 300 m/s or higher. This indicates that the previous design process was accurate and the experimental equipment was well constructed.
- 5) The impact stress on the carrier during the design process was not predictable. It may be possible to build better equipment in the future if the design process makes up for its weaknesses.

Chapter 4. Impact Experiment and Performance Evaluation

A total of three experiments were planned to obtain the data not sufficiently gathered in experiments conducted by other researchers. As mentioned in **Chapter 1**, it is necessary to evaluate the impact resistance of steel fiber-reinforced concrete by examining various steel fiber volume fractions under the same experimental conditions. In the first experiment, the main parameters are the fraction of steel fiber and the presence of wire mesh. The impact resistance of steel fiber-reinforced concrete with various steel fiber volume fractions was studied, and compared with both plain concrete and steel fiber-reinforced concrete. It was possible to indirectly understand the impact resistance performance of reinforced concrete by investigating the impact resistance of concrete reinforced with wire mesh. How the use of steel fiber and wire mesh simultaneously affects the impact resistance of concrete was also examined. Sub-parameters, such as specimen thickness, aggregate size, and velocity, also were investigated.

The second test was planned to investigate the impact resistance of concrete with normal to high strength. As in the first experiment, the focus was on how an increase in concrete strength affects its impact resistance under the same experimental conditions. Also, this will shed light on how penetration depth is affected by differently shaped projectiles. Additionally, high-strength concrete with

steel fibers was tested to study the effect of steel fibers on high-strength concrete.

In the third experiment, the impact resistance performance of ultra-high-performance concrete (UHPC) with 180 MPa will be investigated. This concrete is expected to demonstrate excellent impact resistance because of its high compressive strength. Therefore, the specimens produced will be very thin.

4.1 Specimen Construction

4.1.1 First experiment plan

The first test was planned to compare the impact resistance of normal concrete with those of steel fiber-reinforced, wire mesh-reinforced concrete, and steel fiber-reinforced concrete with wire mesh. There were many variables in the experimental plan such as the size of the coarse aggregates and the impact velocity, as shown in **Table 4-1**. Among those, the steel fiber volume fraction and wire mesh were the main variables. Adding steel fibers to a concrete matrix is known to offer many advantages such as superior crack control, enhanced toughness, greater absorption energy, and so on. (Kang *et al.*, 2012; Wang *et al.*, 2013; Drdlová *et al.*, 2015; Kahanji *et al.*, 2016; Jalasutram *et al.*, 2017; Kim *et al.*, 2017). Some researchers (Yazici *et al.*, 2013; Almusallam *et al.*, 2013; Hrynyk and Vecchino, 2014) have predicted that these advantages could improve the impact resistance of concrete slab, and their claims have been investigated in this study. The previous experiments conducted by other researchers have not had a variety of steel fiber volume fractions, so it is necessary to evaluate the impact resistance according to various steel fiber volume fraction. This current test program was designed such

that the steel fiber volume fraction was divided into 0.5, 1.0, 1.5, and 2.0%. In **Table 4-1**, the steel fiber volume fraction of 0% means plain concrete.

Table 4-1 First experiment plan and specimen details

Specimens	Concrete (MPa)		V_f (%)	a_{gg} (mm)	h (mm)	V_{imp} (m/s)	Wire mesh (mm)
	f'_{c_meas}	f_{r_meas}					
8-0%-series	45.5	6.93	0	8	30 50 70	270 350	Ø3- 30×30 square
8-0.5%-series	40.13	7.19	0.5				
8-1.0%-series	40.30	11.61	1				
8-1.5%-series	31.70	12.94	1.5				
8-2.0%-series	28.67	12.93	2				
20-0%-series	37.85	6.37	0	20			
20-0.5%-series	42.16	9.04	0.5				
20-1.0%-series	33.96	10.21	1				
20-1.5%-series	35.87	10.87	1.5				
20-2.0%-series	36.35	11.81	2				

$f'_{c,meas}$ is the measured compressive strength of the concrete; $f_{r,meas}$ is the measured flexural strength of the concrete; V_f is the steel fiber volume fraction; a_{gg} is the maximum size of the coarse aggregate; h is the thickness of the specimen; and V_{imp} is the impact velocity.

There have also been only a few experiments on the impact resistance of steel reinforced concrete, and the studies of wire mesh-reinforced concrete or steel fiber-reinforced concrete with wire mesh have been rare. Therefore, the impact resistance of wire mesh-reinforced concrete and steel fiber-reinforced concrete with wire mesh were investigated in this test. Since the wire mesh can be regarded as the same as rebar, the impact resistance of reinforced concrete can also be indirectly evaluated. The evaluation of the impact resistance of steel fiber-reinforced concrete with wire mesh helps to understand how much impact resistance improves when

both steel fibers and wire mesh are used.

In order to achieve the goals of this study, the first experiment was planned as shown in **Table 4-1**. Although the fundamental concrete mixture (**Table 4-2**) was the same, the sub-mixtures were divided into 10 types according to their amounts of steel fiber and their aggregate size. Two types of coarse aggregates of 8 mm and 20 mm were used to evaluate the mechanical properties and impact resistance according to the size of the coarse aggregates. The type of aggregate was different, but the total weight of each coarse aggregate was the same. Other components of the concrete mixture were the same. In order to evaluate the impact resistance according to the thickness of the panels, the specimens were produced with the sizes of 200 × 200 × 30 mm, 200 × 200 × 50 mm, and 200 × 200 × 70 mm (width × height × thickness) as shown in **Figure 4-1**. The projectiles were launched at 270 or 350 m/s to study the effect of the impact velocities. According to each variable, the name of the specimen is set as shown in **Figure 4-2**.

Table 4-2 Mix proportion of concrete

Material	Value
Specified compressive strength ($f'_{c,design}$)	30 MPa
W/B (%)	55
S/a (%)	45
V_f (%)	0 ~ 2 %
Water	205 kg/m ³
Cement	373 kg/m ³
Sand	756 kg/m ³
Coarse aggregate (Max. size of 8 and 20 mm)	924 kg/m ³
Steel fibers	0 ~ 157 kg/m ³

$f'_{c,design}$ is the design compressive strength of the concrete (MPa); W/B is the water-binder ratio; S/a is the fine aggregate ratio; and V_f is the steel fiber volume fraction.

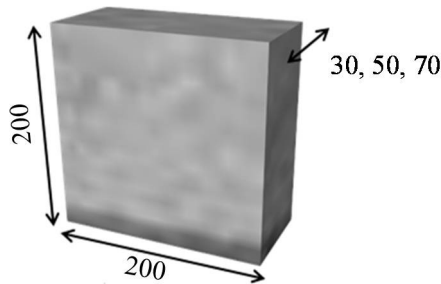


Figure 4-1 Dimension of specimen (unit: mm)

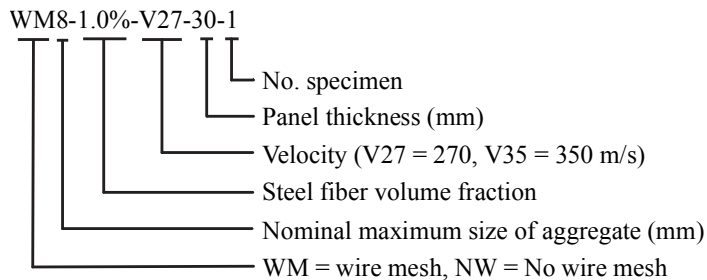


Figure 4-2 Specimen ID of first experiment

To investigate the effect of wire mesh-reinforced and steel fiber-reinforced concrete with wire mesh, the wire mesh was placed 25 mm from the bottom face. Considering the placement of the wire mesh, it was placed only in the specimen thickness of 50 mm and 70 mm (**Figure 4-3**). The wire mesh used in this study was a non-welded crimped wire mesh that took a form of a 30×30 mm square grid with a diameter of 3 mm (**Figure 4-4**). The wire mesh was crimped at intervals of 12 mm and was woven into a grid form without being welding. Its material was SS400 with a specified tensile strength of 400 MPa and yield strength of 205 to 245 MPa.

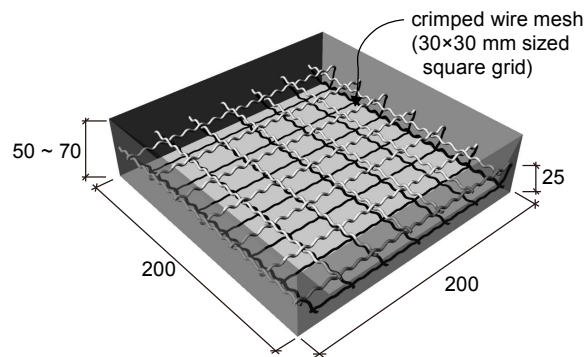


Figure 4-3 Dimensions of specimen and layout of wire mesh (unit: mm)



Figure 4-4 Steel wire mesh

Steel fiber size was $\phi 0.5 \times 30$ mm and the nominal tensile strength of 1100 MPa is shown in **Figure 4-5** and **Table 4-3**. Steel fibers were added into the concrete mixer in two steps to prevent fiber balling (**Figure 4-6**). In order to mold the specimens, a long-large steel frame of 200×200 mm was made and the thickness of the specimen was adjusted with middle partitions (**Figure 4-6**). Three specimens were made per set of specimen thickness, and a set was made for each sub-mixture. The total number of specimens was 90 specimens without wire mesh (= 3 types of thickness \times 3 specimens per each thickness \times 10 sub-mixtures) and 60 with wire mesh. In addition, in order to measure compressive and tensile strength, $\phi 100 \times 200$ mm cylinders were molded and three $100 \times 100 \times 400$ mm concrete prisms were manufactured for each mixture proportion. The specimens, cylinders and prisms underwent an air-dry curing and demolding process for 24 hours, and were finally water-cured for 28 days in a $20 \pm 2^\circ\text{C}$ water tank.



Figure 4-5 Dimension of single hooked steel fiber (unit: mm)

Table 4-3 Properties of end-hooked steel fibers

Type	Single hooked
Specific Gravity	7.85
Diameter (mm)	0.5
Length (mm)	30
Aspect ratio (length to diameter)	60
Tensile strength (MPa)	1100
Elastic modulus (MPa)	205000



Figure 4-6 Process of production of specimens

4.1.2 Second experiment plan

Given the lack of a comparative study of various high-strength concretes under the same conditions, a second experiment was planned to evaluate 80 ~ 120 MPa high-strength concrete under the same impact test conditions and compare its impact resistance (**Table 4-4**). The main parameters were the 6 types of concrete strength, including 2 types of steel fiber reinforced high-strength concrete, and the sub-parameter was the projectile types (described in **Section 4.2.2**). The strength of normal-strength concrete of 35 MPa was used as a reference strength; it was the same measured concrete strength as in the first experiment. High-strength concretes of 80, 100, and 120 MPa were prepared to evaluate the impact resistance and compare normal and high strength concretes. Two specified high-strength concretes, 80-SFRC and 100-SFRC, were mixed with steel fibers. In order to develop the concrete mixture over 80 MPa considering field conditions of the ready-mixed concrete factory, KICT and SIKROAD helped. The trial mix was carried out at the Ssangyong Remicon Plant using the ingredients that the factory has used to mix. Based on the trial mix, the final concrete mixture of 80, 100 and 120 MPa was fixed, and 35 MPa used the existing mixture (**Table 4-4**). The fundamental mixture of 80-SFRC and 100-SFRC were the same 80 and 100 MPa, but 1% of the extra steel fiber volume was added, it was the same that used in first experiment (**Table 4-3** and **Figure 4-5**). The mixture of high strength concrete contained a special admixture known as Zirconia silica fume (ZrSF). The zirconium helps reduce the concrete's viscosity and increase the flowability while maintaining strength capacity. In order to obtain higher fluidity, superplasticizer was mixed.

Table 4-4 Mixed proportions of concrete for second experiment

Material	Value					
	35	80	80 -SFRC	100	100 -SFRC	120
f'_{c_design} (MPa)	35	80	80 -SFRC	100	100 -SFRC	120
f'_{c_meas}	41.3	103.4	100.3	80.6	102.8	96
f_r_meas	5.4	9.2		9.4		7.5
W/B (%)	42	18.8	18.8	14.9	18.8	13.5
S/a (%)	47	40	40	36	40	35
Water (kg/m ³)	96	150	150	140	150	130
Cement (kg/m ³)	210	400	400	470	400	432
Slag powder (kg/m ³)	95	280	280	329	280	384
ZrSF (kg/m ³)	-	120	120	141	120	144
Coarse aggregate (kg/m ³) (max. 20 mm)	942	882	882	876	882	892
Sand (kg/m ³)	576	578	578	484	578	473
HRWR (kg/m ³)		10	10	11.75		
V_f (%)	-	-	1	-	1	-

f'_{c_design} is the specified compressive concrete strength; f'_{c_meas} is the measured compressive concrete strength; f_r_meas is the measured flexural strength; W/B is the water-binder ratio; S/a is the fine aggregate ratio; V_f is the steel fiber volume fraction; ZrSF is the zirconia silica fume; HRWR = High-range water reducer = Superplasticizer; and all values are averages of the three samples.

Based on the results of the first experiment, a thicker specimen was planned for use in the second experiment in order to estimate only the penetration depth without scabbing or perforation. Therefore, the thicknesses of the specimen variants are set equal to 50, 70 and 100 mm. The area of the specimen was planned as 200 × 200 mm in order to maintain consistency with the first experiment. The total number of specimens was 54 (= 3 types of thicknesses × 6 types of concrete mixtures), as classified in **Figure 4-7**. The specimens were produced with the size of 200 × 200 × 50, 200 × 200 × 70 or 200 × 200 × 100 mm (width × height × thickness) (**Figure 4-8**). In addition, in order to measure the compressive and

tensile strength, $\phi 100 \times 200$ mm concrete cylinders and $100 \times 100 \times 400$ mm concrete beams were prisms which were manufactured with nine specimens for each mixture in proportion in accordance with the KS F 2403 (Korea Agency for Technology and Standards, 2014). When designing the concrete mixture, high strength concrete was made for long-term curing after about 4 months (120 days) without the heat and/or water curing. The curing for specimens was planned so that a Vinyl curtain could be sealed to retain the heat of hydration and water (**Figure 4-8**).

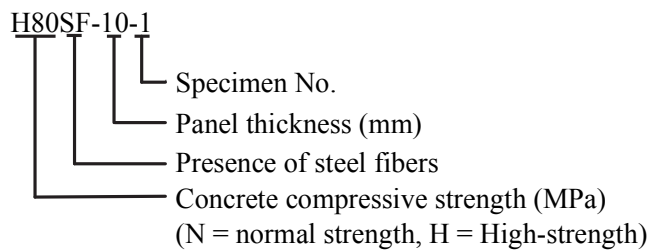


Figure 4-7 Specimen ID of second experiment



Figure 4-8 Production of test panels and mold

4.1.3 Third experiment plan

The third test was planned to assess the impact resistance of the ultra-high performance concrete (UHPC) panel with a “thin” degree of thickness. The thin panel can be used for exterior plates in high-rise buildings. Because of the recent increase in irregularly shaped, tall, and special buildings, the need of various types of exterior and superior strength/durability is rising (**Figure 4-9**). Therefore, the third experiment studied how to evaluate the impact resistance of a thin panel which can be used as an exterior. For comparison with the granite panel, which is currently the most common exterior material, Munkyoung granite and Goheung granite were prepared. The Munkyoung granite was one 20 mm thick and two 30 mm thick specimens, while the Goheung granite were three 30mm thick specimens.



Figure 4-9 Application of ultra-high performance concrete (Musée des Civilisations de l'Europe et de la Méditerranée, France (<http://www.mucem.org>))

The specified concrete compressive strength was 180 MPa (**Table 4-5**), the concrete mixture was based on the KICT ultra-high performance concrete (K-

UHPC) developed by the Korea Institute of Civil Engineering and Building Technology (KICT) (Koh *et al.*, 2012; Korea Concrete Institute, 2012; Joh *et al.*, 2012). A coarse aggregate is not used in UHPC, but rather only the fine aggregate. In order to improve the mechanical properties, a diameter of 0.2 mm and a length of 16 mm steel fibers were used together with 0.5%, and 1.0% of steel fiber, with a diameter of 20 mm were mixed together, making a total steel fiber volume fraction of 1.5%. The specified tensile strength of steel fiber was 1600 MPa. A specimen was manufactured with a space of 400 × 400 mm and the thickness was respectively produced in a thin manner in 10, 20, 30 mm. Four specimens were made for each thickness, a total of 12 specimens. According to panel thickness and the experimental order, specimens were named as shown in **Figure 4-10**.

Table 4-5 Mix proportion of K-UHPC for third test

Material		Value
f'_{c_design} (MPa)		180 MPa
f'_{c_meas}		168 MPa
W/B (%)		20
V_f (%)	16 mm	0.5%
	20 mm	1.0%
Water (kg/m ³)		150
Premixing of binder constitutions (kg/m ³)		400
Fine aggregate (kg/m ³)		867.4
Antifoaming agent (kg/m ³)		0.5
Superplasticizer		18.1

f'_{c_design} is the specified compressive concrete strength; f'_{c_meas} is the measured compressive concrete strength; W/B = water-binder ratio, V_f = steel fiber volume fraction, Premixing of binder constitutions consists of cement, expansive admixture for the cement mixture, zirconia silica fumes, shrinkage reducing admixtures, filler.

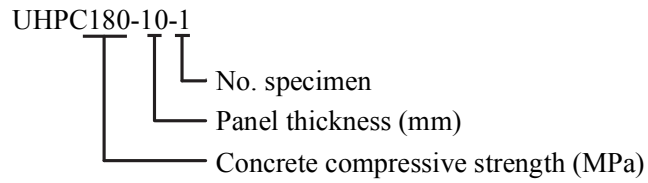


Figure 4-10 Specimen ID of third experiment

The concrete was mixed using a large fan mixer, and the steel fiber was added into the fan mixer little by little in order to suppress fiber balling (**Figure 4-11**). As regards the fabrication of the test specimens, molds with depths of 10, 20, and 30 mm in a space of 400×400 mm were made of wood, respectively. As regards the compressive strength test, five circular cylinders of $\phi 100 \times 200$ mm were produced. The mixed fresh concrete was immersed in the molds of a test specimens and cylinders, and were then sealed and cured. After the concrete hardened, the sealed seal was removed and steam curing was performed at 80 to 90 ° C for 48 hours. The wood molds were removed after the curing process was completed. The removed K-UPHC specimens and the cylinder specimens were cured in water for 4 weeks in a water tank at 20 ± 2 ° C. The test method was KS F 2405 (Korea Agency for Technology and Standards, 2010b), and the compressive strength was measured on the impact test day using a UTM machine.



Figure 4-11 Production of UHPC panel

4.2 Impact Experiment

The three experiments were performed similarly, but differed slightly in the details. This section presents the details of experimental design and procedures.

4.2.1 First experiment

This first program was carried out using the impact test device at Chungnam National University (**Figure 4-12**). The test guideline specifies panel thickness, impact velocity, and the diameter of the projectile to evaluate the impact resistance of the concrete panel is clearly not suggested. This experiment was conducted based on the impact test process from previous researchers (Zhang *et al.*, 2005; Beppu *et al.*, 2008). Two square-void steel frames were attached to both sides of the concrete panel and fastened by 4 bolts as shown in **Figure 4-13**. Two frames made of overlapping parts were placed between the specimens and the frames, left and right 10 mm each, upper 5 mm, and lower 15 mm, the specimen was 140 mm above the floor. The launching system fired a projectile using the compressive force of nitrogen and can control the pressure in the gas chamber in order to change the velocity of a projectile. The projectile is spherical shaped and has a diameter of 20 mm and a weight of 32.8 g. It was fired with 270 or 350 m/s impact velocity.

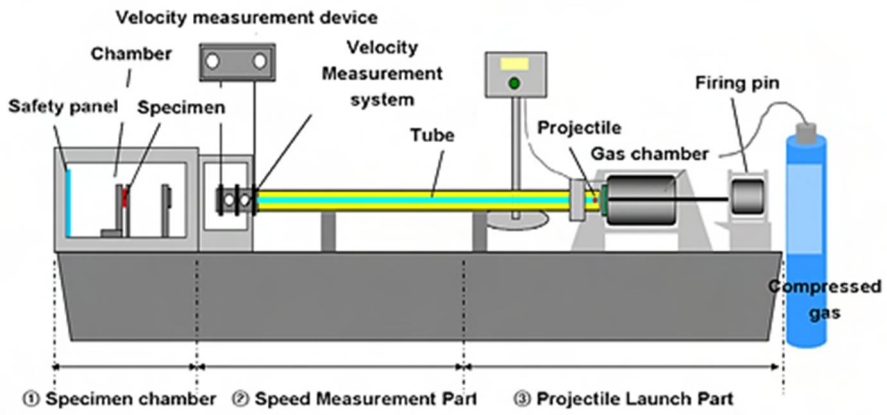


Figure 4-12 Impact test device at Chungnam National University

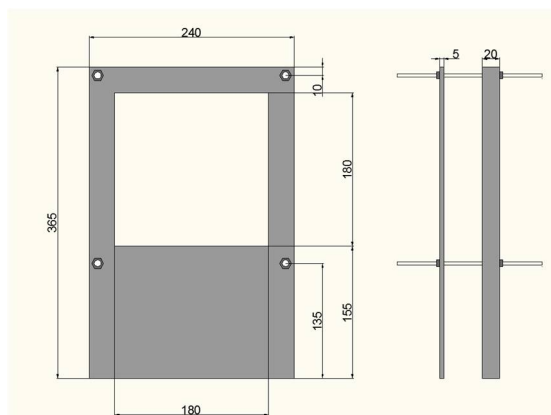


Figure 4-13 Specimen set-up (top) and size of frame (bottom) (unit: mm)

4.2.2 Second experiment

The second experiment was conducted using the equipment designed in this study. The spherical ball was used only once as a projectile in the first experiment. The second experiment was carried out using various types of projectiles such as sphere, long-hemisphere, short-hemisphere, long-conical and short-conical projectile as shown in **Figure 4-14**. The diameter of the spherical projectile was 20 mm and 32.8 g, long-hemisphere. It has a body length of 30 mm and nose length of 10 mm. The short-hemisphere has a body length of 20 mm and nose length of 10 mm. The body length and nose length of long- and short-conical projectiles has the same long- and short-hemisphere length. Three specimens were tested for long type projectile and two specimens were tested for short type projectile. The spherical projectile was fired at a speed of about 200 m/s and other projectiles were fired at 100 to 140 m/s. The experimental data for 270 m/s was acquired in the first experiment, and the impact velocity of the spherical projectile in second experiment set to 200 m/s.

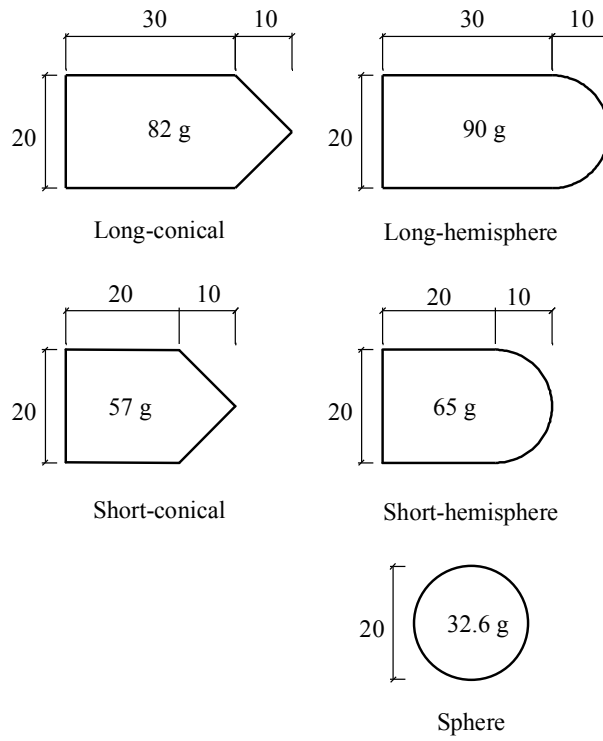


Figure 4-14 Types of projectiles (unit: mm)

4.2.3 Third experiment

The third experiment was performed to evaluate the impact resistance of UHPC using the small impact test device developed in this study. Since it is a concrete panel used as an exterior, it should withstand the impact energy of the bullet from a gun or the flying debris caused by strong wind such as typhoon and hurricane. A spherical steel ball with a diameter of 20 mm and a weight of 32 g can produce a similar level of muzzle energy of the bullet, when it is shot at a speed of approximately 180 m/s. The spherical projectile with a velocity of 180 m/s is equivalent to a 9-mm gun and 40 Smith and Wesson gun as shown in **Figure 4-15**.

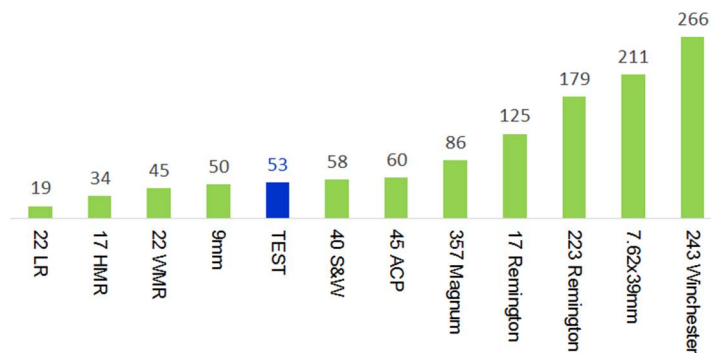


Figure 4-15 Muzzle energy of various cartridges (kgf.m)
(<http://www.shooterscalculator.com>)

For the spherical projectile to have a speed of 180 m/s, the projectile was accelerated after the solenoid valve was opened at a point when the pressure of the air tank was measured at 1 MPa. A velocity measurement device was installed on the front side of the chamber to measure the impact velocity, and a square-void rigid frame was installed fix the 400 × 400 mm specimen (**Figure 4-16**). A concrete strain gauge was attached to the center of the rear face of the test specimen to

investigate the strain history of the rear face. The duration of the impact is less than 0.5 seconds, and the strain data were collected using the Dynamic Data Logger FFT EDX-2000A product. The interval between data was 0.0001 second, and the average of the received data was 0.005 second.



Figure 4-16 Test set-up

4.3 Material Test and Results

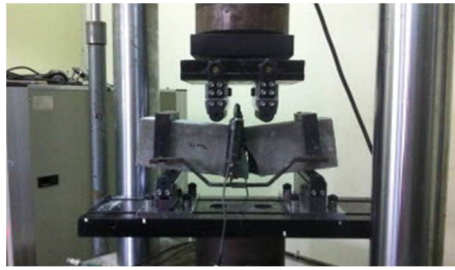
4.3.1 Material test

The average of measured compressive strengths was obtained using the Universal Testing Machine (UTM) according to the KS F 2405 (Korea Agency for Technology and Standards, 2010a) and the test of the averages of measured flexure strength following the KS F 2408 (Korea Agency for Technology and Standards, 2010b). Cylinders and prisms for the first experiment were tested on the test days. The second tests were carried out at 28, 90, 120 (on the test days) days because the high-strength concrete was considered for long-term curing without heat- or water-curing. When measuring the stress and strain relationship, a strain gauge was attached to a concrete cylinder in order to obtain a more accurate strain value.

The 2~3 cylinders from the first experiment were used to estimate the compressive and flexural strength, respectively. Five cylinders in the second experiment were used to measure the compressive strength. Three of them were attached by a strain gauge, others did not have a strain gauge (**Figure 4-17(a)**). This followed KS F 2423 (Korea Agency for Technology and Standards, 2016). Five prisms were also used to measure flexural strength (**Figure 4-17(b)**). 5 cylinders without strain gauges were also used to measure splitting strength (**Figure 4-17(c)**). The tensile stress of the steel fiber of 3 was measured as shown in (**Figure 4-17(d)**).



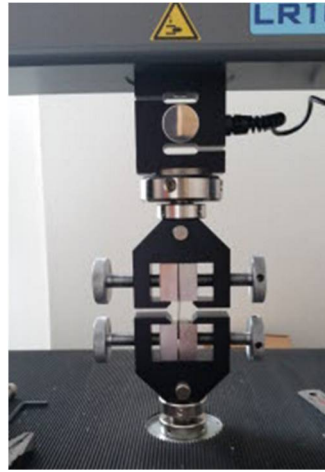
(a) Compressive test



(b) Flexural test



(c) Splitting test
(for second experiment)



(d) Tensile test of steel fibers

Figure 4-17 Material properties tests

4.3.2 Discussion of concrete properties for experiment

4.3.2.1 Effects of steel fibers on properties of concrete

Numerous studies found that steel fibers did not critically affect the increase of concrete compressive strength (Ezeldin and Balaguru, 1992; ACI Committee 544, 2009). The same results for the cylinders test for the first experiment are shown in **Figure 4-18**. The compressive strength of concrete of an 8 mm aggregate

size rather decreased as steel fiber volume fraction increased. The measured compressive strength of 2.0%-A8-series (2.0% steel fiber volume fraction and 8mm aggregate) was even lower than the specified compressive strength (30 MPa). On the other hand, variations of compressive strength with 20mm aggregate were not considerable although the steel fiber volume fraction increased. A concrete strength greater than that of plain concrete had only a 5% steel fiber volume fraction, other volume fractions exhibited lower strength. It was difficult to identify whether the addition of steel fibers influence the compressive strength of SFRC. The modulus of rupture (f_r) of both SFRC types clearly appeared as an increment tendency as the steel fibers volume fraction increased. Compared with the aggregate size, the modulus of rupture of the concrete with 8 mm aggregate increased more than 20 mm. The dispersion of steel fibers improved as the size of the coarse aggregates was reduced, therefore the results are concluded.

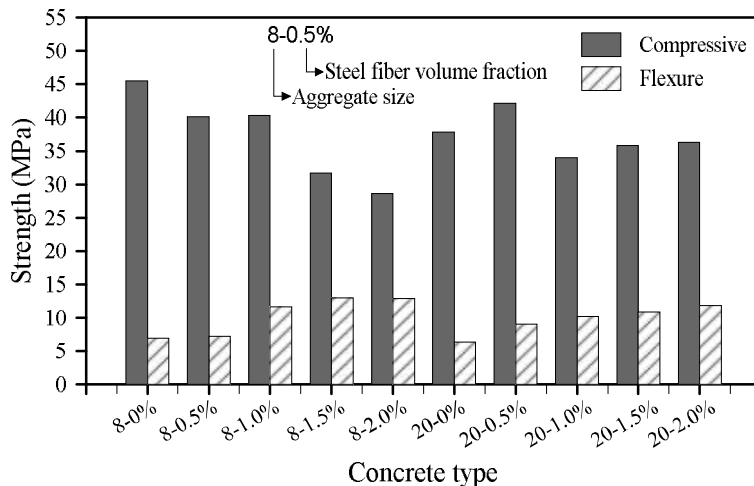


Figure 4-18 Compressive and flexural strengths in first experiment

4.3.2.2 High strength concrete and UHPC's properties

Compressive strength at 28, 90, and 120 days from curing, and the tensile strength at 120 days were measured at the laboratory of Seoul National University. The pictures of concrete cylinders are shown in **Figure 4-2**. Compressive strength at 28, 90, 120 days (test day) was measured and tensile and modulus rupture were measured as shown in **Table 4-6**. The design concrete strength of 35, 80, 80-SFRC and 100-SFRC MPa reached the target strength, but 100 and 120 MPa did not reach this. The ε_{cu} value of 35, 80, 80-SFRC, 100 and 100 MPa (SFRC) was close to 0.003 and the value of 120 MPa was measured as 0.0025. Although 100 MPa and 100-SFRC were the same concrete mixture, only 100 MPa did not reach the target strength. On the other hand, 80 MPa and 80-SFRC had the same mixture and differed only in terms of the presence of steel fiber. Design concrete strength of 100 MPa and 120 MPa failed to reach the target strength is regarded as being a problem other than the concrete mixture. It is considered that unknown segregation due to the moving or mixing process of the remicon vehicle occurred. 100 and 120 MPa were poured in October, and the temperature was too low to cure on site. Although it was fine at the time of determining the long term curing on site, it was judged that the curing temperature was not sufficiently secured due to the delay in the production of the test specimen. To summarize, high strength concrete is considered to be sensitive to transport and curing, so conservative and delicate management is required.

Table 4-6 Measured properties of concrete (unit: MPa)

Design strength	Date	f'_{c_meas} (at 28 ays)	f'_{c_meas} (at 90 days)	f'_{c_meas} (at 120 ays)	f_{sp_meas}	$\frac{f_{sp_meas}}{f'_{c_meas}}$
35	07.31.	37	38.3	41.3	5.4	0.13
80	09.20.	87.3	85	103.4	9.2	0.09
80-SFRC	09.23.	67.3	94.7	100.3	10.6	0.11
100	10.14.	71.7	75.5	80.6	9.4	0.12
100-SFRC	09.29.	92.3	101.3	102.8	12.4	0.12
120	10.02.	69.7	97	96	7.5	0.08

f'_{c_meas} is the measured concrete compressive strength (MPa) and f_{sp_meas} is the measured concrete splitting strength (MPa).

In order to closely examine the cylinders after compression and the splitting test, a cylinder of 35 MPa which did not include Zr had a gray color on a whole inside (**Figure 4-19**). However, the high strength concrete mixed with zirconium showed gray to a depth of about 7 ~ 15 mm from the surface, but the inside showed blue-green as shown in **Figure 4-19**.

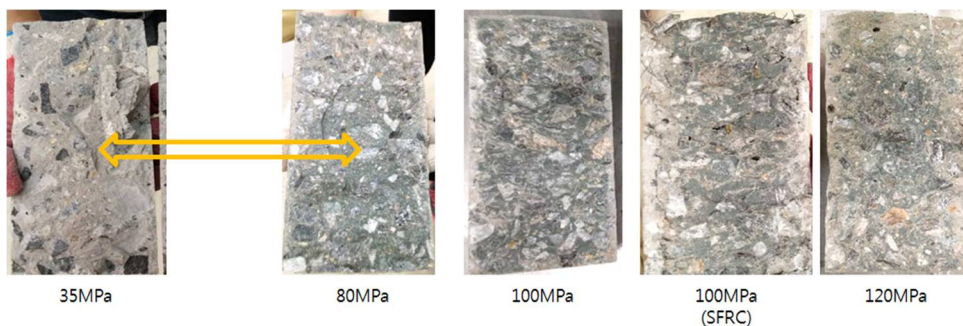


Figure 4-19 Vertical section of cylinders after splitting test

The average compressive strength of concrete of the UHPC in the third experiment was 168 MPa. The average concrete flow was measured as being 250 mm.

4.3.2.3 Steel fiber properties

Three tensile specimens were subjected to a tensile test, and the stress-strain relationship is shown in **Figure 4-20**. Since the steel fiber was short and thin, a slip occurred at the beginning. The average maximum stress was 1185 MPa.

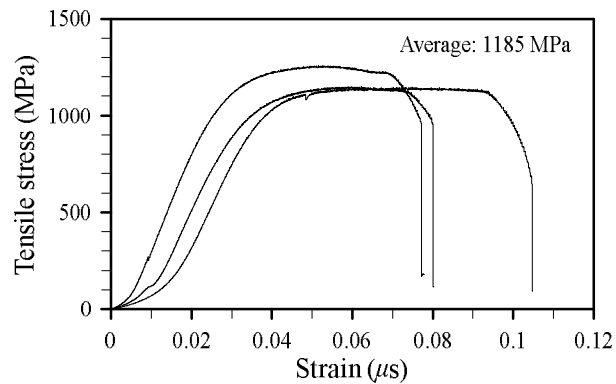


Figure 4-20 Tensile stress-strain curve of steel fibers

4.4 Analysis of Experimental Results

4.4.1 First Experiment

4.4.1.1 Effect of steel fiber and aggregate size

Figure 4-21 shows the penetration depth of all specimens in the first experiment according to the steel fiber volume fraction, where the specimens having only spalling failure were used. The penetration depth increased with a steel fiber volume fraction of 1.5%, but the difference in the penetration depth was not significant.

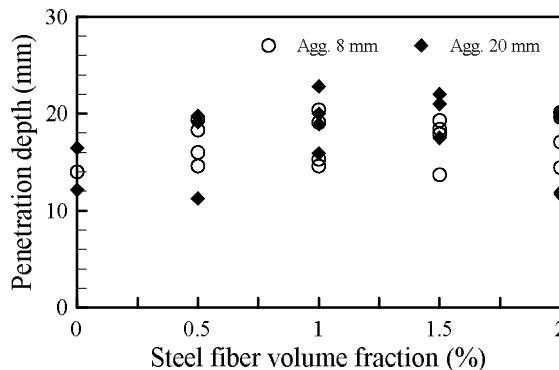


Figure 4-21 Relationship between penetration depth and steel fiber volume fraction

Since the variables of specimens were distinctly from each other, it was difficult to evaluate the impact resistance only by the penetration depth. It was considered to integrate variables such as the compressive strength of concrete, thickness, impact velocity, aggregate size, and steel fiber volume fraction through the *G*-function and *I*-function. The *G*-function and *I*-function can include a

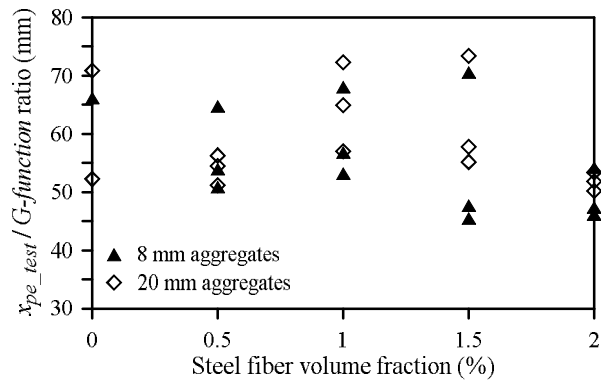
comprehensive set of variables to analyze the penetration depth. These were used to study compressive comparison. The G -function (**Eq. (4-1)**) and I -function of the Haldar formula (I -Haldar, **Eq. (4-2)**), and the I -function of the Hughes formula (I -Hughes, **Eq. (4-3)**) were defined in the modified NDRC formula (NDRC, 1946), Haldar and Hamieh formula (1984), and Hughes formula (1984), respectively. These functions were all dimensionless coefficients, and there was a difference in that I -Haldar used the compressive strength of concrete and I -Hughes used the modulus of rupture.

$$G\text{-function} = 3.8 \times 10^{-5} \frac{NM_p}{d_p \sqrt{f'_c}} \left(\frac{V_{imp}}{d_p} \right)^{1.8} \quad (4-1)$$

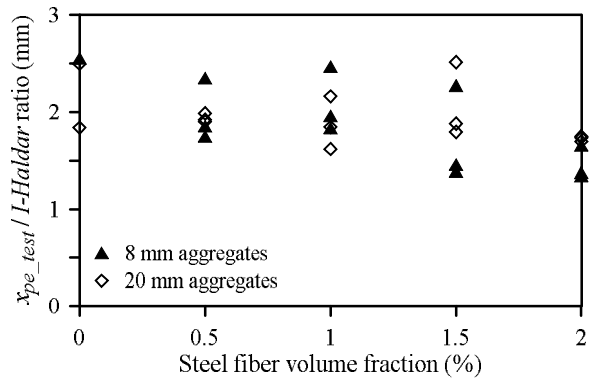
$$I - \text{Haldar} = \frac{M_p N_p V_{imp}^2}{d_p^3 f'_c} \quad (4-2)$$

$$I - \text{Hughes} = \frac{M_p V_{imp}^2}{f_r d_p^3} \quad (4-3)$$

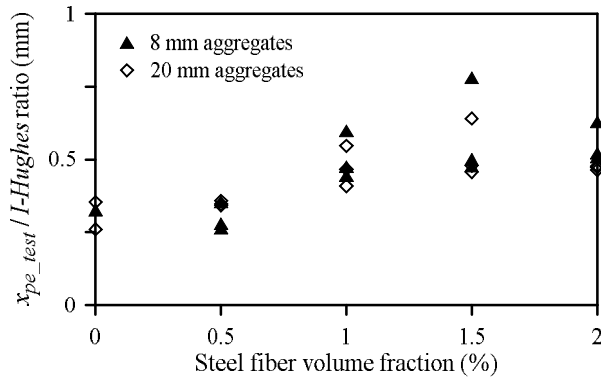
where, N_p is the nose shape factor (0.72, 0.84, 1.0 and 1.14 for flat, hemispherical, blunt and very sharp noses, respectively); M_p is the mass of the projectile (kg); d_p is the diameter of the projectile (m); V_{imp} is the impact velocity of the projectile (m/s); f'_c is the compressive strength of the concrete (Pa); and f_r is the modulus of rupture of the concrete (Pa).



(a) *G-function*



(b) *I-Haldar*



(c) *I-Hughes*

Figure 4-22 Ratio of tested penetrations depth to G-function or impact factors

Table 4-7 Normalized average of penetration depth to *G-I*-functions according to steel fiber volume fraction (unit: mm)

Steel fiber volume fraction (%)	<i>G</i> -function		<i>I-Haldar</i>		<i>I-Hughes</i>	
	8 mm agg.	20 mm agg.	8 mm agg.	20 mm agg.	8 mm agg.	20 mm agg.
0	66.09	61.55	2.55	2.17	0.33	0.31
0.5	56.50	53.97	1.99	1.94	0.30	0.35
1	59.33	64.72	2.09	1.88	0.51	0.47
1.5	54.55	62.11	1.71	2.06	0.59	0.53
2	49.18	51.83	1.46	1.73	0.55	0.47
Average	57.13	58.84	1.96	1.96	0.452	0.426

Figure 4-22 classified the tested penetration depth of the specimens according to the steel fiber volume fraction and the size of aggregate, and divided as the *G*-function or the impact factors. **Table 4-7** presented the average of penetration normalized by *G*-function, *I-Haldar*, or *I-Hughes*. **Table 4-7** presented the average penetration depth to *G*-function (defined in the NDRC formula (NDRC, 1946)), *I-Haldar* (defined in Haldar formula (Haldar and Hamieh, 1984)), *I-Hughes* (defined in Hughes formula (Hughes, 1984)) according to the steel fiber volume fraction.

Up to a steel fiber volume fraction of 1.0%, test specimens with 8 mm aggregates showed larger average penetration depth to *G*-function. But after the fraction exceeded 1.0%, the average was less than the specimens with 20 mm aggregates. The same trend was observed when the *I-Haldar* was used. The specimen with 8 mm aggregates showed a decreasing trend according to the steel fiber volume fraction. On the contrary, specimens with 20 mm aggregates had

almost the same average normalized penetration depth by *G*-function or *I-Haldar*, even as the steel fiber volume fraction increased. **Figure 4-22(c)** shows the tested penetration depth divided by *I-Hughes*. Here, the $x_{pe}/I\text{-Hughes}$ increases as the steel fiber content increases, regardless of the aggregate size. The $x_{pe}/I\text{-Hughes}$ of 8 mm aggregates had better penetration resistance in the case of steel fiber volume fractions of 0 and 0.5%. However, the $x_{pe}/I\text{-Hughes}$ of 8 mm aggregates with a steel fiber volume fraction of 1.0 % and higher had poorer penetration resistance. In other words, the penetration resistance decreased even if the steel fiber volume fraction increased. The Hughes formula predicts that penetration resistance increases as the tensile strength of concrete increases. However, analysis of these experiment results leads to the opposite conclusion. As shown in **Table 4-1**, the strength of concrete using 8 mm aggregates decreased as the steel fiber content increased. The strength of concrete with 20 mm aggregates displayed similar values regardless of steel fiber content. Based on **Table 4-1** and **Table 4-7**, it can be seen that penetration depth is affected by compressive strength, making it more reasonable to use the compressive strength of concrete in the impact formula.

From the view point of weight loss, the specimens with 8 mm aggregates and no steel fibers showed less weight loss than the specimens with 20 mm aggregates and no steel fibers (**Figure 4-23**). The difference of weight loss between the specimens with 8 mm and 20 mm was not reduced as steel fiber volume fraction increased (**Figure 4-23**). This trend was also exhibited in area loss on the front face. It is confirmed that the impact resistance of concrete panels was affected by aggregate size. This can vary depending on which the combination of steel fiber volume fraction and aggregate. When the weight loss and area loss on the front face were compared, the weight loss decreased as the steel fiber content increases

(Figure 4-23) and the area loss on the front face also gradually decreased (Figure 4-24). The addition of steel fibers had little effect on penetration depth, but it was effective in reducing weight loss and the area of the damage. Table 4-8 presented the number of specimens exhibiting scabbing failure, including perforation. The number of scabbing and/or perforation failures decreased when steel fibers were added to the concrete mixture. In other words, steel fibers were effective for the purpose of reducing the scabbing depth.

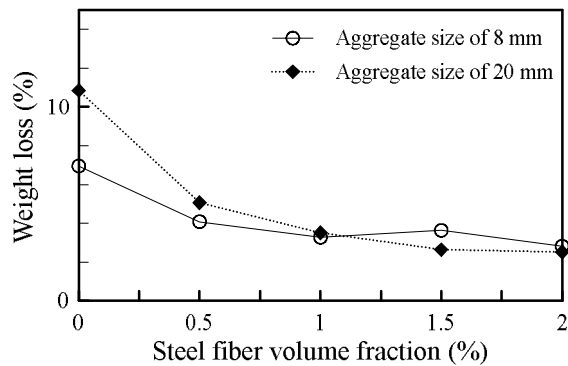


Figure 4-23 Relationship between weight loss and steel fiber volume fraction

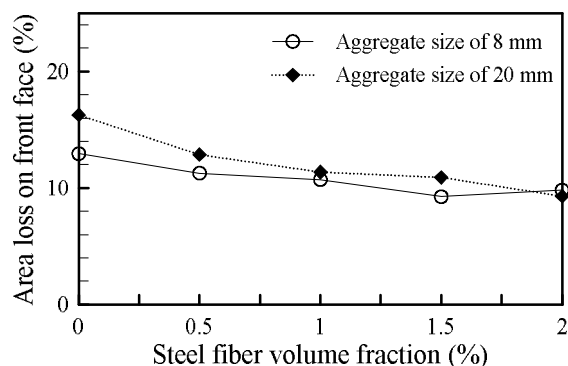


Figure 4-24 Relationship between area loss on front face and steel fiber volume fraction

Table 4-8 Number of specimens with scabbing failure (including perforation)

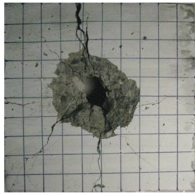
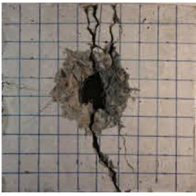
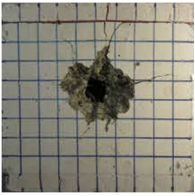
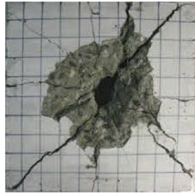
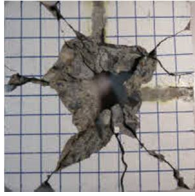
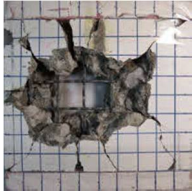
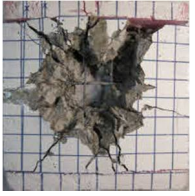
Aggregate size (mm)	Thk. of specimen (mm)	Steel fiber volume fraction (%)				
		0	0.5	1.0	1.5	2.0
8	30	3 of 3	3 of 3	3 of 3	3 of 3	3 of 3
	50	3 of 3	2 of 3	2 of 3	2 of 3	2 of 3
	70	3 of 3	0 of 3	0 of 3	0 of 3	0 of 3
20	30	3 of 3	3 of 3	3 of 3	3 of 3	3 of 3
	50	2 of 2	none	2 of 3	3 of 3	2 of 3
	70	1 of 3	0 of 3	0 of 3	0 of 3	0 of 3

4.4.1.2 Effect of wire mesh

Table 4-9 exhibited a picture of the perforated specimens with/without the wire mesh after the projectile collision. The shape of spalling and scabbing was generally circular, and the loss area of the rear face was larger than the loss area of the front face for NW8-0.5%-V35-50, NW8-1.0%-V35-50, 20NW20-0%-V35-50. Specimens with wire mesh showed typical fracture shapes, but in some specimens could be found many more different shapes of failure modes. There was a circular spalled shape in the front face, while a circular squared scabbing occurred in the rear face, as seen in WM8-0.5%-V35-50 and WM8-1.0%-V35-50. It was speculated that wire mesh divided into 30×30 mm blocks and the specimen was destroyed in the shape of blocks when the projectile hit the specimen. It was considered that this failure occurred when 20 mm aggregate was trapped within a 30×30 mm block and caused the block-shaped failure. This type of failure was also observed in the specimens with a thickness of 50 mm. Thus, it was considered

that a circular squared scabbing occurred when the specimen was thin. Some specimens were observed with a wider area loss of the rear face along the lines of the wire mesh, and this failure was a splitting bond failure. It was assumed that this failure mode was caused by the tensile failure of concrete and tensile elongation of the wire mesh which led to cracks along the wire mesh when the specimen was deformed overall due to the tensile force.

Table 4-9 Comparison of specimens with and without wire mesh

Specimen	NW8-0.5%-V35-50	NW8-1.0%-V35-50	WM8-0.5%-V35-50	WM8-1.0%-V35-50
Front face				
Rear face				
Specimen	NW20-0%-V35-50	WM20-1.0%-V35-50	WM20-0%-V35-50	WM20-0.5%-V35-50
Front face				
Rear face				

Since the shape of the crater was irregular and made the relative comparison much easier, the area of a crater was transformed into an equivalent circle with the same area. The diameter of the equivalent circle diameter of the spalling area was substituted as $D_{eq,front}$, the equivalent circle diameter of the internal perforation area that occurred in the perforated specimen as $D_{eq,hole}$, and the equivalent circle diameter of the scabbing area as $D_{eq,rear}$ (**Figure 4-25**).

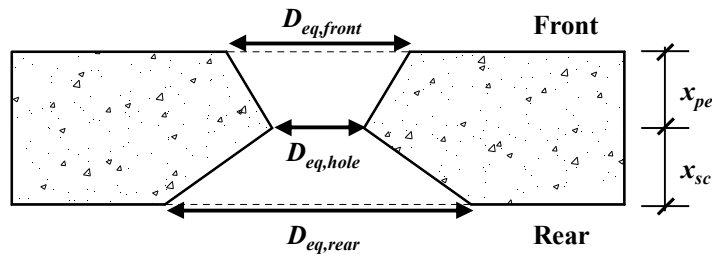


Figure 4-25 Definition of $D_{eq,front}$, $D_{eq,hole}$ and $D_{eq,rear}$

Figure 4-26(a) and **Figure 4-26(b)** display all the specimens that were first classified by the size of the coarse aggregates and were later categorized by the steel fiber volume fraction. **Figure 4-26(c)** shows specimens with perforations $D_{eq,front}$ and $D_{eq,rear}$ that were divided by $D_{eq,hole}$ and then categorized by the steel fiber volume fraction. According to **Figure 4-26(a)**, an impact velocity of 270 m/s when the steel fiber volume fraction was 0% resulted in a failure area of roughly $3.4d_p$, with d_p being the diameter of the projectile, while with an impact velocity of 350 m/s resulted in a failure area of roughly $4.5d_p$.

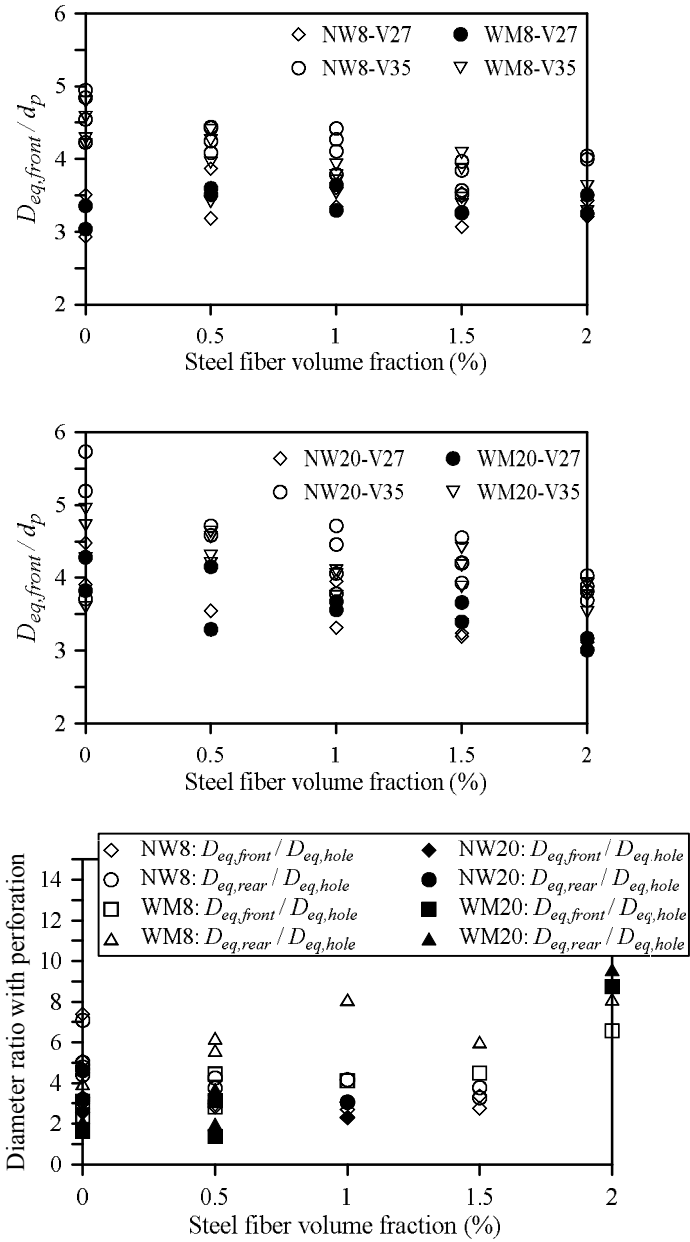


Figure 4-26 $D_{eq,front}$ to d_p ratio and $D_{eq,front}/D_{eq,hole}$ or $D_{eq,rear}/D_{eq,hole}$ according to steel fiber volume fraction

Figure 4-26(a) and **Figure 4-26(b)** show that the value of WM8 and WM20, which were wire mesh reinforced, was lower than the value of NW8 and NW20 which did not have wire mesh reinforcement. Looking at the numerical values, when using 8 mm aggregates and when the steel fiber volume fraction was 0, 0.5, 1.0, 1.5, and 2.0%, the demonstrated surface area loss was $4.30d_p$, $4.04d_p$, $3.92d_p$, $3.58d_p$, $3.74d_p$, respectively. Meanwhile, in the wire mesh-reinforced concrete specimens, the results were $4.04d_p$, $3.85d_p$, $3.64d_p$, $3.55d_p$, and $3.56d_p$ respectively, and the decrease in the numerical values indicated an improvement in impact resistance. Moreover, when using 20 mm aggregates and when the steel fiber volume fraction was 0, 0.5, 1.0, 1.5, and 2.0%, specimens without wire mesh showed numerical values of $4.60d_p$, $4.28d_p$, $4.05d_p$, $3.86d_p$, and $3.59d_p$ respectively, while those wire mesh-reinforced specimens exhibited values of $4.27d_p$, $4.19d_p$, $3.81d_p$, $3.81d_p$, and $3.55d_p$, reducing the overall surface area loss.

In the scatter graph of **Figure 4-26(a)** and **Figure 4-26 (b)**, one can observe that the $D_{eq,front}/d_p$ values of the wire mesh-reinforced specimens were distributed under those specimens without a wire mesh. This helped in qualitatively determining the improvement of the impact resistance. In addition, as the steel fiber volume fraction increased, the $D_{eq,front}/d_p$ values declined. And the steel volume fraction increased to 1.5%, the results showed that there was a noticeable tendency of the impact resistance increasing. In this context, it can be concluded that the steel fiber volume fraction and wire mesh respectively increased the impact resistance in studying the correlation of the front and rear area loss and impact resistance.

Figure 4-26(c) displays the $D_{eq,front}/D_{eq,hole}$ and $D_{eq,rear}/D_{eq,hole}$ values of the specimens, of which $D_{eq,hole}$ was greater than 20 mm among those specimens that

were perforated. Within a range from 0% to 0.5% of the steel fiber volume fraction, the specimens that used wire mesh-reinforced concrete had an even smaller area loss compared to $D_{eq,hole}$. However, there was a specimen which had a considerable $D_{eq,rear}/D_{eq,hole}$ value among the specimens, and this occurred because there was a greater area loss in the rear due to the splitting failure. There were no perforated specimens among the wire mesh-reinforced specimens with a 1.0% and 1.5% steel fiber volume fraction. In this context, it could observe a greater reinforcement effect of impact resistance when a wire mesh was used.

Figure 4-27 shows the penetration and spalling without scabbing and the penetration depth of the specimens that showed a hair crack on the rear face based on a comparison of steel fiber volume fraction. In the figure, the specimens that used 8 mm aggregates showed a steady increase of the penetration depth to 1.5% of the steel fiber volume fraction. Such differences occurred due to the differences in compressive strength. On the other hand, for those specimens that used 20 mm aggregates, a similar penetration depth was shown regardless of the steel fiber volume fraction. Moreover, the specimens that were reinforced by wire mesh also exhibited a similar penetration depth. For NW8-V27, NW8-V35, WM8-V27, WM8-V35, NW20-V27, NW20-V35, WM20-V27, and WM20-V35, the mean average of the penetration depth was 15.29, 18.71, 14.12, 20.32, 14.47, 20.56, 15.91, and 19.08 mm, respectively. By comparing the mean average values of the penetration depth, even if the specimens were reinforced by using wire mesh, there would have been no effect in reducing the penetration depth. This fact was similar to the research results of Dancygier and Yankelevsky (1996).

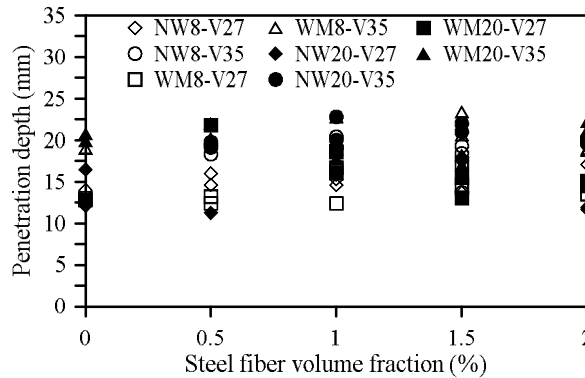


Figure 4-27 Penetration depth for specimens with spalling and spalling (R)

Figure 4-28 and **Table 4-11** categorize the average ratio of tested penetration depth to Haldar impact factor by steel fiber volume fraction. In tests of concrete panels not reinforced by steel fibers, the average ratio of NW8-0% was 2.55 mm and the average ratio of WM8-0% was 2.16 mm, a 0.39 mm difference. The difference between NW20-0% and WM20-0% was 0.3 mm. However, NW8-1.5% showed better results than WM8-1.5%, while NW20-1.0% and WM20-1.0% showed the same values as 2.05 mm. In tests of panels containing a 2.0% steel fiber volume fraction, WM8-2.0% was better than NW8-2.0%, but WM20-2.0% was worse than NW20-2.0%. It is difficult to identify a clear trend in steel fiber-reinforced concrete with wire mesh. In other words, there appears to be no significant difference in penetration resistance ability in concrete panels reinforced only with wire mesh and those containing wire mesh and steel fibers.

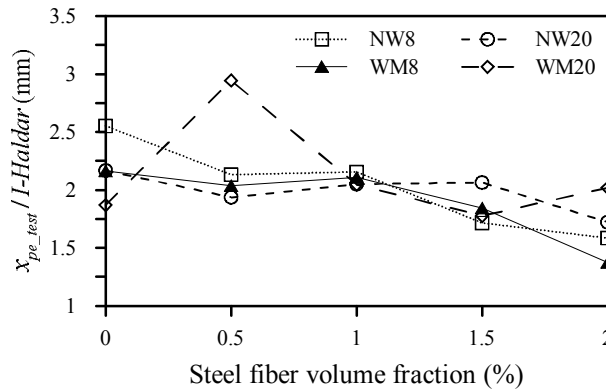


Figure 4-28 Average ratio of tested penetration depth normalized to Haldar impact factor for penetrated specimens

Table 4-10 Average ratios of tested penetration depth to *I-Haldar*

Steel fiber volume fraction (%)	NW8 (mm)	WM8 (mm)	NW20 (mm)	WM20 (mm)
0.0	2.55	2.16	2.17	1.87
0.5	2.13	2.04	1.94	2.95
1.0	2.16	2.11	2.05	2.05
1.5	1.72	1.84	2.06	1.78
2.0	1.58	1.38	1.72	2.02

Figure 4-29 and **Table 4-11** show the scabbing depth of 50 mm specimens by the Haldar impact factor unit, categorized by steel fiber volume fraction. Unlike penetration depth normalized by *I-Haldar*, the scabbing depths normalized by *I-Haldar* decreased sharply. It was again confirmed that the scabbing depth on the rear face of a panel was decreased due to the effect of steel fibers. The difference between NW8-0% and WM8-0% was 0.6 mm, and the difference between NW20-0% and WM20-0% was 0.43 mm. The use of wire mesh had little effect on scabbing depth. However, WM8-2.0% showed worse results than NW8-2.0%, and almost

equivalent results to NW20-2.0% and WM20-2.0%. The value of WM20-1.5% was 1.88 mm, which is worse than the value of 1.7 mm for NW20-1.5%. The use of wire mesh had some effect on reducing scabbing failure, but did not show a consistent trend. It is thought that steel fiber is a significant factor in reducing backside damage.

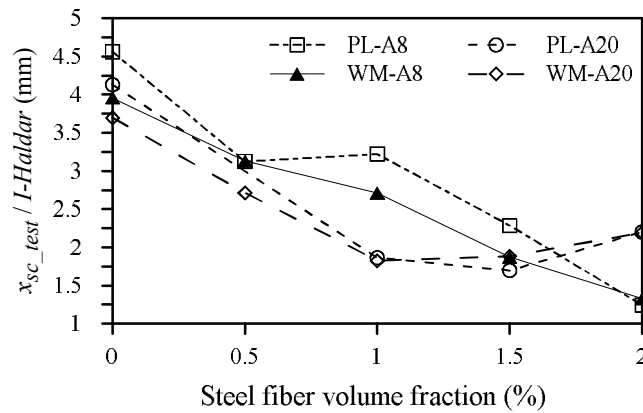


Figure 4-29 Average ratio of tested scabbing depth normalized to Haldar impact factor for scabbed or perforated specimens

Table 4-11 Average ratios of tested scabbing depth to *I-Haldar*

Steel fiber volume fraction (%)	NW8 (mm)	WM8 (mm)	NW20 (mm)	WM20 (mm)
0.0	4.56	3.96	4.13	3.70
0.5	3.13	3.13	-	2.71
1.0	3.22	2.71	1.86	1.83
1.5	2.28	1.87	1.70	1.88
2.0	1.24	1.33	2.20	2.19

Figure 4-30 is a categorization of the spalling and scabbing areas of the perforation specimens by the steel fiber volume fraction. In general, it is common

that the spalling area is larger than the scabbing area. In this experiment, however the spalling area to scabbing area ratio was equal to or lesser than 1, resulting in the larger scabbing area. At a steel fiber volume fraction of 0.5%, the ratio value was also close to 3. Such specimens were the specimens with significant scabbing areas due to the splitting bond failure. Nevertheless, at 0, 0.5, and 1.0% steel fiber volume fractions, the spalling area to scabbing area ratio was within a range of 0.4-0.7, whereas at 1.5% and 2.0% steel fiber volume fractions, the numerical value increased a bit.

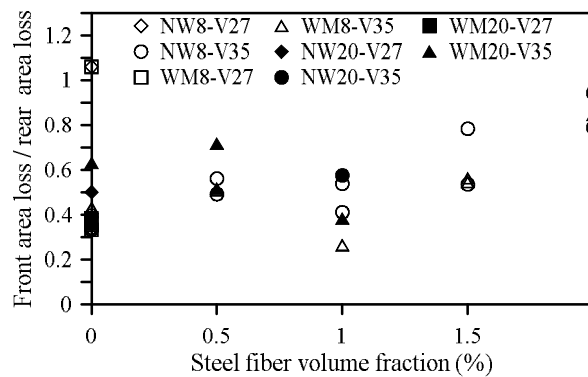


Figure 4-30 Front area loss to rear area loss ratio for specimens with perforation

Figure 4-31 displays the average percentage of weight loss which was measured before and after projectiles with an impact velocity of 350 m/s collided on the specimens. As seen in the figure, as the steel fiber volume fraction increased, the weight loss fell steeply to a point of 1.5% steel fiber volume fraction. It showed a similar weight loss when the steel fiber volume fraction was 1.5% and 2.0%. In the case of the size of coarse aggregates, specimens that used 20 mm aggregates showed a greater weight loss. The impact of wire mesh reinforcements had different results according to the panel thickness.

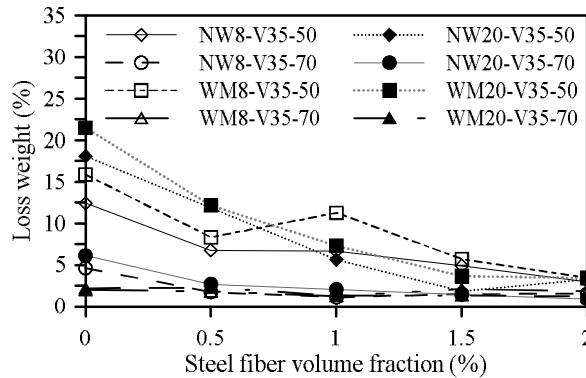


Figure 4-31 Loss-weight for specimens with perforation due to 350 m/s velocity impact

In **Figure 4-31**, WM8-V35-50 and WM20-V35-50 had a greater weight loss compared to NW8-V35-50 and NW20-V35-50, respectively. However, WM8-V35-70 and WM20-V35-70 showed a lesser weight loss than that of NW8-V35-70 and NW20-V35-70. This can be explained by whether an equal amount of kinetic energy can cause a splitting bond failure on the cover of the rear face. In the 50 mm aggregate specimens, an overall response took place because of the thinness which further resulted in a splitting bond failure of the cover due to the tension of the reinforcing bar. However, there was no overall response that occurred in the specimens with a thickness of 70 mm, and this led to less tension on the reinforcing bar, preventing the splitting bond failure.

If the specimen was not thick enough, an overall response occurred which led to tension on the wire mesh which could result in a failure of the cover of the rear face. Such a phenomenon was observed in the steel fiber volume fraction up until 1.0%. However, when the steel fiber volume fraction was 1.5% and 2.0%, the scabbing could be controlled. It is considered the bond-splitting strength of the

cover increased because of the bridging of the steel fiber.

Taking into account the results of **Figure 4-26** and **Figure 4-31**, the spalling area was likely to become smaller when mixing steel fibers, with bridging within the concrete matrix increased, leading to lesser internal damage. Based on the experiment results, using more than 1.5% steel fiber volume fraction increased the bond strength of the concrete matrix with and without the use of wire mesh. This in turn could prevent the splitting bond failure which was a result of tension on the wire mesh.

According to the scabbing theory (Kolsky, 1963; Society of Material Science of Japan, 1988), when a projectile generates a compressive wave (P_{com}) at a contact point between the projectile and the concrete panel, the compressive wave proceeds to the rear face of the concrete. To resist the compressive wave that reaches the rear face, a reflected tensile wave is generated at the free end (P_{ten}) (**Figure 4-32**). Then, the generated tensile stress exceeds the tensile strength of the material and scabbing failure can occur. If a steel wire mesh is placed in the concrete panel, the tensile force can be absorbed by the wire mesh. However, bond splitting between the wire mesh and the cover of the concrete panel can occur in some specimens when the tensile force spreads more broadly through the steel wire mesh. If steel fibers are added to wire mesh-reinforced concrete, however, the splitting bond failure can be reduced because of the bridging effect of the steel fibers.

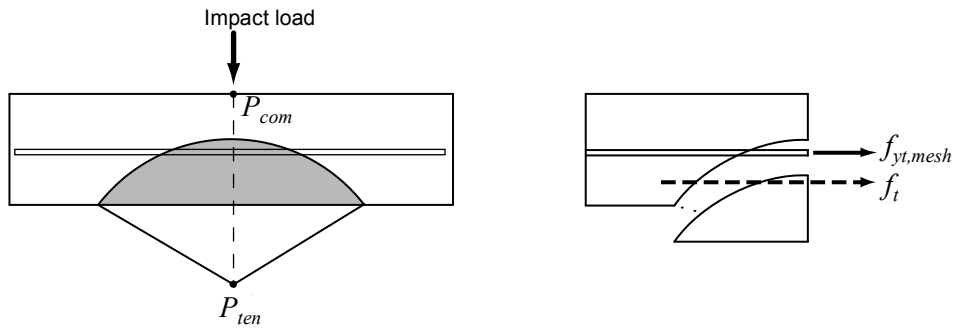


Figure 4-32 Scabbing theory and tension force ($f_{yt, mesh}$ = tensile strength of steel wire mesh, f_t = tensile strength of concrete)

4.4.2 Second experiment

Although the impact resistance of concrete has been studied by many researchers, there have been few experimental studies on the nose shape factor (Lee *et al.*, 2018; Zhang *et al.*, 2017a). While there are not many impact formulae with the nose shape factor, the modified NDRC and Hughes formulae include the nose shape factor.

The nose shape factor in the modified NDRC and Hughes formulae were classified into four types: flat, hemispherical, blunt, and very sharp (**Table 4-12**). The modified NDRC formula presents the nose shape factor with the blunt type with the reference value of 1, while the Hughes presents the flat shape type with the reference value of 1. Since these formulae were developed over a long time, it is necessary to investigate whether the factors proposed by the modified NDRC and Hughes formula can be applied equally to high-strength concrete and even normal concrete. In the second experimental results, the validity of the nose shape factor was analyzed with experimental data using only the long-conical and long-

hemisphere shape (**Figure 4-33**) and the concrete strength of 35, 100, and 120 MPa.

Table 4-12 Nose shape factor in formulae

Nose shape factor	Modified NDRC	Hughes
Flat	0.72	1.0
Hemispherical	0.84	1.12
Blunt	1.0	1.26
Very sharp	1.14	1.39

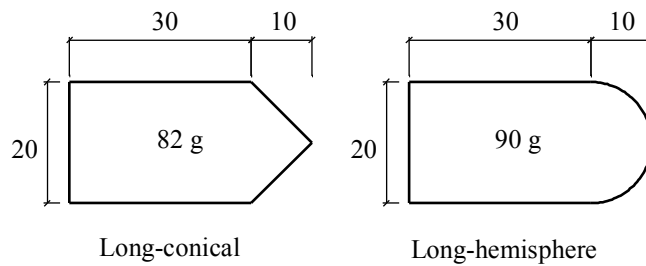


Figure 4-33 Long-conical and long-hemisphere (unit: mm)

Figure 4-34 shows the relationship of the measured compressive strength of concrete and the tested penetration depth according to the nose shape of the projectile. The tested penetration depths of 80 and 96 MPa were significantly less than 40 MPa. However, the difference in the penetration depths between the 80 and 90 MPa was insignificant. There were no significant differences in penetration depths between the two types of projectile for all concrete strengths.

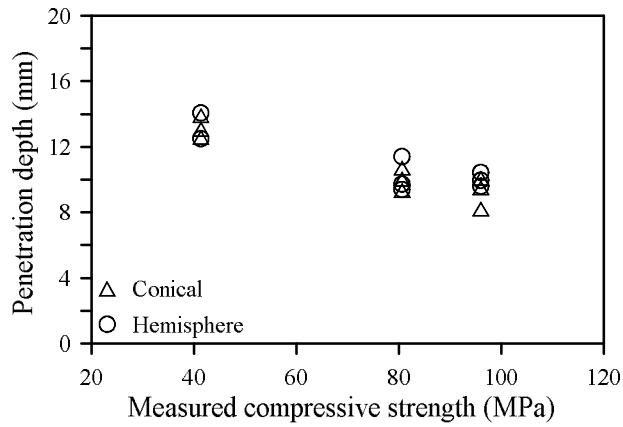


Figure 4-34 Relationship of measured compressive strength of concrete and penetration depth

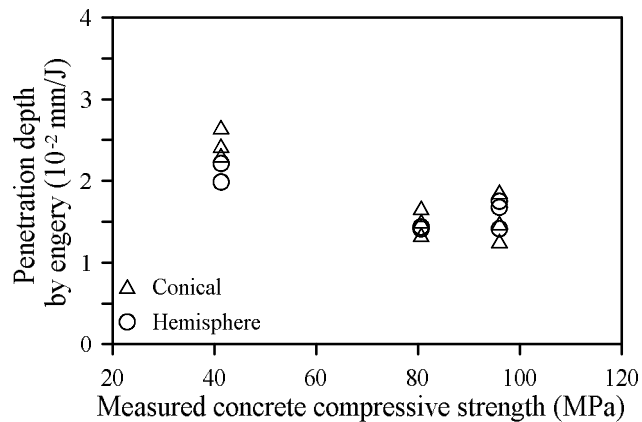


Figure 4-35 Relationship of measured compressive strength of concrete and penetration depth normalized by kinetic energy

However, since each projectile had a different impact velocity and mass, the tested penetration depth was normalized by dividing each projectile's kinetic energy for equal comparison. **Figure 4-35** scatters those values according to the measured concrete strength. **Table 4-13** shows the results of the second test and the value of the tested penetration depth normalized by dividing by the kinetic energy

or the calculated penetration depth based on the modified NDRC/Hughes formulae. In general, the average kinetic energy of the long-hemisphere projectile was 620 J, and the average kinetic energy of the long-conical projectile was 570 J, with the difference between the two being about 30 J. The differences of the values of the penetration depth normalized by kinetic energy between the long-conical and long-hemisphere was significant in the specimens with 35 MPa (**Table 4-13**), with the difference being 0.0037 mm/J.

Table 4-13 Results of second test

Projectile	Long-conical			Long-hemisphere		
f'_{c_design}	35	100	120	35	100	120
f'_{c_meas}	41.3	80.6	96	41.3	80.6	96
x_{pe_test}	13.18	10.02	9.26	13.29	10.18	10
$\frac{x_{pe_test}}{E_K}$	0.0247	0.0151	0.0154	0.021	0.0143	0.0161
$\frac{x_{pe_test}}{(x_{NDRC})^a}$	0.82	0.67	0.63	0.89	0.76	0.78
$\frac{x_{pe_test}}{(x_{NDRC})^b}$	0.88	0.71	0.67	0.82	0.70	0.72
$\frac{(x_{NDRC})^b}{(x_{NDRC})^a}$	1.07	1.06	1.06	0.92	0.92	0.92
$\frac{x_{pe_test}}{(x_{Hughes})^a}$	0.72	0.57	0.53	0.75	0.62	0.63
$\frac{x_{pe_test}}{(x_{Hughes})^b}$	1	0.79	0.73	0.94	0.78	0.79
$\frac{(x_{Hughes})^b}{(x_{Hughes})^a}$	1.39	1.39	1.38	1.25	1.26	1.25

f'_{c_design} is the design compressive strength of concrete (MPa); f'_{c_meas} is the measured compressive strength of concrete (MPa); x_{pe_test} is the measured penetration depth (mm); E_K is the kinetic energy (J); $(x_{NDRC})^a$ is the calculated penetration depth by the modified NDRC formula with the proposed nose shape factor (mm); $(x_{NDRC})^b$ is the calculated penetration depth by the modified NDRC formula without the proposed nose shape factor (mm); $(x_{Hughes})^a$ is the calculated penetration depth by the Hughes formula with the proposed nose shape factor (mm); and $(x_{NDRC})^b$ is the calculated penetration depth by the Hughes formula without the proposed nose shape factor (mm).

The values of the tested penetration depth divided by kinetic energy in the high-strength concrete of 100 and 120 MPa are almost the same regardless of the nose shape of the projectile. The value of x_{pe_test}/E_K of the long-conical projectile was 0.0151 mm/J at 100 MPa, increasingly slightly to 0.0154 mm/J at 120 MPa, but this difference was too small to be negligible. The value of x_{pe_test}/E_K of the long-hemisphere projectile was 0.0143 mm/J at 100 MPa, while it increased to 0.0161 mm/J at 120 MPa, but this difference was smaller than the difference for 35 MPa.

When compared the x_{pe_test}/E_K of the long-conical projectile with the long-hemisphere projectile in the same concrete strength, the ratios of (x_{pe_test}/E_K) of the long-conical to (x_{pe_test}/E_K) of the long-hemisphere projectile were 1.18 (= 0.0247/0.021), 1.06 (= 0.0151/0.0143), and 0.96 (= 0.0154/0.0161). The difference of the value decreases as the compressive strength of concrete increases. In other words, it is considered that the penetration depth in the low compressive strength of concrete was clearly affected by the nose shape of the projectile, while the effect of the nose shape decreases as the concrete strength increases.

In **Table 4-13**, **Figure 4-36**, and **Figure 4-37**, $(x_{pe_test}/x_{NDRC})^a$ and $(x_{pe_test}/x_{Hughes})^a$ are the ratios of the tested penetration depth to the calculated penetration depth per each impact formula considering the nose shape factor proposed by each impact formula, while $(x_{pe_test}/x_{NDRC})^b$ and $(x_{pe_test}/x_{Hughes})^b$ were the ratios without the nose shape factor, meaning that the nose shape factor was neglected.

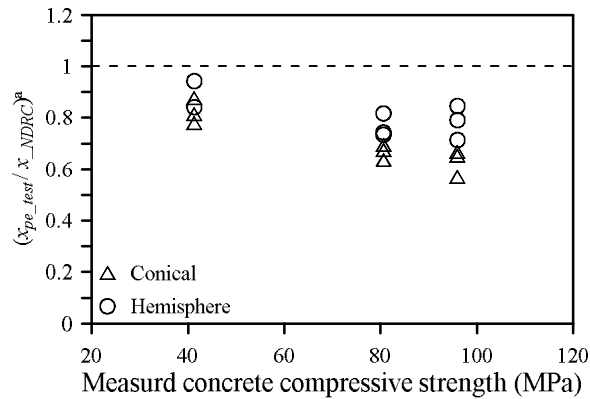


Figure 4-36 Relationship of measured concrete strength and ratio of tested penetration depth to predicted penetration depth of modified NDRC formula

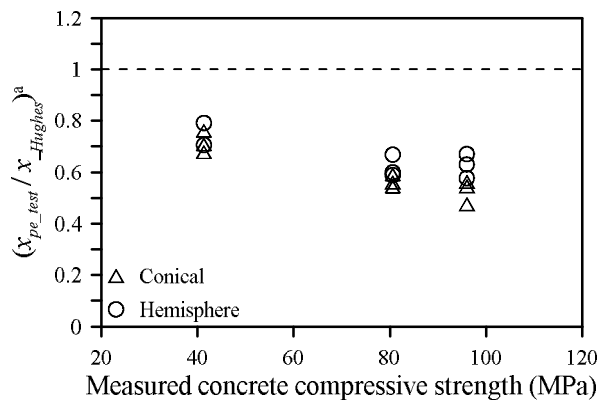


Figure 4-37 Relationship of measured concrete strength and ratio of tested penetration depth to predicted penetration depth of Hughes formula

The experimental results showed the ratio of the results when the bullet shape factor was not taken into account and the resultant values when considering the modified NDRC formula were about 1.08 and 0.93 for the cone and hemispherical shapes, respectively, regardless of the strength, whereas in the Hughes equation they were about 1.38 and 1.27, respectively. The average values of $(x_{pe_test} / x_{NDRC})^{b/a}$ of long-conical and long-hemisphere were 1.07 and 0.92, and their

average values of $(x_{pe_test} / x_{Hughes})^{b/a}$ were 1.39 and 1.25, respectively. Both average values of $(x_{pe_test} / x_{NDRC})^{b/a}$ were close to 1, while both average values of $(x_{pe_test} / x_{Hughes})^{b/a}$ were close to 1.25 or more. That is, the NDRC formula did not consider the effect of the nose shape much, whereas the Hughes considered the nose shape effect to be relatively large.

Figure 4-38 shows the predicted penetration depth by the modified NDRC formula and the Hughes formula with and without nose shape factors if all the conditions were the same and only the nose shape was different. The difference of the predicted penetration depth between the long-conical and long-hemisphere was 1.16 times for the modified NDRC formula and 1.1 times for the Hughes formula, even though the concrete strength increased. The difference of (x_{pe_test} / E_K) between the long-conical and the long-hemisphere projectile decreases as the compressive strength of concrete increases, but the prediction from the two formulae was not so accurate. Therefore, it is necessary to complement the modified NDRC and Hughes formulae to apply them to high-strength concrete.

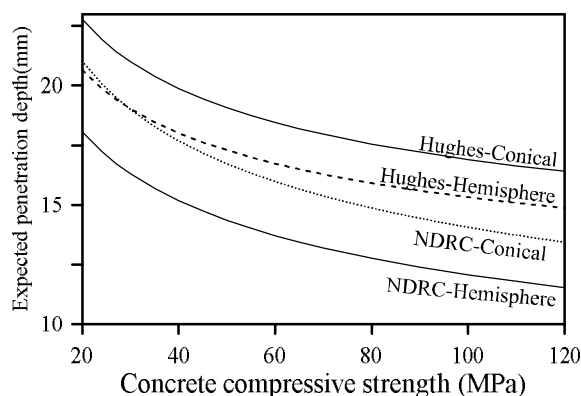


Figure 4-38 Predicted penetration depth of the modified NDRC and Hughes formula according to concrete compressive strength

4.4.3 Third experiment

One of the important perspectives on selecting an exterior panel of a building is the aesthetics. **Figure 4-39** shows the surface of granite, normal concrete, and UHPC panel. Granite was produced with wet rubbing, and its surface was smooth and glossy. The normal concrete was not as smooth as granite, and the particles of cement and aggregate were observed as rough by the naked eye. After 28 days, the UHPC appeared clean overall with no surface voids. The UHPC did not appear rough like normal concrete, and it had a slight shine and gloss. It was determined to have sufficient shine and gloss to use the exterior material, although the shine and gloss was lower than the granite panel, which was finished by the wet rubbing process. The mold side was smooth and the cast side was rough, but some specimens did not show a good-quality gloss. If the quality control is better when the UHPC is manufactured, the UHPC's panel would have a good appearance for use as an exterior material. Because UHPC has excellent formability, it can be manufactured into various shapes and sizes. In addition, UHPC can be colored by adding white cement and various pigments (Ha *et al.*, 2015; Kang *et al.*, 2015).



(a) Munkyung granite



(a) Normal concrete



(a) UHPC

Figure 4-39 Comparison of appearance of each material

Table 4-14 shows the state of the front and back of the experiment after some experiments, where G-White and G-Black were Munkyung granite and Goheung granite, respectively. As shown in **Table 4-14**, the granites were destroyed into

many pieces after the collision, and it was impossible to measure the penetration depth and loss weight. The smashed failure of granite was considered a result of the brittleness characteristic of granite. All UHPC180-10 specimens with 10 mm thickness had perforated failure, and the clearly perforated hole without spalling was observed. The average area of the perforated hole on the front face was approximately 332 mm^2 , which was almost similar to the cross-sectional area of the spherical projectile, which was 314 mm^2 . In general, spalling occurs when the scabbing failure occurs, but the UHPC180-10 specimen did not have this failure pattern. The external energy (kinetic energy) of the projectile was considered significantly larger than the internal energy that can be absorbed by the concrete panel. All UHPC180-20 specimens with a thickness of 20 mm did not exhibit perforated failure but were penetrated by approximately 4 mm into the front face at the collision point, and scabbing failure occurred. In UHPC180-20 specimens, there was a general failure pattern, where scabbing and spalling phenomena simultaneously occurred. On the rear face, the average scabbed area of 6615 mm^2 and a scabbed depth of 13.4 mm were observed. The UHPC180-30 specimens with a thickness of 30 mm had spalling, and the penetration depths were approximately 3.6 mm in all four specimens. Micro cracks were observed on the rear face.

Table 4-14 Selected specimen of UHPC

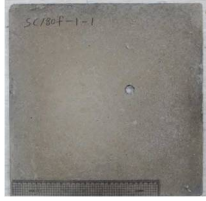
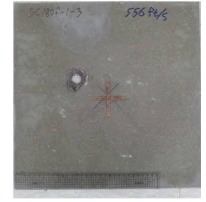
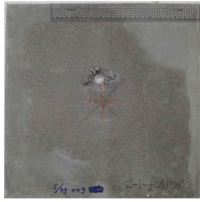
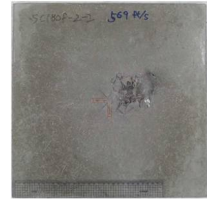
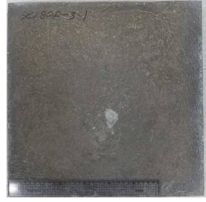
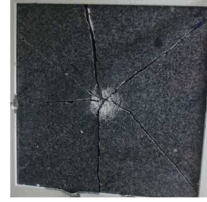
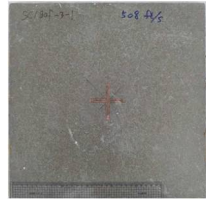
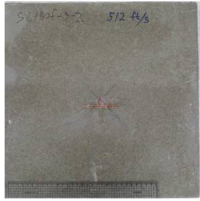
Specimen	UHPC180-10-1	UHPC180-10-2	UHPC180-20-1	UHPC180-20-2
Front face				
Rear face				
Specimen	UHPC180-30-1	UHPC180-30-2	G-White	G-Black
Front face				
Rear face				

Figure 4-40 shows the weight loss of the specimens. The average weight loss of UHPC180-10 and UHPC180-20 specimens was 0.61% and 0.38%, respectively. The average weight loss of UHPC180-30 was 0.16%, and spalling occurred in its front face. The overall weight loss ratio compared to the weight of the specimen decreased with the increase in thickness of the panel. The UHPC180-10 had the largest weight loss because of the perforated failure. There were only micro cracks

on the rear face of UHPC180-30, and the weight loss due to collision was minimal.

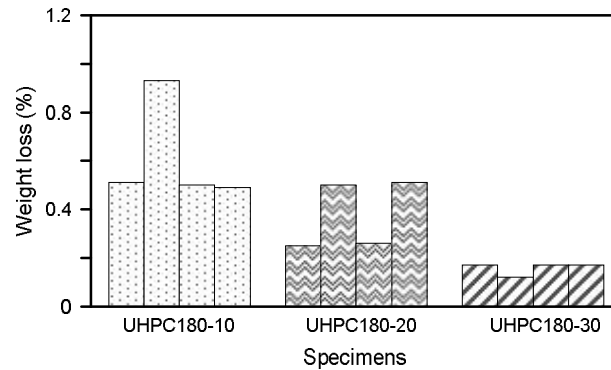


Figure 4-40 Weight loss for specimens

Figure 4-41 shows the area loss of the front and rear faces of all UHPC specimens. The UHPC180-10 and UHPC180-20 specimens exhibited more area loss from their rear face than their front face. The UHPC180-30 specimens only displayed an area loss on their front face and none on their rear face. There was a wide but low degree of failure of the rear face of UHPC180-10. The phenomenon occurred in other experiments and appeared to result from the shear plug deformation as shown in **Figure 4-42** (Yankelevsky, 1997; Li and Tong, 2003; Li *et al.*, 2005). The shear plug model refers to a corn shaped failure that is produced when the impact energy is sufficiently large to perforate the concrete panel. The average front face loss of the UHPC180-20 specimens was 223 mm², whereas the average rear area loss was 6615 mm², which is approximately 30 times of the front face loss. These results suggest that scabbing occurred because of the tension force at the rear face, where the spherical steel ball did not penetrate. The UHPC180-30 specimens had a similar penetration depth to UHPC180-20, but scabbing failure did not occur. Thus, the UHPC180-30 specimens had a sufficient thickness to

withstand the tensile force of the rear surface generated under the identical external impact energy.

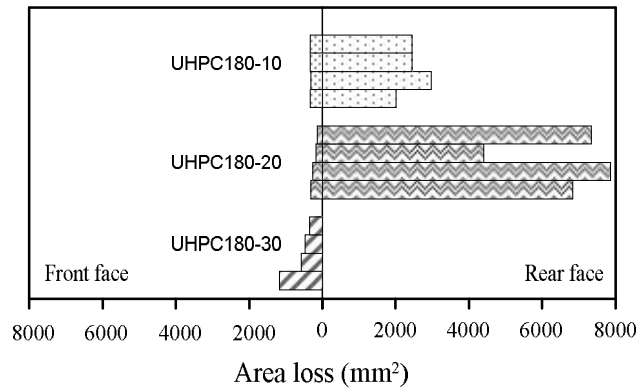


Figure 4-41 Area loss of specimens

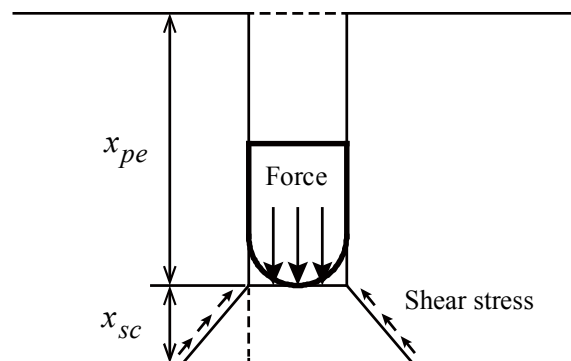
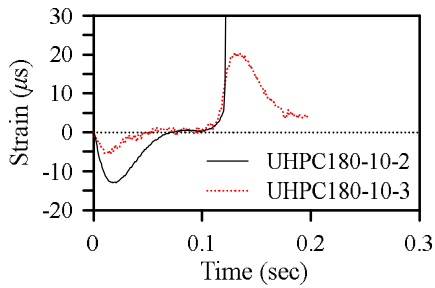


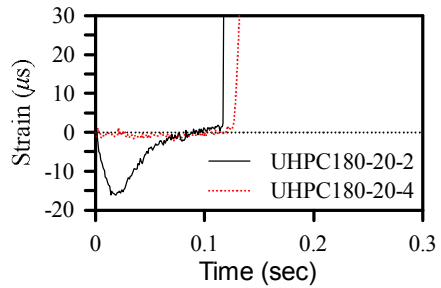
Figure 4-42 Shear plug model (Li and Tong, 2003)

Comparing between UHPC and granite, it was observed that the UHPC180-20 specimens did not exhibit brittle fracture and perforation failure compared to the granite with the thickness of 30 mm, and the UHPC panel showed a much smaller damage range. It is considered that the UHPC panel had excellent impact resistance compared with the granite panel, which is known as a solid exterior material.

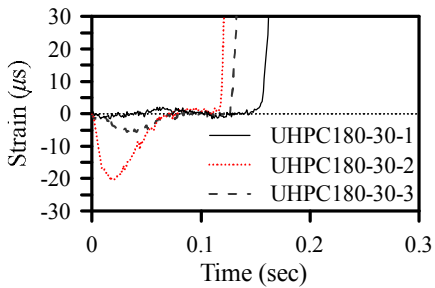
Figure 4-43 shows the strain history of each specimen. As shown in **Figure 4-43**, the rear face of the specimen deforms in the compressive direction because of the initial compression wave. Subsequently, it is expected that the compressive wave is canceled by the reflected tensile wave, and the tensile force increases. **Figure 4-43** shows a similar graph as expected. By closely examining the strain history data, the strain history can be normalized as shown in **Figure 4-44**. Section 1 is the compressive region, where the compressive force generated by the impact force acts on the rear side. The second section is a steady region, where the tension is mainly applied to the rear face by the tensile force of the free end, and the strain is maintained at zero. The third section is a tension region, where scabbing occurs when a tensile wave exceeds the tensile strength of the concrete. The trend of the recorded strain history in this study was found in other studies by Kim *et al.* (2013) and Beppu *et al.* (2008). Considering the shear fracture, the fracture of the rear face may occur even at a lower tensile strength than the uniaxial tensile strength through the material strength test. The maximum compressive strain at the rear face of UHPC was measured as $13 \sim 20 \mu\text{s}$, and the maximum compression strain of granite was measured as $80 \sim 84 \mu\text{s}$. In other words, the maximum compressive strain is similar for the same material, and the compressive strain value varies depending on the material properties.



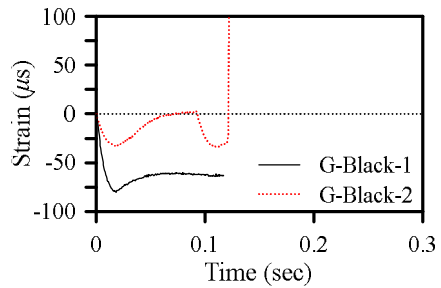
(a) UHPC180-10 specimens



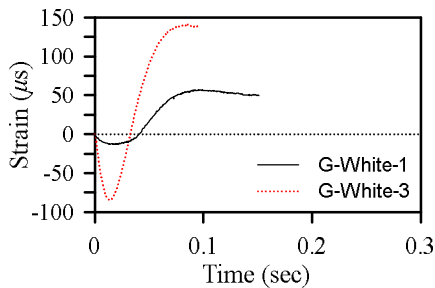
(b) UHPC180-20 specimens



(c) UHPC180-30 specimens



(a) G-White specimens



(d) G-Black specimens

Figure 4-43 Strain history of rear face of tested specimens

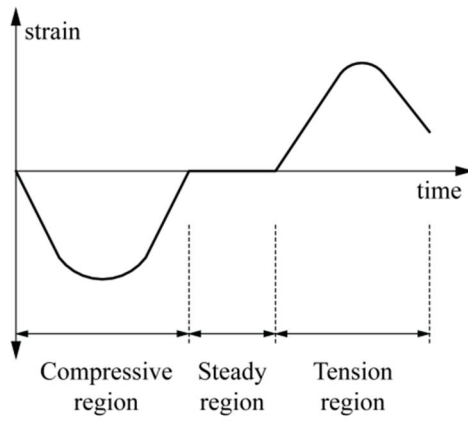


Figure 4-44 Normalized strain history of rear face

4.5 Empirical Parameters

The effect of each parameter on the impact resistance of concrete was examined in a total of three experiments. **Table 2-1** summarizes the available parameters for concrete panels and the projectiles. In this section, the intention was to select parameters that have a large effect on the impact resistance of a concrete panel, which is important for developing a new impact formula.

Parameters related to concrete panels will first be examined. The compressive strength of concrete is the most important parameter related to penetration depth resistance capability. Concrete's tensile strength has a great influence on scabbing failure, but an insignificant effect on penetration depth. Considering the shape of spalled or scabbed cones, spalling and scabbing failure are related to shear failure. Therefore, it can be deduced that spalling failure is related to shear strength associated with compressive strength, while scabbing failure is related to shear strength associated with tensile strength.

The steel fiber-reinforced concrete has improved tensile strength due to its steel fibers. Steel fiber is a material that can greatly improve the tensile strength of concrete. As previously mentioned, high tensile strength has a significant effect on reducing scabbing failure. Therefore, it is important to consider the effect of steel fiber on the impact resistance of a concrete panel when calculating the scabbing limit thickness and perforation limit thickness.

Reinforcing bars did not significantly affect penetration depth. While they were relatively helpful in reducing the depth of scabbing failure, the effect was not very significant. Experiments were carried out using aggregate size as a variable. It

was confirmed that the use of smaller aggregates was better, but it is difficult to determine whether that effect was significant. Therefore, it is unclear if reinforcing bars and aggregate size are important parameters.

The relevant characteristics of projectiles in this experiment were speed and weight. These are important parameters for defining the amount of kinetic energy. The nose shape of a projectile was an important factor in estimating the penetration depth, because the contact area varied depending on the shape of the projectile nose. Finally, the ratio of length to diameter of a projectile was important. The larger this ratio, the larger the impact energy per unit area. This can result in deeper penetration depths. **Table 4-15** shows the parameters that greatly affected impact performance.

Table 4-15 Empirical parameters involved in impact

	Concrete panel	Projectile
Parameter	Thickness of panel Compressive strength Tensile strength Steel fiber volume fraction Strain rate effect	Velocity Mass Shape Diameter Length

4.6 Discussion

In this section, three experiments were conducted to collect new experimental data on impact, which were lacking in previous studies. In order to compensate for this insufficient data, three experiments were performed using different variables. The main parameters were the steel fiber volume fraction and the presence of wire mesh in the first experiment, the strength of high-strength concrete in the second experiment, and the thickness of thin UHPC panels in the third experiment. Experimental results are summarized below:

- 1) Three sets of experiments to evaluate the impact resistance of concrete were designed. The first experiment evaluated normal-strength concrete with the absence or presence of steel fibers. The steel fiber volume fractions of 0.5, 1.0, 1.5, and 2.0% were investigated. Also, wire mesh-reinforced concrete panels and steel fiber-reinforced concrete with wire mesh were tested. The second experiment was conducted for evaluating the impact resistance of high-strength concrete of 80, 100, and 120 MPa. The high-strength SFRC of 80 and 100 MPa was also prepared in order to evaluate the performance of steel fibers in high-strength concrete matrix and compare high-strength concretes with and without steel fibers. The third experiment was performed for examining the impact resistance of ultra-high performance concrete with a design compressive strength of 180 MPa, using thin panels to assess its use for exterior facade applications.
- 2) There are several advantages when steel fibers are incorporated into concrete. In this study, the investigation examined whether steel fibers can

improve the impact resistance of concrete. No significant effect was found on the penetration resistance for concrete reinforced with steel fibers. The use of steel fibers, on the other hand, was effective in reducing scabbing damage, front area loss and weight loss. Scabbing limit thickness and perforation limit thickness can also be reduced by reducing scabbing damage with steel fibers. It was also observed that the smaller aggregate size improved the dispersion of steel fibers, resulting in improved impact resistance.

- 3) The use of wire mesh improved the overall impact resistance of the concrete panel. Although the wire mesh was ineffective in reducing the penetration depth, scabbing and perforation resistance was improved. Additionally, the wire mesh helped reduce area loss and weight loss on the front face, considering the confinement effect of the wire mesh acting on the 30×30 mm concrete block. When wire mesh reinforced a thin concrete panel, splitting bond failures between the concrete cover and the wire mesh were observed on the rear face. If the concrete is reinforced by both wire mesh and steel fibers, splitting bond failure may be reduced due to the bridge effect of steel fibers. However, the penetration depth resistance did not improve, even if wire mesh and steel fibers were used all together.
- 4) The modified NDRC and Hughes formulae predict that the difference between predicted penetration depths by conical and hemispherical projectiles would be maintained even as the compressive strength of concrete increases. Experimental results, however, did not support this prediction. The reason for this is that most impact formulae assume that

the projectile is non-deformable, because the large difference between the compressive strength of the concrete and the projectile. However, high-strength concrete reduces this difference, causing deformation of the projectile that is not predicted by existing formulae. In other words, in order to improve the accuracy of the impact formula for high-strength to very high-strength concrete, it is important to consider the deformation of the projectile.

- 5) The UHPC had better impact resistance than any granite and quite good appearance after impact, which can be used as an exterior material. In the UHPC panel with a thickness of 10 and 20 mm, the collision of a projectile resulted in a rear face failure in the concrete panel in the form of shear failure. The reason is that the shear failure is an outcome of a shear plug deformation, which occurs at the collision point in a diagonal direction.
- 6) The strain history of the center of the rear face can be divided into the compressive region, steady region, and tension region. The compressive region appears to have been created when the compression wave of specimen reached the rear face from the inside. Then, a tension pulse occurred at the free point P' outside the rear face of the panel, which offset the compressive wave. A region where the compressive pulse and tension pulse become similar after the offsetting, i.e., a steady region, appeared. After the impact energy of the projectile was exhausted, the tension force centered around the free point exceeded the concrete fracture strength, which created a scabbing. In other words, scabbing appears to have occurred because of the simultaneous effect of the shear force by the shear

plug deformation and the tension force according to the scabbing theory.

Chapter 5. Development of New Energy-Based Impact Formula

Concrete itself is a composite material and the impact mechanism is not clearly defined, so it is not easy to predict the damage done to the concrete panel. In many cases, the equation is derived from the relationship between kinetic energy and force-penetration depth, and corrected by the experimental data. Unlike the conventional impact model development method, in this paper, a new impact formula will be developed based on both theoretical background and energy conservation. Energy consumption occurs in each impact mechanism step and the total consumed energy by the concrete panel has to be the same as the external energy. Therefore, the impact mechanism will be newly defined in this study. It will describe a consumed quantity based on the energy conservation law between the external energy carried by the projectile and the energy consumption in the impact mechanism. The overall concept of a new impact formula will be introduced and the material properties affected by strain rate effect in impact mechanism will be newly defined. The value of the energy consumption of each step of the impact mechanism will be derived in logical order. Finally, a new impact formula for evaluating the damage done to the (reinforced) concrete panel under a high velocity impact load will be presented.

5.1 Concept of New Formula

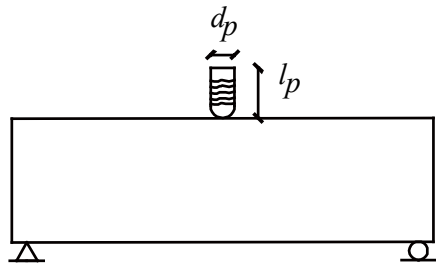
5.1.1 Materials for impact mechanism

Because the measured values of the material are affected by the loading speed, the provisions for measuring the material properties give a range of loading speeds necessary to measure accurately. Even if there is a clear yielding point and perfect plasticity, mechanical properties fluctuate depending on the loading rate/strain rate (POSCO, 2012). The loading velocity plays an important role in determining the material properties of the material. The impact velocity in the impact mechanism determines the material properties of the material. Thus, the material properties of the materials acting in the collision mechanism will be determined in relation to the strain rate/impact velocity.

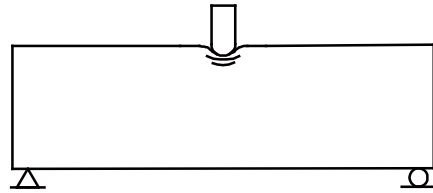
5.1.2 Impact mechanism and energy conservation

Hwang *et al.* (2017) defined the impact mechanism and also derived the consumed energies. In this study, the impact mechanism, regardless of a panel's thickness, is redefined, and each consumed energy is newly derived based on the research of Hwang *et al.* (2017). The energies involved in the impact mechanism can be divided into 5 steps and an additional 2 steps turn up in case of special conditions as shown in **Figure 5-1**. The first is the kinetic energy (E_K) of the projectile as external energy, which is an essential critical energy for concrete failure. The second is the overall deformed energy of the concrete panel (E_{DS}). The third is the elastic deformed energy of the concrete panel (E_{EP}). The fourth is the

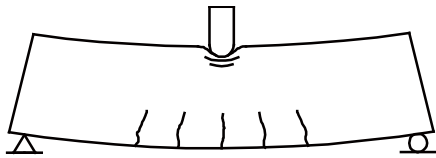
deformed energy of the projectile (E_{DP}) at the moment of contact. The fifth is the concrete drag force that is generated around the collision point, and the magnitude of energy generated by the concrete drag force, spalling-resistant energy (E_{SP}), which determines the type of failure mode. One of additional steps is the tunneling-resistant energy (E_T), which it will occur when a flying projectile has over spalling resistant energy. Other additional steps include the scabbing-resistant energy (E_{SC}) which occurs in case a thickness of panel is insufficient to absorb E_{SP} . The kinetic energy will be transferred to the concrete panel except for E_{DP} . However, if the thickness of the concrete panel is insufficient to absorb the collision energy, it will be reflected from the opposite face and can occur scabbing failure. Conversely, if the panel is thick, the scabbing resistant energy (reflected energy on rear face of the concrete panel) is weak or does not occur. Thus, E_{SC} can occur under certain conditions. This step is not included in the energy conservation between kinetic energy and consummation of concrete panel.



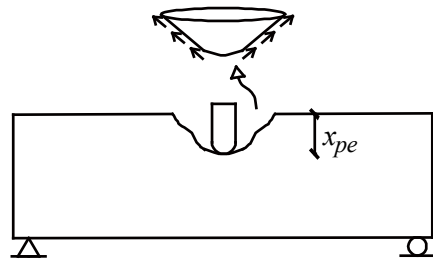
(a) Deformed energy of the projectile (E_{DP})



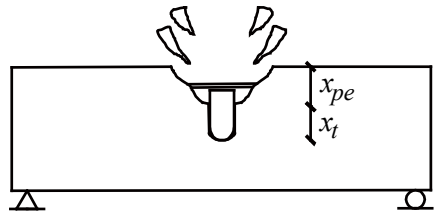
(b) Elastic deformed energy of the concrete panel (E_{EP})



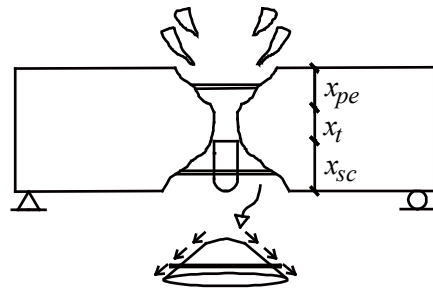
(c) Overall deformed energy of the concrete panel (E_{DS})



(d) Spalling-resistant energy (E_{SP})



(e) Tunneling-resistant energy (E_T)



(f) Scabbing-resistant energy (E_{SC})

Figure 5-1 Energies involved in impact mechanism

5.1.3 Forces acting in impact mechanism

Considering the experimental results and the existing theoretical models, it can be assumed that the penetration depth is affected by compressive strength, and that the scabbing depth is affected by tensile strength. Also, the slope of the spalled cone and scabbed cone is in the form of shear failure. Therefore, it is shown that spalling failure is shear failure affected by compressive strength (**Figure 5-2**), and that scabbing failure is shear failure affected by tensile strength (**Figure 5-3**). It is assumed that the shear and compressive stresses act upon an interface between a spalled concrete cone and a reinforced concrete panel (**Figure 5-2**). Shear and tension stresses act upon an interface between a scabbed concrete cone and a panel (**Figure 5-3**). Based on the punching slab research (Choi and Park, 2010; Choi *et al.*, 2010; Choi *et al.*, 2011; Choi *et al.*, 2014), the shear stress capacities controlled by compression or tension are defined as **Eqs. (5-1) to (5-4)** and **Figure 5-4**, respectively. The $v_{nc,st}(z)$ is the shear stress capacity controlled by compression under the static loading, and $v_{nt,st}(z)$ is the shear stress capacity controlled by tension under the static loading, respectively. Since shear strength is defined under static loading, dynamic material properties should be applied considering dynamic conditions (**Eqs. (5-5) to (5.8)**).

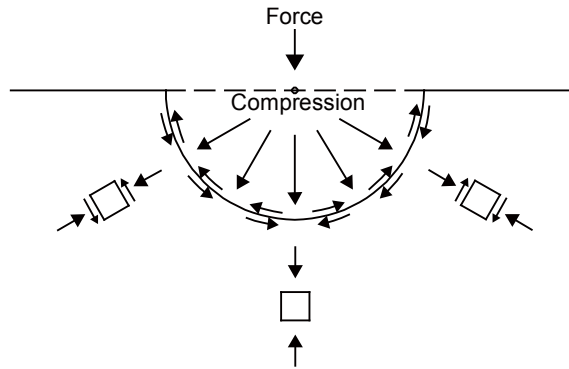


Figure 5-2 Stress flow on interface between spalled concrete and slab

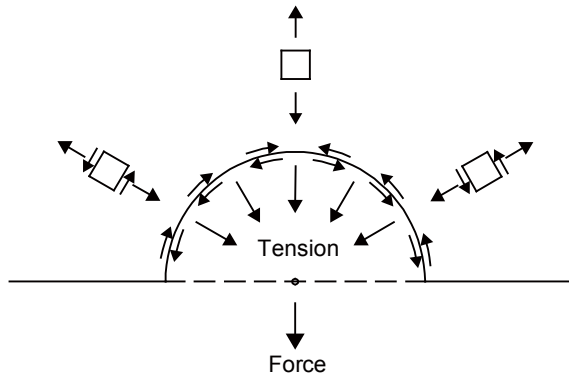


Figure 5-3 Stress flow on interface between scabbled concrete and slab

$$v_{nc,st}(z) = \sqrt{f'_{c,st}(f'_{c,st} - \sigma_{u,st}(z))} \text{ (MPa, mm)} \quad (5-1)$$

$$v_{nc,st}(z) = \sqrt{f'_{t,st}(f'_{t,st} + \sigma_{u,st}(z))} \text{ (MPa, mm)} \quad (5-2)$$

$$\sigma_{u,st}(z) = f'_{c,st} \left[2 \left(\frac{\alpha z}{c_u} \right) - \left(\frac{\alpha z}{c_u} \right)^2 \right] \text{ (MPa, mm)} \quad (5-3)$$

$$f'_{t,st} = f'_{t,st} (1 - \sigma_{u,st}(z) / f'_{c,st}) \text{ (MPa)} \quad (5-4)$$

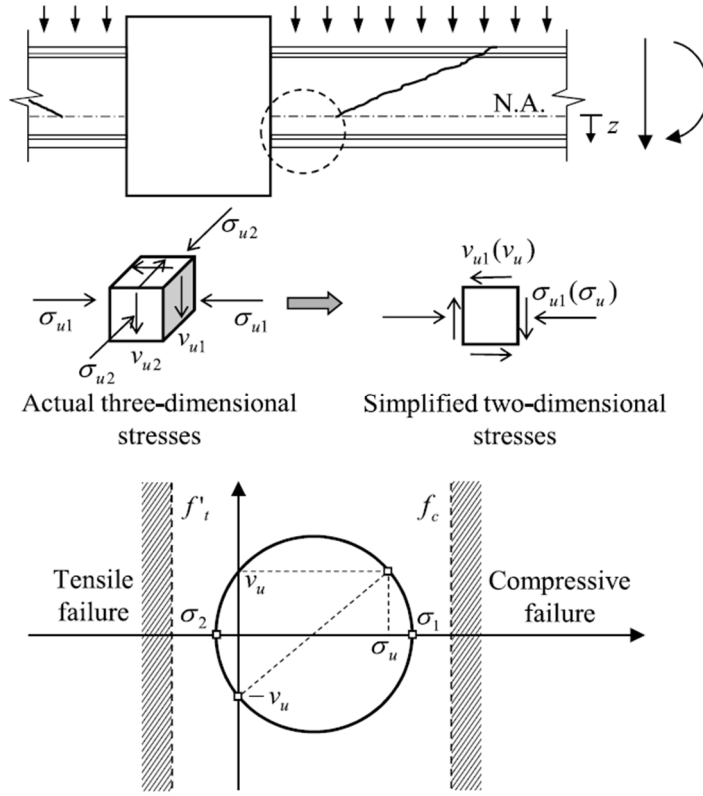


Figure 5-4 Principal stress failure criteria of concrete subjected to shear-compression (Park *et al.*, 2011; Choi *et al.*, 2014)

$$v_{nc,dyn}(z) = \sqrt{f'_{c,dyn}(f'_{c,dyn} - \sigma_{u,dyn}(z))} \quad (\text{MPa, mm}) \quad (5-5)$$

$$v_{nc,dyn}(z) = \sqrt{f'_{t,dyn}(f'_{t,dyn} + \sigma_{u,dyn}(z))} \quad (\text{MPa, mm}) \quad (5-6)$$

$$\sigma_{u,dyn}(z) = f'_{c,dyn} \left[2 \left(\frac{\alpha z}{c_u} \right) - \left(\frac{\alpha z}{c_u} \right)^2 \right] \quad (\text{MPa, mm}) \quad (5-7)$$

$$f'_{t,dyn} = f'_{t,dyn} (1 - \sigma_{u,dyn}(z) / f'_{c,dyn}) \quad (\text{MPa}) \quad (5-8)$$

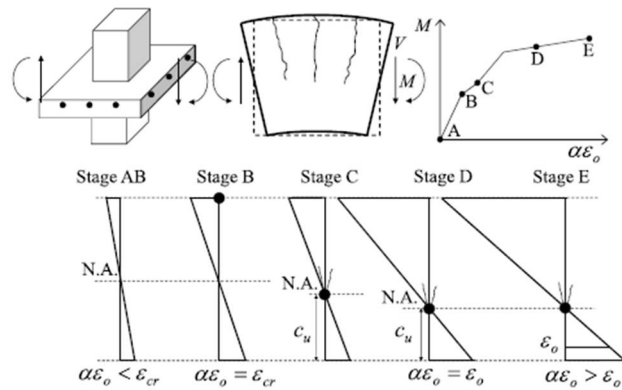
where, $v_{nc,st}(z)$ and $v_{nc,dyn}(z)$ are the static shear stress capacity (MPa) controlled by static compression and the dynamic shear stress capacity (MPa) controlled by dynamic compression, respectively; $v_{nt,st}(z)$ and $v_{nt,dyn}(z)$ are the static shear stress capacity (MPa) controlled by the static tension and the dynamic shear stress capacity (MPa) controlled by the dynamic tension, respectively; z is the distance from the neutral axis (mm); $f'_{c,st}$ and $f'_{c,dyn}$ are the static compressive stress of concrete and the dynamic compressive stress of concrete (MPa), respectively; $f_{t,st}$ and $f_{t,dyn}$ are the static tensile stress of concrete and the dynamic tensile stress of concrete (MPa), respectively; $\sigma_{u,st}$ and $\sigma_{u,dyn}$ are the static compressive stress (MPa) and the dynamic compressive stress affected by strain rate, respectively; $\sigma_{u,st}$ and $\sigma_{u,dyn}$ are related the distance z using the parabolic stress-strain relationship of concrete; $\alpha\varepsilon_o$ is the current compressive strain at the extreme compression fiber of the cross section; α is the ratio of the current compressive strain $\alpha\varepsilon_o$ to the strain ε_o related to the uniaxial concrete compressive strength; and the c_u is the depth of the concrete compression zone (mm). The $f'_{t,st}$ and $f'_{t,dyn}$ are the effective static tensile strength reduced by the transverse compressive stress (MPa) (Park *et al.*, 2011) and the effective dynamic tensile strength reduced by the transverse compressive stress (MPa), respectively. If there is no measured value of static tensile strength of concrete, then the value of $f_{t,st}$ can be obtained from the relationship between the compressive and tensile strength of concrete (Eqs. (5-9) and (5-10)) according to *fib* Model Code 2010 (*fib*, 2010).

$$f_{t,st} = 0.3(f'_{c,st})^{2/3} \text{ for } f'_{c,st} < 50 \text{ MPa} \quad (5-9)$$

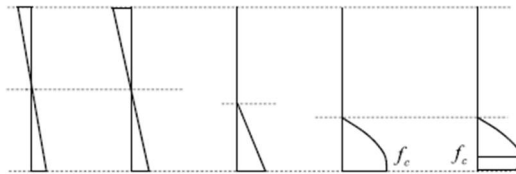
$$f_{t,st} = 2.12 \ln \left[1 + 0.1(f'_{c,st} + 8) \right] \text{ for } f'_{c,st} \geq 50 \text{ MPa} \quad (5-10)$$

where, $f_{t,st}$ is the static tensile strength of concrete (MPa) and $f'_{c,st}$ is the static compressive strength of concrete (MPa).

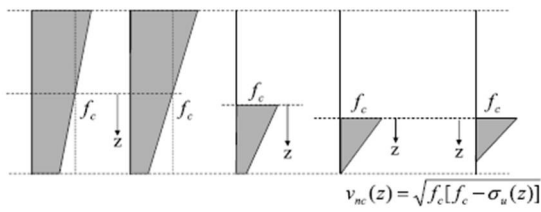
Stresses acting upon a interface between the spalled concrete cone and the concrete panel under impact load are demonstrated in **Figure 5-2**. It is assumed that the amount of deformation of the concrete panel is not large and does not have a critical influence upon the penetration depth (Hwang *et al.*, 2017). Therefore, it is assumed that the curvature of the concrete panel is at stage B, which is the point where the concrete crack starts (**Figure 5-5(a)**). Here, ε_{cr} is the concrete strain at cracking, and its value can be assumed to be the strain at 30% of the uniaxial compressive strength (ACI Committee 224, 2001). Assuming that the relationship between stress and strain is linear, the value of α is 0.2 **Eq. (5-11)**. The value of c_u and z is assumed to be the equal to $0.5h$ in case of an unreinforced and reinforced concrete panel (**Eqs. (5-12) to (5-14)**). Therefore, $v_{nc,st}(z)$ and $v_{nt,st}(z)$ can be reduced to **Eqs. (5-15) and (5-16)**. Considering dynamic loading, **Eqs. (5-15) and (5-16)** are changed to **Eqs. (5-17) and (5-18)**, respectively.



(a) Curvature (strain).

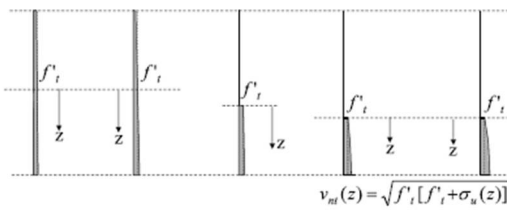


(b) Normal stress of concrete.



(c) Shear stress capacity controlled by compression

$$v_{nc}(z) = \sqrt{f_c [f_c - \sigma_u(z)]}$$



(d) Shear stress capacity controlled by tension

$$v_{nt}(z) = \sqrt{f'_t [f'_t + \sigma_u(z)]}$$

Figure 5-5 Distributions of normal stress and shear stress capacity according to the curvature at cross section (Park *et al.*, 2011)

$$\alpha = \frac{\varepsilon_{cr}}{\varepsilon_o} = \frac{\varepsilon_{peak} \times 30\%}{\varepsilon_o} = \frac{0.002 \times 30\%}{0.002} = 0.3 \quad (5-11)$$

$$\sigma_{u,st}(z) = f'_{c,st} \left[2 \left(\frac{0.3 \times 0.5h}{0.5h} \right) - \left(\frac{0.3 \times 0.5h}{0.5h} \right)^2 \right] \quad (5-12)$$

$$\sigma_{u,st}(z) = 0.51 f'_{c,st} \quad (5-13)$$

$$f'_{t,st} = 0.49 f_{t,st} \quad (5-14)$$

$$v_{nc,st}(z) = 0.7 f'_{c,dyn} \quad (5-15)$$

$$v_{nt,st}(z) = \sqrt{0.24(f_{t,st})^2 + 0.25 f_{t,st} f'_{c,st}} \quad (5-16)$$

$$v_{nc,dyn}(z) = 0.7 f'_{c,dyn} \quad (5-17)$$

$$v_{nt,dyn}(z) = \sqrt{0.24(f_{t,dyn})^2 + 0.25 f_{t,dyn} f'_{c,dyn}} \quad (5-18)$$

where, ε_{peak} is the strain at the ultimate compressive strength of concrete, which is normally 0.002; and ε_o is the compressive strain corresponding to the compressive concrete strength, which is 0.002 in ACI 318-14 (ACI committee 318, 2014).

Steel fibers increase concrete's tensile strength and can reduce its scabbing failure. This should reflect the effect of steel fibers, which play a role in increasing the tensile strength of concrete. Musmar (2013) proposed **Eq. (5-19)** to describe the tensile strength of concrete reinforced with steel fibers under static loading, which can be converted to **Eq. (5-20)** to considering the dynamic loading. The obtained

values can be applied to **Eq. (5-18)**.

$$f_{ts,st} = f_{t,st} \left(1 + \frac{2}{3} \frac{l_f}{d_f} V_f \right) \quad (5-19)$$

$$f_{ts,dyn} = f_{t,dyn} \left(1 + \frac{2}{3} \frac{l_f}{d_f} V_f \right) \quad (5-20)$$

where, $f_{ts,st}$ and $f_{ts,dyn}$ are the static tensile stress of steel fiber-reinforced concrete (MPa) and the dynamic tensile stress of steel fiber-reinforced concrete affected by strain rate, respectively; l_f is the steel fiber length (mm); d_f is the steel fiber diameter (mm); and V_f is the steel fiber volume fraction (%).

5.1.4 Force on nose of projectile

In order to calculate the elastic deformation of the panel, the projectile and the strain rate, Forrestal's study for normal stress on the nose of the projectile is referred (Forrestal *et al.*, 1994; Williams, 1994; Li and Chen, 2003; Li and Tong, 2003). The force (F_{nose}) is represented as shown in **Eqs. (5-21) to (5-26)**.

$$F_{nose} = \pi r_p^2 \left(\tau_{o,st} A + N_p B \rho_c V_{imp}^2 \right) \quad (5-21)$$

$$A = \frac{2}{3} - 2 \left(\frac{\tau_{m,st}}{\tau_{o,st}} \right) \ln \left[\frac{\gamma}{1 + \tau_{o,st} / 2E_{c,st}} \right] \quad (5-22)$$

$$B = \frac{2}{2(1-\eta^*)} + \frac{[3\tau_{0,st} / E_{c,st} + \eta^*(1-3\tau_{0,st} / 2E_{c,st})^2]}{\gamma^2} - \frac{\gamma}{2(1+\tau_{0,st} / 2E_{c,st})^4} \left[1 + \frac{3(1+\tau_{0,st} / 2E_{c,st})^3}{(1-\eta^*)} \right] \quad (5-23)$$

$$\gamma = \left[\left(1 + \frac{\tau_{0,st}}{2E_{c,st}} \right)^3 - (1-\eta^*) \right]^{1/3} \quad (5-24)$$

$$\eta^* = 1 - \rho_0 / \rho^* \quad (5-25)$$

$$N_p = \frac{8CRH - 1}{24CRH^2} \quad (5-26)$$

where, r_p is the radius of the projectile (mm), $\tau_{0,st}$ is the static shear stress without uniaxial load (MPa); $\tau_{m,st}$ is the static shear stress under triaxial loads (MPa); N_p is the nose shape factor of the projectile; ρ_c is the density of the concrete (kg/m^3); V_{imp} is the impact velocity (m/s); $E_{c,st}$ is the elastic modulus of the concrete under the static loading (MPa); η^* is the function related the density of concrete; and CRH is the caliber-radius-head.

η^* can be transferred to the other form using bulk modulus and the relationship of the change in volume to other physical quantities. When acting dynamic loading upon an object, the body will exhibit high hydrostatic pressures on short timescales (Thoma, 2009). Assuming that equal forces act on all surfaces as shown in **Figure 5-6**, the original volume (Vol_{ori}) could be changed to the deformed volume (Vol_{def}). The reduced volume (ΔVol) is defined as original volume minus deformed volume (**Eq. (5-27)**). The reduced volume is related to the bulk

modulus (K), force, area and original volume. η^* is newly derived from Eqs. (5-27) to (5-32).

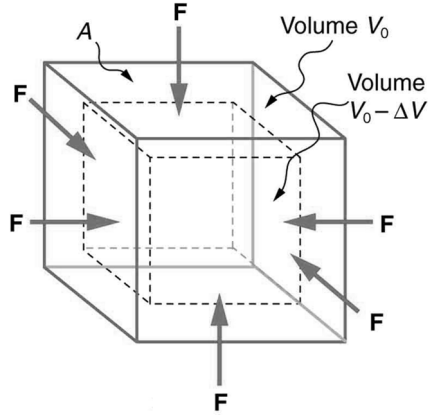


Figure 5-6 Compressive force acting upon all surfaces (hydrostatic condition)

$$\Delta Vol = Vol_{ori} - Vol_{def} = \frac{1}{K} \frac{F_{cube}}{A_{cube}} Vol_{ori} \quad (5-27)$$

$$Vol_{def} = Vol_{ori} - \frac{1}{K} \frac{F_{cube}}{A_{cube}} Vol_{ori} = Vol_{ori} \left(1 - \frac{1}{K} \frac{F_{cube}}{A_{cube}} \right) \quad (5-28)$$

$$K = \frac{E_{c,st}}{3(1-2\nu_{c,st})} \quad (5-29)$$

$$Vol_{def} = Vol_{ori} \left(1 - \frac{3(1-2\nu)}{E_{c,st}} \frac{F_{cube}}{A_{cube}} \right) = Vol_{ori} \left(1 - \frac{3(1-2\nu)}{E_{c,st}} \sigma_{c,st} \right) \quad (5-30)$$

$$\eta^* = 1 - \rho_0 / \rho^* = 1 - \frac{\text{weight/original volume}}{\text{weight/deformed volume}} = 1 - \frac{Vol_{def}}{Vol_{ori}} \quad (5-31)$$

$$\eta^* = 1 - \frac{Vol_{def}}{Vol_{ori}} = 1 - \frac{Vol_{ori} \left(1 - \frac{3(1-2\nu_{c,st})}{E_{c,st}} \sigma \right)}{Vol_{ori}} = \frac{3(1-2\nu_{c,st})}{E_{c,st}} \sigma_{c,st} \quad (5-32)$$

where, ΔVol is the volume obtained by subtracting the changed volume from the original volume (mm^3); Vol_{ori} is the volume of original cube (mm^3); Vol_{def} is the changed volume of the cube under triaxial loads (mm^3); K is the bulk modulus (MPa); F_{cube} is the acting force on the surface of the cube (N); A_{cube} is the area of the one cube's face (mm^2); $\nu_{c,st}$ is Poisson's ratio of the concrete under the static loading; $\sigma_{c,st}$ is the compressive strength of the concrete under the static loading (MPa); and $E_{c,st}$ is the elastic modulus of the concrete under the static loading (MPa).

The expression of γ can be changed using the newly derived η^* to **Eq. (5-33)**, and A is also changed to **Eq. (5-34)**.

$$\gamma = \frac{V}{c} = \left[\left(1 + \frac{\tau_{0,st}}{2E_{c,st}} \right)^3 - \left(1 - \frac{3(1-2\nu_{c,st})}{E_{c,st}} \sigma_{c,st} \right) \right]^{1/3} \quad (5-33)$$

$$A = \frac{2}{3} - 2 \left(\frac{\tau_m}{\tau_0} \right) \ln \left[\frac{\left[\left(1 + \frac{\tau_0}{2E} \right)^3 - \left(\frac{E_c - 3(1-2\nu)\sigma}{E_c} \right) \right]^{1/3}}{(1 + \tau_0 / 2E)} \right] \quad (5-34)$$

where, $\tau_{0,st}$ is $0.33\lambda(f'_{c,st})^{0.5}$ and $\tau_{m,st}$ can be considered as $v_{nc}(z)$ because both τ_m and $v_{nc}(z)$ are affected by compressive stress. Therefore, the ratio of $\tau_{m,st}$ to $v_{nc,st}(z)$ is $2.12(f'_c)^{0.5}$ when using normal weight concrete (Eqs. (5-35) and (5-36)). Given that the concrete is normal weight concrete, the A can be reduced as in Eq. (5-37).

$$A = \frac{2}{3} - 2 \left(2.12 \sqrt{f'_{c,st}} \right) \ln \left[\frac{\left[\left(1 + \frac{(0.33 \sqrt{f'_{c,st}})^3}{2E_{c,st}} \right) - \left(\frac{E_{c,st} - 3(1-2\nu)f'_{c,st}}{E_{c,st}} \right) \right]^{1/3}}{\left(1 + \frac{(0.33 \sqrt{f'_{c,st}})^3}{2E_{c,st}} \right)} \right] \quad (5-35)$$

$$E_{c,st} = wc^{1.5} 0.043 \sqrt{f'_{c,st}} \quad (5-36)$$

$$E_{c,st} = 4700 \sqrt{f'_{c,st}} \quad \text{for normal weight concrete}$$

$$A = \frac{2}{3} - 2 \left(2.12 \sqrt{f'_{c,st}} \right) \ln \left[0.073 \left(\sqrt{f'_{c,st}} + 0.275 \right)^{1/3} \right] \quad (5-37)$$

The value of B has a narrow range and is suggested as 1.0 for concrete (Li and Chen, 2003; Forrestal *et al.*, 1994). Here, the value of B also follows 1.0. Finally, the force on the nose of the projectile is presented as Eqs. (5-38) to (5-40).

$$F_{nose} = \pi r_p^2 (\tau_{o,st} A + N_p \rho_c V_{imp}^2) \quad (5-38)$$

$$A = \frac{2}{3} - 2 \left(2.12 \sqrt{f'_{c,st}} \right) \ln \left[0.073 \left(\sqrt{f'_{c,st}} + 0.275 \right)^{1/3} \right] \quad (5-39)$$

$$N = \frac{8CRH - 1}{24CRH^2} \quad (5-40)$$

where, F_{nose} is the normal force on the nose of the projectile (N); r_p is the radius of the projectile (mm); $\tau_{0,st}$ is the static shear stress without uniaxial load (MPa); N_p is the nose shape factor of the projectile; ρ_c is the density of concrete (kg/m^3); V_{imp} is the impact velocity (m/s); $f'_{c,st}$ is the compressive strength of concrete under the static loading (MPa); and CRH is the caliber-radius-head (R_{nose}/d_p).

5.2 Properties of Materials Affected by Strain Rate

5.2.1 Definition of strain rate

In this impact study, the properties of materials are related to the strain rate by the short-term huge load (**Figure 3-2** and **Figure 5-7**). The material under dynamic loads exhibits difference properties than quasi-static loading, a yielding stress and/or elastic modulus of material increase as the strain-rate increases (Qi *et al.*, 2009). Since the material strength increases rapidly in the high strain-rate, it is essential to study and consider the strain-rate effect in impact load studies. In particular, the strain-rate is closely related to the velocity of a projectile, and is very sensitive and difficult to predict. Since it is difficult to study these matters separately, the strain rate will follow the Ramesh study (2008), and the properties of materials affected by the strain rate will follow *fib* Model Code 2010 (*fib*, 2010).

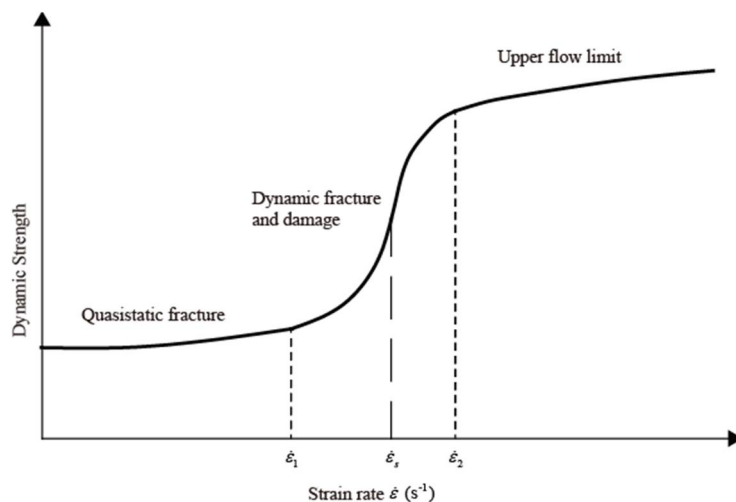


Figure 5-7 Strength of brittle materials affected by strain-rate (redrawn from Qi *et al.*, 2009)

Strain rate is an important factor for evaluating the impact resistance and is dependent on the material properties of the projectile and the target. In order to generally estimate the dynamic properties of materials, the Split-Hopkinson Pressure Bar (SHPB) and Kolsky Bar are used. They exhibit a difference. SHPB implies the performance of compression experiments, whereas the Kolsky bar covers various properties such as compression, tension, torsion, etc. (Ramesh, 2008). Because of this difference, this study refers to the Kolsky Bar (**Figure 5-8** and **Figure 5-9**).

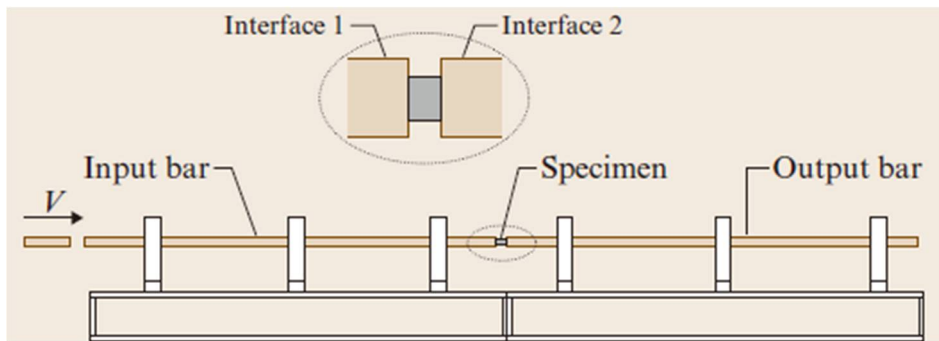


Figure 5-8 Schematic of compression Kolsky bar (Ramesh, 2008)

When imposing the impact load on the input bar, the incident pulse (ϵ_I) is generated after which that bar transfers the incident pulse at the end of the bar to the specimen connected with the other end of the bar. Initially, the incident pulse reaches a test specimen, after which the incident pulse will be separated into a reflected pulse (ϵ_R) and a transmitted pulse (ϵ_T) as shown in **Figure 5-9**. The particle velocity (v_I) at the interface 1 is defined as **Eq. (5-41)**, and particle velocity (v_2) at the interface 2 is defined as **Eq. (5-42)**.

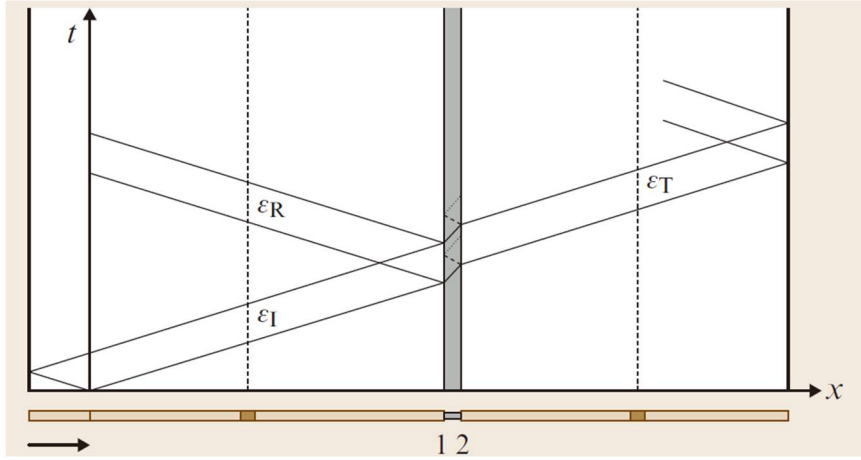


Figure 5-9 Wave propagation diagram using Kolsky Bar (Ramesh, 2008)

$$v_1(t) = c_b(\varepsilon_I - \varepsilon_R) = \sqrt{\frac{E_b}{\rho_b}}(\varepsilon_I - \varepsilon_R) \quad (5-41)$$

$$v_2(t) = c_b \varepsilon_T = \sqrt{\frac{E_b}{\rho_b}} \varepsilon_T \quad (5-42)$$

where, v_1 and v_2 are the particle velocity at interfaces 1 and 2 (m/s), respectively; ε_I is incident pulse; ε_R is reflected pulse; ε_T is the transmitted pulse; c_b is the bar wave speed; E_b is the elastic modulus of the bar (MPa); and ρ_b is the density of the input bar (kg/m^3).

The mean axial strain rate ($\dot{\varepsilon}_s$) in the specimen can be obtained from these pulses, the length of specimen, the elastic modulus and the density of the input bar (**Eq. (5-43)**).

$$\dot{\epsilon}_s = \frac{1}{l_0} \sqrt{\frac{E_b}{\rho_b}} (\epsilon_I - \epsilon_R - \epsilon_T) \quad (5-43)$$

where, l_0 is the length of specimen (mm); E_b is the elastic modulus of the bar (MPa); and ρ_b is the density of the bar (kg/m^3).

The initial length (l_0) of specimen is known and the input and output bars are in elastic condition, the normal forces at interface 1 and 2 are derived as **Eqs. (5-44)** and **(5-45)**, respectively. And the mean nominal axial stress (σ_s) in the specimen is derived using P_1 and P_2 .

$$P_1 = E_{b,in} (\epsilon_I + \epsilon_R) A_{b,out} \quad (5-44)$$

$$P_2 = E_{b,out} \epsilon_T A_b \quad (5-45)$$

$$\sigma_s(t) = \frac{P_1 + P_2}{2} \frac{1}{A_s} = \frac{E_b}{2} \frac{A_b}{A_s} (\epsilon_I - \epsilon_R - \epsilon_T) \quad (5-46)$$

where, P_1 and P_2 are the normal forces at interface 1 and 2, respectively (N); $E_{b,in}$ and $E_{b,out}$ is the elastic moduli of the input bar and output bar, respectively (MPa); E_b is the elastic modulus of the input or output bar (MPa); ϵ_I is incident pulse; ϵ_R is reflected pulse; ϵ_T is the transmitted pulse; and A_b is the sectional area of input or output bar (mm^2); and A_s is the sectional area of the specimen (mm^2).

It is assumed that P_1 and P_2 are equal considering the equilibrium condition, and the sum of the incident pulse and reflected pulse is equal to the transmitted pulse **Eq. (5-47)**. And the nominal strain rate ($\dot{\epsilon}_s$) (**Eq. (5-48)**) can be derived

using Eqs. (5-47) and (5-43). And the nominal strain (e_s) is derived as Eq. (5-49). In Eq. (5-47), the negative sign means the compressive pulse, which means that \dot{e}_s is the compressive nominal strain rate.

$$\varepsilon_I + \varepsilon_R = \varepsilon_T \quad (5-47)$$

$$\dot{e}_s = -\frac{2}{l_0} \sqrt{\frac{E_b}{\rho_b}} \varepsilon_R(t) \quad (5-48)$$

$$e_s(t) = \int_0^t \dot{e}_s(\tau) d\tau \quad (5-49)$$

where, P_1 and P_2 are the normal forces at interfaces 1 and 2, respectively (N); E_b is the elastic modulus of the input or output bar (MPa); ε_I is the incident pulse; ε_R is the reflected pulse; ε_T is the transmitted pulse; l_0 is the length of specimen (mm); E_b is the elastic modulus of the input or output bar (MPa); ρ_b is the density of the input or output bar (kg/m^3); and e_s is the nominal strain.

The $\varepsilon_R(t)$ is the reflected strain and its value can be derived from Forrestal's research. The maximum value of $\varepsilon_R(t)$ is when the force on nose of the projectile is high. Considering impact mechanism, the input bar is like the projectile and ε_R is the reflected strain of the projectile. The reflected strain occurs due to the reaction force between the projectile and concrete, and the reaction force is the same as the force on nose of the projectile. Therefore, Eq. (5-48) can be converted to Eq. (5-50), and the stress and strain relationship is Eq. (5-51). The nominal strain rate of concrete panel is derived to Eq. (5-53) using Eqs. (5-50) and (5-52). As the HPSB and Kolsky bar assumes that the Input/output bars are elastic conditions, the

elasticity of the modulus is constant (e.g., 20500 MPa for steel).

$$\dot{\epsilon}_s = -\frac{2}{h} \epsilon_R \sqrt{\frac{E_{p,st}}{\rho_p}} \quad (5-50)$$

$$\sigma_{nose} = E_{p,st} \epsilon_p \quad (5-51)$$

$$\frac{F_{nose}}{A_p} = E_{p,st} \epsilon_p \quad (5-52)$$

$$\dot{\epsilon}_s = 2 \frac{1}{h} \frac{F_{nose}}{A_p E_{p,st}} \sqrt{\frac{E_{p,st}}{\rho_p}} \times 10^6 \quad (5-53)$$

where, σ_{nose} is the stress on the nose of the projectile (MPa) and can be obtained from the Forrestal research (**Eq. (5-38)**); $E_{p,st}$ is the elastic modulus of the projectile under the static loading (MPa); and ϵ_p is the strain of the projectile in **Eq. (5-51)** and ϵ_p is the same as the reflected strain (ϵ_R) that is defined in the Kolsky bar test. From these, the true strain rate ($\dot{\epsilon}_s$) is obtained as shown in **Eq. (5-54)** (Ramesh and Narasimhan, 1996). The maximum value of the concrete nominal strain at ultimate strength is normally 0.002, and the true strain rate is close to the nominal strain rate **Eq. (5-54)**. From **Eqs. (5-50)** and **(5-51)**, true strain rate can be expressed using the variable in the high velocity impact test **Eq. (5-55)**.

$$\dot{\epsilon}_s = \frac{\dot{\epsilon}_s}{1 - e_s} \approx \dot{\epsilon}_s \quad (5-54)$$

$$\dot{\epsilon}_s = 2 \frac{1}{h} \frac{F_{nose}}{A_p E_{p,st}} \sqrt{\frac{E_{p,st}}{\rho_p}} \times 10^6 \quad (5-55)$$

where, h is the thickness of target panel (mm); F_{nose} is the force obtained from **Eq. (5-38)** (N); A_p is the sectional area of projectile (mm²); $E_{p,st}$ is the elastic modulus of projectile under the static loading (MPa); and ρ_p is the density of projectile (kg/m³).

The basic concept of the experimental system to estimate the strain rate for tension is identical to the compression system. And the equation is also identical, but uses the length of the gauge instead of the specimen. Because the length of the gauge is unknown in this study, it is assumed that length of gauge is equal to that of the specimen. Therefore, the strain rate for tension can be assumed to be equal to the strain rate for compression, because the maximum force acting on the rear face is assumed the same as the compression force.

5.2.2 Properties of concrete affected by strain rate

Properties of materials have to be considered in relationship to the strain rate effect for short-term huge load. The relationships between compressive strength and strain rate are specified as **Eqs. (5-56)** and **(5-57)** in the Model Code 2010 (*fib*, 2010). The properties of tensile strength and strain under impact loading are changed as **Eqs. (5-58)** and **(5-59)**. The modulus of elasticity of concrete is also affected with respect to the strain rate and estimated from **Eqs. (5-60)** and **(5-61)**.

$$\frac{f'_{c,dyn}}{f'_{c,st}} = \left(\frac{\dot{\epsilon}_c}{30 \times 10^{-6}} \right)^{0.014} \quad \text{for } \dot{\epsilon}_c \leq 30 \text{ s}^{-1} \quad (5-56)$$

$$\frac{f'_{c,dyn}}{f'_{c,st}} = 0.012 \left(\frac{\dot{\epsilon}_c}{30 \times 10^{-6}} \right)^{1/3} \quad \text{for } \dot{\epsilon}_c > 30 \text{ s}^{-1} \quad (5-57)$$

$$\frac{f'_{t,dyn}}{f'_{t,st}} = \left(\frac{\dot{\epsilon}_t}{1 \times 10^{-6}} \right)^{0.018} \quad \text{for } \dot{\epsilon}_{ct} \leq 10 \text{ s}^{-1} \quad (5-58)$$

$$\frac{f'_{t,dyn}}{f'_{t,st}} = 0.0062 \left(\frac{\dot{\epsilon}_t}{1 \times 10^{-6}} \right)^{1/3} \quad \text{for } \dot{\epsilon}_{ct} > 10 \text{ s}^{-1} \quad (5-59)$$

$$\frac{E_{cc,dyn}}{E_{cc,st}} = \left(\frac{\dot{\epsilon}_c}{30 \times 10^{-6}} \right)^{0.026} \quad \text{for compression} \quad (5-60)$$

$$\left(\frac{E_{ct,dyn}}{E_{ct,st}} \right) = \left(\frac{\dot{\epsilon}_t}{1 \times 10^{-6}} \right)^{0.026} \quad \text{for tension} \quad (5-61)$$

where, $f'_{c,dyn}$ is the compressive stress of concrete under the dynamic loading (MPa); $f'_{c,st}$ is the the compressive stress of concrete under the static loading (MPa); $f'_{t,dyn}$ is the tensile stress of concrete under dynamic loading (MPa); $f'_{t,st}$ is the tensile stress of concrete under the static loading (MPa); $E_{cc,dyn}$ and $E_{ct,dyn}$ are the compressive and tensile elastic modulus of concrete under the dynamic loading, respectively (MPa); and $E_{cc,st}$ and $E_{ct,st}$ are the compressive and elastic modulus of concrete under the static loading (MPa).

5.2.3 Properties of steel affected by strain rate

Comité Euro-International du Béton (CEB, 1988) proved several formulae according to the type of steel, such as hot rolled reinforcing steel, RTS-steel, cold-steel, mild steel and high-quality steel. The reinforcing steel is normally manufactured hot rolled, so the formula used in this study is **Eq. (5-62)**, $f_{y,dyn}$ is the dynamic yield stress and f_y is the nominal yield stress. It is assumed that elastic modulus is not affected by the strain rate (CEB, 1988).

$$\frac{f_{y,dyn}}{f_{y,st}} = 1 + \frac{6}{f_{y,st}} \ln \frac{\dot{\epsilon}}{5 \times 10^{-5}} \quad (5-62)$$

where, $f_{y,dyn}$ is the tensile stress of steel under the dynamic loading (MPa); and $f_{y,st}$ is the tensile stress of steel under the static loading (MPa).

5.3 Involved Energies in Impact Mechanism

5.3.1 Kinetic energy (E_K)

The flying projectile has the kinetic energy (E_K) that consists of mass (kg) and flying velocity (m/s) shown in **Eq. (5-63)**. The kinetic energy is the important external energy that can occur prior to the failure of a reinforced concrete panel. This energy is the fundamental type of energy that constitutes the law of conservation of energy in the impact mechanism. The velocity of the projectile is a key point for defining the strain-rate and changing the properties of the material.

$$E_K = \frac{1}{2} M_p V_{imp}^2 \quad (5-63)$$

where, E_K is the kinetic energy (N-mm); M_p is the mass of the projectile (kg), and V_{imp} is the velocity of the projectile at the moment of collision (m/s).

5.3.2 Deformed energy of projectile (E_{DP})

Many other pieces of research or formulae neglected the deformation of projectile. It was assumed that a projectile is non-deformable and as hard as a steel. Since the strength difference between a projectile and concrete is reduced at the time when ultra-high strength concrete is being developed, it is difficult to assume that projectile is no longer non-deformable. As the difference of strength between them decreases, the deformation of the projectile needs to be considered. At the moment of the collision, the reaction force also acts on the projectile, it will create

deformation of the projectile. When impact force is suddenly applied to a projectile, deformed energy (E_{DP}) is stored in the body as shown in **Eq. (5-64)**.

$$E_{DP} = \frac{F_{nose}^2 l_p}{2E_{p,dyn} A_p} \quad (5-64)$$

where, F_{nose} is the applied load to projectile (N); l_p is the length of the projectile (mm); $E_{p,dyn}$ is the elastic modulus of the projectile affected by strain rate (MPa); and A_p is the sectional area of projectile (mm²).

5.3.3 Resistance energy to penetration

5.3.3.1 Elastic penetrated energy of concrete panel (E_{EP})

When two bodies touch, each body consumes energy and this energy will create elastic deformation. Energy occurs when an elastic deformation of a reinforced concrete slab is defined as the elastic deformed energy (E_{EP}). It follows Hertzian contact theory (Hertz, 1882) but frictional contact energy is neglected. Hertz (1982) was the first researcher to study the mechanics of contact between two elastic bodies and the deformation that is related to the modulus of elasticity of bodies. The elastic penetration depth between a sphere and a half-space is derived as shown in **Eqs. (5-65) and (5-66)** and **Figure 5-10**. Hertzian contact theory assumed that the thickness of space is infinite. However, realistic concrete panels have a particular thickness. The test specimen thickness may be smaller than the thickness required, showing elastic deformation. Given that maximum strain of concrete is normally 0.002, the elastic deformed energy (E_{EP}) according to the type

of nose of the projectile can be obtained as Eqs. (5-67) to (5-69) (Johnson, 1985; Hanaor *et al.*, 2015; Sneddon, 1965; www.wikipedia.org)

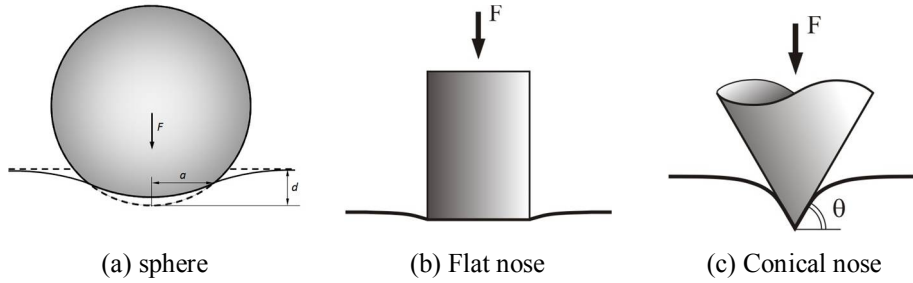


Figure 5-10 Hertz contact theory (www.wikipedia.org)

$$d_{elastic} = \left(\frac{9F^2}{16E^{*2}r} \right)^{1/3} \quad (5-65)$$

$$\frac{1}{E^*} = \frac{1-\nu_p^2}{E_{p,dyn}} + \frac{1-\nu_c^2}{E_{c,dyn}} \quad (5-66)$$

$$E_{EP} = F_{nose} \times \left[d_{elastic} \text{ or } 0.002h \right]_{min} \text{ for sphere or hemisphere} \quad (5-67)$$

$$E_{EP} = F_{nose} \times \left[\frac{F_{nose}}{2aE^*} \text{ or } 0.002h \right]_{min} \text{ for flat nose} \quad (5-68)$$

$$E_{EP} = F_{nose} \times \left[\sqrt{\frac{F_{nose}\pi(1-\nu_c^2)\tan\theta}{2E_{c,dyn}}} \text{ or } 0.002h \right]_{min} \quad (5-69)$$

for conical, sharp, or ogive nose

where, $d_{elastic}$ is the elastic penetration depth by Hertzian contact theory (mm); F is the acting force (N); ν_p and ν_c is Poisson's ratios of sphere and half-space

(projectile and concrete panel in this study, respectively); $E_{p,dyn}$ and $E_{cc,dyn}$ are the elastic modulus of the sphere and the half-space under the dynamic loading, respectively; E_{EP} is the elastic penetrated energy (N-mm); F_{nose} is the force on the nose of the projectile (N) that is defined by **Eq. (5-38)**; h is the thickness of the concrete panel (mm); and $\tan\theta$ is the angle between the plane and the side surface of the cone.

5.3.3.2 Overall deformed energy of concrete panel (E_{SD})

The overall slab will be deformed under a load, so some of the kinetic energy is converted to overall deformed energy of the concrete panel (E_{SD}). This energy can be derived from a bending moment of (reinforced) concrete panel. Assuming that flexural deformation of the (reinforced) concrete slab is not critically affected by the impact loads and the deformation of the (reinforced) concrete panel is a cracked condition. The reinforced concrete panel can be considered as a simply supported beam with the deformed bending moment equal to the cracking moment, as obtained according to ACI 318-14 (ACI Committee 318, 2014). The overall deformed energy of the reinforced concrete panel can be obtained as shown in **Eqs. (5-70) to (5-72)**.

$$f_{r,dyn} = 0.62\lambda\sqrt{f'_{c,dyn}} \quad (5-70)$$

$$M_{cr} = \frac{f_{r,dyn} I_g}{y_{l,dyn}} \quad (5-71)$$

$$E_{DC} = \frac{M_{cr}^2 L_s}{2E_{cc,dyn} I_g} \quad (5-72)$$

where, M_{cr} is the cracking moment (N-mm), $f_{r,dyn}$ is the modulus of rupture of the concrete (MPa) affected by the strain rate, I_g is the moment of inertia of the gross concrete section about the centroidal axis (mm^4), L_s is the long direction length of the slab (mm), $E_{cc,dyn}$ is the modulus of elasticity of concrete affected by the strain rate (MPa).

5.3.3.3 Spalling-resistant energy (E_{SP})

Some impact energy will transfer to a concrete panel and that transferred energy becomes some part of the concrete panel spall. The shape of spalling was normally a truncated cone in previous experimental work. **Figure 5-11** shows the idealized concrete failure and spalling-resistant energy is determined by the kinetic energy of spalled concrete that has also mass (kg) and velocity (m/s) as shown in **Eq. (5-73)**. The spalled cone is caused by a drag force (F_{drag}) to impact energy (**Eqs. (5-74) to (5-76)**). This kinetic energy is the same as was the case when the force acting upon an area of spalled concrete and a volume of spalled concrete were multiplied **Eq. (5-77)**. It is known as energy density (energy/volume).

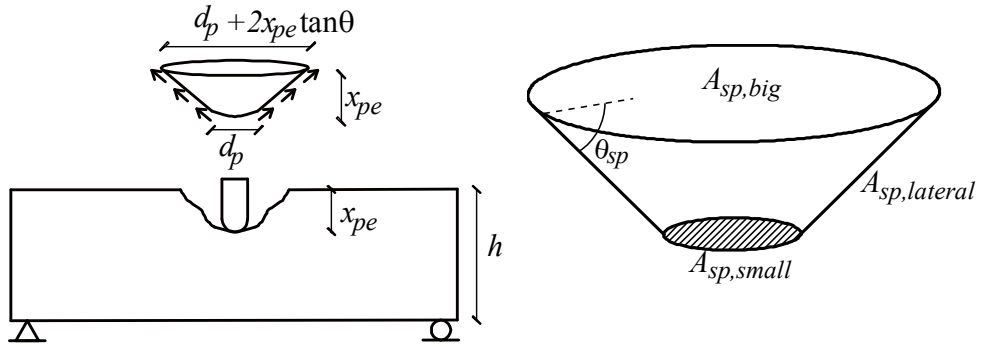


Figure 5-11 Spalled cone and truncated shape

$$E_{sp} = \frac{1}{2} M_{sp} V_{sp}^2 \quad (5-73)$$

$$F_{drag} = \frac{\rho V_s^2}{2} A_{sp} \quad (5-74)$$

$$F_{sp} = \frac{\rho_{sp} V_{sp}^2}{2} A_{sp} = \frac{V_{sp}^2}{2} A_{sp} \frac{M_{sp}}{Vol_{sp}} \quad (5-75)$$

$$F_{sp} \frac{Vol_{sp}}{A_{sp}} = \frac{M_{sp}}{2} V_{sp}^2 = E_{sp} \quad (5-76)$$

$$E_{sp} = F_{sp} \frac{Vol_{sp}}{A_{sp}} \quad (5-77)$$

where, E_{sp} is the spalling-resistant energy (J); M_{sp} is the mass of the spalled concrete cone (kg); F_{sp} is the force between the spalled cone and the concrete slab (N); V_{sp} is the velocity of the spalled concrete cone (m/s); Vol_{sp} is the volume of the idealized concrete cone (mm^3); A_{sp} is the projected area of the idealized concrete cone (mm^2); and ρ_{sp} is the density of spalled cone (kg/mm^3). The volume and area

can be obtained from **Eqs. (5-78) to (5-81)**.

$$Vol_{sp} = \frac{\pi x_{pe}}{12} (4x_{pe}^2 \tan^2 \theta_{sp} + 6d_p x_{pe} \tan \theta_{sp} + 3d_p^2) \quad (5-78)$$

$$A_{sp, big} = \frac{\pi}{4} (d + 2x_p \tan \theta_{sp})^2 \quad (5-79)$$

$$A_{sp, little} = \frac{\pi d^2}{4} \quad (5-80)$$

$$A_{sp, lateral} = \pi (d_p + x_p \tan \theta_{sp}) \frac{x_p}{\cos \theta_{sp}} \quad (5-81)$$

where, Vol_{sp} is the volume of the spalled cone (mm^3); x_{pe} is the penetration depth (mm); d_p is the diameter of the projectile (mm); $A_{sp, big}$ is the top area of spalled cone in **Figure 5-11** (mm^2); $A_{sp, little}$ is the base area of spalled cone in **Figure 5-11** (mm^2); $A_{sp, lateral}$ is the lateral area of spalled cone in **Figure 5-11** (mm^2); and θ_{sp} is the slant angle of the lateral surface (degree).

Finally, the spalling-resistant energy formula can be derived as shown in **Eqs (5-82) to (5-85)**, the concrete spalling resistance force (F_{sp}) is defined using shear stress controlled by compression, a spalled cone area. The reinforcing bar's action is neglected, because the spalled cone is pressured under compression in the spalling condition. When the projectile has a long length or hyper velocity, the energy per unit area becomes large, so these effects should be applied to the penetration prediction formula. α_l is the velocity effect factor that is applied at a velocity greater than 340 m/s. 340 m/s is 1 Mach, and if the velocity of the

projectile exceeds 340m/s, it will be hypersonic. This can lead to totally different shock phenomenon (Anderson Jr., 2006). Depending on the speed, it can be assumed that the speed of transferring the energy of the projectile to the concrete will also vary. In addition, if the projectile is slender, the energy per unit area will be increased. The effect factor takes into account the fact that the length of the projectile is α_2 . In other words, energy transference velocity and energy per unit area should be considered, even with the same kinetic energy.

$$F_{sp} = \text{shear stress (controlled by comp.)} \times \text{spalled cone area} \\ \times \text{velocity effect factor} \times \text{projectile size factor} \quad (5-82)$$

$$F_{sp} = 0.7 f'_{c,dyn} \left[\pi (d_p + x_{pe} \tan \theta_s) \frac{x_{pe}}{\cos \theta_s} + \frac{\pi d_p^2}{4} \right] \\ E_{SP} = 0.7 f'_{c,dyn} \left[\pi (d_p + x_{pe} \tan \theta_s) \frac{x_{pe}}{\cos \theta_s} + \frac{\pi d_p^2}{4} \right] \alpha_1 \alpha_2 \frac{Vol_{sp}}{A_{sp,big}} \quad (5-83)$$

$$\alpha_1 = \left(\frac{V_{imp}}{340} \right)^{0.15} \quad (5-84)$$

$$\alpha_2 = \ln \left(0.8 + \frac{l_p}{d_p} \right) \quad (5-85)$$

where, F_{sp} is the force between the spalled cone and the concrete slab (N); $f'_{c,dyn}$ is the compressive strength of the concrete affected by dynamic load; d_p is the sectional diameter of the projectile (mm); x_{pe} is the penetration depth (mm); $\cos \theta_s$ is the angle of the truncated cone (degree); Vol_{sp} is the volume of the spalled cone (mm^3); $A_{sp,big}$ is the based area of the spalled cone (mm^2); α_1 is the velocity effect

factor; α_2 is the projectile length factor; and l_p is the length of the projectile (mm).

5.3.3.4 Tunneling-resistant energy (E_T)

As mentioned in **Section 5.3.3.3**, when projectile has huge energy per unit area by hyper velocity or mass, the projectile can penetrate deep into a concrete panel. Energy beyond the energy required for the step to spalling can cause tunneling depth (x_t). Tunneling-resistant energy can be obtained using the energy density and the bearing bond strength (**Eqs. (5-86) and (5-87)**). The force acting on the side of the cylindrical tunnel is shown in **Eq. (5-88)**. The impact energy of the projectile can be resisted by the bearing bond strength between the projectile and concrete. According to previous studies (Eligehausen *et al.*, 1983; Lowes and Altoontash, 2003; Hwang *et al.*, 2015), the average bond stress under the static loading is $2.2(f'_{c,st})^{0.5}$, and it will be modified to $2.2(f'_{c,dyn})^{0.5}$ considering the dynamic loading as shown in **Eq. (5-89)**. This stress is obtained from an interface between a deformed reinforcing bar and a concrete, since there are no lugs on projectile in many cases, the bearing stress should be reduced, and then it is assumed to be 50% in this study. If there are reinforcing bars in line of projection, shear stress of reinforcing bar has to be considered.

$$E_T = \underbrace{\frac{F_t}{A_t} V_t}_{\text{energy density of tunnel}} + \underbrace{\tau_{dyn} x_t}_{\text{energy of bond}} \quad (5-86)$$

$$E_T = \underbrace{F_t x_t}_{\text{energy density of tunnel}} + \underbrace{\tau_{dyn} x_t}_{\text{energy of bond}} \quad (5-87)$$

$$F_t = N_p 2\pi d_p x_t 0.7 f'_{c,dyn} \quad (5-88)$$

$$\tau_{dyn} = 1.1 \sqrt{f'_{c,dyn}} \quad (5-89)$$

$$E_T = \underbrace{\left(N_p 2\pi d_p x_t 0.7 f'_{c,dyn} \right) x_t}_{\text{energy density of tunnel}} + \underbrace{1.1 \sqrt{f'_{c,dyn}} x_t}_{\text{energy of bond}} \quad (5-90)$$

where, F_T is the force of tunneling-resistant force on side of the cylindrical tunnel (N); d_p is the diameter of the projectile (mm); x_t is the length of the tunnel (mm); N_p is the nose shape factor; τ_{dyn} is the bond stress under the dynamic loading (MPa); ρ_p is the density of the projectile (kg/m^3); A_t is the sectional area of the tunnel (mm^2); and M_p is the mass of the projectile (kg).

5.3.3.5 Scabbing-resistant energy (E_{SC})

The scabbing theory is introduced in order to derive the scabbing-resistant energy. According to the scabbing theory (Society of Material Science of Japan, 1988; Kolsky, 1963) compressive stress is generated and radiated from the force pressing at an impact point on the front face, P in **Figure 5-12**, the compressive stress is transferred to the rear face of a panel. The transferred stress is changed to the tensile stress, which assumes that tensile stress is generated and reflected at the free point (P') in **Figure 5-12**. If the tensile stress exceeds the properties of the

concrete, scabbing occurs. The force (F_{sc}) acting upon between the scabbed concrete cone and the slab can be obtained in the same way as spalling-resistant energy (Eq. (5-91)). The scabbing-resistant energy should be taken into consideration for the tensile effect of the rebar. The scabbing-resistant energy (Eq. (5-92)) is obtained using the acting force and the energy density.

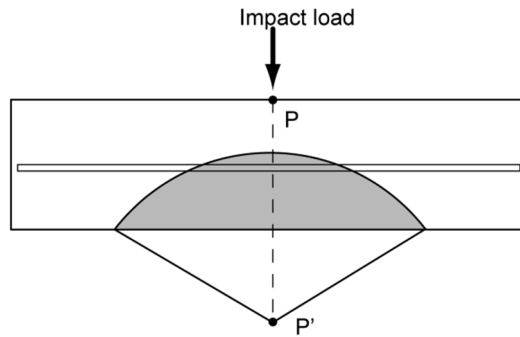


Figure 5-12 Scabbing theory (Kolsky, 1963; Society of Material Science of Japan, 1988)

$$F_{sc} = [\text{shear stress (controlled by tension)} \times \text{spalled cone area}]$$

$$F_{sc} = \left[v_{nt,dyn} \pi (d_p + x_{sc} \tan \theta_{sc}) \frac{x_{sc}}{\cos \theta_{sc}} + v_{nt,dyn} \frac{\pi d_p^2}{4} \right] \quad (5-91)$$

$$E_{sc} = \left[v_{nt,dyn} \pi (d_p + x_{sc} \tan \theta_s) \frac{x_{sc}}{\cos \theta_s} + v_{nt,dyn} \frac{\pi d_p^2}{4} \right] \alpha_2 \frac{V_{sc}}{A_{sc}} \quad (5-92)$$

where, F_{sc} is the force upon between the scabbed concrete cone and the concrete panel (N); E_{sc} is the scabbing-resistant energy (kN-m); $v_{nt,dyn}$ is the tensile strength of concrete controlled by the compression under the dynamic loading (MPa); d_p is the sectional diameter of the projectile (mm); x_{sc} is the scabbing depth (mm); θ_{sc} is

the angle of the scabbed cone (degree); Vol_{sc} is the volume of the scabbed cone (mm^3); and A_{sc} is the base area of the scabbed cone (mm^2).

Herein, how much energy reaches and is reflected from a rear face of a concrete panel is very important for predicting scabbing phenomenon. In order to estimate the amount of the reached energy or reflected energy, the stress-depth relationship of contact theory is used. The stress distribution for half space along the z -axis is as in **Eq. (5-93)** (Williams and Dwyer-Joyce, 2000), and if a sphere and cylinder is in contact on half-space, the stresses along the axis can be drawn as shown in **Figure 5-13**.

$$\sigma_z = -P_{ct,max} \left(\frac{z_{ct}^2}{a_{ct}^2} + 1 \right)^{-1} \quad (5-93)$$

where, σ_z is the stress at z_{ct} point; $P_{ct,max}$ is the maximum force on contact point; z_{ct} is the distance from a contact point along z -direction; and a_{ct} is the radius of the contact area.

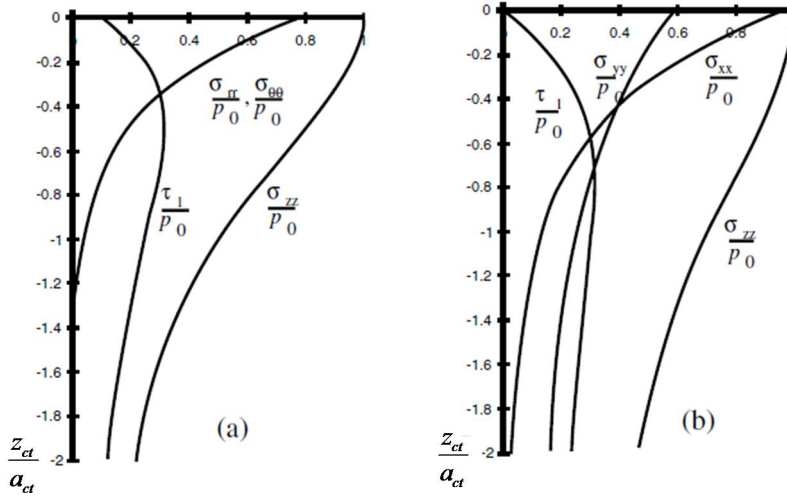


Figure 5-13 Stress distribution when sphere (a) or cylinder (b) contact half-space with Poisson's ratio of 0.3 (Williams and Dwyer-Joyce, 2000)

Load ($P_{ct,max}$) of **Eq. (5-93)** can be considered as an energy, which can be expressed as **Eq. (5-94)**. In the previous chapter, a_{ct} is assumed to be equal to the sectional radius of the projectile. If the penetration depth (x_{pe}) is deeper than the sectional radius of the projectile, a_{ct} can be considered as the penetration depth. However, if the penetration depth is less than the radius of the sectional radius of the projectile, the value of a_{ct} should be changed. In Hertzian contact theory, a_{ct} is the radius of the contact area, which is the penetration depth (x_{pe}) in this study. In other words, it can be assumed that the spalled cone is in contact with the unpenetrated slab at the penetration depth as shown in **Figure 5-14**. In summary, a_{ct} is the penetration depth if the penetration depth is greater than the radius of the projectile, and a_{ct} is the radius of the projectile if the penetration depth is less than the radius of the projectile. Therefore, the energy reflected from the rear face of the slab can be defined as **Eq. (5-95)**. Since E_z is E_{sc} , **Eqs. (5-92)** and **(5-95)** become **Eq. (5-96)**.

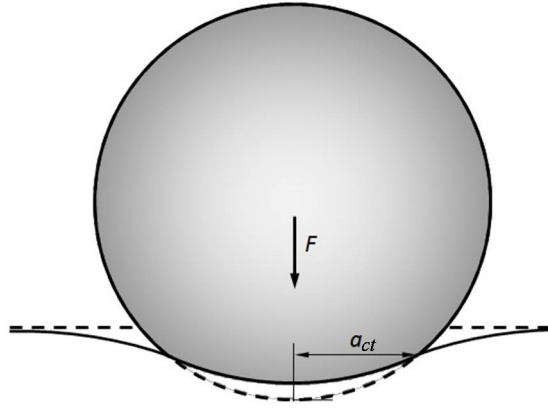


Figure 5-14 Definition of a_{ct}

$$E_z = -E_{\max} \left(\frac{z_{ct}^2}{a_{ct}^2} + 1 \right)^{-1} \quad (5-94)$$

$$E_z = -E_{\max} \left(\frac{(h - x_{pe} - x_t)^2}{(x_{pe} - x_t)^2} + 1 \right)^{-1} = E_{sc,\max} \quad (5-95)$$

$$E_{sc,z} = E_{sc,\max} \left(\frac{(h - x_{pe} - x_t)^2}{(x_{pe} - x_t)^2} + 1 \right)^{-1} \quad (5-96)$$

$$= \left[v_{nt,dyn} \pi (d_p + x_{sc} \tan \theta_s) \frac{x_{sc}}{\cos \theta_s} + v_{nt,dyn} \frac{\pi d_p^2}{4} \right] \alpha_2 \frac{Vol_{sc}}{A_{sc}}$$

where, $E_{sc,z}$ is the scabbing energy at z_{ct} point (N-mm); $E_{sc,\max}$ is the maximum energy on contact point (N-mm); z_{ct} is the distance from a contact point along z -direction (mm); a_{ct} is the radius of the contact area (mm); h is the thickness of reinforced concrete panel (mm); x_{pe} is the penetration depth (mm); x_t is the

tunneling depth (mm); $v_{nt,dyn}$ is the shear stress controlled by tension under the dynamic loading (MPa); d_p is the diameter of the projectile (mm); x_{sc} is the scabbing depth (mm); A_s is the sectional area of reinforcing bar (mm); α_2 is the projectile length factor; Vol_{sc} is the volume of scabbed cone (mm³); and A_{sc} is the area of scabbed cone (mm).

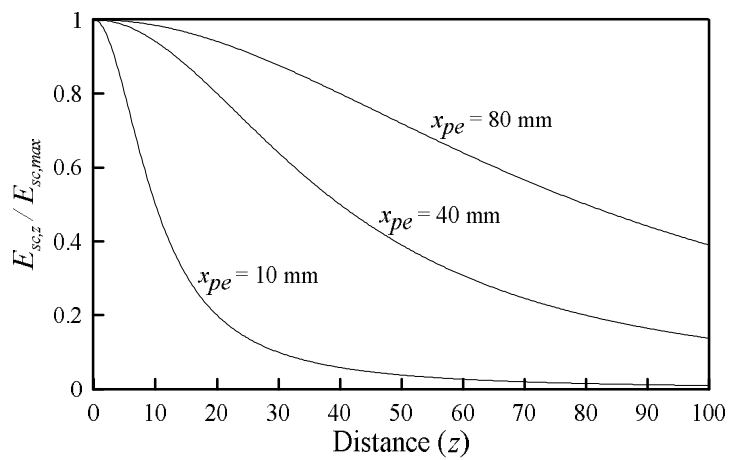


Figure 5-15 Relationship of the distance (z) and the penetration depth (x_{pe})

5.4 Derivation of New Energy-Based Impact Formula

In the previous chapters, each type of energy's value is identified in accordance with a theoretical rationale and codes. By combining these energies based on the energy conservation, the new impact formula for predicting the damage level of a reinforced concrete panel can be derived.

5.4.1 Penetration depth formula

The penetration depth can be determined using energy equilibrium. The kinetic energy (E_K) basically equals the sum of the deformed energy of projectile (E_{DP}), the elastic penetrated energy of the concrete panel (E_{EP}), the overall deformed energy of the slab (E_{SD}) and the spalling-resistant energy of the panel (E_{SP}) as shown in **Eq. (5-97)**, the tunneling-resistant energy (E_T) will be added to **Eq. (5-97)** in special cases. Since the value to be obtained from the impact formula is the penetration depth, the equation of energies can be summarized as shown in **Eq. (5-98)**. If the energy concentration effect ($\alpha_1\alpha_2$) is less than 1, the spalling-resistant energy may exceed the kinetic energy, which does not satisfy the law of conservation of energy. Therefore, when the value of the energy concentration effect is less than 1, the value of the energy concentration effect is set equal to 1 in order to satisfy the law of energy conservation (**Eqs. (5-99) to (5-103)**). In contrast, when the energy concentration effect exceeds 1, E_{SP} is smaller than E_K . As a result, in order to satisfy the law of energy conservation, overflow energy will produce the tunneling depth. Assuming that the cone shape is hemispherical in order to simplify the equation (see **Figure 5-16**), the final penetration depth can be summarized as

shown in Eqs. (5-99) to (5-103). In Eq. (5-88), the tunnel energy is obtained and the tunneling depth can be obtained by summarizing the tunneling depth (x_t) following Eqs. (5-104) to (5-106).

$$E_K = E_{DP} + E_{EP} + E_{SD} + E_{SP} + (E_T) \quad (5-97)$$

$$E_K - E_{DP} - E_{EP} - E_{SD} = E_{SP} \leq E_K \quad (5-98)$$

$$(E_K - E_{DP} - E_{EP} - E_{SD}) = 0.7 f'_{c,dyn} \left[\pi (d + x_{pe} \tan \theta_s) \frac{x_p}{\cos \theta_s} + \frac{\pi d_p^2}{4} \right] \alpha_1 \alpha_2 \frac{V_{sc}}{A_{sp}} \leq E_K \quad (5-99)$$

$$x_{pe} = \sqrt[3]{E_{SP} \frac{6}{8 \times 0.7 \times f'_{c,dyn} \times \alpha_1 \alpha_2 \alpha_3 \times \pi}} \quad (1 \leq \alpha_1 \alpha_2) \quad (5-100)$$

$$\alpha_1 = \left(\frac{V_{imp}}{340} \right)^{0.15} \quad (5-101)$$

$$\alpha_2 = \ln \left(0.8 + \frac{l_p}{d_p} \right) \quad (5-102)$$

$$\alpha_3 = \left(\frac{h}{d} \right)^{0.1} + 0.2 \quad (5-103)$$

$$(E_K - E_{DP} - E_{EP} - E_{SD}) - (E_K - E_{DP} - E_{EP} - E_{SD}) \frac{1}{\alpha_1 \alpha_2} = E_T \quad (5-104)$$

$$E_T = \pi d_p (2x_t^2 + 0.25d_p x_t + x_t^2 N_p \tau_{dyn}) \quad (5-105)$$

$$x_t = \frac{\sqrt{\frac{E_T}{\pi d_p} (2 + N_p \tau_{dyn}) + 0.016 d_p^2} - 0.125 d_p}{2 + N_p \tau_{dyn}} \quad (5-106)$$

where, $f'_{c,dyn}$ is the compressive strength of the concrete affected by the dynamic load;; x_{pe} is the penetration depth (mm); α_1 is the velocity effect factor; α_2 is the projectile length factor; α_3 is the factor related the panel thickness and the diameter of the projectile; d_p is the diameter of the projectile (mm); x_t is the length of the tunnel (mm); N_p is the nose shape factor; τ is the bond stress (MPa); and M_p is the mass of the projectile (kg).

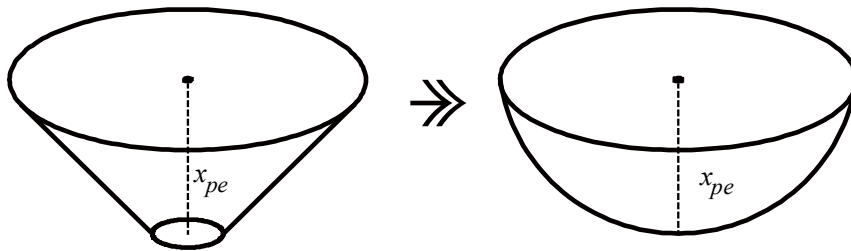


Figure 5-16 Idealized spalled cone

5.4.2 Scabbing depth formula

Scabbing depth (x_{sc}) can be obtained using the scabbing-resistant energy (see **Eq. (5-107)**). When the scabbed cone shape is assumed to be hemispherical, **Equation (5-107)** is rearranged with respect to scabbing depth as in **Eqs. (5-108)** and **(5-109)**.

$$\begin{aligned}
E_{sc,z} &= E_{sc,max} \left(\frac{(h - x_{pe} - x_t)^2}{(x_{pe} - x_t)^2} + 1 \right)^{-1} \\
&= \left[v_{nt,dyn} \pi (d_p + x_{sc} \tan \theta_s) \frac{x_{sc}}{\cos \theta_s} + v_{nt,dyn} \frac{\pi d_p^2}{4} \right] \alpha_2 \frac{Vol_{sc}}{A_{sc}}
\end{aligned} \tag{5-107}$$

$$x_{sc} = \sqrt[3]{\frac{E_{sc,z} \times 6 \times \alpha_2}{8 \times v_{nt,dyn} \times \pi}} \tag{5-108}$$

$$\alpha_2 = \ln \left(0.8 + \frac{l_p}{d_p} \right) \tag{5-109}$$

where, $E_{sc,z}$ is the scabbing energy at z_{ct} point (N-mm); $E_{sc,max}$ is the maximum energy on contact point (N-mm); h is the thickness of reinforced concrete panel (mm); x_{pe} is the penetration depth (mm); x_t is the tunneling depth (mm); $v_{nt,dyn}$ is the shear stress controlled by tension under the dynamic loading (MPa); d_p is the diameter of the projectile (mm); x_{sc} is the scabbing depth (mm); A_s is the sectional area of reinforcing bar (mm); θ_{sc} is the angle of the scabbed cone (degree); Vol_{sc} is the volume of scabbed cone (mm³); A_{sc} is the area of scabbed cone (mm); and α_2 is the projectile length factor.

5.4.3 Scabbing limit thickness formula

Equation (5-95) converges to zero as the distance (z) from the collision point is deeper, but it does not reach 0. At this time, partial reflected energy would offset E_{EP} and E_{SD} , because the overall deformed and elastic penetrated slab will be to return to normal. The remaining thickness ($h - x_{pe} - x_t$) for prevent scabbing

phenomenon can be able to absorb the remained energy that subtracts E_{EP} and E_{SD} from E_{SP} as shown in **Eq. (5-110)**. However, E_{EP} and E_{SD} cannot be calculated because the slab thickness is unknown. Since the energies consumed by E_{EP} and E_{SD} are not large, it is neglected here in **Eq. (5-111)**. As mentioned above, the equation converges but does not reach zero, so the appropriate lower limit value should be presented. Here, the lower limit assumes 5% of E_{SC} . The 5% of remaining energy is expected to be consumed by cracks in the rear face of a reinforced concrete panel. Therefore, the value of h in **Eq. (5-112)** can be summarized as **Eq. (5-113)**, where h is equal to the scabbing limit thickness (h_{sc}).

$$E_{SP} - E_{EP} - E_{SD} = E_{SC,remain} \quad (5-110)$$

$$E_{SP} = E_{SC,remain} \quad (5-111)$$

$$E_{sc} \left(\frac{(h - (x_{pe} + x_t))^2}{(x_{pe} + x_t)^2} + 1 \right)^{-1} = E_{sc,remain} = 0.05E_{SP} \quad (5-112)$$

$$h = h_{sc} = 5.36(x_{pe} + x_t) \quad (5-113)$$

where, E_{SP} is the spalling resistant energy (N-mm); E_{EP} is the elastic penetrated energy (N-mm); E_{SD} is the overall deformed energy of panel (N-mm); $E_{SC,remain}$ is the remaining energy (N-mm) to be absorbed in the panel; E_{SC} is the scabbing resistant energy (N-mm); h is the thickness of the panel (mm); x_{pe} is the penetration depth (mm); h_{sc} is the scabbing limit thickness (mm); and x_t is the tunneling depth (mm).

5.4.4 Perforation limit thickness formula

A perforation can occur when the sum of penetration depth (x_{pe}), tunneling depth (x_t) and scabbing depth (x_{sc}) exceeds the panel thickness as shown in **Figure 5-17**. Therefore, in this study, the perforation limit thickness (h_{pf}) can be obtained as the sum of x_{pe} , x_t and x_{sc} as shown in **Eq. (5-114)**.

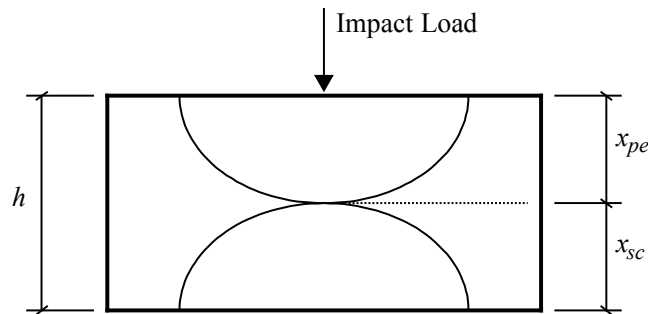


Figure 5-17 Perforation definition in this study

$$h_{pf} = x_{pe} + x_t + x_{sc} \quad (5-114)$$

where, h_{pf} is the perforation limit thickness (mm); x_{pe} is the penetration depth (mm); x_t is the tunneling depth (mm); and x_{sc} is the scabbing depth (mm).

Like the scabbing limit thickness, the perforation limit thickness should calculate the thickness of a reinforced concrete panel to prevent the perforation. The elastic penetrated energy (E_{EP}) and overall deformed energy (E_{SP}), which can be obtained only by knowing the thickness of a reinforced concrete panel, should be neglected. When calculating the penetration depth, tunneling depth, and scabbing depth required in **Eq. (5-114)**, only the energy measured by not considering E_{EP} and E_{SP} should be used.

5.5 Verification of Developed Impact Formula

In this Section, the validity of the proposed impact formulae will be verified using the previous experimental studies conducted by other researchers and new experimental data from **Chapter 4**. The proposed impact formula is analyzed and compared to existing impact formulae and experimental results. In addition, the new impact formula will analyze each variable in detail to determine its range of applicability. Finally, the proposed formula will be tested for applicability to certain buildings and flying objects.

5.5.1 Comparison between test results and predictions

A total of 24 existing impact formulae are summarized and reviewed in **Chapter 2**. Some of them have similar formulations or require further research. Therefore, some representative formulae such as the modified NDRC, ACE, Hughes, Haldar, UKAEA, UMIST, Li-Chen impact formulae will be used to compare the degree of accuracy with which it predicts penetration depth, scabbing limit thickness, and perforation limit thickness. Regarding the evaluation of the proposed formula, 230 experimental results conducted by others researchers and 200 experimental results obtained from these experimental programs (first, second and third programs corresponding to **Chapter 4**) are used. The data by Forrestal *et al.* (1994), Forrestal *et al.* (1996), Frew *et al.* (1998), Forrestal *et al.* (2003), Zhang *et al.* (2005), Almusallam *et al.* (2013), Soe *et al.* (2013), and Abdel-Kader and Fouda (2014) were introduced in **Chapter 2** and summarized in **Table 5-1** according to the parameters. The total number of specimens is 404, and the

diameter of the projectile (d_p) ranges from 20 to 76 mm; the length of projectile (l_p) ranges from 24 to 531 mm; the mass of the projectile (M_p) ranges from 15 ~ about 13000 g (13 kg); the impact velocity (V_{imp}) ranges from 91 ~ 1358 m/s; the concrete compressive strength (f'_c) ranges from 26 ~ 237 MPa; the concrete slab thickness (h) ranges from 55 ~ 2740 mm; ρ ranges from 0 to 0.75%; and the steel fiber volume fraction (V_f) ranges from 0.5 to 2.33%. Of the many experimental data, only general impact experiment data were used, where the general impact experiment involves a solid projectile colliding with a concrete panel, which is reinforced with reinforcing bars at the top and/or bottom. Therefore, only the experimental results corresponding to these conditions are used. Some experimental results having special condition such as multiple reinforcing layers, steel plates, and inside-hollow projectile were excluded. Since the concrete failure mechanism is very complex, it is difficult to conclude that a single parameter is the one and only factor affecting the impact resistance. By analyzing the experimental results according to each major parameter, the application range of the new proposed formula will be determined.

Table 5-1 Summary of previous test and current test programs

Test	Projectile					Concrete panel			
	d_p	l_p	M_p	V_{imp}	N_p	f'_c	h	V_f	$\rho_{steel}(\%)$
Abdel-Kader and Fouda (2014)	23	64	175	201 ~ 354	Blunt	26	100	-	0.4
Almusallam <i>et al.</i> (2013)	40	115	800	91 ~ 135	Sharp	29 ~ 71	90	0 ~ 0.9	0.75
Soe <i>et al.</i> (2013)	13	24	15	306 ~ 658	Ogive	45 ~ 90	55	0, 2.33	
Frew <i>et al.</i> (2006)	76	531	about 13000	164 ~ 335	Ogive	23	910 ~ 1830		
Zhang <i>et al.</i> (2005)	12.6	24	15	620 ~ 704	Ogive	45 ~ 237	150	0, 1.5	
Forrestal <i>et al.</i> (2003)	76	531	about 13000	200 ~ 448	Ogive	23, 39	1220 ~ 1830	-	
Frew <i>et al.</i> (1998)	20, 31	203, 305	478, 1600	442 ~ 1225	Ogive	58	940 ~ 3050		
Forretal <i>et al.</i> (1996)	20, 31	203, 305	478, 1600	405 ~ 1358	Ogive	51, 63	910 ~ 2740		
Forrestal <i>et al.</i> (1994)	27	242	906	277 ~ 800	Ogive	32 ~ 108	760 ~ 1830	-	
This study (first test)	20	20	33	270, 350	Hemisphere	29 ~ 42	30 ~ 70	0.5 ~ 2.0	
This study (second test)	20	20 ~ 40	33 ~ 90	95 ~ 200	Hemisphere Sharp	41 ~ 103	50 ~ 100		
This study (third test)	20	20	33	200	Hemisphere	168	10 ~ 30	1.5	
Total	20 ~ 76	20 ~ 531	15 ~ 13000	91 ~ 1358	Ogive, Blunt, Sharp Hemishpere	26 ~ 237	55 ~ 2740	0 ~ 2.33	

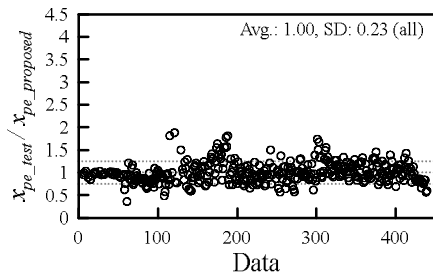
d_p is the diameter of the projectile (mm); l_p is the length of the projectile (mm); M_p is the mass of the projectile (kg); V_{imp} is the impact velocity of the projectile (m/s); N_p is the nose shape of the projectile; f'_c is the compressive strength of the concrete (MPa); h is the thickness of the concrete panel target (mm); V_f is the steel fiber volume fraction (%); ρ_{steel} is the bottom reinforcing ratio in bd for each face; b_{panel} is the width of the specimens (mm); and d_{panel} is the average effective depth (mm).

5.5.2 Penetration depth assessment

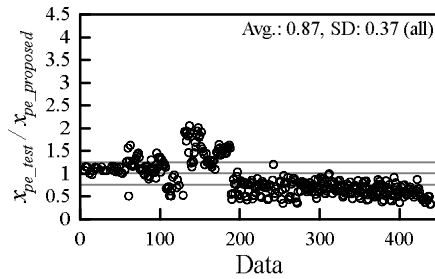
The tested penetrated depth to the predicted penetration depth ratios are compared in **Figure 5-18** and **Table 5-2**, where the proposed formula, modified NDRC, ACE, Haldar, Hughes, UKAEA, UMIST and Li-Chen formulae are applied. The experimental results in **Figure 5-18** are not classified according to specific conditions. The penetration depths of the perforated specimens were also used. In the **Table 5-2**, the data include the specimens in which the penetration depth was measured, a total of 402 specimens are used to verify the validity. The overall average ratios are found to be 1.00, 0.87, 0.85, 1.2, 0.74, 1.13, 1.97 and 1.36, when the proposed formula, modified NDRC, ACE, Haldar, Hughes, UKAEA, UMIST and Li-Chen formulae are used, respectively. Even if the overall average ratio for each formula seems to be good, the average value in each test is varied (**Table 5-2**).

Table 5-2 Average ratio of tested to predicted penetration

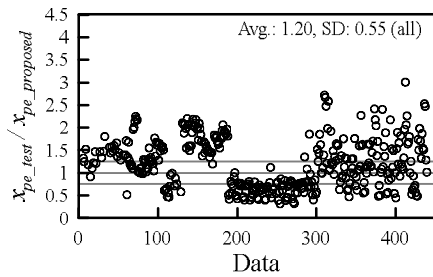
Test (Data No.)	Data (ea)	Proposed formula	Modified NDRC	ACE	Halar	Hughes	UKAEA	UMIST	Li-Chen
Abdel-Kader and Fouda (2014)	7	0.76	0.62	0.56	0.57	0.60	0.64	0.69	1.78
Almusallam <i>et al.</i> (2013)	24	0.97	1.09	1.09	1.40	1.01	1.36	3.17	0.84
Soe <i>et al.</i> (2013)	16	1.23	0.77	0.91	0.80	0.58	0.80	1.12	1.27
Frew <i>et al.</i> (2006)	7	1.03	1.85	1.50	2.01	1.87	1.88	1.87	0.48
Zhang <i>et al.</i> (2005)	33	0.86	1.13	1.35	1.31	0.78	1.16	1.88	1.04
Forrestal <i>et al.</i> (2003)	15	0.88	1.62	1.34	1.89	1.63	1.64	1.67	0.58
Frew <i>et al.</i> (1998)	18	1.35	1.59	1.55	1.81	1.41	1.53	1.65	0.91
Forretal <i>et al.</i> (1996)	18	1.06	1.29	1.27	1.54	1.19	1.30	1.33	1.06
Forrestal <i>et al.</i> (1994)	17	0.88	1.27	1.18	1.57	1.13	1.28	1.27	1.08
This study (first test)	86	0.95	0.68	0.71	0.63	0.55	0.76	1.50	1.69
This study (second test)	149	1.06	0.65	0.59	1.22	0.53	1.12	2.32	1.47
This study (third test)	12	0.76	0.42	0.31	1.70	0.29	1.59	2.69	2.31
Total	402	1.00	0.87	0.85	1.20	0.74	1.13	1.97	1.36



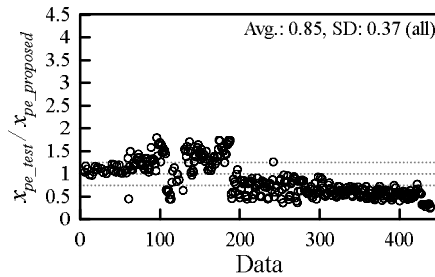
(a) Proposed formula



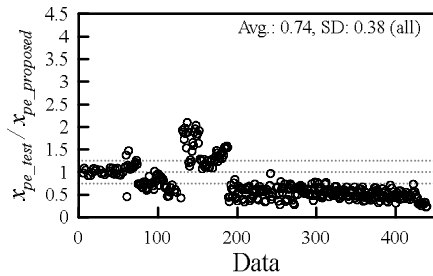
(b) Modified NDRC



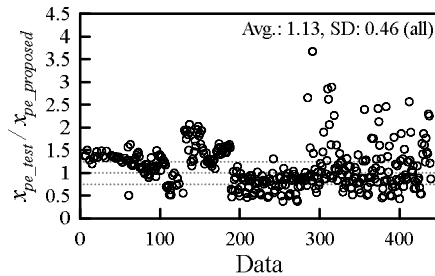
(c) ACE formula



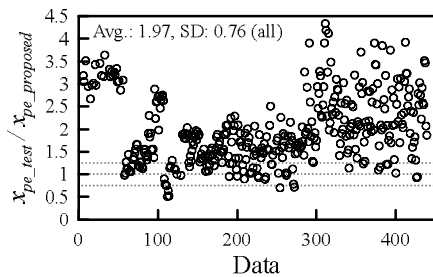
(d) Haldar formula



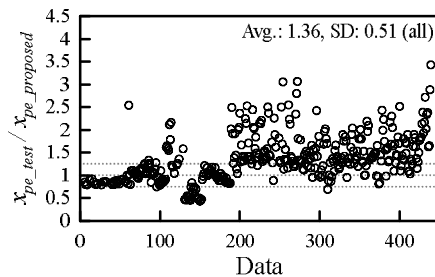
(e) Hughes formula



(f) UKAEA formula



(g) UMIST



(h) Li-Chen formula

Figure 5-18 Ratio of tested to predicted penetration depth (Avg. is the average and SD is the standard deviation)

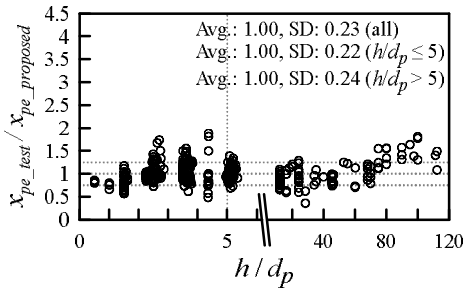
The proposed impact formula predicts the average value well as being 1.0. However, the test results of Abdel-Kader and Fouda (2014) are predicted to be 0.76 and those of Frew *et al.* (1998) to be 1.35. However, the proposed formula is closer to 1 than other formulae, which means that the proposed formula is better. Unfortunately, the data of Abdel-Kader and Fouda (2014) and Frew *et al.* (1998) were respectively seven and eighteen. If there were more test specimens, the average predicted value might to be closer to 1. Other experimental results are predominantly close to 1. The more the data, the closer it gets to 1.

The modified NDRC formula overestimates the depth of penetration as a whole. The results of experiments with small diameter-to-thickness values are particularly underestimated. The ACE formula also overestimates the penetration depth as a whole, and the trend is similar to the modified NDRC. The Haldar and Hughes formulae are very similar and the trend of the ratios of tested to predicted penetration depth is similar up to the first test. For the second and third experiments, the Haldar formula is predicted to be 1.2 and above. However, the Hughes formula overestimates, as in the first test, and its trend is similar to the modified NDRC and ACE formulae. The Haldar formula looks better considering overall average ratios of tested to predicted penetration depth, but the Hughes formula predicts consistently for each test, so it appears to be the better formula. The UKAEA formula shows a similar trend to the Haldar formula, predicting better results for these test programs. The UMIST underestimates the predicted penetration depth as a whole, and the data points in **Figure 5-18(g)** are scattered widely, so it presents that there is no other inconsistency in each of the experiments. The ratios of tested to predicted penetration depth by Li-Chen formula is close to be 1.36, which slightly underestimates the penetration depth, but shows close to 1

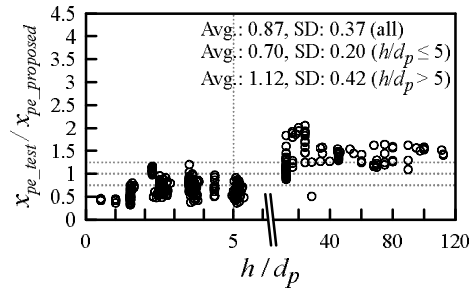
in all of the experiments.

5.5.2.1 Penetration depth assessment according to thickness to diameter of projectile

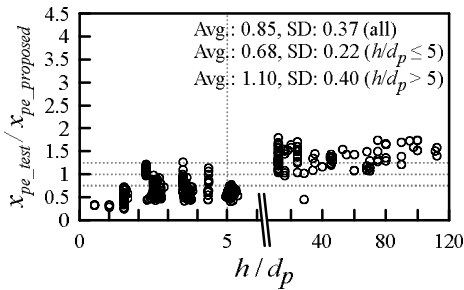
In order to find the application range of a new impact formula according to the thickness (h) to the diameter of projectile (d_p), the ratios of tested to predicted penetration depth are classified according to the ratio of the slab thickness (h) to the diameter of the projectile (d_p) as shown in **Figure 5-19**. The classification of experimental results using the ratio of two parameters is a method that has been used many times in other researcher' impact studies (Hughes, 1984; Li *et al.*, 2005). The Hughes impact formula is conservative when the ratio of h to d_p is less than 3.5, because the elastic and global effects of the reinforced concrete panel are neglected. The UMIST and Li-Chen formulae suggested that the reference ratio of h to d_p was 5 (described in **Chapter 2**). Therefore, the ratio of 5 for h to d_p is as a reference ratio for evaluating the impact formulae in this chapter, and the additional line representing the ratio of 5 is added to **Figure 5-19**.



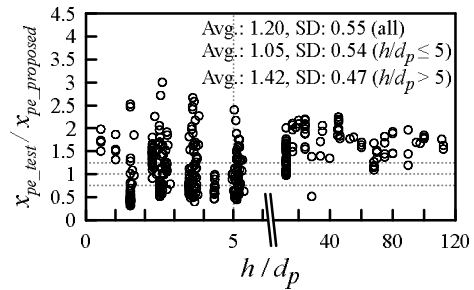
(a) Proposed formula



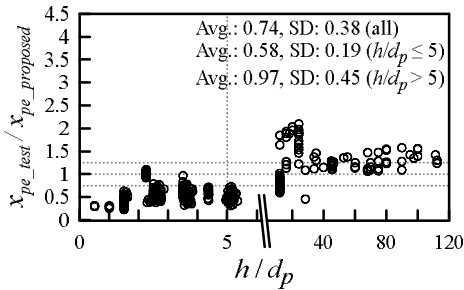
(b) Modified NDRC



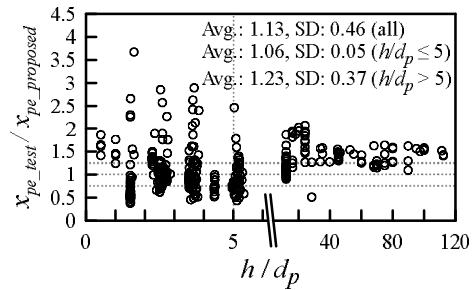
(c) ACE formula



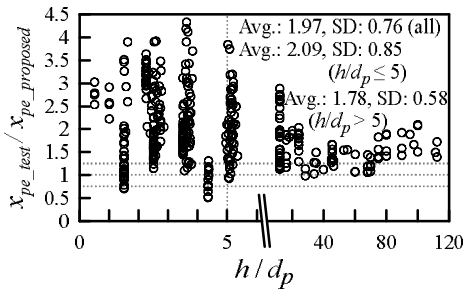
(d) Haldar formula



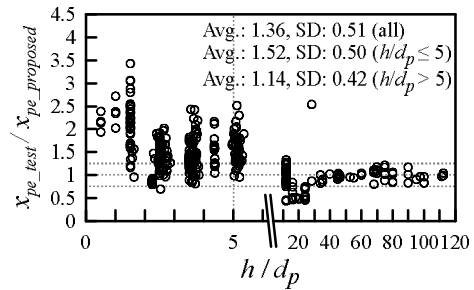
(e) Hughes formula



(f) UKAEA formula



(g) UMIST



(h) Li-Chen formula

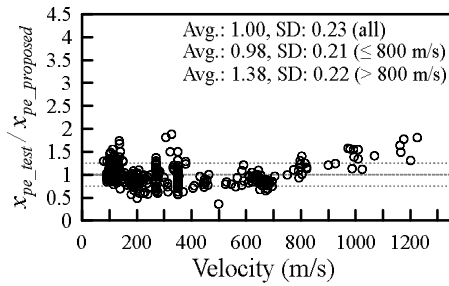
Figure 5-19 Ratio of tested to predicted penetration depth according to h to d_p (Avg. is the average and SD is the standard deviation)

The modified NDRC, ACE, Hughes, and UKAEA formulae overestimate penetration depth when the ratio of h to d_p is less than 5, while the UMIST formula underestimates this. The Li-Chen formula slightly underestimates penetration depth when the ratio of h to d_p is between 2 and 5, and greatly underestimates it when the ratio of h to d_p is less than 2. The Haldar formula underestimates penetration depth in all cases. The modified NDRC, ACE, Haldar, Hughes, UKAEA and UMIST formulae underestimate penetration depth when the ratio is more than 5, and they are consistent. However, the proposed formula performs well overall (**Figure 5-19(a)**), though it slightly underestimates penetration depth when the ratio of h to d_p is more than 60. As mentioned in the Hughes study (1984), this study reaffirms that the previous formulae overestimate penetration depths when the ratio of h to d_p is low. The proposed formula consistently predicts penetration depths of various plain concrete, reinforced concrete and SFRC panels.

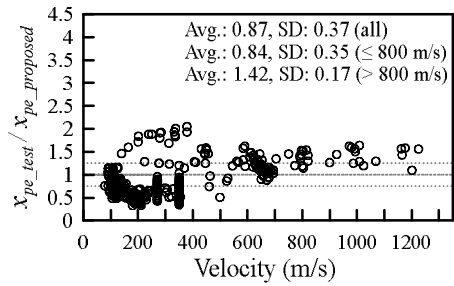
5.5.2.2 Penetration depth assessment according to impact velocity

In order to find the application range of a new impact formula according to the impact velocity (V_{imp}), the ratios of tested to predicted penetration depth are classified according to the impact velocity as shown in **Figure 5-20**. The modified NDRC, ACE and Hughes formulae present similar trends, the ratio of the tested to the predicted penetration depth tends to increase as the impact velocity increases. The Haldar and UKAEA formulae also present a similar trend. The data points are scattered widely under 200 m/s. This means that the accuracy of a prediction was lower. However, the accuracy of Haldar and UKAEA formulae was similar to the modified NDRC, ACE, and Hughes formula over 200 m/s. The accuracy of UMIST

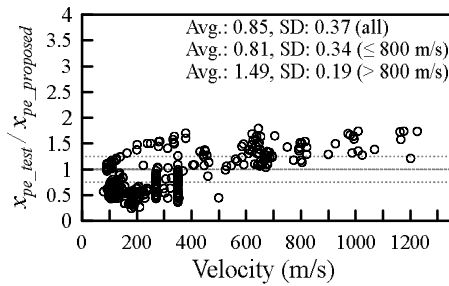
formula is poor as whole. When an experimental parameter goes beyond the verified range for $3 < V_{imp} < 66.2$ m/s (Li *et al.*, 2005), the accuracy appears to be low. Regarding the Li-Chen formula, its accuracy below 800 m/s is not good with a ratio value of 1.38, despite being very good at velocities of more than 800 m/s with a ratio value of 0.99. The proposed formula shows the best accuracy with an average of 0.99 at impact velocities of less than 800 m/s. However, above 800 m/s, the average accuracy is 1.38, the third highest.



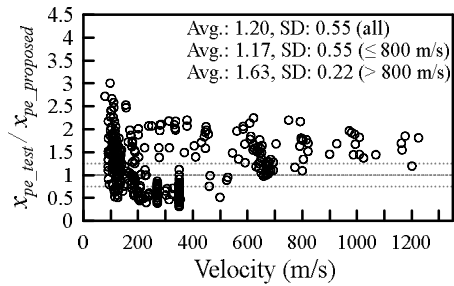
(a) Proposed formula



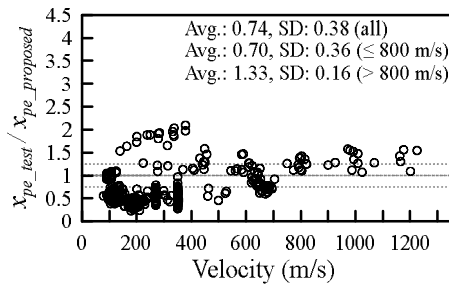
(b) Modified NDRC



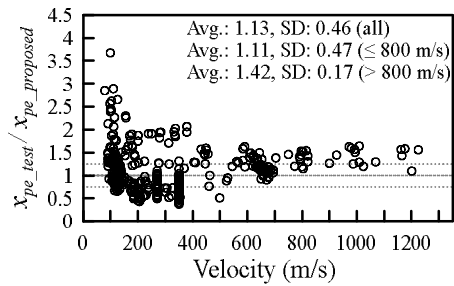
(c) ACE formula



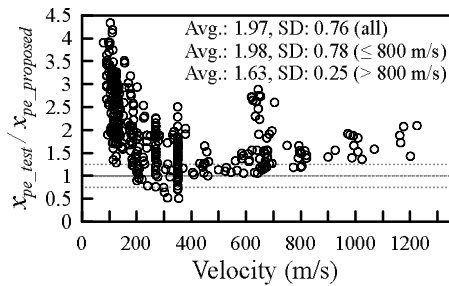
(d) Haldar formula



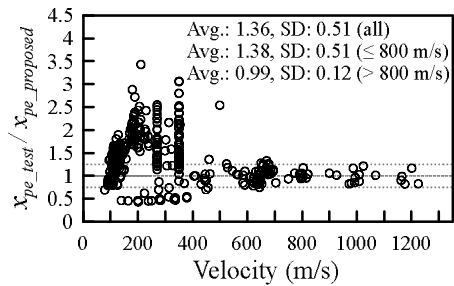
(e) Hughes formula



(f) UKAEA formula



(g) UMIST



(h) Li-Chen formula

Figure 5-20 Ratio of tested to predicted penetration depth according to velocity (Avg. is the average and SD is the standard deviation)

5.5.2.3 Penetration depth assessment according to concrete strength

In order to find the application range of a new impact formula according to concrete's compressive strength, the ratios of tested-to-predicted penetration depths are classified according to the concrete's compressive strength as shown in **Figure 5-21**. The proposed formula performs well overall. The accuracy is 0.99 in concrete with a compressive strength of less than 80 MPa, and the accuracy is 1.02 when the compressive strength is more than 80 MPa. The modified NDRC, ACE, and Hughes formulae show similar trends with respect to this parameter, given that they have good accuracy for concrete with a compressive strength of less than 80 MPa. However, at more than 80 MPa, the accuracy of the modified NDRC, ACE, and Hughes formulae are 0.74, 0.72, and 0.57, respectively. This is evidence that the characteristics of impact resistance of high strength concrete are not reflected properly by these formulae. The Haldar and UKAEA formulae exhibit good prediction below 80 MPa, but both underestimate observed results when the concrete compressive strength is more than 80 MPa. The UMIST formula is much less accurate over the entire range. A trend of the Li-Chen formula line is similar to the UMIST formula, but its accuracy is better than that of the UMIST formula. Most of all, the proposed formula consistently predicts the penetration depth for varied concrete strength, with greatest accuracy.

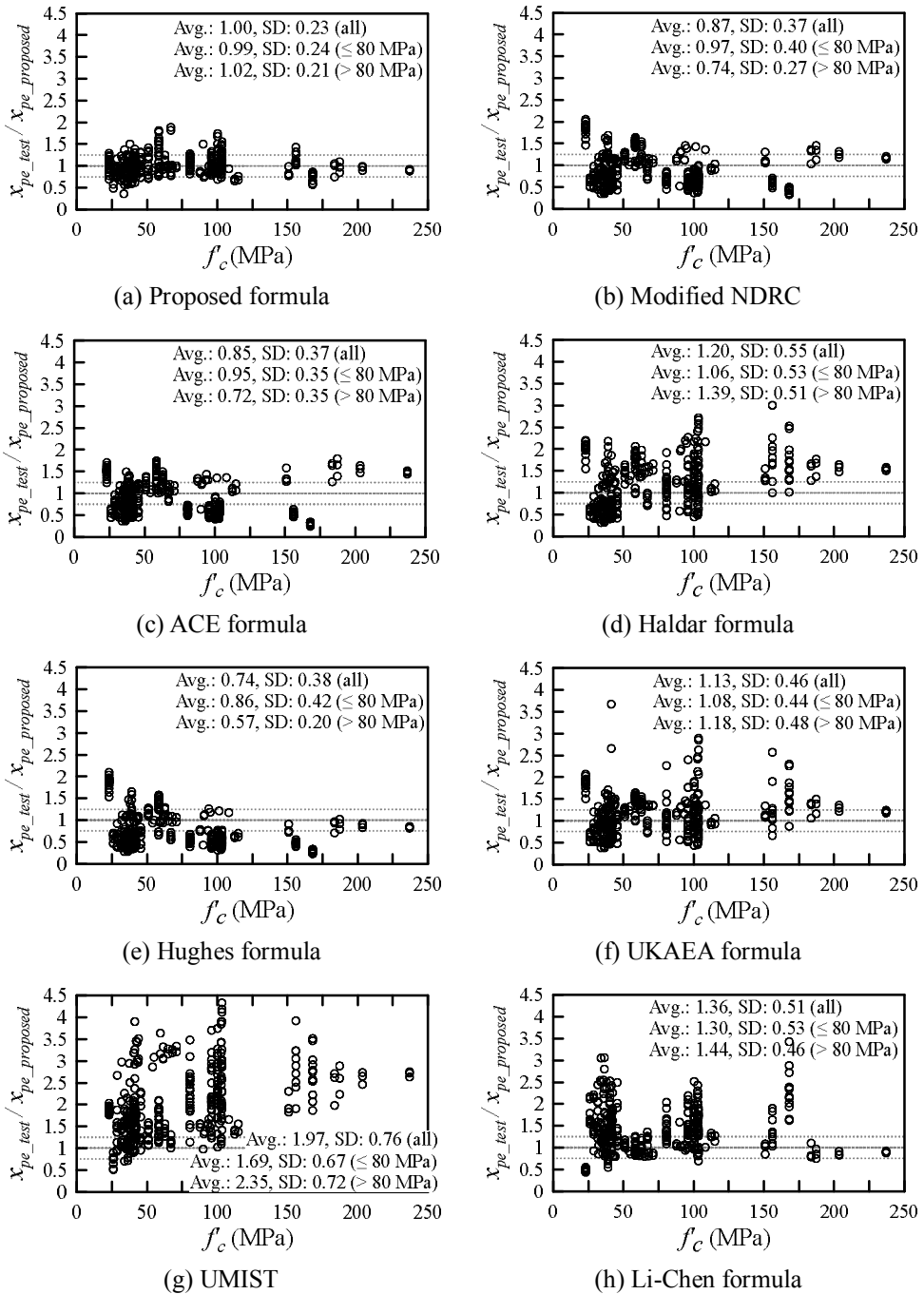


Figure 5-21 Ratio of tested to predicted penetration depth according to concrete compressive strength (Avg. is the average and SD is the standard deviation)

5.5.2.4 Penetration depth assessment according to kinetic energy per contact area

In order to find the application range of a new impact formula according to kinetic per contact area, the ratios of tested-to-predicted penetration depths are classified according to kinetic energy per contact area (**Figure 5-22**), where the contact area term is $(d_p N_p)^2$. Since the projectiles differ by diameter, length, and shape, kinetic energy per contact area $(E_K/(d_p N_p)^2)$ is used to integrate and compare different projectiles. The kinetic energy per contact area $(E_K/(d_p N_p)^2)$ is similar to G -function or impact factor.

The proposed formula exhibits excellent predictions well when The kinetic energy per contact area was lesser 10×10^6 N-mm/mm². In view of this parameter, the modified NDRC, ACE and Hughes formulae also exhibits similar trends, but the ACE formula exhibits better good prediction over 10×10^6 N-mm/mm². When the range is under 10×10^6 N-mm/mm², they have almost the same data distribution as shown in the **Figure 5-22(b)**, **Figure 5-22(c)** and **Figure 5-22(e)**. The Haldar and UKAEA formulae exhibit similar distributions in figures. The accuracy of the UMIST formula is not good in low projectile energy concertation, but the accuracy improves as that increases. The Li-Chen formula shows that the ratios of the tested to predicted penetration depth are 1 to 1.6 when the projectile energy concertation is below 10×10^6 N-mm/mm². The Li-Chen formula only offers good accuracy when the projectile energy concertation is over 10×10^6 N-mm/mm².

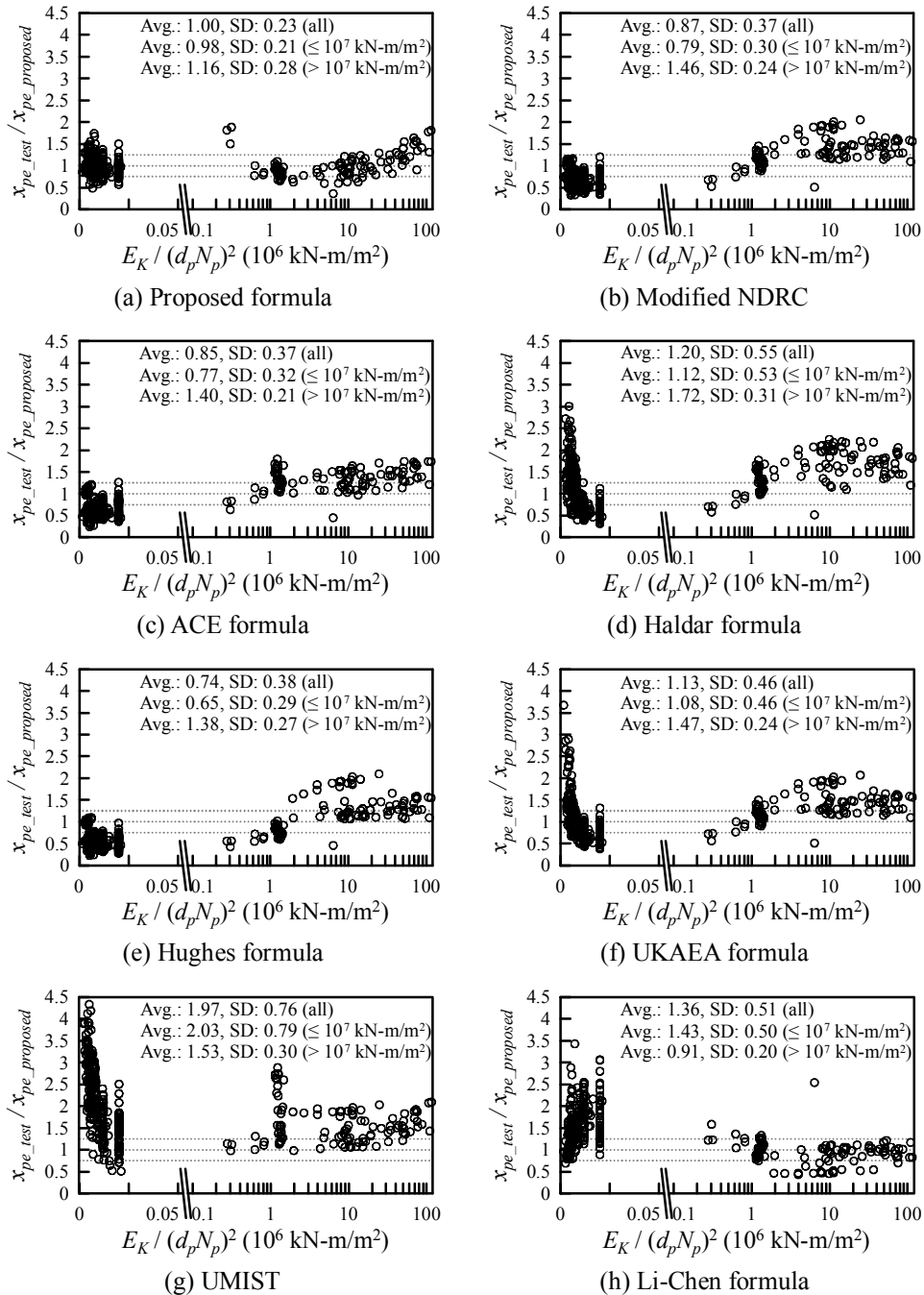


Figure 5-22 Ratio of tested to predicted penetration depth according to kinetic energy per contact area (Avg. is the average and SD is the standard deviation)

5.5.3 Scabbing depth assessment

As mentioned in **Section 5.4**, there is no formula which predicts the scabbing depth which is a failure on a rear face of the concrete panel. In this chapter, the new proposed scabbing depth formula will be verified using the experimental results. Unfortunately, there is little experimental data on scabbing depth, since a penetration depth and penetration were the main objectives in impact studies. Of the data obtained by other researchers' experiments and the current program in **Table 5-1**, a total of 81 specimens were measured for scabbing depth, and the ratios of tested to predicted scabbing depth are shown in **Figure 5-23**.

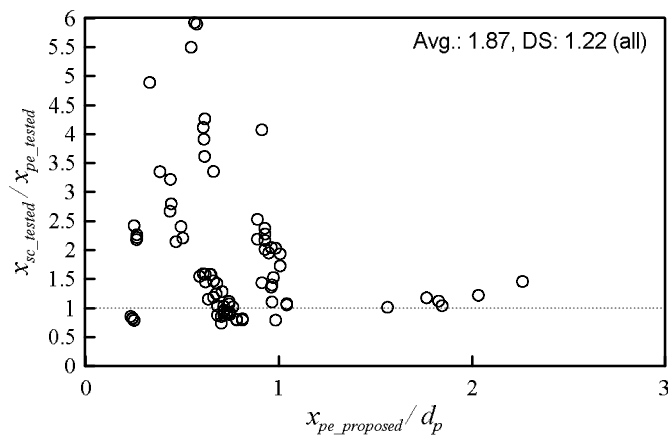


Figure 5-23 Ratio of tested to predicted scabbing depth

The minimum ratio of the tested to predicted scabbing depth is 0.74 and maximum ratio is 5.92. The 52 of the 81 specimens are predicted at a ratio of 2 or less and their average is 1.16. The number of specimens with a ratio of 2 or more is 29, and their average is 3.14 (**Table 5-3**). The accuracy is lower than that of the penetration depth prediction formula. Similar penetration depths are observed in

the impact experiments with similar conditions. However, the scabbing depths are not similar even under the same conditions. **Figure 5-24** shows the ratios of tested scabbing depth to the tested penetration depth. Most of the ratios are scattered below 2.5, but for some specimens observed to be more than 3, and the maximum value is about 5. In other words, it can be seen that it is quite difficult to predict the scabbing depth. Since the reflected energy may be amplified depending on the reflection angle and the properties of materials in the concrete matrix, it is not easy to predict the reflected energy accurately. Despite these difficulties, it seems that the scabbing depth prediction formula presented in this study predicts quite well.

Table 5-3 Number of specimens with scabbing failure

Ratio range	Number of specimens	Average ratio
Under 1	19	0.85
Under 1.5	43	1.05
Under 2	52	1.16
Over 2	29	3.14

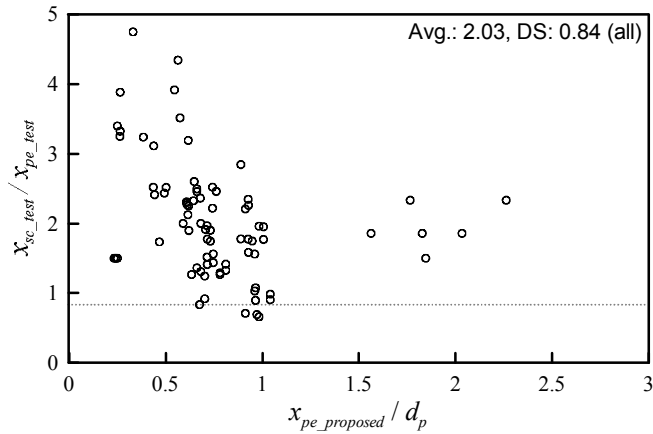


Figure 5-24 Ratio of tested penetration depth to scabbing depth

5.5.4 Scabbing limit thickness assessment

Based on the Hertzian contact theory, the new scabbing limit thickness formula is proposed. The thickness required to absorb the spalling and tunneling energy of 95% was suggested in Chapter 4. **Figure 5-25** shows the panel thickness (h) divided by the predicted scabbing limit thickness (h_{sc}) based on the new proposed formula. The modified NDRC, Hughes and UKAEA formulae are the formulae which predict the penetration depth well as shown in the previous section. Only the experimental results from the current test program described in **Chapter 4** are used for the analysis of scabbing limit thickness, because all other experimental results in other pieces of research presented unclear scabbing depth and scabbing failures.

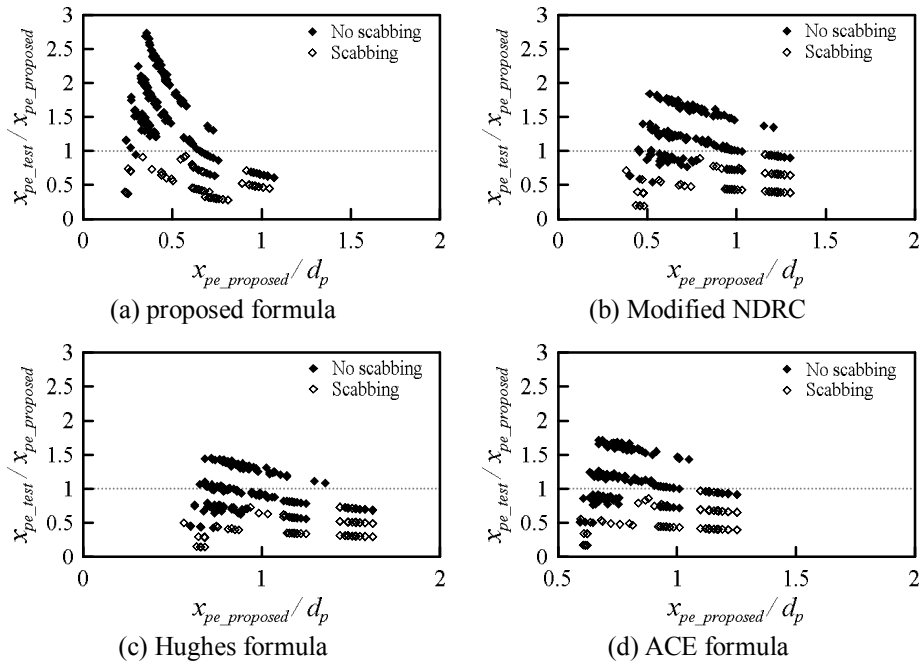


Figure 5-25 Panel thickness (h) divided by predicted scabbing limit thickness (h_{sc})

In **Figure 5-25**, the specimen with the scabbed failure is supposed to lie below 1 (Williams, 1994). **Table 5-4** shows the accuracy of the scabbing limit thickness formula. The four formulae predict such that all specimens have the scabbing failure. However, each formula shows different prediction results in which the specimens should not scab on the rear face of the concrete panel. The proposed scabbing limit thickness formula predicts such that 139 specimens would not have scabbing failure. No scabbing failure was observed in 172 specimens, and the proposed formula is about 81% accurate. Thirty-three specimens are predicted to have the scabbing failure, but did not occur. The NDRC, Hughes and ACE formulae are 66, 43, and 66% accurate, respectively. Therefore, the scabbing limit thickness formula proposed in this study turns out to be the most accurate.

Table 5-4 Accuracy of scabbing limit thickness formula

Formula	Scabbing failure (predicted / tested)	No scabbing failure (predicted / tested)
Proposed	100% (75 of 75 specimens)	81% (139 of 172 specimens)
Modified NDRC	100% (75 of 75 specimens)	66% (113 of 172 specimens)
Hughes	100% (75 of 75 specimens)	43% (74 of 172 specimens)
ACE	100% (75 of 75 specimens)	66% (113 of 172 specimens)

5.5.5 Perforation limit thickness assessment

In **Section 5.4**, the perforation limit thickness formula is newly suggested. The perforation limit thickness proposed in this study is equal to the sum of the penetration depth (x_{pe}), tunneling depth (x_t), and scabbing depth (x_{sc}). In order to verify the new perforation limit thickness formula, only the results of the experiments performed in this study are used in the scabbing limit thickness formula analysis. The modified NDRC, Hughes, and ACE formulae are used for comparison.

In **Figure 5-26**, the specimen with the perforation failure is supposed to lie below 1 (Williams, 1994). **Table 5-5** classifies between the perforated and the non-perforated specimens, and summarizes how many of them fit. The 63 specimens were perforated in the experiments, and the proposed formula got 41 specimens out of the total, with 63% accuracy. Thirty-seven percent of the specimens are

predicted not to perforate, but the perforated failures were observed. On the contrary, the proposed formula predicts that 180 out of 182 specimens would not have the perforated failure, and it is 99% accurate. The ACE formula predicts that 57 of the 63 perforated specimens would perforate, which was about 88% accurate. Six specimens are predicted not to perforate, but were perforated in practice. The ACE formula predicts that 166 out of 182 unperforated specimens would not perforate, it was 91% accurate. The ACE formula has the good accuracy compared with other formulae. From the viewpoint that the perforation limit thickness is calculated to prevent a perforation, the proposed formula predicts with an accuracy rate of 99% that the calculated thickness from the proposed formula can prevent perforation.

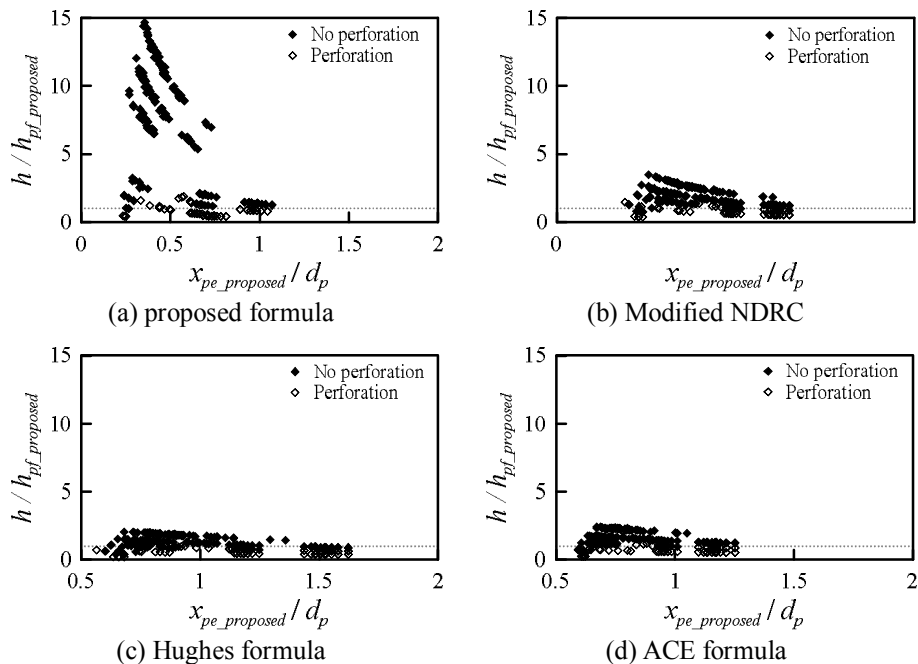


Figure 5-26 Panel thickness (h) divided by predicted perforation limit thickness (h_{pf})

Table 5-5 Accuracy of scabbing limit thickness formula

Formula	Perforation failure	No perforation failure
Proposed	63% (41 of 65 specimens)	99% (180 of 182 specimens)
Modified NDRC	77% (50 of 65 specimens)	93% (170 of 182 specimens)
Hughes	100% (65 of 65 specimens)	67% (125 of 182 specimens)
ACE	88% (57 of 65 specimens)	91% (166 of 182 specimens)

5.6 Critical Impact Mechanism

Table 5-6 shows energy portions for each experiment, while **Figure 5-27** shows the average energy portion for all impact experiments. The deformed energy of the projectile accounted for 0.1 ~ 7.4% of kinetic energy. The elastic penetrated energy of the concrete panel accounted for 0 ~ 3.8% of kinetic energy. The overall deformed energy of the concrete panel accounted for 0 ~ 2.7% of kinetic energy. The average sum of spalling-resistant energy and tunneling-resistant energy accounted for 97.9% of kinetic energy, which was the largest proportion in all experiments. The sum of the spalling-resistant and tunneling-resistant energies is overwhelming, while the other energies are small. In other words, E_{DP} , E_{EP} and E_{SD} can be ignored in the impact mechanism, with E_K being applied only to E_{SP} and E_T . That is, **Eqs. (5-100) to (5-106)** can be modified to **Eqs. (5-115) to (5-119)**.

Table 5-6 Energy Portion

Test (Data No.)	E_{DP}/E_K (%)	E_{EP}/E_K (%)	E_{SD}/E_K (%)	$(E_{SP}+E_T)/E_K$ (%)
Almusallam <i>et al.</i> (2013)	0.3 (0.1 ~ 0.5)	0.7 (0.5 ~ 1.2)	0.1	98.9 (98.1 ~ 99.4)
Forrestal <i>et al.</i> (1994)	0.8 (0.4 ~ 1.3)	0.2 (0.1 ~ 0.3)	0.3 (0.1 ~ 0.6)	98.7 (98.0 ~ 99.2)
Zhang <i>et al.</i> (2005)	3.3 (0.1 ~ 7.4)	0.5 (0.3 ~ 0.9)	0.2 (0.1 ~ 0.3)	95.9 (91.4 ~ 98.7)
Abdel-Kader and Fouda (2014)	0.07 (0.06 ~ 0.08)	0.24 (0.2 ~ 0.28)	0.04 (0.02 ~ 0.06)	99.7 (99.6 ~ 99.7)
Soe <i>et al.</i> (2013)	1.86 (1 ~ 4.2)	0.2 (0.1 ~ 0.5)	0.1 (0.1 ~ 0.3)	97.8 (95.1 ~ 98.8)
Forrestal <i>et al.</i> (2003)	1.6 (0.6 ~ 4.8)	0.2 (0.1 ~ 0.5)	0.2 (0.1 ~ 0.5)	98 (94.8 ~ 99.2)
Frew <i>et al.</i> (2006)	0.9 (0.7 ~ 1.7)	0.2 (0.1 ~ 0.4)	0.1 (0 ~ 0.1)	98.8 (97.9 ~ 99.2)
Forretal <i>et al.</i> (1996)	1.0 (0.8 ~ 1.4)	0.1	0.1 (0 ~ 0.2)	98.8 (98.4 ~ 99.0)
Frew <i>et al.</i> (1998)	1.0 (0.9 ~ 1.3)	0.1 (0 ~ 0.1)	0.1 (0 ~ 0.1)	98.8 (98.5 ~ 99.0)
This study (first test)	0.2	0.4 (0.2 ~ 0.8)	0	99.3 (98.9 ~ 99.6)
This study (second test)	1.2 (0.2 ~ 4.6)	1.9 (0.4 ~ 3.8)	0.1 (0 ~ 0.3)	96.8 (92.2 ~ 99.2)
This study (third test)	2.4 (1.9 ~ 3.1)	1.1 (0.5 ~ 2.1)	0.4 (0.2 ~ 2.7)	96 (94 ~ 97.1)
Total	1.1 (0.1 ~ 7.4)	0.9 (0 ~ 3.8)	0.1 (0 ~ 2.7)	97.9 (91.4 ~ 99.6)

E_K is the kinetic energy (N-mm); E_{DP} is the deformed energy of projectile (N-mm); E_{EP} is the elastic penetrated energy of concrete panel (N-mm); E_{SD} is the overall deformed energy of concrete panel (N-mm); E_{SP} is the spalling-resistant energy (N-mm); E_T is the tunneling-resistant energy (N-mm); E_{SC} is the scabbing-resistant energy (N-mm).

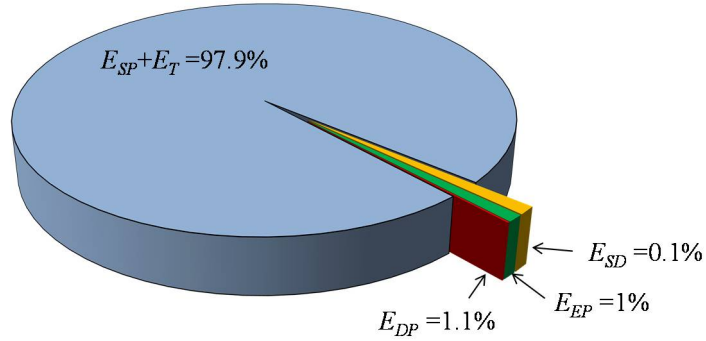


Figure 5-27 Average energy portion

$$\begin{aligned}
 x_{pe} &= \sqrt[3]{\frac{E_K \times 6}{8 \times 0.7 \times f'_{c,dyn} \times \alpha_3 \times \pi}} \\
 &= \sqrt[3]{\frac{0.5357 \times M_p V_{imp}^2}{f'_{c,dyn} \times \alpha_3 \times \pi}} \quad (\text{for } \alpha_1 \alpha_2 \leq 1)
 \end{aligned} \tag{5-115}$$

$$\begin{aligned}
 x_{pe} + x_t &= \sqrt[3]{\frac{E_K \times 6}{8 \times 0.7 \times f'_{c,dyn} \times \alpha_1 \alpha_2 \alpha_3 \times \pi}} \\
 &+ \frac{\sqrt{\frac{(E_K - E_K / \alpha_1 \alpha_2)}{\pi d_p} (2 + N_p \tau_{dyn}) + 0.016 d_p^2 - 0.125 d_p}}{2 + N_p \tau_{dyn}}
 \end{aligned} \tag{5-116}$$

(for $\alpha_1 \alpha_2 > 1$)

$$\alpha_1 = \left(\frac{V_{imp}}{340} \right)^{0.15} \tag{5-117}$$

$$\alpha_2 = \ln \left(0.8 + \frac{l_p}{d_p} \right) \tag{5-118}$$

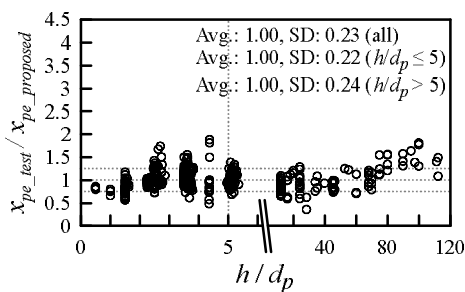
$$\alpha_3 = \left(\frac{h}{d_p} \right)^{0.1} + 0.2 \quad (5-119)$$

where, x_{pe} is the penetration depth (mm); E_K is the kinetic energy (N-mm); $f'_{c,dyn}$ is the compressive strength of the concrete affected by the dynamic load; α_1 is the velocity effect factor; α_2 is the projectile length factor; α_3 is the ratio of thickness of the concrete panel to the diameter of projectile; M_p is the mass of the projectile; V_{imp} is the impact velocity; τ_{dyn} is the bond stress under the dynamic loading; l_p is the length of the projectile; d_p is the diameter of the projectile; h is the target's thickness; and N_p is the nose shape factor.

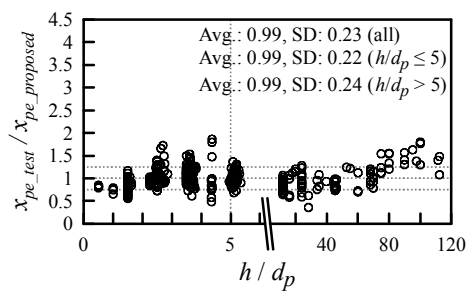
Table 5-7 and **Figure 5-28** compare the average ratios of tested-to-predicted penetration depths using the detailed formula and the simplified formula. The overall average of the detailed formula fell by 0.01, from 1.00 to 0.99, but this can still be considered equal. The standard deviation for both the detailed and simplified formulae was 0.23. It was reconfirmed that no significant difference is observed between the detailed formula and the simplified formula.

Table 5-7 Average ratio of tested to predicted penetration according to proposed and simplified formulae

Test (Data No.)	Data (ea)	Detailed formula	Simplified formula	Test (Data No.)	Data (ea)	Detailed formula	Simplified formula
Abdel-Kader and Fouda (2014)	7	0.76	0.76	Frew <i>et al.</i> (1998)	18	1.35	1.34
Almusallam <i>et al.</i> (2013)	24	0.97	0.96	Forretal <i>et al.</i> (1996)	18	1.06	1.06
Soe <i>et al.</i> (2013)	16	1.23	1.22	Forrestal <i>et al.</i> (1994)	17	0.88	0.88
Frew <i>et al.</i> (2006)	7	1.03	1.02	This study (first test)	86	0.95	0.95
Zhang <i>et al.</i> (2005)	33	0.86	0.84	This study (second test)	149	1.06	1.05
Forrestal <i>et al.</i> (2003)	15	0.88	0.87	This study (third test)	12	0.76	0.75
All avearge	402	1.00	0.99	All standard derivation		0.23	0.23



(a) Detailed formula



(b) Simplified formula

Figure 5-28 Tested to penetration depth by detailed formula and simplified formula

5.7 Potential Application Example

As mentioned in the introduction, many buildings are made of concrete, including private homes, military facilities and special structures (power plants, dams, etc.). There are also various high-velocity flying objects such as conventional weapons (guns, cannons), cars, airplanes, debris propelled by hurricane or tornados, etc. Some concrete structures, such as military facilities, are designed with special codes and guidelines to protect them from military weapons, and there are standards for construction of private concrete structures built for general use such as homes and office buildings. However, flying objects in addition to for conventional weapons may also cause local impact to military facilities. Conversely, conventional weapons can also cause local impact failure to private concrete structures. This relationship can be expressed as shown in **Figure 5-29** using the four-quadrant system.

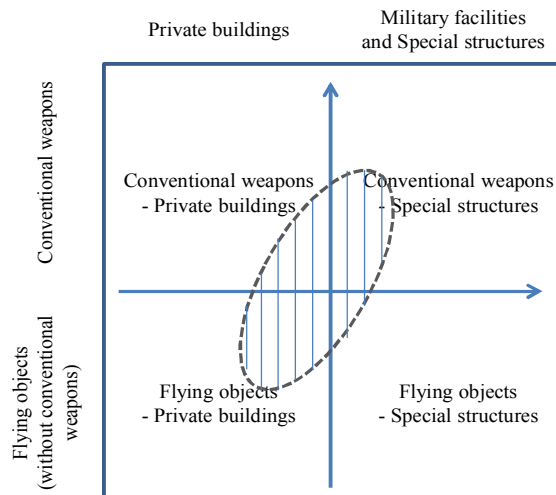


Figure 5-29 Classification of flying objects and concrete structures

Projectiles in experiments conducted by other researchers and these current programs have much in common with conventional military weapons. The experimental projectiles and conventional weapons are both long objects with an ogive nose. The projectiles used in the experiments were steel, which is a non-deformable material. Conventional weapons are manufactured with non-deformable materials like titanium, steel, and iron. Kinetic energies of 500 ~ 2000 J were tested in these experiments, which were similar to the kinetic energy of conventional weapons (**Table 5-8**). From the viewpoint of building type, the concrete panels used in these experiments were non-reinforced concrete panels, or reinforced panels with a low reinforcing ratio. These concrete panels are difficult to compare to special buildings or military facilities designed to meet special design codes or guidelines. Considering the projectiles and concrete panels used in prior experiments, it is appropriate to apply the new impact formula presented in this paper to the hatched area in **Figure 5-29**.

Table 5-8 Characteristics of small arms and aircraft cannon

Caliber	Warhead			
	Shape	Mass (g)	Velocity (m/s)	Kinetic energy (J)
Revolver				
7.62 mm	Ball	3.9 ~ 4.8	290 ~ 457	164 ~ 501
9 mm	Ball	8.1 ~ 10.4	302 ~ 389	369 ~ 787
11.43 mm	ball	13.5 ~ 15.2	250 ~ 259	422 ~ 510
Small-caliber gun				
5.56 mm	Ball, tracer	2.8 ~ 3.6	945 ~ 1015	1250 ~ 1850
7.62 mm	Ball, tracer, armor piercing	4.8 ~ 12.1	421 ~ 878	425 ~ 4660
Machine gun				
7.62 mm	Ball, tracer, armor piercing	9.7 ~ 11.8	816 ~ 869	3230 ~ 4460
12.7 mm	Ball, tracer, armor piercing, armor piercing incendiary	40.2 ~ 46	838 ~ 1067	14100 ~ 26200
14.5 mm	Ball, tracer, armor piercing, armor piercing incendiary	59.6 ~ 63.5	975	28300 ~ 30200
Aircraft cannon				
23 mm	Ball, armor piercing, armor piercing incendiary	200	689	47500
30 mm	Ball, armor piercing, armor piercing incendiary	409.5	780	125,000
37 mm	Ball, armor piercing, armor piercing incendiary	735.5	689	175000
40 mm	Ball, armor piercing, armor piercing incendiary	972	1000	486,000

5.8 Discussion

In this chapter, the impact formula for evaluating the resistance of the concrete panel is derived using various factors. And the new impact formula was verified with impact test results concerning high velocity impact loads, which were conducted by other researchers and the author as in **Chapter 4**. The results of comparisons of impact test results and impact formulae are summarized below:

- 1) There are five types of energy involved in the impact mechanism: the kinetic energy (E_K); the deformed energy of the projectile (E_{DP}); the elastic penetrated energy (E_{EP}); overall deformed energy (E_{SD}); and the spalling-resistant energy of the concrete panel (E_{SP}). In addition, the tunneling-resistant energy (E_T) can occur when the kinetic energy is concentrated by long projectiles and/or high velocity, and the scabbing-resistant energy (E_{SC}) can only occur when the thickness of the panel is not large enough to absorb impact energy.
- 2) The spalled cone is related to shear stress controlled by compression, and the scabbed cone is related to shear stress controlled by tension. These shear stresses have to take into account the strain rate effect, where *fib* Model Code 2010 (*fib*, 2010) is used in this study. The strain rate is defined as the force on nose of the projectile, as suggested by Forrestal *et al.* (1994). The force on the projectile nose was newly-derived using a theoretical background in this study.
- 3) The penetration depth formula is derived using drag force, volume and the area of the spalled cone which lead to an energy density. The spalling

energy can be concentrated by high velocity and/or long projectile, these effects can be applied to the penetration depth formula. The concentrated energy can produce the tunneling depth, which is also derived from the energy density.

- 4) The scabbing depth is derived by using the same concept of the penetration depth based on Hertzian contact theory, but it is not applied with the energy concentration effect by velocity of impact and shape of projectile. The scabbing limit thickness can be obtained from scabbing depth formula. The scabbing limit thickness which is equal to that makes scabbing depth zero.
- 5) The perforation limit thickness can be obtained from the penetration depth, the tunneling depth, and the scabbing depth. The sum of these is the minimum thickness required to prevent a perforation. This is equal to the perforation limit thickness. In order to prevent perforation, the slab thickness should be equal to or greater than the sum of the penetration depth, the tunneling depth, and scabbing depth.
- 6) The accuracy of the new impact formula was examined and compared with existing impact formulae, such as the modified NDRC, ACE, Haldar, UKAEA, UMIST, and Li-Chen formulae. The mean value of the tested penetration depth compared to the predicted penetration depth of the new impact formula was 1, meaning it was the best of these impact formulae. The standard derivation of the new impact formula for predicting the penetration depth was 0.23, which was also the best. Analysis by other parameters showed slightly differing accuracies. The proposed formula

was best at velocities of less than 800 m/s, while the Li-Chen formula was the best at over 800 m/s. The proposed formula had the best for the whole h/d_p range, and showed the best results for the whole concrete strength and whole kinetic energy per contact area.

- 7) The scabbing depth formula was proposed and then verified using experimental data. The mean value of the ratio of tested scabbing depth to predicted scabbing depth was 1.87, and the standard deviation was 1.22. The scabbing depth formula was less accurate than the penetration depth formula. This is because it is difficult to predict scabbing depth due to the amplification of energy by reinforcing bars and/or aggregate and reflection angle. Despite these challenges, in 52 of 81 specimens (64%), there was a scattered ratio of 2, and the average ratio was 1.16. Therefore, the scabbing depth formula is good overall. The Hughes formula was the best for predicting perforation failure, while the proposed equation was the worst. However, the proposed formula was the best for predicting non-penetration, with 99% accuracy. The border between perforation and non-perforation was properly divided.
- 8) A new formula to predict the scabbing limit and perforation limit thickness was derived using a theoretical framework and verified using experimental data. The proposed formulae predicted all scabbing failures. However, non-scabbing failure was predicted with an accuracy of 81%. This formula was the most accurate among those compared.
- 9) The projectiles examined in the study on the validity of a new impact formula were similar to those of conventional military weapons. In

addition, the concrete panels studied were similar to ordinary reinforced concrete panels, even with reinforcing bars. The proposed formula can be of use when a private building is under the threat of damage by conventional military weapons.

Chapter 6. Supplementary Nonlinear Analysis

Previously, in **Chapter 5**, parameters such as concrete compressive strength, concrete tensile strength, elastic modulus, aggregate size, steel fiber volume fraction, projectile velocity, projectile shape, and projectile length were examined. However, some parameters are insufficiently verified in experiments conducted by others or the author. Firstly, the effect of reinforcement on the impact resistance of reinforced concrete slab, which was not sufficient in the previously investigated impact experiment as reviewed in **Chapter 5**, will be studied through the nonlinear analysis. The diameter of the projectile was particularly smaller than the spacing of the reinforcing bars in the reviewed test in **Chapter 5**. There was no collision between the projectile and the reinforcing bar. Therefore, the purpose of nonlinear analysis is to investigate the effect of reinforcing bars when the spacing of reinforcing bars is similar to, or larger than, a diameter of projectile and/or the reinforcing bar is placed on the line of projection.

It was assumed that the same kinetic energy will have a deeper penetration depth when the energy per unit area increases and the projectile length factor is applied. While this was suggested by experimental data, it was necessary to verify it through nonlinear analysis. Also, the evaluation of the specimens with various areas and thicknesses under the same conditions has been insufficient. Therefore, the effect of panel width and thickness is specifically investigated.

6.1 Modeling of Impact Test Model

The model of nonlinear analysis will be similar to the concrete panel in the first experiment of this study. The proposed RHT concrete model for the impact study of concrete is considered valid and will be used for the nonlinear analysis. The compressive strength of concrete is 35 MPa, and other values, such as tensile strength, bulk modulus, shear strength, follow the RHT concrete model. First, the RHT concrete model will be verified once again to determine if the penetration depths are similar to the results of the first experiment, and some values will be adjusted according to the situation. A nonlinear analysis will be performed to examine the effects of the reinforcing bar, the projectile size, the panel area, and the panel thickness with the identified material model.

6.1.1 Validation of concrete model

The RHT concrete model introduced in **Chapter 2** was used, because the RHT model is valid for application to the study of impact resistance of concrete. The material of the concrete panel was obtained from the *Concrete-35 MPa* (**Table 6-1**) which is contained within the Material Library-Explicit Material, which was provided by ANSYS for analyzing explicit materials. The provided concrete model in the Material Library was developed by Riedel *et al.* (1999), Riedel (2004), and Riedel *et al.* (2009). The concrete compressive strength was 35 MPa, and tensile strength was 3.5 MPa, and the shear strength was 9.8 MPa.

Table 6-1 Key parameters of concrete for explicit analysis

Parameter	Value	Parameter	Value
Equation of state	P-alpha	Tensile strength	3.5 MPa
Bulk modulus	3.527×10^4 MPa	Shear strength	9.8 MPa
Concrete type	RHT concrete	Damage constant, ψ_3	0.04
Compressive strength (f'_c)	35 MPa	Damage constant, ψ_4	1
Tensile failure	Hydro	Erosion strain	2.0

An unreinforced concrete panel was tested in order to verify the material model by the preliminary study. The mesh size was set to 5 mm and the velocity of the projectile was set to 200 m/s. Examining the results of nonlinear analysis, the deepest penetrated depth was 140 mm as shown in **Figure 6-1**. The penetration depth was predicted to be 25 mm by the developed formula in this study and 45 mm by the modified NDRC. It is difficult to achieve deep penetration even when deduced from the results of impact test results as reviewed in **Section 5**. The strain rate effect was considered to have been underestimated. The value of compressive and tensile strain rate dependence exponent, which is an optional function, was increased to 0.135, and the results of re-analysis showed a penetration depth of about 35 mm, which was close to a predicted penetration value according to the proposed formula. The modified concrete material was adopted to analyze a reinforced concrete panel.

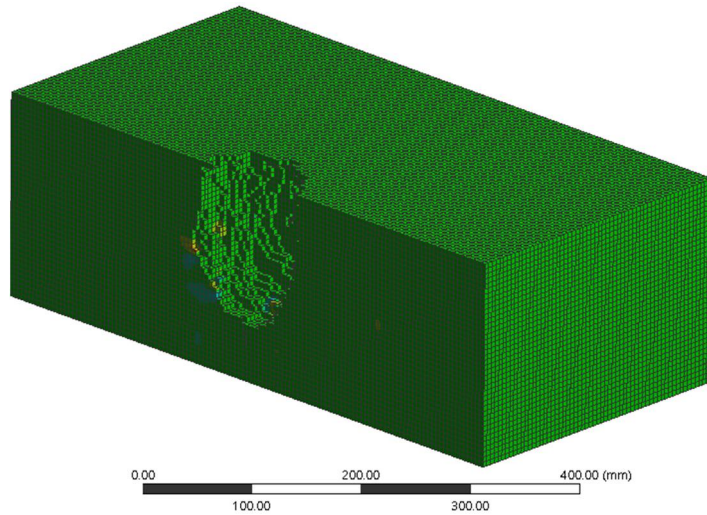


Figure 6-1 Penetrated specimen with provided concrete materials

The new material values were compared with experimental results (**Table 6-2**). The same collision conditions as those in **Section 4.1.1** were set. The specimen size was 200×200 mm, the projectile diameter was 20 mm and the speed was 350 m/s. The distance between the concrete panel and the projectile was 5 mm. The specimen thicknesses in the nonlinear analysis were 30 mm and 70 mm. The penetration depths for these panels were similar to the results of impact testing. However, the spalling and scabbing areas were much larger in the experiment than in the nonlinear analysis. In this nonlinear analysis, investigating penetration depth was the main research objective, so it was possible to use the modified material model for performing nonlinear analysis according to various parameters.

Table 6-2 Results of nonlinear analysis for 30, 70 mm thickness

Thickness	30 mm		70 mm	
	Tested	Analyzed	Tested	Analyzed
Penetration depth (mm)	12	15	20	15
Scabbing depth (mm)	18	15	-	-
Front area loss (mm ²)	3600	900	4800	800
Rear area loss (mm ²)	6800	2025	-	-

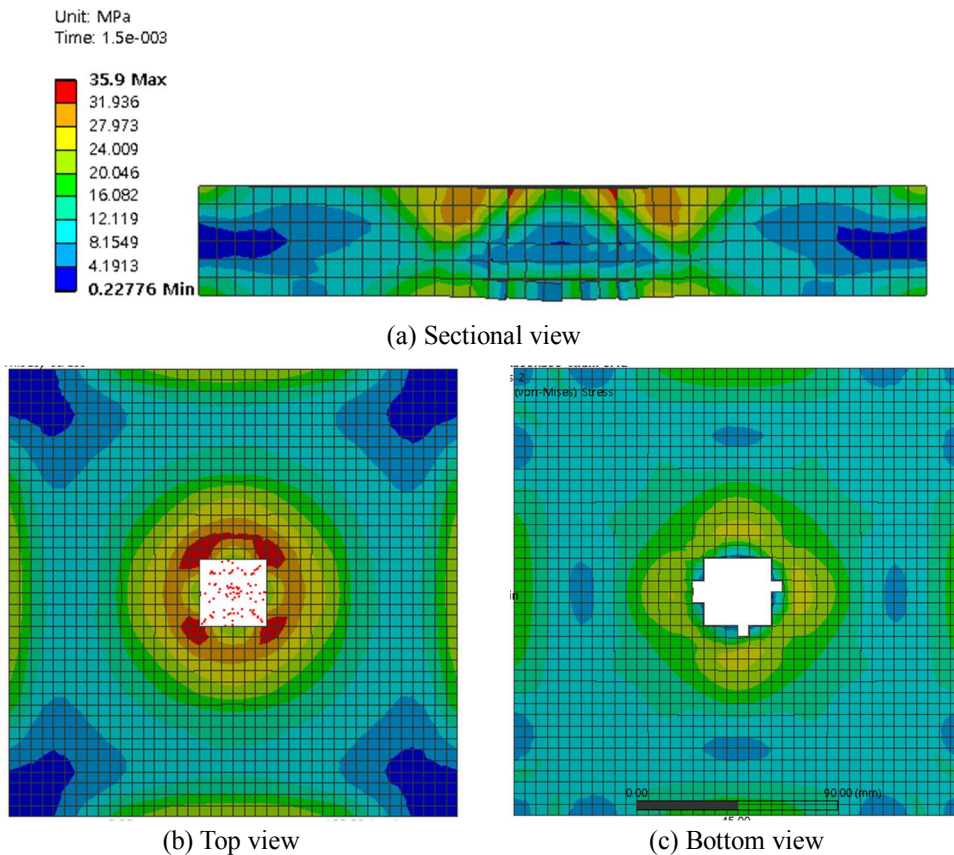
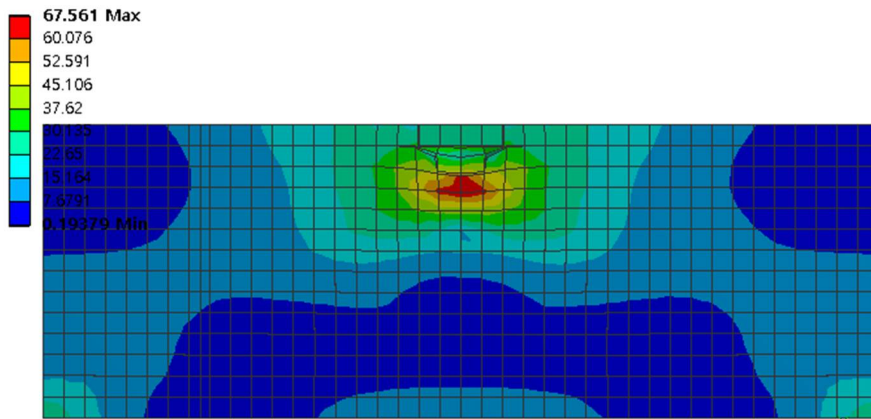
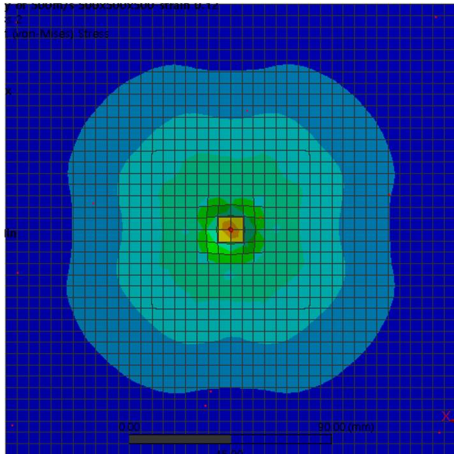


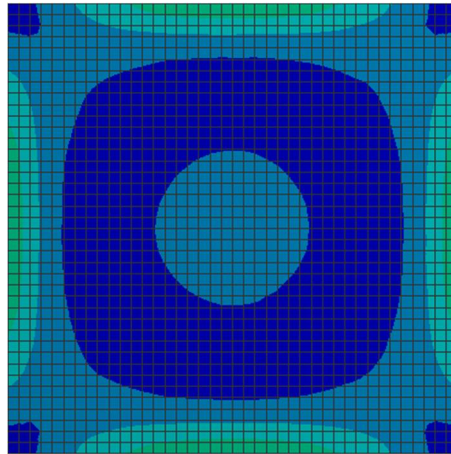
Figure 6-2 Equivalent stress on sectional, top, and bottom of 30 mm thickness



(a) Sectional view



(b) Top view



(c) Bottom view

Figure 6-3 Equivalent stress on sectional, top, and bottom of 70 mm thickness

The material model of the reinforcing bar was also obtained from the *Iron-C.E.* (Table 6-3) in the Material Library-Explicit Material. It was developed by Johnson and Cook (1985). It was assumed that a projectile does not fail, when structural steel was used as an elastic material.

Table 6-3 Key parameters of steel for explicit analysis

Parameter	Value	Parameter	Value
Initial yielding stress	290 MPa	Melting temperature	1538
Hardening Constant	339 MPa	Reference strain rate	1
Hardening exponent	0.4	Bulk modulus	1640 MPa
Strain rate constant	0.055	Shear modulus	800 MPa
Thermal softening exponent	0.55		

6.1.2 Plan of nonlinear analysis on effect of rebar

In order to examine the effect of steel reinforcing bars on a reinforced concrete failure under high velocity impact load, ANSYS AUTODYN was used for nonlinear analysis. The size of the concrete panel and the diameter of the rebar to be used for the nonlinear analysis are planned as shown in **Table 6-4** and **Figure 6-4**. The size of the reinforced concrete panel was $600 \times 600 \times 200$ mm, and the concrete compressive strength was 35 MPa with maximum aggregate size of 25 mm. A diameter of a reinforcing bar was 10 mm and its spacing was 40, 50, and 100 mm as shown in **Figure 6-5**. Its nominal strength was 290 MPa. The distance from the concrete panel face to the center of the reinforcing bar was 25 mm.

Table 6-4 Plan of nonlinear analysis

Panel	Reinforcement	Projectile
Size: $600 \times 600 \times 200$ f'_c : 35 MPa Max. of agg : 20 mm	D10@40, 50, 100 mm f_y : 290 MPa	Type: sphere Diameter: 40 mm Velocity: 200 m/s

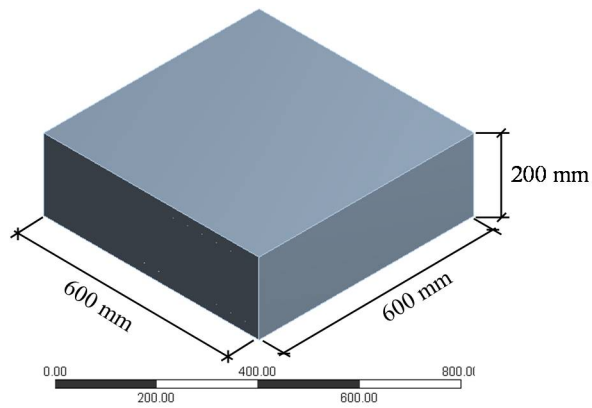


Figure 6-4 Dimensions of concrete panel for nonlinear analysis

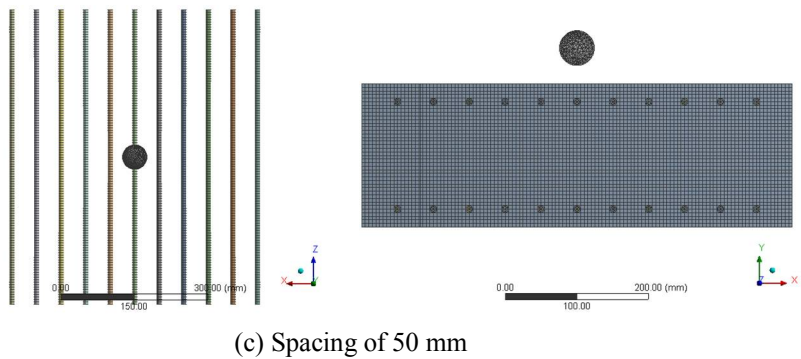
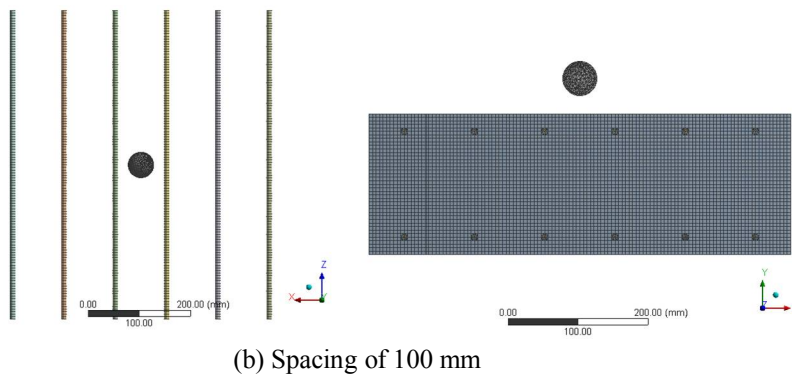
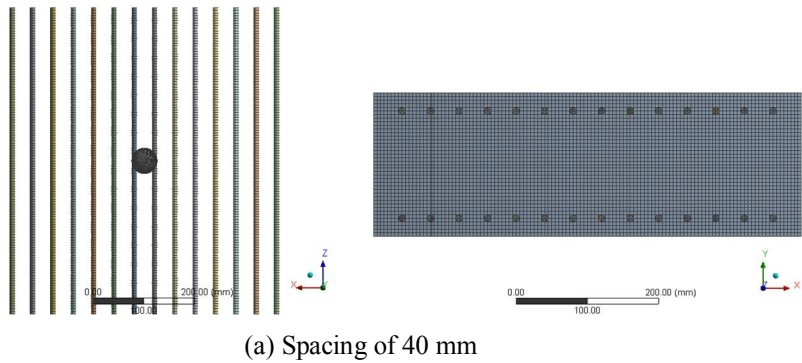


Figure 6-5 Plan of reinforcing bar lay-out

- 1) The reinforced concrete panel with a spacing of 40 mm had a total of 14 reinforcing bars that were placed on the top and the bottom, and the reinforcing ratio was 0.00325. There were no reinforcing bars at the center

of the concrete panel. The reinforcing bars were placed at a distance of 20 mm in both directions from the center of the concrete panel (**Figure 6-5(a)**). Therefore, a projectile and two reinforcing bars were overlapping on each side of 5 mm.

- 2) The reinforced concrete panel with a spacing of 100 mm had a total of 6 reinforcing bars that were also placed on the top and the bottom, and the reinforcing ratio was 0.00125 (**Figure 6-5(b)**). There were no reinforcing bars in the line of projection.
- 3) The reinforced concrete panel with a spacing of 50 mm had a total of 11 reinforcing bars that were also placed on the top and bottom, and the reinforcing ratio was 0.00625 (**Figure 6-5(c)**). One reinforcing bar was placed in the line of projection.

The projectile was sphere shaped with a diameter of 50 mm. It was assumed that its material has no failure, which was defined as elastic material. The distance from the center of the concrete panel front face to the center of the projectile was 30 mm, there was a gap 5 mm between a face of the concrete panel and the projectile (**Figure 6-6**). In order to observe that a projectile enters the concrete panel behind the reinforcing bar, the velocity was set at 200 m/s along the Y-axis direction. When a diameter of 50 mm of projectile shoots at 200 m/s, the penetration depth was predicted to be 35 mm according to the proposed impact formula, which was deeper than the distance from the face of the concrete panel to the center of the reinforcing bar.

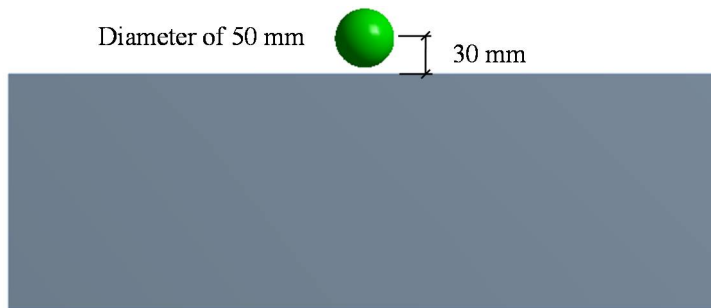


Figure 6-6 Plan of projectile

The concrete panel and projectile were solid body elements and the reinforcing bars were modeled as line body elements following the plan of nonlinear analysis (**Figure 6-7**). A circle section with a diameter of 50 mm was created and connected to linear bodies in order to have sectional area.

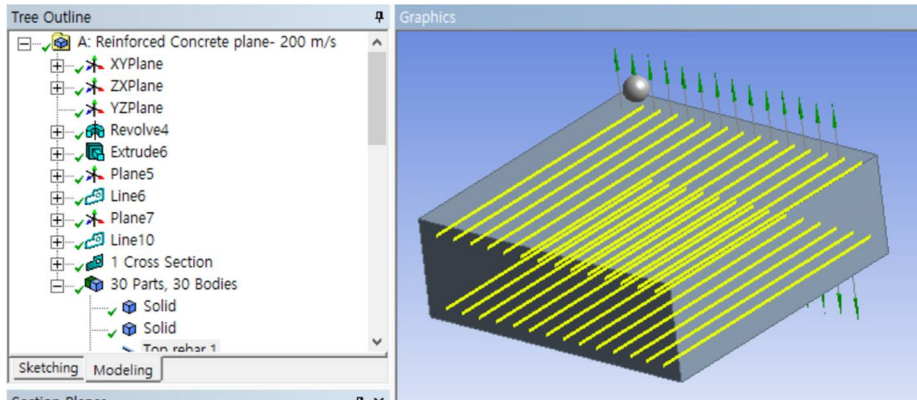


Figure 6-7 Modeling in Modeler

The mesh size was 5 mm and set to be a cube type, and it was automatically controlled by ANSYS. The purpose was to make the mesh line and the line body overlap with each other (**Figure 6-8**). The 4 side face of the concrete panel was fixed as the fixed support. The reference velocity of the projectile was 200 m/s on

the Y-axis direction, and the angle between the projectile and the panel was at a right angle (**Figure 6-9**). The connection between the concrete panel and the reinforcing bars was set to “reinforcement.” The analysis time was 0.0015 sec for 200 m/s and recorded the 100 output data.

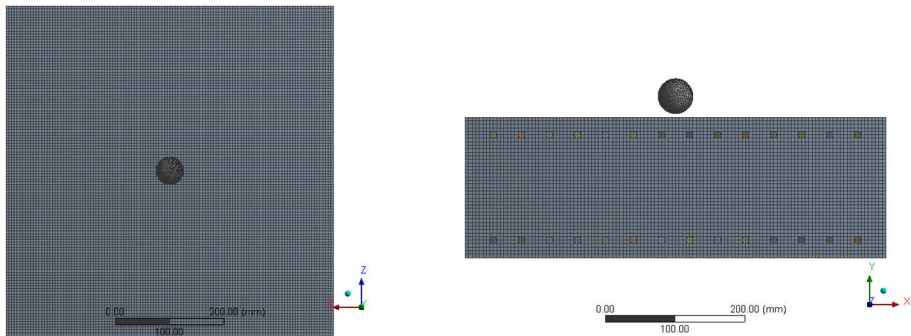


Figure 6-8 Mesh of reinforced concrete panel with spacing of 40 mm

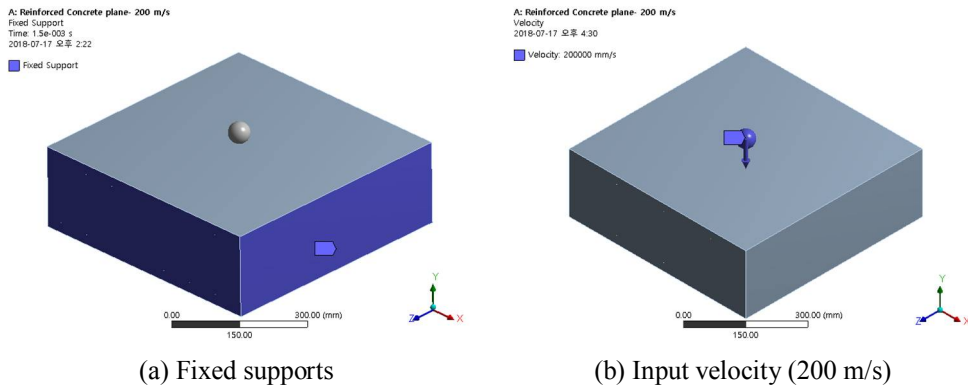


Figure 6-9 Boundary conditions and initial velocity

6.1.3 Projectile aspect ratio

It was confirmed that projectile shape greatly influenced penetration depth in the experiments. When the projectile was long with the same weight, the amount of kinetic energy per unit area was high, resulting in deeper penetration depth. A projectile size factor considering the effect of projectile aspect ratio was also applied to the new impact formula. In this experiment, the effect of projectiles with the same aspect ratio but different sizes was not investigated. The effect of a long-shaped projectile was applied to the new impact formula, but this effect was derived from assumptions based on experimental results. Using nonlinear analysis, the effect of variously-shaped projectiles on penetration depth was closely investigated in two cases: projectiles with the same aspect ratio but different sizes, and projectiles with the same sectional area but different lengths (i.e., different aspect ratios).

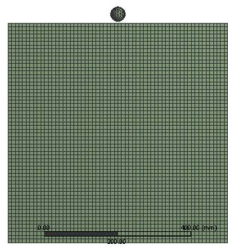
In order to investigate the effect of a projectile with the same aspect ratio but a different density, the Sphere-40-1 with diameter 40 mm and normal density (7850 kg/m^3) was prepared as the reference specimen, and Sphere-40-2, Sphere-40-3, and Sphere-40-4 were prepared, where Sphere-40-2, Sphere-40-3, and Sphere-40-4 had densities of 26505, 62800, and 122674 kg/m^3 , respectively (**Table 6-5** and **Figure 6-10**). Additionally, in order to investigate the effect of projectiles with the same aspect ratio but different sizes, a spherical shape was first chosen, with diameters of 60 mm, 80 mm, and 100 mm. The names of the specimens were Sphere-60, Sphere-80, and Sphere-100, respectively. And their weights were 263 g, 888 g, 2104 g, and 4110 g, respectively. In order to examine the effect of projectiles with the same sectional area but different aspect ratios, a diameter of 40 mm was chosen,

with lengths of 96 mm, 220 mm, and 423 mm (**Table 6-5** and **Figure 6-10**). Their weights were 888 g, 2104 g, and 4110 g, respectively. The pairs of Sphere-40-2 and Long-hemisphere-96, Sphere-40-3 and Long-hemisphere-220, and Sphere-40-4 and Long-hemisphere-423 had the same kinetic energy per unit area, respectively. The criterion chosen for the projectile aspect ratio was the weight of the projectile. This was to examine the effect of projectiles with the same kinetic energy but different aspect ratios. By choosing a long-hemisphere diameter of 40 mm, front loss area from collisions with Sphere-40 and long projectiles was compared. At the same time, the penetration depths of the Long-hemisphere-96, Long-hemisphere-220, and Long-hemisphere-423 were compared to the penetration depths of the Sphere-40-2 or Sphere-60, Sphere-40-3 or Sphere-80, and Sphere-40-4 or Sphere-100, respectively. By analyzing the results, the effect of the aspect ratios will be studied in cases where the specimens have the same mass.

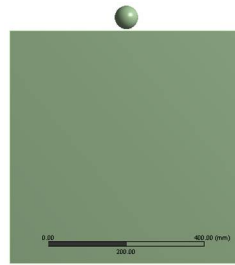
Table 6-5 Projectiles in nonlinear analysis

Projectiles	Density (kg/m ³)	d_p	l_p	l_p/d_p	Mass (g)	E_K	E_K/A_p
Sphere-40-1	7850	40	40	1	263	11835	9.42
Sphere-40-2	26505	40	40	1	888	39960	31.82
Sphere-40-3	62800	40	40	1	2104	94680	75.38
Sphere-40-4	122674	40	40	1	4110	184950	147.25
Sphere-60	7850	60	60	1	888	39960	14.14
Sphere-80	7850	80	80	1	2104	94680	18.84
Sphere-100	7850	100	100	1	4110	184950	23.56
Long- hemisphere- 96	7850	40	96.67	2.4	888	39960	31.82
Long- hemisphere- 220	7850	40	220	5.5	2104	94680	75.38
Long- hemisphere- 423	7850	40	423.33	10.5	4110	184950	147.25

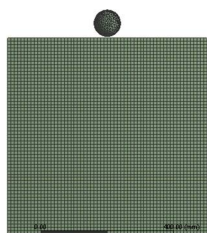
d_p is the sectional diameter of projectile (mm); l_p is the projectile length (mm); E_K is the kinetic energy (J); and A_p is the sectional area of projectile (mm²).



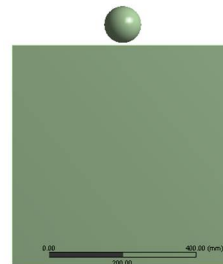
(a) Sphere-40-1 ~ 4



(b) Sphere-60



(c) Sphere-80



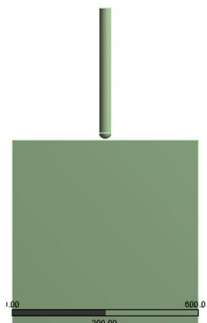
(d) Sphere-100



(e) Long-hemisphere-96



(f) Long-hemisphere-220



(g) Long-hemisphere-423

Figure 6-10 Models with various shapes of projectile

The concrete's compressive strength was 35 MPa, and the specimen size was $600 \times 600 \times 600$ mm with four fixed side faces. The projectile velocity was 350 m/s, and the distance between the specimen and the projectile was 5 mm.

6.1.4 Panel area

There were no experiments conducted to evaluate the effect of the panel area. This section will examine how the panel area affects the impact resistance. Four types of panels were prepared, and all the specimens had a thickness of 200 mm – $400 \times 400 \times 200$ mm, $600 \times 600 \times 200$ mm, $1000 \times 1000 \times 200$ mm, and $2000 \times 2000 \times 200$ mm (**Figure 6-11**). The nonlinear models for evaluating the effect of the panel area were created using the same procedure except for the mesh size and the value of the compressive and tensile strain rate dependence exponent. Since rebars were a key variable, the mesh size was set to 5 mm for an accurate analysis in the previous section. However, since the panel area was not expected to have a significant effect on the impact resistance, the mesh size was set to 10 mm to reduce the analysis time. The value of the compressive and tensile strain rate dependence exponent was set to 0.12. In the analysis results of $600 \times 600 \times 200$ mm, three elements downward from the surface were destroyed, as can be seen on a vertical line in **Figure 6-12**. This result showed a penetration depth of about 30 mm, so the value of 0.12 was appropriate.

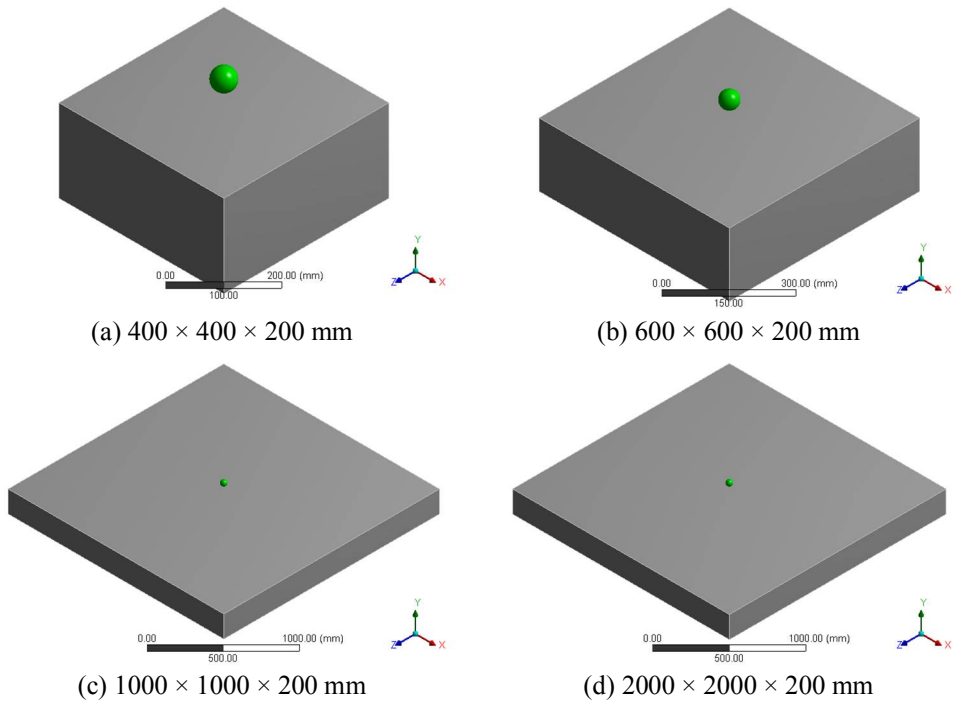


Figure 6-11 Models with various areas

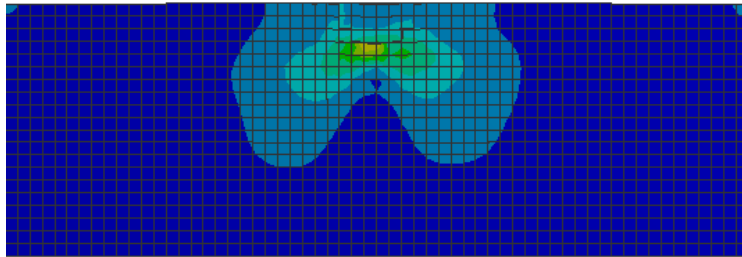
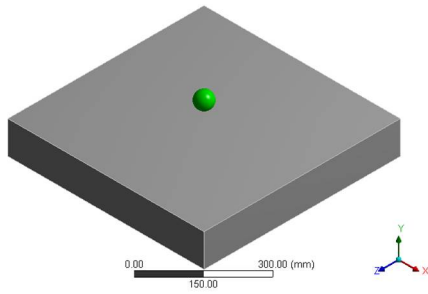


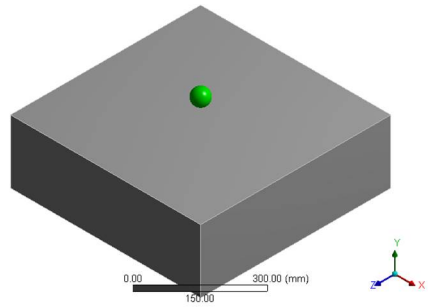
Figure 6-12 Analysis results of specimen of $600 \times 600 \times 200$ mm with 10 mm mesh size

6.1.5 Panel thickness

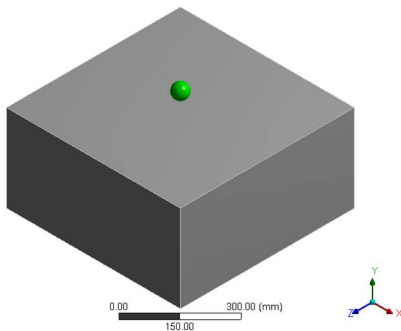
The specimens with thickness (h) to projectile diameter (d_p) ratios of 1.5 to 5 were tested in the first and third experiments, and five or more were tested in other experiments conducted by other researchers. Since the thickness and other experimental conditions were different for each experiment, it was difficult to analyze the effect of the specimen thickness under the same conditions. Therefore, it was necessary to analyze only the thickness as a variable with the same condition, and thus nonlinear analysis was performed. The effect of the thickness on the impact resistance was investigated under the same conditions except that the area of the panel was created as $600 \times 600 \times 100 \sim 600$ mm, as shown in **Figure 6-13**. Nonlinear models for evaluating the effects of the various thicknesses were created using the same procedure as in **Section 6.1.2**.



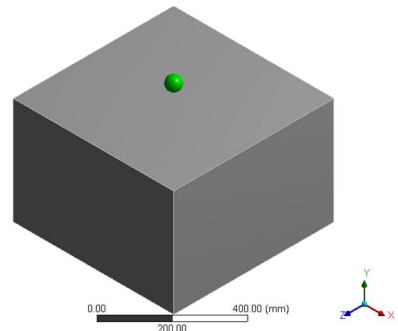
(a) $600 \times 600 \times 100$ mm



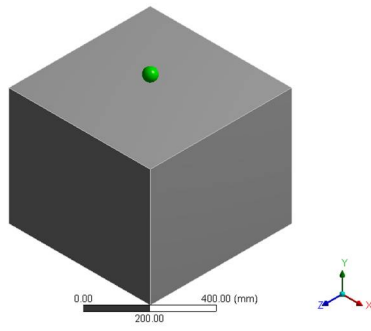
(b) $600 \times 600 \times 200$ mm



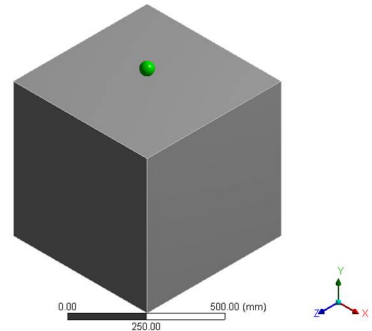
(c) $600 \times 600 \times 300$ mm



(d) $600 \times 600 \times 400$ mm



(e) $600 \times 600 \times 500$ mm



(f) $600 \times 600 \times 600$ mm

Figure 6-13 Nonlinear analysis model with various thicknesses

6.2 Results of Nonlinear Analysis

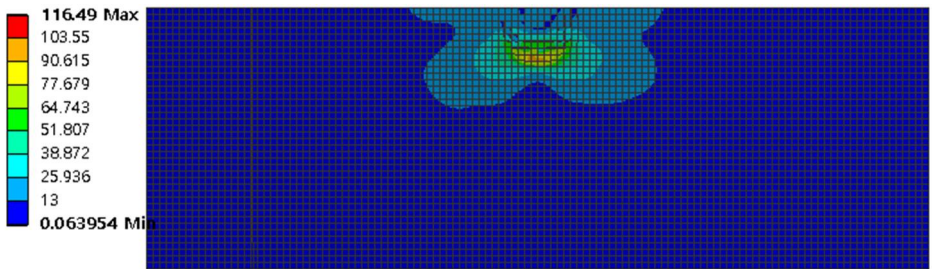
6.2.1 Reinforcing bars

Table 6-6, **Figure 6-14** and **Figure 6-15** present the penetration depth predicted by the proposed formula and the results of nonlinear analysis. Comparing the results of unreinforced and reinforced concrete panels, the penetration depth of the reinforced concrete panel with a spacing of 40 mm was the largest. The other specimens had the same penetration depth. The 7 elements (35 mm, one element size is 5 mm) of unreinforced and reinforced concrete panels with spacing of 100 and 50 mm in vertical axis had failures. The 9 elements (45 mm) of reinforced concrete panels with a spacing of 40 mm also had failures. This value exceeded the predicted penetration under the proposed formula. In the conclusions of experimental test research by Kim *et al.* (2018), Dancygier and Yankelevsky (1996), and Kojima (1991), the reinforcement did not significantly increase in the impact resistance of a reinforced concrete panel. The results of a nonlinear analysis showed similar behavior, and the deeper penetration depth was observed in cases where reinforced concrete panels had a spacing of 40 mm. The plan of the impact test called for a wider spacing to allow reinforcing of the bars than the diameter of projectile, while the spacing of the reinforcing bars through nonlinear analysis was smaller than the diameter of each projectile. The projectile did not directly touch any reinforcing bar in an impact test, but the projectile in nonlinear analysis did hit two reinforcing bars. In the case of reinforced concrete panels with a spacing of 100 mm, there were no reinforcing bars in the straight line from the center of the projectile. It is the same as when there was no obstruction element (reinforcing bars) of the shock wave going from the projectile center. As a result, penetration depth

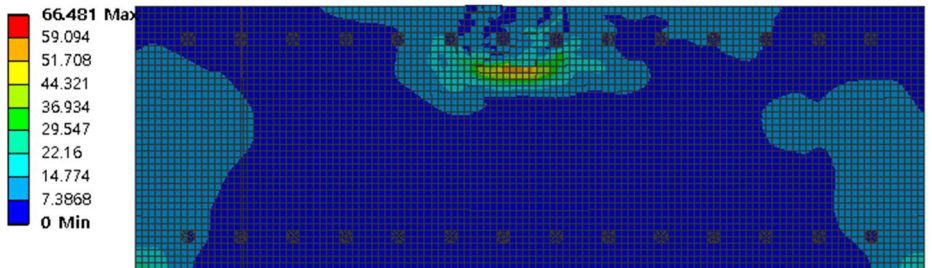
was not reduced.

Table 6-6 Penetration depth according to proposed formula and nonlinear analysis

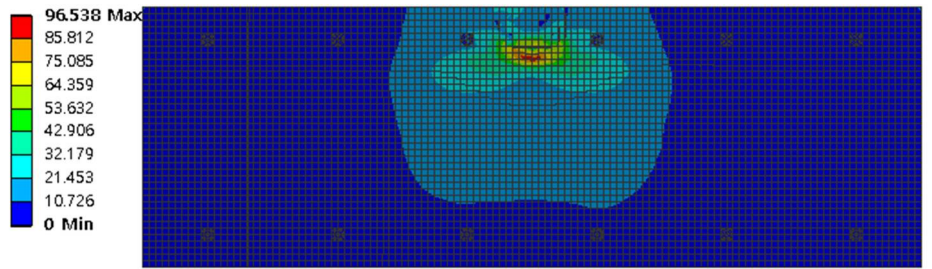
	Reinforcement	Unreinforced	Reinforced		
	Spacing (mm)	None	40	100	50
Penetration depth (mm)	Proposed formula	35	35	35	35
	ANSYS AUTODYN	35	45	35	30
Maximum equivalent stress of concrete body (MPa)		116.49	107.97	96.5	94.14
Shear stress (MPa)		62.9	35.7	49.0	94.1
Peak of plastic energy (kJ)		6.96	6.86	6.98	6.96



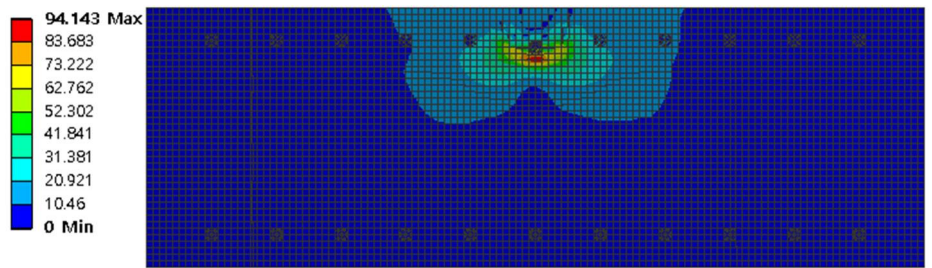
(a) Unreinforced concrete panel



(b) Reinforced concrete panel with spacing of 40 mm

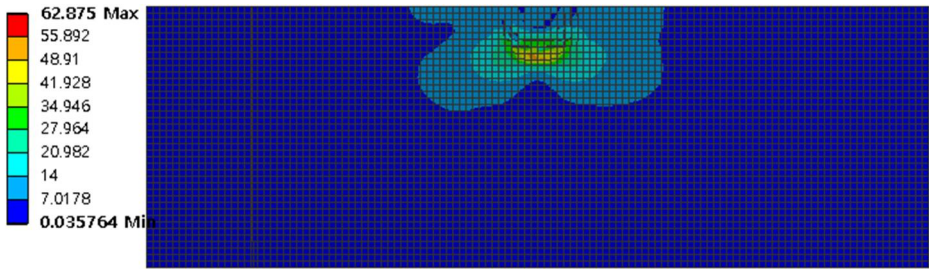


(c) Reinforced concrete panel with spacing of 100 mm

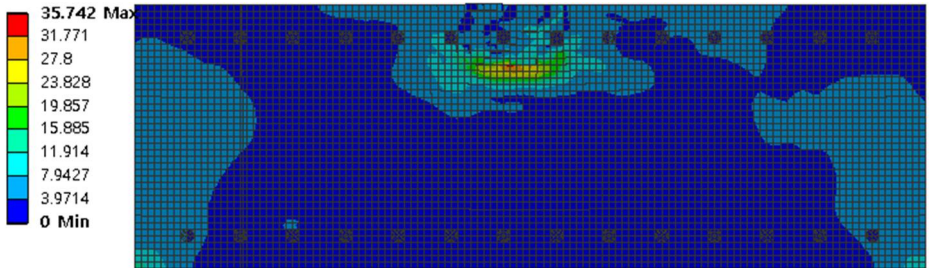


(d) Reinforced concrete panel with spacing of 50 mm

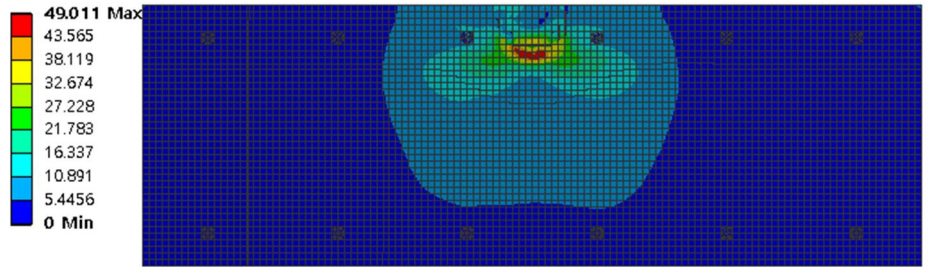
Figure 6-14 Equivalent stress of concrete body at peak stage (MPa)



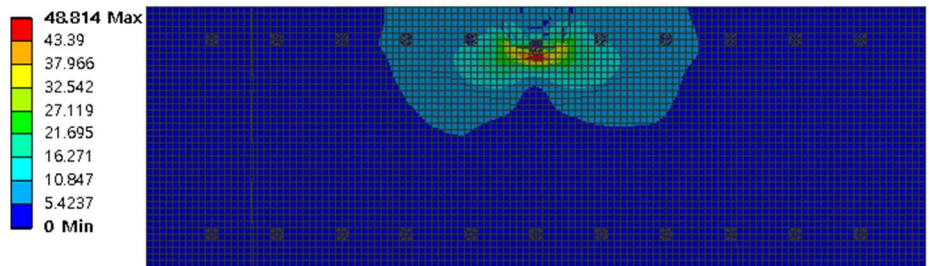
(a) Unreinforced concrete panel



(b) Reinforced concrete panel with spacing of 40 mm



(c) Reinforced concrete panel with spacing of 100 mm



(d) Reinforced concrete panel with spacing of 50 mm

Figure 6-15 Shear stress of reinforced concrete panel (MPa)

In case of the reinforced concrete panels with a spacing of 50 mm, it was observed that the projectile was stopped by the reinforcing bar as shown in **Figure 6-16**. In other words, the reinforcing bars prevented the penetration of the projectile and the depth of penetration could be reduced.

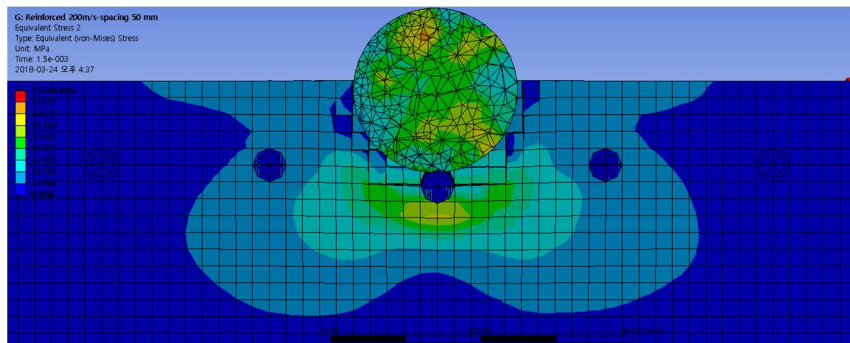


Figure 6-16 Penetration depth of results of reinforced concrete panel with spacing of 50 mm

Figure 6-17 shows the plastic energy of the concrete panel according to the time. Except for specimens with a spacing of 40 mm between the bars, the other three specimens overlapped in the same way. The maximum plastic energy of all of the specimens was about 7 kJ, but the specimen with a spacing of 40 mm occurred at 0.0001 s, and other specimens reached at 0.00025 sec. It is assumed that the projectile reached its maximum plastic energy value a little earlier than was the case for the other specimens because it overlaps with the two reinforcing bars. The plastic energy of the specimen with a spacing of 40 mm was slightly amplified at 0.0008 sec (**Figure 6-17**).

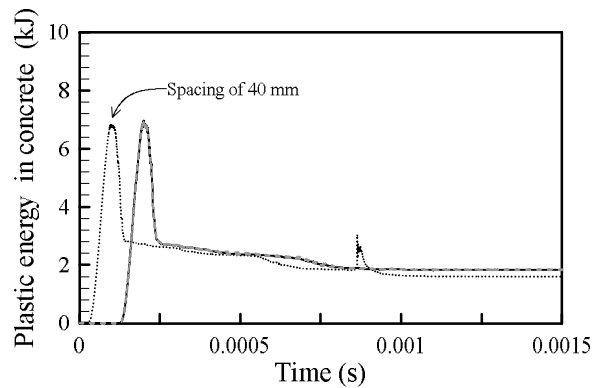


Figure 6-17 Plastic energy in concrete body

There was a point of collision at the surface of the specimen, and the stresses were radially released from there. It was assumed that some of the energies reflected by the reinforcing bars gathered/merged on the line of projection, and that the merged energy can produce the plasticity of the concrete (**Figure 6-18**). To be more specific, when initial energy meets a reinforcing bar, some will be reflected and some will pass through. The reflected energy will be directed to the projection line of the collision point. Reflected energies gathered on the projection line will produce the plasticity of the concrete.

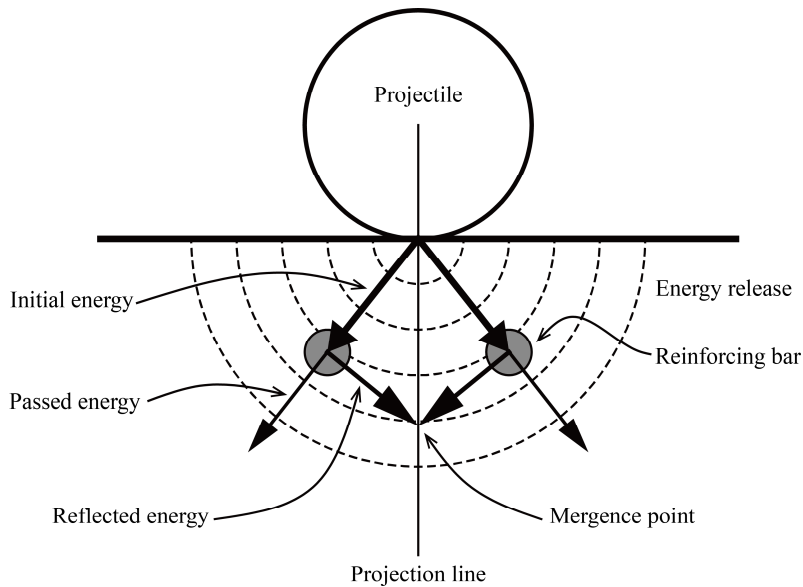


Figure 6-18 Stress reflection and mvergence on projection line

In case of the specimen with a spacing of 40 mm, the energy reflected at 90 degrees from the reinforcing bar would be collected about 41 mm from the surface of the specimen. This distance was a similar to the penetration depth in **Table 6-6**. In this case, it was considered that the reflection energy was combined on the projection line with almost no loss because the projection line and the reinforcing bars were close to each other. The distance between the projection line and the left reinforcing bar was 15 mm.

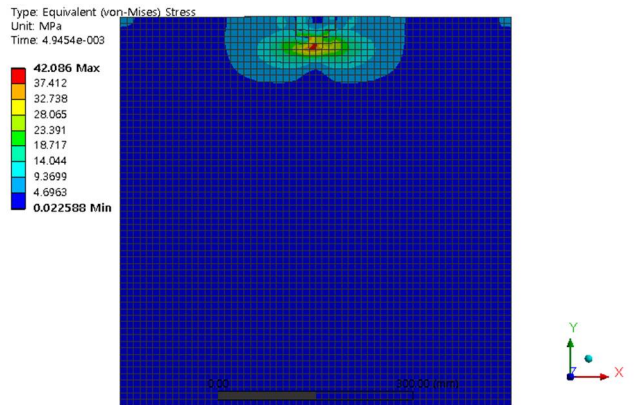
The specimen with a spacing of 100 mm did not show any additional penetration depth even if some energy was reflected. Since the spacing of the reinforcing bars was wide, it is presumed that the reflection energy was partially lost during the re-directing to the projection line, and the mvergence point was deeper than the specimen with the spacing of 40 mm. **Figure 6-15(c)** showed the deep energy spread due to the reflected energy.

6.2.2 Projectile aspect ratio

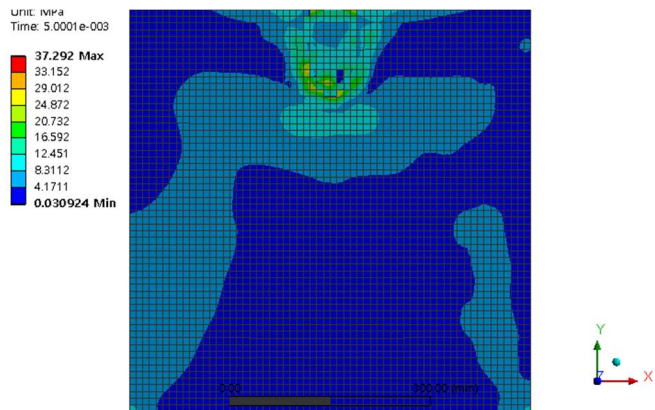
The Sphere-40-1, Sphere-60, Sphere-80, and Sphere-100 had the same shape but different diameters. It is natural that the front loss area increases as the diameter of the projectile increases. When the front area loss of each specimen was divided by πr_p^2 for comparison, r_p is the projectile radius and the average front area loss was about $3 \times \pi r_p^2$ (Table 6-7). On the other hand, penetration depth was observed to be deeper as the projectile size increased (Table 6-7 and Figure 6-19). This was caused by the increase in kinetic energy due to the larger mass of the projectile.

Table 6-7 Results of nonlinear analysis with various projectiles

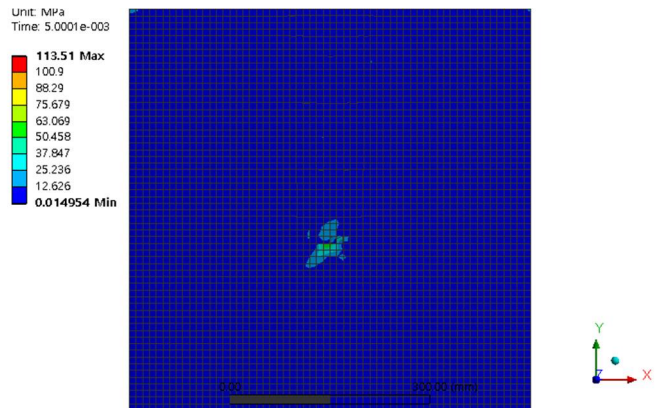
Specimens	Penetration depth (mm)	Front area loss (mm ²)	Maximum equivalent stress (MPa)	Maximum plastic energy (kJ)
Sphere-40-1	40 mm ($1 \times d_p$)	3600 ($2.86 \times \pi r_p^2$)	42.09	6.6958
Sphere-40-2	130 ($3.25 \times d_p$)	6300 ($5.01 \times \pi r_p^2$)	37.29	10.85
Sphere-40-3	350 ($8.75 \times d_p$)	7300 ($5.8 \times \pi r_p^2$)	113.51	13.87
Sphere-40-4	perforation	8700 ($6.92 \times \pi r_p^2$)	25.39	14.66
Sphere-60	120 ($2 \times d_p$)	9300 ($3.29 \times \pi r_p^2$)	54.25	17.696
Sphere-80	200 ($2.5 \times d_p$)	14100 ($2.81 \times \pi r_p^2$)	36.29	31.683
Sphere-100	300 ($3 \times d_p$)	25700 ($3.27 \times \pi r_p^2$)	50.68	53.193
Long-hemisphere-96	130 ($3.25 \times d_p$)	5100 ($4.06 \times \pi r_p^2$)	26.64	12.565
Long-hemisphere-220	240 ($6 \times d_p$)	6100 ($4.85 \times \pi r_p^2$)	113.6	14.08
Long-hemisphere-423	350 ($8.75 \times d_p$)	7900 ($6.29 \times \pi r_p^2$)	131.9	14.097



(a) Sphere-40-1

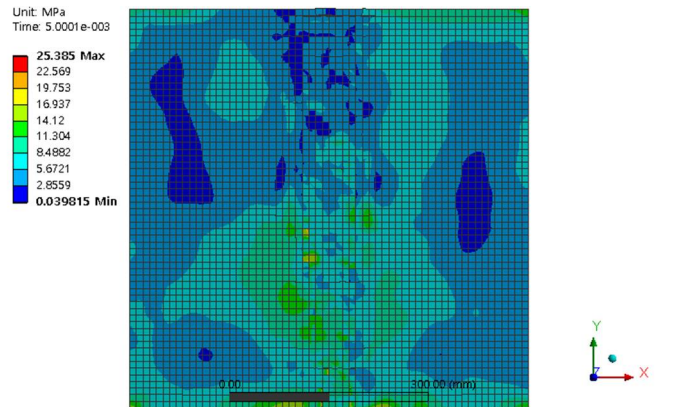


(b) Sphere-40-2

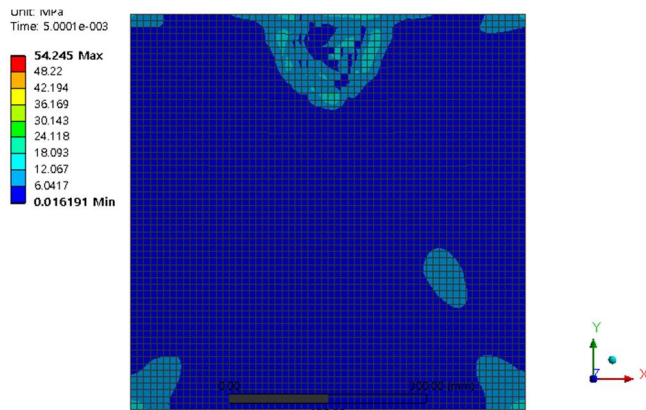


(c) Sphere-40-3

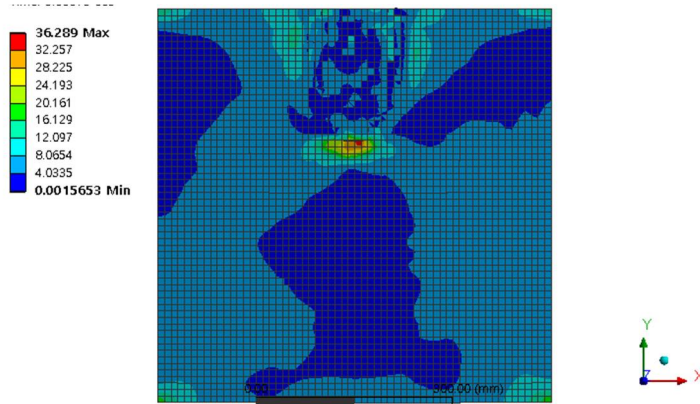
Figure 6-19 Equivalent stress of concrete body at peak stage (MPa) (continue)



(d) Sphere-40-4

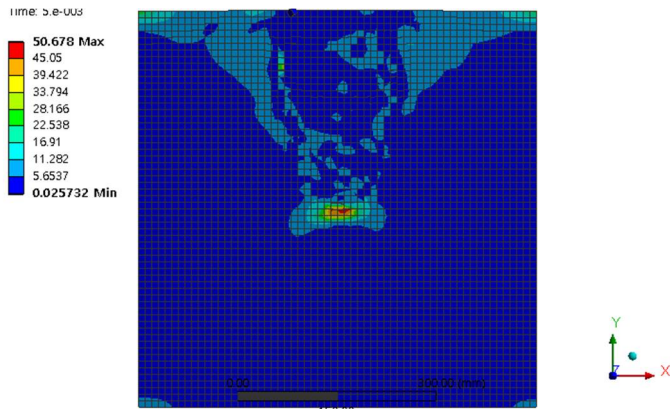


(e) Sphere-60

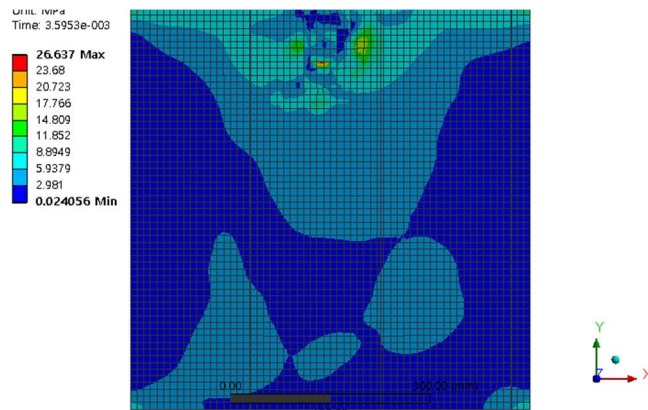


(f) Sphere-80

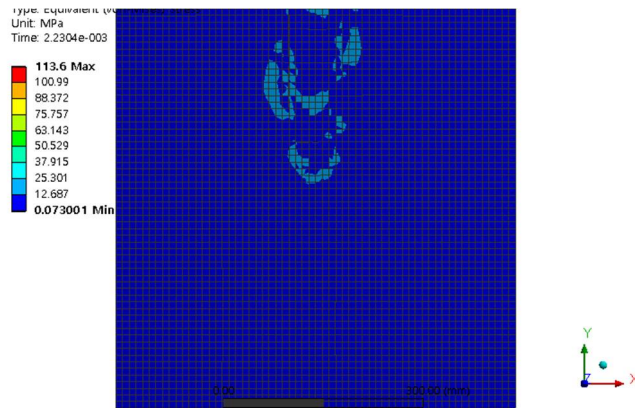
Figure 6-19 Equivalent stress of concrete body at peak stage (MPa) (continue)



(g) Sphere-100

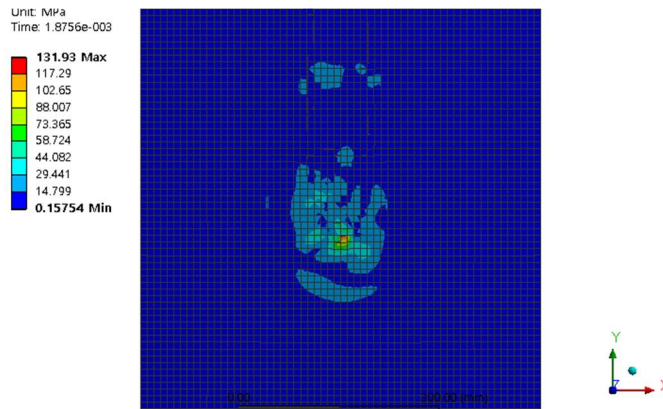


(h) Long-hemisphere-96



(i) Long-hemisphere-220

Figure 6-19 Equivalent stress of concrete body at peak stage (MPa) (continue)



(j) Long-hemisphere-423

Figure 6-19 Equivalent stress of concrete body at peak stage (MPa)

The Sphere-40-2, Sphere-60 and Long-hemishpre-96 had different shapes but the same mass. The Sphere-40-2 and Long-hemisphere-96 showed a 130 mm penetration depth, while the Sphere-60 caused a 120 mm penetration depth, which was 10 mm less. The Sphere-80 and Sphere-100 showed the smallest penetration depth among the same weighted group. It is thought that the shallower penetration depth was caused by the smaller energy per unit area. On the other hand, even though the mass per unit area was equal, penetration depth varied depending on projectile shape. The Sphere-40-2 and Long-hemishpere-96 had the same kinetic energy per unit area and equal penetration depths. However, comparing the Sphere-40-3 and the Long-hemisphere-220, the Sphere-40-3 showed a 110 mm deeper. Also, the Sphere-40-4 showed a deeper penetration depth than the Long-hemisphere-423. It was confirmed that even with the same kinetic energy per unit area and same contact area, higher energy densities produced the larger penetration depths. However, objects with higher densities than iron are uncommon. The densest solids are osmium, which has a density of 22570 kg/m^3 , about three times that of steel. The density of Sphere-40-2 was 26505 kg/m^3 , which is higher than

osmium. Since the penetration depth of Sphere-40-2 was similar to that of Sphere-60 and Long-hemisphere-96, it is difficult to consider the density of a projectile in developing an impact formula.

Another way to increase kinetic energy per unit area is to increase the length of the projectile. The Sphere-60 and Long-hemisphere-96 had the same kinetic energy and equivalent penetration depths, but the Long-hemisphere-96 had lesser front-area loss than Sphere-60. At the same time, the Sphere-80 and Long-hemisphere-220 had the same kinetic energy, but the penetration depth of the Long-hemisphere-220 was deeper by about 30 mm. Sphere-100 and Long-hemisphere-423 also had the same kinetic energy, but the penetration depth of the Long-hemisphere-423 was deeper by about 80 mm. However, considering that the penetration depths of Sphere-60 and Long-hemisphere-96 were the same, penetration depth was affected when a projectile was long enough. Front-area losses for the Long-hemisphere-220 and Long-hemisphere-423 were 6100 mm^2 and 7800 mm^2 , respectively, which were less than Sphere-60 (9100 mm^2). Therefore, it was an appropriate assumption that penetration depth increases when the aspect ratio of projectile is larger.

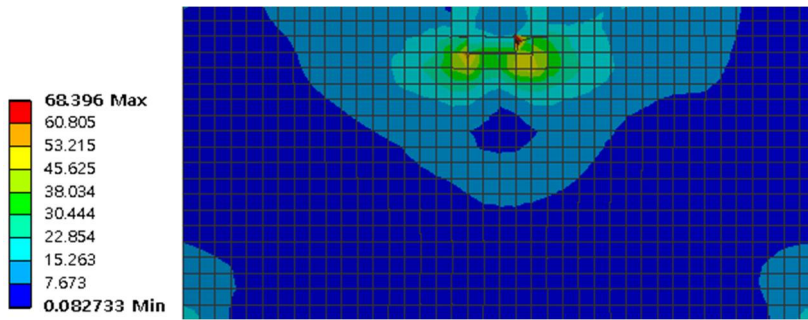
6.2.3 Panel area

Table 6-8 summarizes the results of the nonlinear analysis, and **Figure 6-20** shows the equivalent stress of each specimen, where each specimen of $1000 \times 1000 \times 200 \text{ mm}$ and $2000 \times 2000 \times 200 \text{ mm}$ are enlarged at the center to be shown more clearly. Comparing the penetration depth among various panel sizes, all of the test specimens had three failure elements on the line of projection, meaning that the

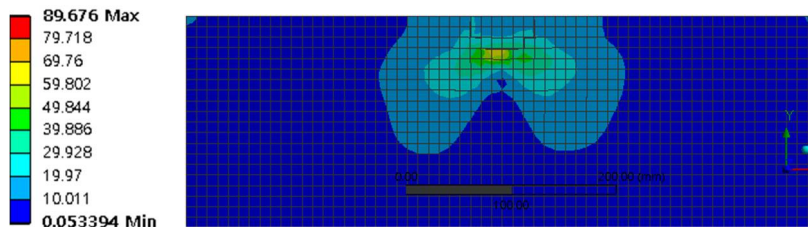
penetration depth was 30 mm. The maximum equivalent stress of $400 \times 400 \times 200$ mm was 68.4 MPa. Hence, the larger the panel size, the larger the maximum equivalent stress. However, the difference in the maximum equivalent stress values between the specimen of $1000 \times 1000 \times 200$ mm and the specimen of $1000 \times 1000 \times 200$ mm was very small, only about 1 MPa. **Figure 6-21** shows the vertical displacement of each specimen's bottom face. The contour maps tended to be different according to each panel size, but the panels of $1000 \times 1000 \times 200$ mm and $2000 \times 2000 \times 200$ mm had similar patterns. Considering the equivalent stress and vertical displacement, it can be assumed that the influence of the panel size on the impact resistance performance is limited. It was predicted that the width of the panel would not significantly affect the impact resistance in **Chapter 5**, and this prediction was appropriate.

Table 6-8 Results of nonlinear analysis with various panel areas

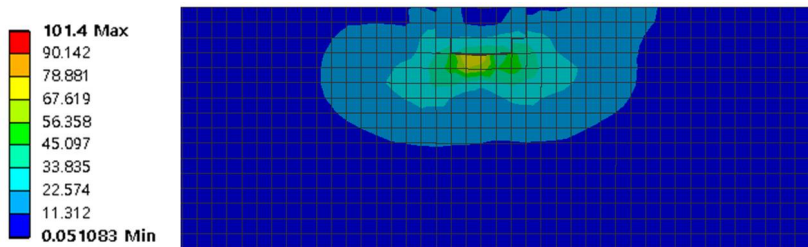
Specimens	Penetration depth (mm)	Maximum equivalent stress (MPa)	Maximum displacement (mm)	Maximum plastic energy (kJ)
$400 \times 400 \times 200$ mm	30	68.4	-0.039775	6.4835
$600 \times 600 \times 200$ mm	30	89.7	-0.027606	6.48
$1000 \times 1000 \times 200$ mm	30	101.4	-0.094572	6.4845
$2000 \times 2000 \times 200$ mm	30	102.5	-0.094591	6.4845



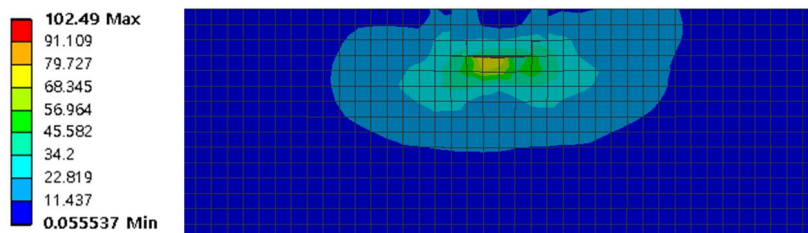
(a) $400 \times 400 \times 200$ mm



(b) $600 \times 600 \times 200$ mm



(a) $1000 \times 1000 \times 200$ mm



(a) $2000 \times 2000 \times 200$ mm

Figure 6-20 Equivalent stress of various panel models (MPa)

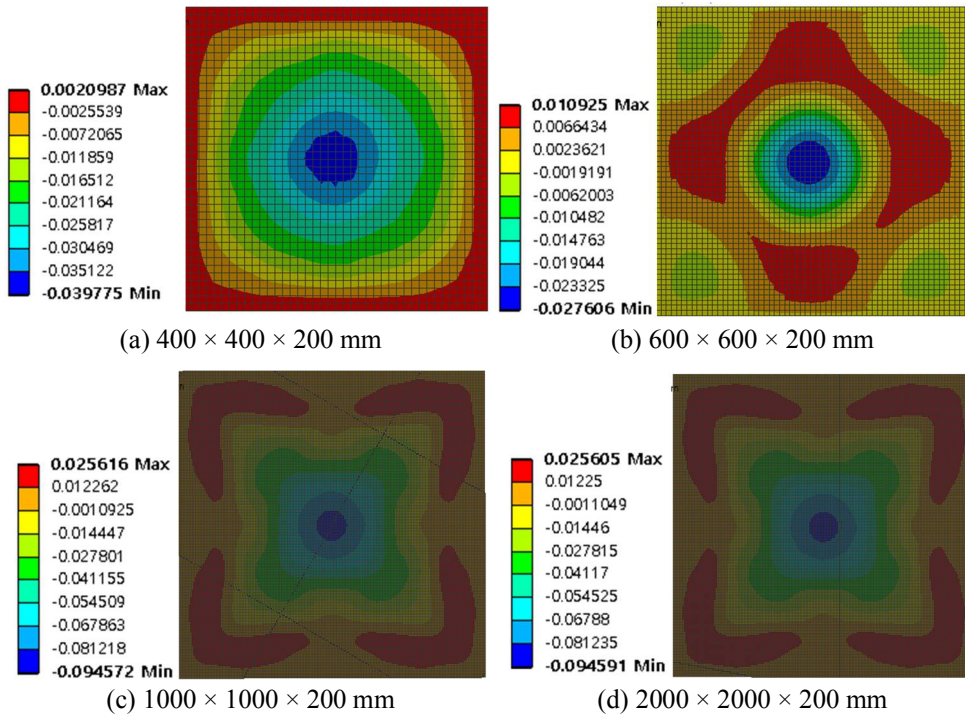
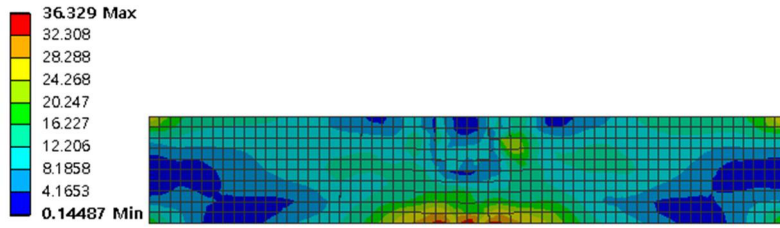


Figure 6-21 Contour maps of vertical displacement on bottom face (unit: mm)

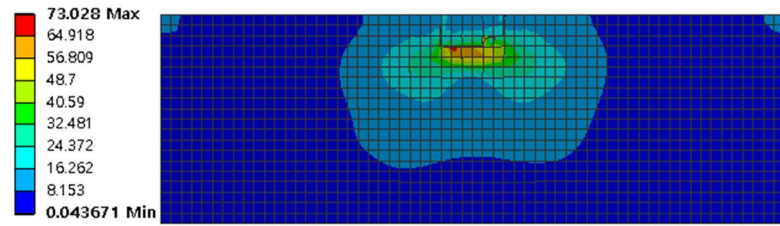
6.2.4 Panel thickness

It was expected that the penetration depth would not be greatly affected, even if the thickness became thick, if it was more than a scabbing limit thickness, and the results of the nonlinear analysis showed a similar expectation. Except for the specimen with a thickness of 100 mm, the penetration depth was equal to 30 mm (**Figure 6-22** and **Table 6-9**). The penetration depth of the specimen with a thickness of 100 mm was 60 mm, and scabbing failure was also observed with a scabbing depth of 20 mm. Regarding the plastic energy and equivalent stress, as well as the penetration depth, similar values were obtained when the specimen

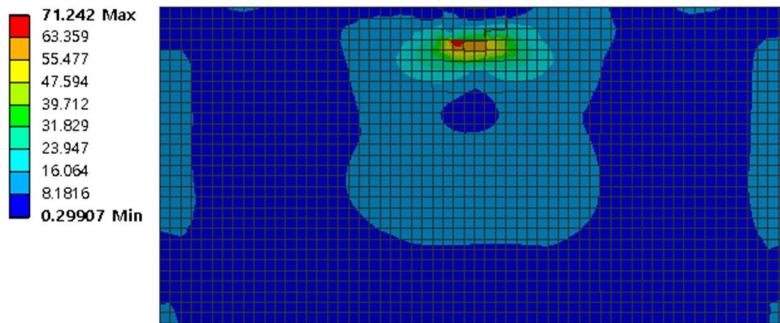
thickness was more than 200 mm. **Figure 6-23** shows the plastic energy over time. Except for the specimen with a thickness of 100 mm, the plastic energy flows of the other specimens were almost the same. The maximum amount of plastic energy was similar in all the specimens. It was concluded that the impact resistance of the concrete panel was not significantly affected by the thickness of the specimen, which was larger than a scabbing limit thickness. If the panel thickness was less than that of the scabbing limit thickness then the reflected energy had an influence on penetration. On the other hand, if the thickness of the panel was greater than the scabbing limit thickness, its effect on the impact resistance is relatively low because the reflected energy is accordingly small. In the first experiment in **Section 4.3.1**, the average penetration depths of the specimens with steel fibers of 30, 50, 70 mm thickness under 350 m/s high velocity impact loading were 11.07, 16.4, and 25 mm, respectively. The specimens with 30 and 50 mm thicknesses were perforated, and one of the specimens with 70 mm thickness was perforated. Though it had the same collision conditions, the penetration depth became greater as the thickness of the specimen increased. In other words, the reflected energy was considered to have had an influence on penetration depth. Conversely, if the panel thickness was larger than the scabbing limit thickness, the reflected energy was small and the influence of the reflected energy was not very significant as it relates to penetration depth.



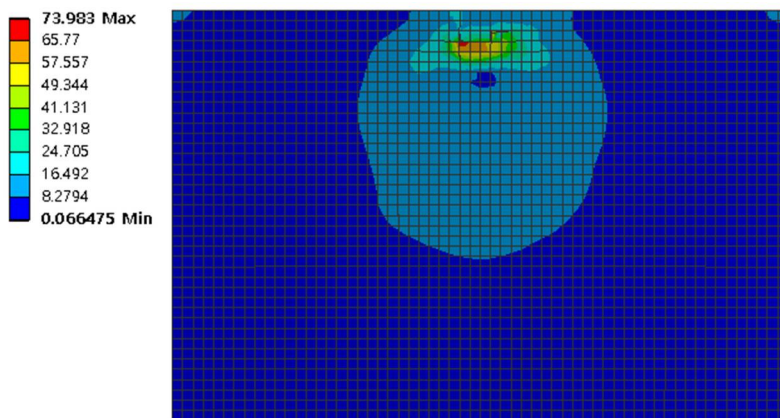
(a) $600 \times 600 \times 100$ mm



(b) $600 \times 600 \times 200$ mm

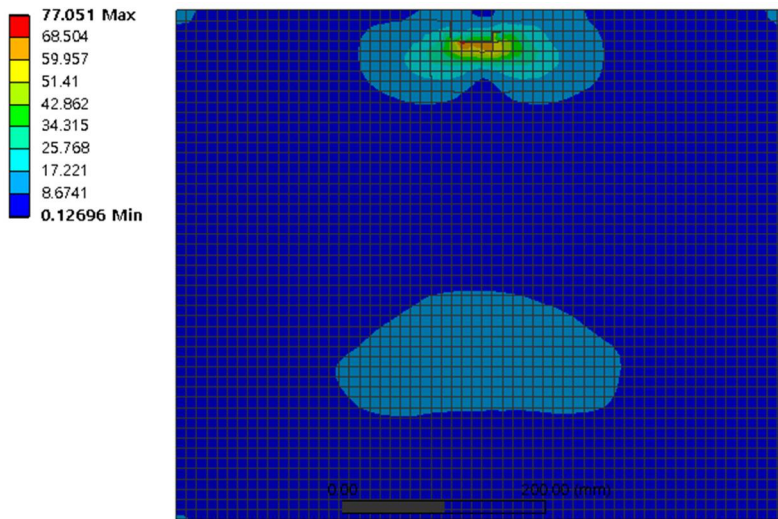


(c) $600 \times 600 \times 300$ mm

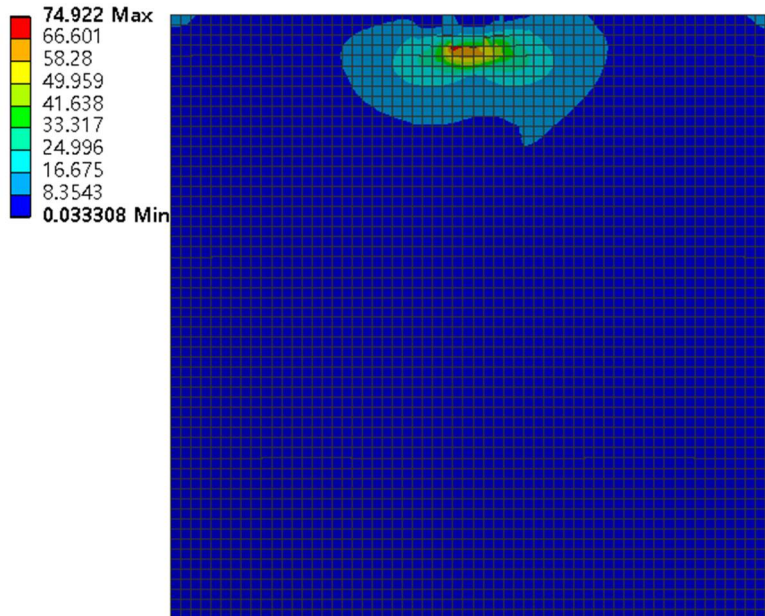


(d) $600 \times 600 \times 400$ mm

Figure 6-22 Equivalent stress of analyzed specimens (MPa) (continue)



(e) $600 \times 600 \times 500$ mm



(f) $600 \times 600 \times 600$ mm

Figure 6-22 Equivalent stress of analyzed specimens (MPa)

Table 6-9 Results of nonlinear analysis according to various thicknesses

Thickness of specimen (mm)	h/d_p	Penetration depth (mm)	Maximum plastic energy (kJ)	Equivalent stress (MPa)
100	2	60 (scabbing 20 mm)	6.430577	36.329
200	4	30	6.553571	73.028
300	6	30	6.552159	71.242
400	8	30	6.552174	73.983
500	10	30	6.552162	77.051
600	12	30	6.552162	74.922

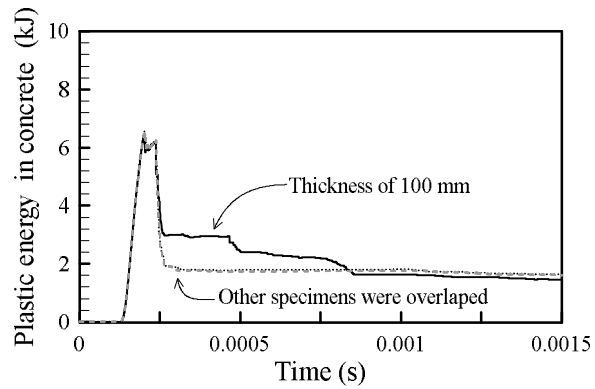


Figure 6-23 Plastic energy of specimens

6.3 Discussion

In this chapter, nonlinear analysis was conducted to study the effect of the reinforcing bars in the concrete panel and the area and thickness of the concrete panel. Four specimens were modeled to evaluate the effect of the reinforcing bars. The first was the unreinforced concrete panel, and the second, third, and fourth were the reinforced concrete panels with a spacing of 40, 100, and 50mm, respectively. The four specimens with different areas were created under the same conditions to evaluate the effect of the panel size. Nonlinear analysis was also performed on six specimens with different thicknesses. The results of the nonlinear analysis are summarized below:

- 1) The impact resistance of reinforced concrete panels can be affected by reinforcing bars, but there are special conditions which involve the spacing of reinforcing bars. Even if there are reinforcing bars in the concrete panel, the penetration depth was not affected unless the projectile was in contact with the reinforcing bars. Therefore, when estimating the penetration depth, the diameter of the projectile and the spacing of the reinforcing bars should be taken into consideration.
- 2) Penetration depth was affected by how much the projectile and reinforcing bar overlapped. The projectile and the reinforcing bars overlapped with each side 5 mm in the reinforced concrete panel with the spacing of 40 mm while overlapping. They were perfectly overlapping in the reinforced concrete panel with a spacing of 50 mm. The penetration depth of the specimen with the spacing of 40 mm deeper than the unreinforced

concrete panel.

- 3) It was examined how the change in panel width and thickness affects the impact resistance using nonlinear analysis, and the effect of the panel's area was limited. Therefore, when evaluating the impact resistance, it is considered that it is preferable to limit the appropriate area of the panel when the area is more than the effective area. Also, it was confirmed that when the thickness exceeds a scabbing limit thickness, the impact resistance is unaffected.
- 4) Even with the same kinetic energy, the higher energy per unit area can lead to deeper penetration depths. In addition, even though the energy per unit area is the same, a higher-density projectile can cause deeper penetration depths. However, since the formula development was based on iron, it is difficult to account for solid density as a variable. Consideration should be given to long forms of extrema that are likely to increase energy per unit area. If the aspect ratio of a projectile is larger, its ratio should be considered, because this can increase its energy per unit area.

Chapter 7. Summary and Conclusions

In this PhD dissertation, three impact experiments and nonlinear analytical studies were conducted to examine the impact resistance of various kinds of concrete in order to obtain new and relevant impact test and analysis results. The impact experiments thoroughly investigated variables including the steel fiber volume fractions, wire mesh, aggregate size, panel thickness, compressive strength of concrete, etc. Nonlinear analyses were performed to study variables that were not verified experimentally and were difficult to understand. Based on the experimental results and theoretical framework, a new impact formula was proposed. The summary and major conclusions are as follows:

7.1 Summary

A new impact formula for predicting penetration depth, scabbing depth, scabbing limit thickness, and perforation limit thickness of a reinforced concrete panel was derived. To develop the formula, the contact force on the nose of a projectile was derived from the cavity expansion model. The strain rate was derived from the Kolsky strain rate formula. Penetration depth was obtained from the energy density of the spalled concrete cone and bond stress between the projectile and the concrete. A scabbing depth was obtained from the stress-distance

relationship and the energy density. Using penetration depth, tunneling depth, and scabbing depth, the scabbing limit thickness and perforation limit thickness were derived. To validate the new impact formula, impact tests were conducted to collect new test data not obtained in previous research, using a small impact test device developed for this study and other devices. Using the impact experiment results along with data collected from previous research, the new formula was verified. It was difficult to determine the effect of reinforcing bars, projectile size, panel size, and panel thickness using the reviewed impact test data. Therefore, nonlinear analysis was conducted to investigate these phenomena.

7.2 Conclusions

Based on these analytical and experimental studies, the following conclusions were derived:

- 1) In order to conduct cost-effective impact experiments, a small impact test device was developed. When designing this small impact test device, the main priorities were the tank size, the length and sectional area of the barrel, and the air pressure. To keep the pressure of the tank stable, a receiver tank and a pressure control device were installed to suppress any abnormal rise in pressure. A solenoid valve allowed the tank pressure to be momentarily applied to the carrier and projectile, and was conveniently operated with a foot button. The length of the barrel was about 2 m, and a space for loading and retrieving a projectile was installed. The inside of

the barrel was smoothed with a honing process. The experimental chamber was designed for two specimens. Two velocity measurement devices were installed to measure the specimen velocity before impact and after perforation.

- 2) The steel fiber-reinforced concrete panels were manufactured to evaluate the impact resistance of SFRC with four steel fiber volume fractions (0.5, 1.0, 1.5, 2.0%). As anticipated, even with the addition of steel fibers, the effect of increasing compressive strength was not significant. On the other hand, the steel fibers had a great effect on the increase of the tensile strength of the concrete. The steel fibers did not contribute significantly to reducing penetration depth, but helped greatly in reducing scabbing failure, front area loss, and weight loss. Front area loss and weight loss decreased sharply up to a steel fiber content of 1.0%, while the decline weakened just below 1.0%. As a result, it is considered effective to use a steel fiber content of 1.0% or more to improve the impact resistance of concrete.
- 3) The effect of the use of reinforcing bars on the impact resistance of reinforced concrete panels was investigated using wire mesh. There was no significant reduction in penetration depth for concrete panels reinforced with wire mesh. The scabbing depth was slightly reduced by wire mesh, but not to a significantly different degree than that of plain concrete panels. Rather, bond splitting failure occurred between the wire mesh and the concrete cover in the panel, which was 50 mm thick. Bond splitting failure did not occur in wire mesh-reinforced concrete panels with a steel fiber volume fraction of more than 1.5%, due to the bridging effect of the steel fibers.

- 4) The aggregate size affected the impact resistance of concrete panels, but this was not significant. The use of smaller aggregates improved impact resistance by increasing the dispersion of steel fibers in the concrete matrix. However, this was not significant enough to consider in the development of the new impact formula.
- 5) Conical and hemispherical projectiles were collided with concrete panels of varying strengths to study the effect of a projectile's nose shape. It was found that the nose shape was an important factor for low-strength concrete, but had an unclear effect on high-strength concrete. Therefore, the nose shape factors suggested by the modified NDRC and Hughes formulae are not appropriate for high-strength concrete.
- 6) From test results for the steel fiber-reinforced concrete, it was found that spalling failure was related to compressive strength, and scabbing failure was related to tensile strength. The shape of the spalled cone and scabbed cone were controlled by shear failure. Therefore, spalling failure was dominated by shear stress related to the compressive strength of the concrete, and scabbing failure was dominated by shear stress related to its tensile strength. Therefore, shear stress controlled by tensile strength should be considered when developing new formulae for predicting scabbing depth, scabbing limit thickness, and perforation limit thickness.
- 7) The force on the nose of the projectile was derived using experimental data from Forrestal's study (1994), but its value was newly derived using a theoretical approach. The force on the nose of the projectile was used to determine material properties under high strain rates, following the *fib*

Model Code (*fib*, 2010) and the deformed energy of the projectile.

- 8) The proposed impact formula was derived from energy consumption at each stage of the impact mechanism, as well as energy density. The impact mechanism can be divided into four stages: the deformed energy of the projectile, the elastic penetrated energy of the concrete panel, the overall deformed energy of the concrete panel, and the spalling-resistant energy. Additionally, the tunneling-resistant energy and the scabbing-resistant energy can only be seen under certain conditions. Tunneling-resistant energy is observed when the kinetic energy is concentrated by high velocity and/or long projectiles, and scabbing-resistant energy is observed when the concrete panel does not absorb the energy reflected at the rear face. The penetration depth was derived using the law of energy conservation and energy density. Tunneling depth was derived using the energy density and bond stress between the projectile and concrete. The scabbing depth and scabbing limit thickness were derived using a stress-depth relationship, and the perforation limit thickness was equal to the sum of the predicted penetration depth, tunneling depth, and scabbing depth.
- 9) The proposed impact formula and the existing impact formulae were examined and compared with the experimental data. The overall average and standard deviation values of the proposed impact formula were 1 and 0.22, respectively. The new formula was the most accurate values among all formulae considered. By analyzing each parameter, the application ranges of the new impact formula were investigated. These were best at velocities of less than 800 m/s, kinetic energy per contact area of less than 107 kN-m/m², ratios of panel thickness to projectile diameter that were

lower than 40, and an over-compressive strength of 237 MPa (verified in this study).

- 10) The new scabbing limit thickness formula was the most accurate among the modified NDRC, ACE, Hughes, and the proposed formulae. The proposed formula predicted scabbing failure with 100% probability, and no scabbing failure with a probability of 81%. In addition, the perforation limit thickness formula predicted perforation failure with 63% probability, and no perforation failure with a probability of 99%. This formula for predicting perforation not as good as that predicting scabbing failure; nonetheless, the proposed perforation limit thickness formula can be safely used for design.
- 11) The experimental data used in formula verification showed that the diameter of the projectile was smaller than the spacing of the reinforcing bars. It was unclear how reinforcing bars affect impact resistance. Nonlinear analysis was conducted to investigate the effect of the reinforcing bars. This showed that if the reinforcing bar and the projectile do not come into direct contact, the influence of the reinforcing bars might be insignificant. The results of this analysis conform with the experimental results. However, if there is direct contact with reinforcing bars, penetration can be suppressed.
- 12) It was confirmed that projectile shape affected the penetration depth and the tunneling depth. Again using nonlinear analysis, it was found that impact resistance was not significantly affected when impacted by projectiles of the same shape but different sizes. However, when using

projectiles with equal weight but varying aspect ratios, a deeper penetration depth was observed for longer projectiles with a larger aspect ratio. This is believed to be an effect of energy concentration, and is reflected in the new impact formula as the projectile shape factor.

References

1. Abdel-Kader, M. and Fouda, A. (2014). “Effect of Reinforcement on the Concrete Panels to Impact of Hard Projectiles,” *International Journal of Impact Engineering*, Vol. 63, pp. 1-17.
2. ACE. (1946). *Fundamentals of Protective Structures*, Report AT120 AT1207821, Army Corps of Engineering.
3. ACI Committee 224. (2001). *Control of Cracking in Concrete Structures (ACI 224R-01)*, American Concrete Institute, Farmington Hills, MI, 46 pp.
4. ACI Committee 318. (2014). *Building Code Requirement for Structural Concrete and Commentary (ACI 318-14)*, American Concrete Institute, Farmington Hills, MI, 520 pp.
5. ACI Committee 544. (2009). *Design Considerations for Steel Fiber Reinforced Concrete (ACI 544.4R-88 (Reapproved 2009))*, American Concrete Institute, 2009.
6. Almusallam, T. H., Siddiqui, N. A., Iqbal, R. A., and Abbas, H. (2013). “Response of Hybrid-Fiber Reinforced Concrete Slabs to Hard Projectile

- Impact,” *Internal Journal of Impact Engineering*, Vol. 58, pp. 17-30.
7. Amirikian, A. (1950). *Design of Protective Structures*, Report NT-3726, Bureau of Yards and Dock, Department of the Navy.
 8. Ammann, O. and Whitney, C. (1963). *Industrial Engineering Study to Establish Safety Design Criteria for Use in Engineering of Explosive Facilities and Operations*, Report for Picatinny Arsenal, Ammann and Whitney Consulting Engineers.
 9. Anderson Jr., J. D. (2006). *Hypersonic and High Temperature Gas Dynamics (2nd Edition)*, American Institute of Aeronautics and Astronautics, USA, 811 pp.
 10. ANSYS. (2011). *Explicit Dynamics*, Brochure, 8 pp.
 11. ANSYS. (2015). *Introduction to ANSYS Explicit STR - Lecture 5 Material Models*.
 12. ANSYS. (2017). AUTODYN-Help Menu, *ANSYS release 18.2 Documentation for ANSYS Workbench*, Century Dynamics Inc., Concord
 13. Architectural Institute of Korea. (2016). *Korean Building Code and Commentary 2016 (KBC-16)*, Kimoon dang Publishing Company, Korea, 1221 pp. (in Korean).
 14. ASCE. (1985). *Design of Structures to Resist Nuclear Weapons Effects (Manual 42)*, American Society of Civil Engineers.
 15. ASCE. (1997). *Guidelines for Blast-Resistant Building in Petrochemical*

Facilities, American Society of Civil Engineers.

16. ASCE. (1999). *Design for Physical Security*, State of the Practice Report, American Society of Civil Engineers.
17. Bangash, M. Y. H. (1993). *Impact and Explosion*, Blackwell Science, Oxford, 880 pp.
18. Bangash, M. Y. H. (2001). *Manual of Numerical Methods in Concrete-Modelling and Applications Validated by Experimental and Site-Monitoring Data*, Thomas Telford, 918 pp.
19. Barr, P. (1990). *Guidelines for the Design and Assessment of Concrete Structures subjected to Impact*, Report, UK Atomic Energy Authority, Safety and Reliability Directorate, HMSO, London.
20. Bechtel Power Corporation (1974). *Design of Structures for Missile Impact*, Topical Report BC-TOP-9A Revision 2.
21. Ben-Dor, G., Dubinsky, A., and Elperin, T. (2013), *High-Speed Penetration Dynamics Engineering Models and Methods*, World Scientific Publishing Company, 696 pp.
22. Beppu, M., Miwa, K., Itoh, M., Katayama, M., and Ohno, T. (2008). "Damage Evaluation of Concrete Plates by High-Velocity Impact," *International Journal of Impact Engineering*, V. 35, No. 12, pp. 1419-1426.
23. Bergman, S. G. A. (1950). *Inträngning Av Pansarbrytande Projektiler Och Bomber I Armerad Betong*, FortF Rapport B2, Stockholm.

24. Berriaud, C. Sokolovsky, A., Gueraud, R., Dulac, J., and Labrot R. (1978). "Local Behaviour of Reinforced Concrete Walls under Missile Impact," *Nuclear Engineering and Design*, Vol. 45, pp. 457-469.
25. Beth R. A. (1941). *Penetration of Projectiles in Concrete*, Committee on Passive Protection Against Bombing, Interim Report No. 3.
26. Bishop, R. F., Hill, R., and Mott, N. F. (1945). "The Theory of Indentation and Hardness Test," *Proceedings of the Physical Society*, Vol. 57, Part 3, pp. 147-159.
27. BNFL. (2003). *Reinforced concrete slab local damage assessment, R3 Impact Assessment Procedure*, Appendix H, Vol. 3, Magnox Electric plc & Nuclear Electric Limited.
28. Chelapati, C. V., Kennedy, R. P. and Wall, I. B. (1972). "Probabilistic Assessment of Aircraft Hazard for Nuclear Power Plant," *Nuclear Engineering and Design*, Vol. 19, No. 2, pp.333-364.
29. Chen, Q. and Andawes, B. (2012). "3D Finite Element Modeling to Study the Behavior of Shape Memory Alloy Confined Concrete," *Proceedings of 15th World Conference on Earthquake Engineering (15 WCEE)*, 15 WCEE, Lisboa, Portugal.
30. Chen, W. F. (1982). *Plasticity in Reinforced Concrete*, McGraw Hill, 474 pp.
31. Chen, X. W. and Li, Q. M. (2002). "Deep Penetration of A Non-Deformable Projectile with Different Geometrical Characteristics,"

International Journal of Impact Engineering, Vol. 27, pp. 619-637.

32. Choi, K.-K. and Park, H.-G. (2010). "Shear Strength Model for Interior Flat Plate-Column Connections," *Journal of the Korea Concrete Institute*, Vol. 22, No. 3, pp. 345-356. (in Korean)
33. Choi, K.-K., Kim, S.-H., Kim D.-H., and Park H.-G. (2011). "Direct Punching Shear Strength Model for Interior Slab-Column Connections and Column Footings with Shear Reinforcement," *Journal of the Korea Concrete Institute*, Vol. 23, No. 2, pp. 159-168. (in Korean)
34. Choi, K.-K., Park, H.-G., and Kim, H.-M. (2010). "Shear Strength Model for Slab-Column Connections," *Journal of the Korea Concrete Institute*, Vol. 22, No. 4, pp. 585-593. (in Korean)
35. Choi, K.-K., Shin, D.-W., and Park, H.-G. (2014). "Shear-Strength Model for Slab-Column Connections Subjected to Unbalanced Moment," *ACI Structural Journal*, Vol. 111, No. 3, pp. 491-502.
36. Comité Euro-International du Béton (CEB). (1988). *Concrete Structures under Impact and Impulsive Loading*, Synthesis report, CEB Bulletin No. 187, 184 pp.
37. Dancygier, A. N. and Yankelevsky, D. Z. (1996). "High Strength Concrete Response to Hard Projectile Impact," *International Journal of Impact Engineering*, Vol. 18, No. 5, pp. 583-599.
38. Department of Army. (1986). *Fundamentals of Protective Design for Conventional Weapons (TM 5-855-1)*.

39. Department of Army. (1990). *Structures to Resist the Effects of Accidental Explosions (TM 5-1330)*.
40. Drdlová, M., Buchar, J., Řídký, R., and Krátký, J. (2015). “Blast Resistance Characteristics of Concrete with Different Types of Fibre Reinforcement,” *Structural Concrete*, Vol. 16, No. 4, pp. 508-517.
41. Eligenhausen, R., Popov, E. P., and Bertero, V. V. (1983). *Local Bond Stress-Slip Relationships of Deformed Bars under Generalized Excitations*, Earthquake Engineering Research Council Report No. 83/23, University of California, Berkeley, Berkeley, CA, 1983, 162 pp.
42. EPTC. (2017). *Introduction of Extreme Performance Testing Center*, brochure, Extreme Performance Testing Center. (in Korean)
43. Ezeldin, A. S. and Balaguru, P. N. (1992). “Normal-and High-Strength Fiber-Reinforced Concrete under Compression,” *Journal of Materials in Civil Engineering*, Vol. 4, No. 4, pp. 415-429.
44. Feng, J., Li, W., Wang, X., Song, M., Ren, H., and Li, W. (2015). “Dynamic Spherical Cavity Expansion Analysis of Rate-Dependent Concrete Material with Scale Effect,” *International Journal of Impact Engineering*, Vol. 84, pp. 24-37.
45. fib. (2010). *fib Model Code for Concrete Structures 2010 (fib Model Code 2010)*, Ernst & Sohn, Germany, 420 pp.
46. Folsom, E. N. Jr. (1987). *Projectile Penetration into Concrete with An Inline Hole*, Report UCRL-53786, Lawrence Livermore National

Laboratory.

47. Forrestal M. J. and Luk V. K. (1988). "Dynamic Spherical Cavity-Expansion in a Compressible Elastic-Plastic Solid," *Journal of Applied Mechanics*, Vol. 55, pp. 275-297.
48. Forrestal M. J., Altman, B. S., Cargile, J. D., and Hanchak, S. J. (1994). "An Empirical Equation for Penetration Depth of Ogive-Nose Projectiles into Concrete Targets," *International Journal of Impact Engineering*, Vol. 15, No. 4, pp. 395-405.
49. Forrestal, M. J. and Luk, V. K. (1992). "Penetration into Soil Targets," *International Journal of Impact Engineering*, Vol. 12, No. 3, pp. 427-444.
50. Forrestal, M. J. Frew, D. J., Hanchak, S. J., and Brar, N. S. (1996). "Penetration of Grout and Concrete Targets with Ogive-Nose Steel Projectiles," *International Journal of Impact Engineering*, Vol. 18, No. 5, pp. 465-476.
51. Forrestal, M. J., Altman, B. S., Cargile, J. D., and Hanchak, S. J. (1994). "An Empirical Equation for Penetration Depth of Ogive-Nose Projectiles into Concrete Targets," *International Journal of Impact Engineering*, Vol. 15, No. 4, pp. 395-405.
52. Forrestal, M. J., Frew, D. J., Hickerson, J. P., and Rohwer, T. A. (2003). "Penetration of Concrete Targets with Deceleration-Time Measurements," *International Journal of Impact Engineering*, Vol. 28, pp. 479-497.
53. Frew, D. J., Forrestal, M. J., and Cargile, J. D. (2006). "The Effect of

- Concrete Target Diameter on Projectile Deceleration and Penetration Depth,” *International Journal of Impact Engineering*, Vol. 32, pp. 1584-1594.
54. Frew, D. J., Hanchak, S. J., Green, M. L., and Forrestal, M. J. (1998). “Penetration of Concrete Targets with Ogive-Nose Steel Rods,” *International Journal of Impact Engineering*, Vol. 21, No. 6, pp. 489-497.
55. Ha, Y. J., Kang, S. H., and Hong, S. G. (2015). “An Experimental Study on the Chromaticity and Compressive Strength of Ultra High Performance Color Concrete Mixed with Pigments,” *Proceedings of 2015 Fall Korean Concrete Institute Convention*, Vol. 27, No. 2, pp. 603-604. (in Korean)
56. Haladar, A. and Miller, F. J. (1982). “Penetration Depth in Concrete for Nondeformable Missiles,” *Nuclear Engineering and Design*, Vol. 71, pp. 79-88
57. Haldar, A. and Hamieh, H. (1984). “Local Effect of Solid Missiles on Concrete Structures,” *ASCE Journal of Structural Engineering*, Vol. 110, No. 5, pp. 948-960
58. Hanaor, D. A. H., Gan, Y., and Einav, I. (2015). “Contact Mechanics of Fractal Surfaces by Spline Assisted Discretisation,” *International Journal of Solids and Structures*, Vol. 59, pp. 121–131.
59. Healey, J. J. and Weissman S. (1974). “Primary Fragment Characteristics and Impact Effects in Protective Design,” *Minutes of the 16th Explosives Safety Seminar, Department of Defense Explosives Safety Board*, pp.

1107-1141.

60. Hertz, H. (1881). "Über die berührung fester elastischer Körper (On the contact of rigid elastic solids)," *Journal Für Die Reine Und Angewandte Mathematik* 92, pp. 156-171.
61. Hong, S. and Kang, T. H.-K. (2016). "Dynamic Strength Properties of Concrete and Reinforcing Steel Subject to Extreme Loads," *ACI Structural Journal*, Vol. 113, No. 5, pp. 983-995.
62. Hopkins, H. G. (1960). "Dynamic Expansion of Spherical Cavities on Metal," Chapter III, *Progress in Solid Mechanics*, Vol. 1, Eds., Sneddon, I. N. and Hill, R., North-Holland Publishing Company, Amsterdam, New York.
63. Hrynyk T. D. and Vecchio F. J. (2014). "Behavior of Steel Fiber-Reinforced Concrete Slabs under Impact Load," *ACI Structural Journal*, Vol. 111, No. 5, pp. 1213-1224
64. Hu, G., Wu, J., and Li, L. (2016). "Advanced Concrete Model in Hydrocode to Simulate Concrete Structures under Blast Loading," *Research Article in Advances in Civil Engineering*, Vol. 2016, 13 pp. <http://dx.doi.org/10.1155/2016/7540151>
65. Hughes, G. (1984). "Hard Missile Impact on Reinforced Concrete," *Nuclear Engineering and Design*, Vol. 77, pp. 23-25.
66. Hwang, H.-J., Eom, T.-S., and Park, H.-G. (2015). "Bond-Slip Relationship of Beam Flexural Bars in Interior Beam-Column Joints,"

ACI Structural Journal, Vol. 112, No. 6, pp. 827-837.

67. Hwang, H.-J., Kim, S., and Kang, T.H.-K. (2017). "Energy-Based Penetration Model for Local Impact Damaged Concrete Members," *ACI Structural Journal*, Vol. 114, No. 5, pp. 1189-1200.
68. Ito, C., Ohnuma, H., Sato, K., and Takano, H. (1984). *Dynamic behavior of reinforced concrete beam subjected to impact load*. CRIEPI Report No.383046, Denryoku Chuo Kenkyusho Hokoku, 42 pp. (in Japanese)
69. Jalasutram, S., Sahoo, D. R., and Mastsagar, V. (2017). "Experimental Investigation of the Mechanical Properties of Basalt Fiber-Reinforced Concrete," *Structural Concrete*, Vol.18, No. 2. pp. 292-302.
70. Jankov, Z. D., Shanahan J. A., and White, M. P. (1976), "Missile Tests of Quarter-Scale Reinforced Concrete Barriers," *Proceedings of the Symposium on Tornadoes*, Assessment of knowledge and implications for Man, Institute for Disaster Research, Texas Tech University, Lubbock, TX
71. Joh, C., Kwark, J. W., Kwak, I. J., Kang, J., Lee, J., and Choi, E. S. (2012). "Design Technology of K-UHPC," *Proceedings of the Korean Concrete Institute*, Vol. 24, No. 2, pp. 863-864. (in Korean)
72. Johnson, K. L, 1985, *Contact mechanics*, Cambridge University Press.
73. Johson, G. R. and Cook, W. H. (1985). "Fracture Characteristics of Three Metals Subjected to Various Strains, Strain rates, Temperatures and Pressures," *Engineering Fracture Mechanics*, Vol. 21, No. 1, pp. 31-

48.

74. Kahanji, C., Ali, F., and Nadjai, A. (2016). "Structural Performance of Ultra-High-Performance Fiber-Reinforced Concrete Beams," *Structural Concrete*, Vol. 18, pp. 249-258.
75. Kang, S. H., Kim S. J., and Hong, S. G. (2015). "Development of Ultra High Performance White Concrete (UHPWC) for Cladding of Busan Opera House," *Proceedings of 2015 Spring Korean Concrete Institute Convention*, Vol. 27, No. 1, pp. 337-338. (in Korean)
76. Kang, T. H.-K., Kim, W., Massone, L. M., and Galleguillos, T. A. (2012). "Shear-Flexure Coupling Behavior of Steel Fiber-Reinforced Concrete Beams," *ACI Structural Journal*, Vol. 109, No. 4, pp. 435- 444.
77. Kar, A. K. (1978). "Local Effects of Tornado Generated Missiles," *ASCE Journal of Structural Engineering*, Vol. 4, No. 5, pp. 809-816.
78. Kenndy R. P. (1996). *Effects of an Aircraft Crash into a Concrete Reactor Containment Building*, Anaheim, CA: Holmes & Narver Inc.
79. Kennedy, R. P. (1976). "A Review of Procedures for the Analysis and Design of Concrete Structures to Resist Missile Impact Effects," *Nuclear Engineering and Design*, Vol. 37, pp. 183-203.
80. Kim, H. S., Kim G. Y., Choe, G. C., Kim, J. H., Han, S. H., and Yoo, J. C. (2014). "Local Fracture Properties of Fiber Reinforced Concrete by the Impact of Small Projectile," *Proceedings of 2014 Fall Korean Concrete Institute Convention*, Vol. 26, No. 2, pp. 537-538. (in Korean).

81. Kim, H.-S., Kim, G.Y., Koo, K.-M., Cheo, G.-C., Yoo, J.-C., and Kim, M.-H. (2013). "Evaluation of Local Failure of Concrete by High-Velocity Impact", *Proceeding of Architectural Institute of Korea*, Vol.33, No.2, pp.617-618. (in Korean)
82. Kim, S., Kang, T. H.-K., and Yun, H. D. (2017). "Evaluation of Impact Resistance of Steel Fiber-Reinforced Concrete Panel Using Design Equations," *ACI Structural Journal*, Vol. 114, No. 4, pp. 911-921.
83. Kim, S., Kang, T. H.-K., Jang, S. J., Kim, K. S., and Yun, H. D. (2018). "High-Velocity Impact Experiment of Concrete Panels Reinforced with Crimped Wire Mesh and Steel Fibers," *Structural Concrete*, 2018, pp. 1-11 (first published)
84. Kim, T.-W. and Hahm, H.-G. (2015). "The Strength Properties Activated Granulated Ground Blast Furnace Slag with Aluminum Potassium Sulfate and Sodium Hydroxide," *Journal of the Korea Concrete Institute*, Vol. 27, No. 2, pp. 95-102. (in Korean)
85. Kim, U. S. (2009). "ANSYS EXPLICIT STR for Easy and Convenient Collision Analysis," *Magazine of Cad & Graphics*, pp. 164-169. (in Korean)
86. Koh, K. T., Ryu, G. S., Park, J. J., and Kim, S. W. (2012). "Material Characteristics of K-UHPC", *Proceedings of the Korean Concrete Institute*, Vol. 24, No. 2, pp. 861-862. (in Korean)
87. Kojima, I. (1990). "An Experimental Study on Local Behavior of Reinforced Concrete Slabs to Missile Impact," *Nuclear Engineering and*

Design, Vol. 130, No. 2, pp. 121-132.

88. Kolsky, H. (1963). *Stress Waves in Solid*, Dover Publications, Inc. 224 pp.
89. Kong, X. Z., Wu, H., Fang, Q., and Peng, Y. (2017). “Rigid and Eroding Projectile Penetration into Concrete Targets Based on an Extended Dynamic Cavity Expansion Model,” *International Journal of Impact Engineering*, Vol. 100, pp. 13-22.
90. Korea Agency for Technology and Standards. (2010a). *Method of Test for Flexural Strength of Concrete, KS F 2408:2010*, Korea Standards Association, 11 pp. (in Korean)
91. Korea Agency for Technology and Standards. (2010b). *Concrete Compressive Strength Test Method, KS F 2405:2010*, Bulletin No. 2010-0654, Korea Standards Association, 6 pp. (in Korean)
92. Korea Agency for Technology and Standards. (2014). *Standard Test Method for Making and Curing Concrete Specimens KS F 2403:2014*, Korea Standards Association, 8 pp. (in Korean)
93. Korea Agency for Technology and Standards. (2016). *Standard Test Method for Tensile Splitting Strength of Concrete KS F 2423:2016*, Korea Standards Association, 13 pp. (in Korean)
94. Korea Agency for Technology and Standards. (2018). *Carbon steel pipes for pressure service KS D 3562:2018*, Korea Standards Association, 123 pp. (in Korean)

95. Korea Concrete Institute. (2012). *K-UHPC Structure Design Guideline*, Korea Concrete Institute, 68 pp. (in Korean)
96. Krauthammer, T. (2008). *Modern Protective Structures*, Taylor & Francis Group, LLC., 393 pp.
97. Lee, C. H. (2007). "Structural Behavior and Progressive Collapse Prevention under Abnormal Extreme Loading," Special article, *Magazine of Architectural Institute of Korea*, Vol. 51, No. 8, pp. 15-15. (in Korean)
98. Lee, C.-D., Kim, W.-J., Cho, K.-S., and Kim, J.-H. (2011). "Design of UHPC (Ultra High Performance Concrete) Girder Cable Stayed Footbridge," Technology Articles, *Magazine of Korean Concrete Institute*, Vol. 23, No. 5, pp. 38-44. (in Korean).
99. Lee, S., Cho, S.-S., Jeon, J.-E., Kim, K.-Y., and Seo, K.-S. (2013). "Impact Analyses and Tests of Concrete Overpacks of Spent Nuclear Fuel Storage Casks," *Nuclear Engineering and Technology*, Vol. 46, No. 1, pp. 73-80.
100. Lee, S., Kim, G., Kim, H. Son, M., Choe, G., and Nam, J. (2018). "Strain Behavior of Concrete Panels Subjected to Different Nose Shapes of Projectile Impact," *Materials*, Vol. 11, No. 3, pp. 1-15.
101. Li Q. M. and Chen, X. W. (2003). "Dimensionless Formulae for Penetration Depth of Concrete Target impacted by a non-deformable Projectile," *Internal Journal of Impact Engineering*, Vol. 28, pp. 93-116

102. Li, Q. M., Reid, S. R., Wen, H. M., and Telford, A. R. (2005). "Local Impact Effects of Hard Missiles on Concrete Targets," *International Journal of Impact Engineering*, Vol. 32, pp. 224-284
103. Li, Q. M. and Tong, D. J. (2003). "Perforation Thickness and Ballistic Limit of Concrete Target Subjected to Rigid Projectile Impact," *Journal of Engineering Mechanics*, Vol. 129, No. 9, pp. 1083-1091.
104. Lowes, L. N. and Altoontash, A. (2003). "Modeling Reinforced-Concrete Beam-Column Joints Subjected to Cyclic Loading," *ASCE Journal of Structural Engineering*, Vol. 129, No. 12, pp. 1686-1697.
105. Luk, V. K. and Forrestal, M. J. (1987). "Penetration into Semi-Infinite Reinforced-Concrete Targets with Spherical and Ogival Nose Projectiles," *International Journal of Impact Engineering*, Vol. 6, No. 4, pp. 291-301.
106. Musmar, M. (2013). "Tensile Strength of Steel Fiber Reinforced Concrete," *Contemporary Engineering Sciences*, Vol. 6, No. 5, pp. 225-237.
107. NDRC. (1946). *Effect of Impact and Explosion*, Summary Technical Report of Division 2, Vol. 1, National Defense Research Committee.
108. Park, H.-G., Choi, K.-K., and Chung, L. (2011). "Strain-Based Strength Model for Direct Punching Shear of Interior Slab-Column Connections," *Engineering Structures*, Vol. 33, pp. 1062-1073.
109. POSCO. (2012). *Protection of Buildings against Explosions*, Gumi Book, 147 pp.

110. Qi, C. Z., Wang, M. Y. and Qian, Q. H. (2009). "Strain-Rate Effects on The Strength and Fragmentation Size of Rocks," *International Journal of Impact Engineering*, Vol. 36, pp. 1355-1364.
111. Ramesh, K. T. (2008). "High Rates and Impact Experiments," *Chapter 33 in Springer Handbook of Experimental Solid Mechanics*, pp. 929-960.
112. Ramesh, K. T. and Narasimhan, S. (1996). "Finite Deformations and the Dynamic Measurement of Radial Strains in Compression Kolsky Bar Experiments," *International Journal of Solids and Structures*, Vol. 33, No. 25, pp. 3723-3738.
113. Reid, S. R. and Wen, H. M. (2001). *Predicting Penetration, Cone Cracking, Scabbing and Perforation of Reinforced Concrete Targets Struck by Flat-faced Projectiles*, UMIST Report ME/AM/02.01/TE/G /018507/Z.
114. Riedel, W. (2004). *Beton unter Dynamicschen Lasten: Meso- und makromechanische Modelle und ihre Parameter*, Fraunhofer EMI, IRB – Verlag, ISBN 978-3-8167-6340-6
115. Riedel, W., Thoma, K., Hiermaier, S., and Schmolinske E. (1999). "Penetration of Reinforced Concrete by BETA-B-500, Numerical Analysis using a New Macroscopic Concrete Model for Hydrocodes," *Proceeding of Internationales Symposium, Interaction of the Effects of Munitions with Structures*, Berlin Strausberg, pp. 315-322.
116. Riedel, W., Kawai, N., and Kondo, K. (2009). "Numerical Assessment for Impact Strength Measurements in Concrete Materials," *International*

Journal of Impact Engineering, Vol. 36, No. 2, pp. 283-293.

117. Sneddon, I. N. (1965). "The Relation Between Load and Penetration in the Axisymmetric Boussinesq Problem for a Punch of Arbitrary Profile," *International Journal of Engineering Science*, Vol. 3, No.1, pp. 47–57.
118. Soe, K. T., Zhang, Y. X., and Zhang, L. C. (2013). "Impact Resistance of Hybrid-Fiber Engineered Cementitious Composite Panels," *Composite Structures*, Vol. 104, pp. 320-330.
119. Teland, J. A. (2007). *A Review of Empirical Equations for Missile Impact Effects on Concrete*, Report FFI/RAPPORT-97/05856, Norwegian Defence Research Establishment, 38 pp.
120. Society of Material Science of Japan. (1988). *Impact Engineering*, Nikkan Kogyo Shimbun Ltd. (in Japanese)
121. Thoma, K. (2009). *Predictive Modeling of Dynamic Processes*, Springer, 460 pp.
122. Tolch, N. A. and Bushkovitch, A. V. (1947). *Penetration and Crater Volume in Various Kinds of Rocks as Dependent on Caliber, Mass, Striking Velocity of Projectile*, BRL Report No. 641.
123. Vretblad, B. (1988). "Penetration of Projectiles in Concrete According to FortH 1," *Proceedings from the Workshop on Weapon Penetration into Hard Targets* (Kjeller, Norway, 1988), Norwegian Defense Research Establishment (FFI).
124. Wang, Z. L., Zhu, H. H., and Wang, J. G. (2013). "Repeated-Impact

- Response of Ultrashort Steel Fiber Reinforced Concrete,” *Experimental Techniques*, Vol. 37, 2013, pp. 6-13.
125. Whiffen, P. (1943). *UK Road Research Laboratory Note No. MOS/311*, UK Road Research Laboratory
 126. Williams, J. A. and Dwyer-Joyce, R. S. (2000). “Contact Between Solid Surfaces,” *Chapter 3 in Modern Tribology Handbook*, Two Volume Set (Editor-in-Chief, Bhushan, B), CRC Press, pp. 121-162.
 127. Williams, M. S. (1994). “Modeling of Local Impact Effects on Plain and Reinforced Concrete,” *ACI Structural Journal*, Vol. 91, No. 2, pp.178-187.
 128. Yankelevsky, D. Z. (1997). “Local Response of Concrete Slabs to Low Velocity Missile Impact,” *International Journal of Impact Engineering*, Vol. 19, No. 4, pp.331-343.
 129. Yazici, S., Arel, H. S., and Tabak, V. (2013). “The Effects of Impact Loading on The Mechanical Properties of the SFRCs,” *Construction and Building Materials*, Vol. 41, pp. 68-72.
 130. Young, C. W. (1997). *Penetration Equations*, Report Sand97-2426, Distribution Category UC-705, Sandia National Laboratories, 24 pp.
 131. Zaidi, A. M. A., Latif, Q. B. A. I., Rahman, I. A., and Ismail, M. Y., (2010). “Development of Empirical Prediction formula for Penetration of Ogive Nose Hard Missile into Concrete Targets,” *American Journal of Applied Sciences*, Vol. 7, No. 5, pp. 711-716.

132. Zhang, M. H., Shim, V. P. W., Lu, G., and Chew, C. W. (2005). "Resistance of High-Strength Concrete to Projectile Impact," *International Journal of Impact Engineering*, Vol. 31, No. 7, pp. 825-841.
133. Zhang, S., Wu, H., Zhang, X., Liu, J., and Huang, F. (2017). "High-Velocity Penetration of Concrete Targets with Three Types of Projectiles: Experiments and Analysis," *Latin American Journal of Solids and Structures*, Vol. 14, No. 9., pp.1614-1628
134. Zhang, Y., Chen, W., Cheng, S., Zou, H., and Guo, Z. (2017). "Penetration of Rigid Projectiles into Concrete Based on Improved Cavity Expansion Model," *Structural Concrete*, Vol. 18, No. 6, pp. 974-985.

국 문 초 록

고속충돌 하중을 받는 고성능 콘크리트 패널의 내충격성 평가 및 설계식 개발

콘크리트 구조물의 안전을 위협하는 충돌 및 폭발 사고가 빈번하게 발생하고 있어서 충격과 폭발에 관한 많은 연구가 진행되고 있지만, 고속충돌 하중을 받는 콘크리트의 파괴 메커니즘은 복잡하기 때문에 콘크리트의 손상을 예측하기 쉽지 않다. 본 논문에서는 콘크리트의 내충격성 평가를 위해 다양한 변수를 가지는 실험과 해석 연구를 수행하였으며, 국부 손상 정도를 예측할 수 있는 새로운 국부충격 설계식을 제안하고자 한다.

충분히 연구되지 않은 다양한 변수들의 내충격성능을 평가하기 위해서, 서로 다른 3번의 실험을 수행하였다. 첫번째 실험은 강섬유와 와이어 매쉬가 내충격성 향상에 얼마나 효과가 있는지 파악하고자 하였으며, 추가적으로 골재 크기와 패널 두께 그리고 비상체 속도를 변수로 하였다. 두 번째 실험은 콘크리트 강도와 탄환의 형태에 따른 내충격성능을 파악하고자, 콘크리트 강도 35 ~ 120 MPa 그리고 5종류의 탄환을 사용하였다. 세번째 실험은 180 MPa 초고성능 콘크리트를 사용한 얇은 패널의

내충격성능을 평가하였다. 또한 두번째, 세번째 실험을 위해서 소형 충돌 실험 장치를 개발하였다.

실험 결과를 바탕으로 충돌 메카니즘을 총 6가지(비상체 변형에너지, 탄성관입 저항에너지, 패널 전체 변형에너지, 전면파괴 저항에너지, 터널 저항에너지, 배면파괴 저항에너지)로 구분하였고, 각각의 단계의 에너지를 수식으로 정리하였다. 에너지 보존의 법칙과 충돌 메카니즘에 관여하는 에너지를 활용하여 관입 깊이, 배면 파괴 깊이, 배면 박리 한계 두께 그리고 관통 한계 두께를 예측할 수 있는 새로운 국부충돌 설계식을 제시하였다. 본 연구와 다른 연구자들의 실험 결과를 통해 제시된 식을 검증하였다.

실험에서 철근이 내충격성에 미치는 영향에 대해 명확하게 검토되지 못하였기 때문에, 철근이 철근콘크리트 패널의 내충격성에 얼마나 영향이 있는지 파악하기 위하여 비선형 해석을 수행하였다. 추가적으로 실험에서 검증하기 부족하였던 비상체의 크기, 패널의 넓이와 두께가 내충격성에 어떻게 작용하는지도 비선형 해석을 통해 검토하였다.

핵심용어: 충돌, 국부 충격 설계식, 고속충돌 하중, 내충격성, 철근콘크리트 슬래브, dynamic cavity expansion model, 에너지 보존의 법칙; 에너지 밀도, 헤르츠 접촉 이론, 소형 충격 시험 장치.

학번: 2014-30188

Acknowledgement

It is acknowledged that the academic advisor of this doctoral dissertation is Prof. Thomas Kang in the Department of Architecture & Architectural Engineering at Seoul National University.